Advanced Ultracold Sources for Atomic Physics and Atom Interferometry

Julien Dugué

DÉPARTEMENT DE PHYSIQUE
DE L'ÉCOLE NORMALE SUPÉRIEURE

LABORATOIRE KASTLER-BROSSEL

THÈSE DE DOCTORAT DE L'UNIVERSITÉ PARIS VI
EN CO-TUTELLE AVEC L'AUSTRALIAN NATIONAL UNIVERSITY

Spécialité : Physique Quantique

présentée par

Julien DUGUÉ

Pour obtenir le grade de

Docteur de l'Université Pierre et Marie Curie (Paris VI)

Sujet de la Thèse:

Sources Ultrafroides Avancées
pour l'Interférométrie et la Physique Atomiques

Soutenue le 25 juin 2009 devant le jury composé de :

Hans BACHOR	Président
Michèle LEDUC	Co-Directrice de Thèse
John CLOSE	Co-Directeur de Thèse
Isabelle BOUCHOULE	Rapporteur
Peter HANNAFORD	Rapporteur
Anne-Marie CAZABAT	Examinateur

Acknowledgements

During the realization of this thesis I had the opportunity to work on both sides of the world, getting help and support from many colleagues and friends. To these people I would like to say thank you:

First, I would like to thank my two supervisors Michèle Leduc (Paris) and John Close (Canberra) for giving me the opportunity to work in their research groups, in an exciting and fast moving research field. I met Michèle in the middle of the australian desert when I was a student doing a training period with John, so I guess I was meant to start my thesis in collaboration between both groups. I am very grateful for their constant support throughout my PhD work. Michèle and John were always very helpful and encouraging, and despite all their other commitments they had always enough time for me.

I am very much indebted to all members of the australian group where I started my PhD. In particular, I would like to thank Nick Robins for the important input he had contributed during my time in Canberra, both inside and outside the lab. His profound understanding of physics and his help in the lab had a great impact on this thesis. I would also like to thank Cristina Figl who I spent a lot of time working with in the lab. I would like to thank Matt Jeppesen, Simon Haine, Paul Summers, Mattias Johnsson and Graham Dennis not only for the many fruitful work discussions we shared, but also for creating a good working environment. Thanks also to Andrew Moylan for all our squash and soccer games.

I am equally indebted to all members of the french group where I completed the second part of my PhD. In particular, I thoroughly enjoyed working with Maximilien Portier, Juliette Simonet and Steven Moal. I would like to thank them for the great relationship we had, both inside and outside the lab. They are not only my colleagues, but also my friends. I had the chance to work with Jaewan Kim, Sanjukta Roy, Christian Buggle, Ennio Arimondo and Jérôme Beugnon. They all had an important input on the experiment and it was a pleasure working with them although our collaboration was rather short. I was fortunate to have several opportunities to interact in

discussions with Claude Cohen-Tannoudji. I always found this very inspiring and motivating therefore, I would like to thank him.

I would like to thank the members of the jury. Hans Bachor and Anne-Marie Cazabat have been of great help with the organization of the cotutelle. For their constant help, patience and support I would like say thanks to both of them. Thank you to Isabelle Bouchoule and Peter Hannaford for reading the manuscript so carefully and giving me comments to improve it. Including my co-supervisor, three members of the jury came a very long way from Australia to attend the defense in Paris. It was very much appreciated and I would like to thank them again for that.

I would like to thank all my family and friends. In particular I want to thank my parents for their unconditional support throughout my entire life. Also a special thanks to Guillaume and Arnaud for their long-term friendship.

Finally, there is no doubt that the biggest event that happened during my thesis was meeting Gráinne. Gráinne, my thanks to you cannot be expressed only in a few lines. It is the person you are who makes my life so happy. I am fortunate to have you...

CONTENTS

INTRODUCTION

The physics of ultra-cold atoms is a very rich area of investigation, where atomic, condensed matter, and many body physics meet together. The study of ultra-cold gases began more than twenty years ago, with a search for Bose-Einstein Condensation (BEC) in spin-polarized atomic hydrogen. The discovery of BEC in trapped clouds of alkali atoms (Rb [1], Na [2], Li [3]) in 1995 stimulated a tremendous boost in the field, as testified by the award of the 2001 Noble Prize to Eric Cornell, Wolfgang Ketterle and Carl Wieman. This very active field of research is the meeting point of several communities. The first generation of BEC experiments revealed that the behavior of dilute Bose-Condensed gases was governed by a unique matter wave-function. For the first time, it was possible to transpose to matter waves the concepts of spatial and temporal coherence, originally introduced to describe the properties of laser light. At present, experiments are to a large extent concentrated on the investigation of phenomena based on phase coherence. The present thesis aims at contributing to this field by creating advanced systems with the possibility of experimentally addressing fundamental questions of atomic physics. The work achieved during the time of this thesis was performed at the Australian National University in Canberra and at the Laboratoire Kastler-Brossel (ENS) in Paris. Consequently, the body of the thesis has two parts. First, the production of a ^{87}Rb atom laser, a matter wave of high brightness and coherence, opens the route towards atom interferometry experiments. Second, a BEC of metastable Helium atoms is planned to be transferred into a three-dimensional optical lattice, with the goal of studying the real-time dynamics of the quantum phase transition occurring in such a system. The two parts are motivated by a common theme, to provide advanced ultra-cold atom sources for precision measurement and for investigations in fundamental physics.

1. Atom Interferometry

The quest for more precise measurements is at the heart of the technological revolution experienced in the last half-century, and is mainly based on the manipulation of laser light. After optical lasers were first demonstrated in 1960 [4], they rapidly revolutionized many fields of physics such as optics and precision measurement. The main reasons for the importance of optical lasers are their unique coherence properties and high brightness, which offer significant advantages over thermal light sources, allowing precision interferometry experiments to be performed. They enabled non-linear optics and quantum optics as well as experimental investigations of quantum

information, quantum computing and quantum cryptography to name but a few. Technologies reliant on lasers are now an integral part of the lives of billions of people. One can think of the application of lasers as optical storage devices such as CDs and DVDs, fiber-optic communication or laser surgery.

Over the last decade, a somewhat similar level of control was gained over atoms. Compared to photons, atoms offer the advantage of having an intrinsically richer structure and of responding far more strongly to gravity, rotations and external fields. Consequently, matter-wave interferometry was envisaged for its potential to be an extremely sensitive probe for inertial forces [5] and inertial sensors like gyroscopes and accelerometers started to develop. In 1991, atom inteference techniques were used in proof-of-principle work to measure rotations [6] and accelerations [7]. Atom interferometry is nowadays one of the most promising candidates for precision measurement and several groups are developing instruments for practical experiments. For instance, there has been a number of fundamentally important experiments making use of the atomic mass to measure the Newtonian gravitational constant G [8, 9] and the fine structure constant α [10, 11]. These experimental measurements were conducted with thermal atoms. Alternatively, atom interferometer gyroscopes and accelerometers have been produced from laser-cooled atoms in a magneto-optical trap and improved sensitivities have been achieved [12, 13]. Moreover, the realization of BEC and atom lasers has produced the matter-wave analog of the laser in optics and has opened new avenues to explore. Like the revolution brought by lasers in optical interferometry, it is expected that the use of condensed atoms will bring the science of atom optics, and in particular atom interferometry, to an unprecedented level of accuracy. For example, in a Mach-Zehnder gyroscope rotating at a frequency Ω_r, the phase shift between two interfering particles after propagating half of the loop is given by [14]

$$\Delta\phi = \frac{4\pi\Omega_r A}{v\lambda} \tag{1}$$

where A is the area enclosed by the interferometer, v is the velocity of the particles (either atoms or photons) and λ is the particle wavelength. For photons, $v\lambda = c\lambda$ with λ the wavelength of the laser beam, whereas for atoms, the relation $v\lambda = h/m$ defines the De Broglie wavelength of the matter-wave with m the mass of the atom and h Planck's constant. Therefore, for an interferometer of fixed area and a fixed number of round trips, the inherent sensitivity of a matter-wave gyroscope (e.g. with alkali atoms) will exceed that of a (e. g. visible) photon-based system by a

factor of $mc^2/\hbar\omega \sim 10^{11}$, where ω is the photon angular frequency ($\omega = 2\pi c/\lambda$) and $\hbar = h/2\pi$. In comparing the sensitivity of two interferometers, the signal to noise ratio per root Hertz of measurement bandwidth ($SNR/\sqrt{Hz}$) is the critical parameter. To improve this quantity, one must either increase the measured signal or decrease the noise from the measurement process. Ultimately, the noise in any interferometric measurement utilizing either an optical or an atom laser scales as the square root of the particle flux ($\sqrt{N}$ if N is the flux of particles). The phase sensitivity of an interferometric measurement is thus given by $\Delta\phi_{min} = 1/\sqrt{N}$ radians per root Hertz of measurement bandwidth. This minimum measurable phase decreases as the flux increases, scaling inversely as the square root of N. For instance, 1 W of visible light is roughly 10^{18} photons per second and the smallest rotation that could be measured is on the order of 10^{-9} rad/Hz$^{1/2}$. Comparatively, the flux from present day atom lasers is 12 orders of magnitude lower, with $N \sim 10^6$ atoms.s^{-1}. The smallest phase shift that can be measured is thus $\Delta\phi_{min} \sim 10^{-3}$ rad/Hz$^{1/2}$. In comparison with the photon interferometer, the atom laser looses 6 orders of magnitude in sensitivity due to lower flux, but gains 11 orders of magnitude in signal, making it 5 orders of magnitude more sensitive provided similar enclosed area and number of round trips can be achieved. Although optical gyroscopes are realized with enclosed areas orders of magnitude larger than atomic gyroscopes, advances towards truly continuous atom laser beams could narrow this existing gap. Higher precision gyroscopes could find practical applications in navigation, analysis of earth structures, in geophysical studies and also in tests of general relativity. Given that atomic beams offer enhanced sensitivity for many precision measurements, there still remains the option of using either thermal beams, laser cooled atoms, or atom lasers derived from a Bose-Einstein condensate. State selected thermal beams and laser cooled atoms have the advantage of relatively high flux, roughly three orders of magnitude higher than has been achieved with BEC sources [15, 16]. However, the narrow transverse velocity distribution in an atom laser combined with the low velocity of the atoms offer the possibility of a large momentum transfer beam splitting and a relatively large enclosed area in a compact device. Furthermore, in theory, the inherent non-linearity in an atomic beam (resulting from atom-atom interactions) can, if properly controlled through a Feshbach resonance, squeeze the shot noise or quantum noise on the beam through the atomic equivalent of the Kerr effect [17]. With current fluxes available in a standard BEC experiment ($\sim 10^6$ atoms per second), the potential improvement in signal to noise through squeezing is 3 orders of magnitude, at least in theory. It is the potential increase in sensitivity of precision interferometric measurements performed with an atom laser, that mo-

tivated the ANU group to study and further develop the atom laser towards a source that could be useful for precision interferometric measurement.

Six groups have carried out most of the experimental work on atom lasers so far. The MIT group led by Wolfgang Ketterle produced the first Radio-Frequency (RF) output-coupled atom laser [18]. The NIST group led by Bill Phillips produced and studied the first Raman output-coupled atom laser [19]. In the Institut d'Optique in Orsay, Alain Aspect's group made the first measurements of the transverse spatial mode of RF output-coupled atom lasers [20] and developed theory to describe and analyse this spatial mode [21]. The Orsay group has also studied guided atom lasers [22]. The ETH group at Zurich led by Tilman Esslinger measured the linewidth of RF out-coupled atom lasers [23]. In recent times, the ETH group has also concentrated on the quantum properties of the atom laser [24–26] and have measured the second order correlation function of an RF outcoupled atom laser [27]. Before commencing the work presented in this thesis, the ANU group concentrated on understanding the classical noise properties of high flux atom lasers [28–30] with the aim of developing the atom laser to a device that is truly useful. In more recent times, the ANU group has produced and studied the first pumped atom laser [31]. The LKB group led by David Guery Odelin have also made contributions to the investigation of the pumped or continuous atom laser [32–34]. The research presented in the first part of this thesis builds on the earlier work of these groups.

2. He BEC in optical lattices

The realization of BEC has enabled many fascinating experiments in which fundamental quantum mechanics was studied from a macroscopic system where the weakly interacting condensed atoms can be described by a single wave-function. Similarly, the atom laser, introduced in the previous section, can be described by a single macroscopic wave-function which can be precisely probed experimentally in interference experiments. Important advances towards control of atoms occurred when one started loading BECs into light-induced periodic potentials which exploit the interference pattern created by two or more overlapping laser beams and the resulting dipolar force exerted on the atoms. To transfer a Bose-Einstein condensate from a magnetic trap to an optical lattice, the condensate is illuminated by 1, 2 or 3 pairs of counter-propagating beams to form 1, 2 or 3D lattices respectively. Matter waves inside 3D optical lattices share many features with electrons in crystal lattices and form a model crystal. Optical lattices, however, have the major advantage that a large number of real-time lattice parameters can be controlled, mak-

ing them a versatile tool to study atomic physics properties in analogy with quantum phenomena predicted in solid state physics. The physics of BEC in optical lattices provides a rich playground for both theory and experiments [35, 36]. It has opened new views on solid state physics, fermion-boson mixtures [37, 38], vortices in lattices [39] and quantum computation [40]. In 1998, P. Zoller *et al.* suggested that it should be possible to convert a weakly interacting Bose gas (Superfluid) into a strongly interacting quantum state (Mott insulator) by loading atoms into an optical lattice [36]. A real breakthrough occurred with the experimental observation of this Superfluid-Mott insulator quantum phase transition by Greiner *et al.* [41, 42]. In the regime where the inter-atomic interaction in a lattice site is small compared to the tunneling process across the lattice, each atom is delocalized over the entire lattice characterizing a superfluid state. In this case, the atoms exhibit long-range phase coherence and can be described by a macroscopic wave-function. However, in the regime where the atom-atom interaction on a lattice site is no longer weak compared to the tunneling coupling, each atom is localized to a lattice site and the long-range phase coherence vanishes so that the atoms can no longer be described by a macroscopic wave-function. In this case, a novel quantum system of strongly correlated atoms is created which is well described by a Bose-Hubbard model.

Optical lattices have also been used to investigate various intriguing aspects of 1D quantum gases. The dimensionality of a macroscopic quantum system can have a large impact on its physical behavior, and it is therefore crucial to understand the role and effects of reduced dimensionality, which is made possible by the flexibility of optical lattices. The group of Tilman Esslinger in Zurich demonstrated that 1D quantum gases with extreme aspect ratios can be created and compared the oscillations of such clouds [43, 44]. In parallel, the group of Bill Phillips at NIST studied the initial effects on 1D quantum gases as they become more strongly interacting [45]. As 1D bosonic quantum gases become even more strongly interacting, it is possible to enter the regime of a Tonks-Girardeau gas [46] where repulsive interactions tend to separate individual atoms, causing the bosonic particles to exhibit fermionic properties. In addition to displaying novel quantum phases of many-body states, BEC in optical lattices also offer great opportunity for quantum information processing. Atoms in a Mott insulating state can be viewed as a natural quantum register in which each quantum bit is represented by a single atom and an interesting challenge is to construct quantum logic gates between atoms trapped in different lattice sites.

In our group at LKB, we plan to load optical lattices using metastable helium atoms. In the case of helium, Penning collisions produce helium ions (He^+ or He^{2+}) and an electron (e^-),

providing a sensitive method to detect the atomic collisions using a channel electron multiplier (channeltron). This represents a substantial advantage by comparison with alkali atoms, commonly detected by destructive optical observation methods (absorption or fluorescence). In particular, we aim at using Penning ionization to perform a real-time detection and study the kinetics of the Superfluid-Mott insulator transition.

3. Outline of the thesis

1. The first part of my thesis work presents the work achieved in the group of John Close at ANU between 2005 and 2007 using ^{87}Rb atoms to create atom laser beams as an advanced ultra-cold source for atom interferometry and precision measurement applications.

   - The first chapter is an introductory study defining the basic concepts of 'atom lasers'. A general overview on various techniques which can be used to create such beams of atoms from an initially trapped Bose-Einstein Condensate is given. Technical aspects of the out-coupling process are also discussed.

   - Chapter 2 presents a detailed description of the third generation of the BEC machine which co-workers and myself achieved during the first year of my time at ANU. The apparatus is based on a double Magneto-Optical Trap structure and involves physical transport of the atoms. This is followed by a presentation of a Raman optical setup which I implemented in order to transfer the trapped atoms into the atom laser mode.

   - In Chapter 3 I describe the production of a high flux atom laser beam with a nearly-Gaussian spatial mode using a Raman out-coupling technique. In contrast to a standard RF out-coupling method, the initial momentum transfer imparted to the atoms by the two optical Raman lasers reduces the divergence of the atomic beam and improves its spatial profile. The quality factor of a Raman atom laser (factor M^2 defined similarly as in optics) is shown to be largely improved compared to RF out-coupling, which is an important requirement for interferometric applications.

   - In chapter 4, a stable and efficient beam splitter for atom laser interferometry is implemented in a straightforward experimental setup. It is based on a Bragg diffraction process where the grating arises from each of the Raman beams (independently) and from a very small fraction of back-reflected light. Such beam-splitters are impor-

tant tools in any atom interferometry experiment and the one I present here has the advantage to be extremely simple and versatile.

- In the last chapter of the first part (Chapter 5), I investigate theoretically the dynamics of several atom laser systems out-coupled by an RF technique. For that purpose, I use a 1-dimensional model based on solving the Gross-Pitaevski equations. I validate the model by comparing the theoretical predictions to previous experiments carried out in our lab. I use it further to investigate important parameters of an atom laser such as population evolution, spatial dynamics and density fluctuations.

2. The second part of the thesis presents the work achieved in the group of Michèle Leduc at LKB-ENS between 2007 and 2009 with the aim of manipulating optically ^{4}He metastable atoms for the investigation of atomic physics.

- Chapter 6 presents a detailed description of the machine used to produce a BEC of metastable helium atoms. Co-workers and myself have achieved major improvements from the previously existing setup. In particular, a Channel Electron Multiplier was added in the Science cell where the BEC is produced, providing a non-destructive real-time detection method. The optical setup was also redesigned and entirely fiber-coupled in order to improve the stability of the system.

- In Chapter 7, I summarize the general principle and properties of optical trapping of neutral atoms. This is followed by a description of the laser configuration which we are currently implementing on our setup. Several experiments are planned using an optical dipole trap, in particular a measurement of inelastic rate constants in a gas of spin-polarized metastable helium, which I present with regard to theoretical predictions by Shlyapnikov *et al*.

- Finally, chapter 8 opens a perspective for loading metastable helium atoms in 3-dimensional optical lattices. The aim of our group is to investigate the dynamics of the Superfluid-Mott insulator quantum phase transition occurring in such a system. For that purpose, I describe the design of a new type of magnetic trap which we conceived and constructed in order to allow for atomic Bose-Einstein condensation to be compatible with in-situ loading of the condensed gas into the lattice.

CHAPTER 1

EXPERIMENTAL AND THEORETICAL BACKGROUND OF ATOM LASERS

This chapter summarizes the basic concepts of atom lasers. First, a brief description on the atom laser is given in analogy to the well-known optical laser. This is followed by a discussion on the different out-coupling methods which can be used to extract atoms from a magnetically trapped ultra-cold sample. Finally, the last two sections concentrate on important technical aspects, determined by the Rabi frequency, which should be considered when producing an atom laser beam.

1.1 GENERAL OVERVIEW OF ATOM LASERS

1.1.1 Background

In 1923, Louis De Broglie extended the particle-wave duality of light to any massive particle, defining the De Broglie wavelength of a particle as

$$\lambda_{dB} = \frac{h}{p} \tag{1.1}$$

where h is the Planck constant and p is the momentum of the particle. His intuition was later verified by the experiments of Davisson and Germer [47] who performed diffraction of electrons on a crystal. In the case of a gas in thermodynamic equilibrium, the mean quadratic velocity of the atoms is related to the temperature of the cloud T and the thermal De Broglie wavelength can be written as :

$$\lambda_{dB} = \sqrt{\frac{2\pi\hbar^2}{mk_BT}} \tag{1.2}$$

where m is the atomic mass, k_B the Boltzmann constant and $\hbar = h/2\pi$. λ_{dB} is commonly thought of as the spatial spread, or coherence length, of the atomic wave-packet with respect to the velocity distribution of the gas. Cooling of atoms therefore appears very appealing: first, it can reduce the velocity dispersion (divergence) of a sample of atoms and increase the coherence of the source; second, by increasing the atomic wavelength, wave effects are emphasized. It is only after 1980 that the new field of atom optics started to be developed, taking advantage of the

advent of optical lasers to provide efficient cooling of thermal clouds.

In 1995, a new state of matter was observed [1–3] from cooling an atomic sample to ex-tremely low temperatures. This Bose-Einstein Condensate (BEC) was predicted theoretically by A. Einstein [48] 70 years before its experimental realization. The theory of BEC is centered around the statistical mechanics of an ideal monoatomic gas and was inspired by the work of S. Bose on photon (which is a boson) statistics and the Planck radiation distribution law [49]. Following De Broglie's work, Einstein claimed that any bosonic particles should thus obey the same statistics as photons. As a result, the Bose-Einstein distribution function was formulated for a system of N non-interacting, indistinguishable bosonic atoms, giving the mean number of particles in the ith energy state as

$$n_i = \frac{1}{e^{(\varepsilon_i - \mu)/k_B T} - 1}$$ (1.3)

where ε_i is the particle energy in the ith state and k_B is the Boltzmann constant. The chemical potential μ and the temperature T reflect the constraints on the total number of particles N and the total energy E in the system [50, 51]. Below a certain critical temperature T_c, the lowest energy state of the system becomes macroscopically occupied. For a uniform Bose gas of non-interacting particles confined in a trap, the transition temperature at which this effect begins is

$$T_c = \frac{\hbar \bar{\omega}}{k_B} \left[\frac{N}{\zeta(3)} \right]^{1/3}$$ (1.4)

where $\bar{\omega} = (\omega_x \omega_y \omega_z)^{1/3}$ is the geometric mean of the trapping frequencies and ζ is the Riemann zeta function. The number of particles in the lowest energy state can finally be written as

$$N_0 = N[1 - (T/T_c)^{3/2}].$$ (1.5)

In a BEC, a large number ($N_0 \sim 10^6$) of ultra-cold dilute neutral atoms is confined by either a magnetic or an optical trapping potential and undergo a dramatic transition to quantum degen-eracy. Consequently, a macroscopic fraction of the atoms occupy the same coherent quantum state (usually the ground state of the trap). In this case, the De Broglie wavelength of each in-dividual atom becomes comparable to the size of the condensate so that the atoms are no longer indistinguishable but rather acquire collective properties which can be described by a unique wavefunction.
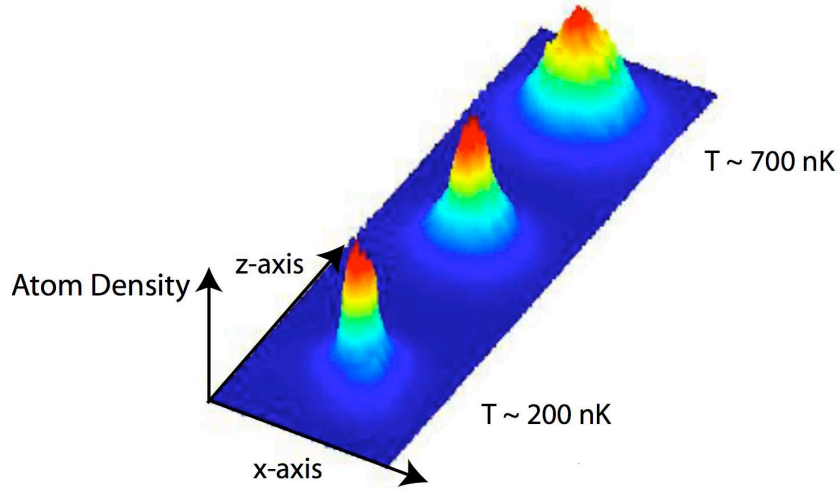
Figure 1.1: Demonstration of Bose-Einstein Condensation in a dilute alkali gas of ^{87}Rb atoms in the ANU experiment. The density distributions of each image are obtained from absorption imaging. The image on the right shows a thermal cloud of atoms just prior to condensation. The central image displays a characteristic change in the density distribution indicating the onset of a BEC. The left image shows an almost pure BEC.

A demonstration of Bose-Einstein condensation in a dilute alkali gas of ^{87}Rb atoms generated in our lab at ANU is shown figure 1.1 for a typical final temperature of $T = 200$ nK.

A consequence of Bose-Einstein condensation is that a matter-wave can be released from the trap without disturbing the initial coherence between the atoms. Due to the gravitational acceleration that they experience, a directional, bright and spectrally narrow beam of coherent out-coupled atoms can thus be created, which is commonly called an 'Atom Laser' (see figure 1.2). In this regime, the energy of the atoms, and thus the wavelength λ_{AL} of the atomic beam, far from the BEC after the initial mean-field driven acceleration, is dominated by the effect of gravity following

$$\frac{\hbar^2 k_{AL}^2}{2m} = mg\Delta z \tag{1.6}$$

where $k_{AL} = 2\pi/\lambda_{AL}$ is the atom wave number and Δz the distance over which the atoms have fallen. Finally, $\lambda_{AL} = h/(m\sqrt{2g\Delta z})$. The wavelength of the atom wave decreases as the atoms propagate under gravity so that it is only defined locally.

$\vec{g}$

Bose-Einstein Condensate
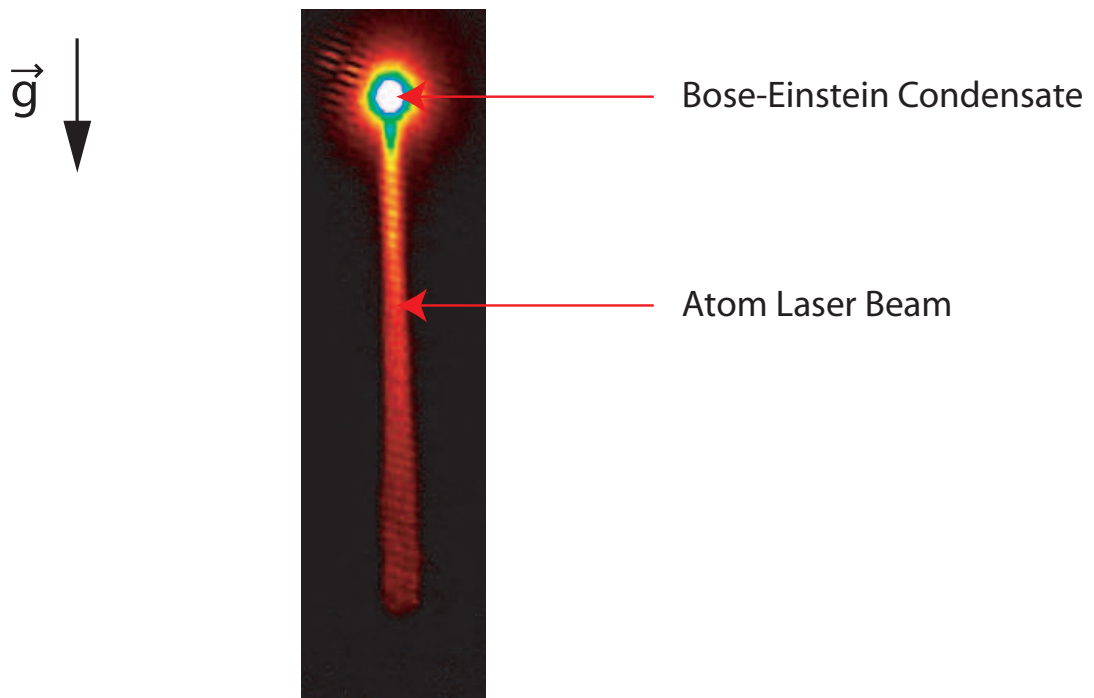
Atom Laser Beam

Figure 1.2: Atom laser produced in our lab after a long (10 ms) pulse of out-coupling. The atoms have fallen under gravity creating an atom laser beam 0.5 mm long. At the top of the figure is the BEC. The time of flight for imaging the system was on the order of 3 ms.

1.1.2   An Analogy with Optical Lasers

In the very general picture depicted in figure 1.3, the atom laser can be thought of as an analog to the well-known optical laser. The following points briefly outline this analogy:

- Just as the lasing mode in an optical laser is a source of coherent photons, the lasing mode of an atom laser is a BEC, a source of coherent atom waves.

- In an optical laser, the photons are held within a cavity created from two optical mirrors. Similarly, for an atom laser, the BEC is constrained by either a magnetic or an optical trapping potential.

- In an optical laser, the extraction of the beam can be achieved as one of the mirrors forming the cavity has been carefully chosen to partially transmit the light. Comparatively, atom laser beams are usually extracted by transferring the atoms from their initial magnetically trapped internal state into a state that does not interact with the trapping field, leading the

a)

b)
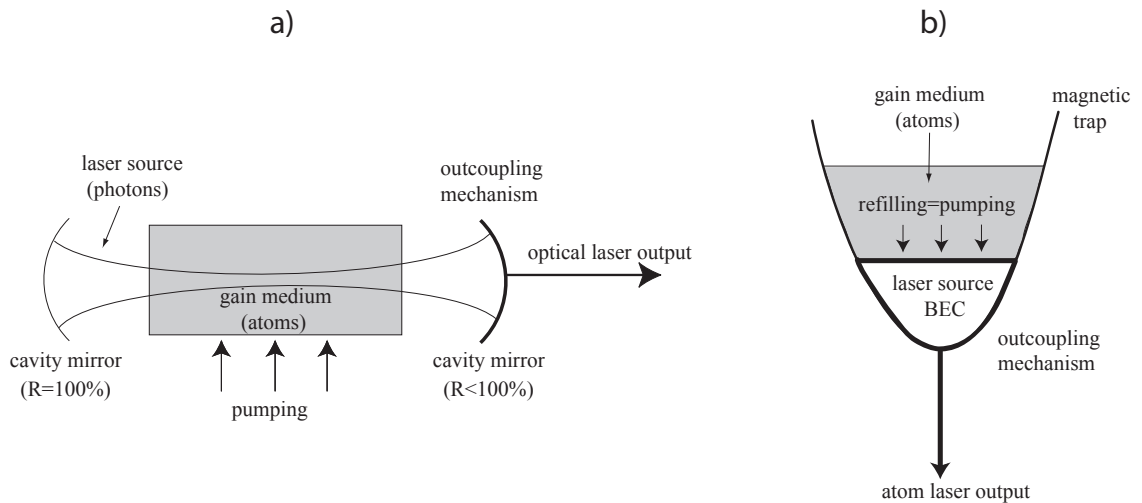
Figure 1.3: Physical elements constituting an optical laser (a) and an atom laser (b). In both cases, the lasing mode has a macroscopic population of bosons. In an optical laser, the lasing mode is multiple wavelengths long. In an atom laser, the lasing mode is the ground state of the trap. Both lasers rely on an irreversible stimulated process to populate the lasing mode.

way for atoms to fall away under gravity. This extraction process can be applied either as short or long (quasi-continuous) pulses.

- Both optical and atom lasers are extracted from a macroscopically populated mode of the cavity (or the trap). In the case of optical lasers, this mode is highly excited and multiple wavelengths long whereas in the case of an atom laser it is the lowest energy mode (usually the ground state of the trap).

- Finally, in order to maintain the production of a laser beam, one has to continuously refill the lasing mode as it is depleted. In an optical cavity, a gain medium of atoms is pumped by some source of energy in order to sustain a population inversion that coherently amplifies the lasing mode via stimulated emission of photons. Pumping (or refilling) of an atom laser is nowadays a real challenge in the field of atom lasers. Recently, a method has been demonstrated in our group [31] to out-couple an atom laser beam while simultaneously and irreversibly pumping new atoms from a physically separate cloud into the trapped Bose-Einstein condensate that forms the laser source.

1.1.3   Definition of an 'Atom Laser'

The term 'atom laser' has become widely used in the last decade and it is therefore important to have a more rigorous definition of what really defines an atom laser. For Wiseman [52], a general laser is a device containing a highly populated mode of a boson field. This so-called 'laser mode' is continuously replenished so that the output continues indefinitely. The output beam is formed via an out-coupling mechanism and is well approximated by a classical wave of fixed amplitude and phase. This definition leads to four properties defining the atom laser, in analogy with optical lasers :

1. The output beam must be highly directional, clearly defining a longitudinal direction along which propagation and dispersion occur and two transverse directions along which diffraction may occur. The directionality condition does not necessarily imply that the laser output must travel in free space and wave-guides have been proved to be useful for atom lasers to support against gravity, prevent spreading due to diffraction, and also improve the spatial profile [53].

2. The beam must be narrow in linewidth. There is a limit on the uncertainty δk of the longitudinal spatial frequency of the output such that $\delta k \ll k_{AL} = 2\pi/\lambda_{AL}$, where k_{AL} is the wave vector of a boson in the output which, as mentioned earlier, continuously changes during the propagation.

3. The output beam must have a well defined phase, implying that phase fluctuations in the output beam are small. This condition can be expressed quantitatively using Glauber's normalized first order coherence function [54] defined by

$$G^{(1)}(\tau) = \langle \Psi^\dagger(t+\tau)\Psi(t) \rangle \qquad (1.7)$$

or its normalized form

$$g^{(1)}(\tau) = \frac{\langle \Psi^\dagger(t+\tau)\Psi(t) \rangle}{\langle \Psi^\dagger(t)\Psi(t) \rangle} \qquad (1.8)$$

where $\Psi(t)$ is the complex amplitude of the field. For $\tau = 0$, $|G^{(1)}(\tau)|$ is simply the mean intensity $\langle I \rangle$ of the field. However, as τ increases, $|G^{(1)}(\tau)|$ decreases as the phase of

the field gradually becomes decorrelated from its value at time t with $|G^{(1)}(\tau)| \to 0$ when $\tau \to \infty$. By contrast, an ideal first order coherent source will have $g^{(1)}(\tau) = 1$ for all τ. In practice, the phase of an atom laser, and hence $G^{(1)}(\tau)$, will remain constant over a long period (t_{coh}) before significantly decaying and this coherence time is defined by

$$t_{coh} = \int_0^{+\infty} |g^{(1)}(\tau)| d\tau. \tag{1.9}$$

The first order temporal coherence of an atom laser was demonstrated in [55] where the authors showed that the linewidth of the atom laser, defined as $\Gamma = 1/t_{coh}$, was Fourier limited (by the out-coupling duration and the detection resolution) giving an upper limit on the phase fluctuations of the atom laser. The first order spatial coherence of an atom laser beam was also demonstrated experimentally [56, 57] by observing high contrast interference patterns from two interfering atom laser beams that were phase related (created from the same initial source).

4. Finally, the output beam must have a well defined intensity. Like the previous condition, this can be expressed in terms of correlation functions. The second order normalized correlation function is given by

$$g^{(2)}(\tau) = \frac{\langle \Psi^\dagger(t+\tau)\Psi^\dagger(t)\Psi(t+\tau)\Psi(t)\rangle}{\langle \Psi^\dagger(t)\Psi(t)\rangle^2} \tag{1.10}$$

which is also commonly written as

$$g^{(2)}(\tau) = \frac{\langle : I(t+\tau)I(t) :\rangle}{\langle I(t)\rangle^2} \tag{1.11}$$

where $I = \Psi^\dagger(t)\Psi(t)$ is the intensity of the field and $\langle :: \rangle$ denotes normal ordering (i.e. all creation operators to the left of all annihilation operators). For fields that are second order coherent, the intensity fluctuations are small in the sense that $|g^{(2)}(\tau) - 1|^2 \ll 1$ and the only intensity noise contribution is quantum noise (also called shot noise). Second order coherence of an atom laser has been demonstrated experimentally using a Hanbury Brown-Twiss type experiment where the second order correlation function was measured to be $g^{(2)}(\tau) = 1.00 \pm 0.01$ [27].

It is important to note that the use of the term 'atom laser' in the literature has not followed completely Wiseman's definition. Indeed, it has been widely used for out-coupled beams which are either short or long-pulsed but not rigorously continuous since the condensate (i.e. the laser source) was not continuously replenished. In our experiment, the atomic beams are almost always long-pulsed (quasi-continuous) unless specified otherwise. The notion of short and long atomic pulses will be described in section 1.4.3. For consistency with the literature the term 'atom laser' will be used although the condensate is never replenished and the output cannot continue infinitely.

1.2 ATOM LASER OUT-COUPLING TECHNIQUES

Although all atom lasers produced to date utilize a Bose-Einstein condensate as a source (or reservoir) to populate the atomic beam, they can be distinguished by the different techniques used to out-couple the atoms. There are many ways of coherently transferring atoms from a condensate into the propagative matter-wave of the laser. These methods can be classified in two main groups namely the non-state changing and the state changing out-coupling techniques. A non-state changing out-coupling technique is a method where the internal state of the atoms is not modified during the out-coupling process. Conversely, a state changing out-coupling process couples the magnetically trapped atoms out of the condensate by transferring them into a different internal state which is magnetically un-trapped and falls under gravity. To do so, one can use either a radio-frequency (RF) (or microwave) field, or alternatively an optical Raman field. Both techniques are described in detail in the following sections.

1.2.1 Non-State Changing Out-coupling

Although the majority of the experimentally demonstrated out-coupling mechanisms are based on either Raman or RF transfer of atoms from a magnetically trapped into an un-trapped Zeeman state, it is interesting to mention a few examples of non-state changing out-coupling techniques.

The first atom laser beam was created when the first time-of-flight measurement of a condensate was performed after switching off the magnetic trap. The pulse of atoms falling under gravity can be considered as forming a coherent matter-wave. This is analogous to the optical 'cavity dumping' where all the photons in a cavity would be extracted at once. This very simple

technique is also very limited since, by definition, it is a short-pulse method, with the repetition rate being the time it takes to create a new BEC (typically a few tens of seconds) and the linewidth of the beam being very broad, on the order of the full width of the condensate (see section 1.3.2).

The second technique was a quantum tunneling effect demonstrated by Anderson and Kasevich [58]. In this experiment, a condensate was loaded into the top of a vertical array of optical traps created by a standing wave. Acceleration due to gravity induced tunneling between the traps and constructive interference between the lattice sites resulted in falling pulses of atoms. The size of the pulses could be adjusted by altering the depth of the optical wells. However, this outcoupling technique has important limitations. First, the atomic beam is again inherently pulsed and cannot work in a continuous regime. Second, the density of these pulses is limited as for large densities, mean-field interactions cause significant dephasing between lattice sites, thus degrading the interference process. No further consideration was given to this technique in the development of an atom laser.

A further unconventional form of an atom laser was produced in [59], again using an optical method. In this experiment, a single spin state condensate was produced in a strongly focused optical trap by applying a magnetic field gradient stronger than the transverse optical confining force. All atoms were removed by this field gradient, except those in the magnetically insensitive ($m_F = 0$) state which stayed confined in the optical dipole trap. Here m_F is the projection of the total angular momentum F of the hyperfine atomic state that is considered. An atom laser was finally produced by smoothly lowering the optical trapping potential so that atoms from the condensate could fall under gravity. The benefits of this scheme are that the outcoupling is not limited by the stability of magnetic fields. It is dependent only on the laser intensity fluctuations but stabilizing laser intensities is technically easier than eliminating stray magnetic fields and producing a highly stable magnetic trap. However, magnetic fields are still required to produce cold atoms that will continuously replenish the condensate. Moreover, the use of strong magnetic field gradients and shallow optical potentials could make it difficult to extend this method in the case of a pumped atom laser.

1.2.2 State Changing Out-coupling

In order to illustrate the state changing out-coupling process, the atomic spectroscopy of the ^{87}Rb ground state is presented in figure 1.4. It has two distinct hyperfine states of total angular momentum $F = 1$ and $F = 2$ characterized by Landé factors of $g_F = -1/2$ and $g_F = 1/2$
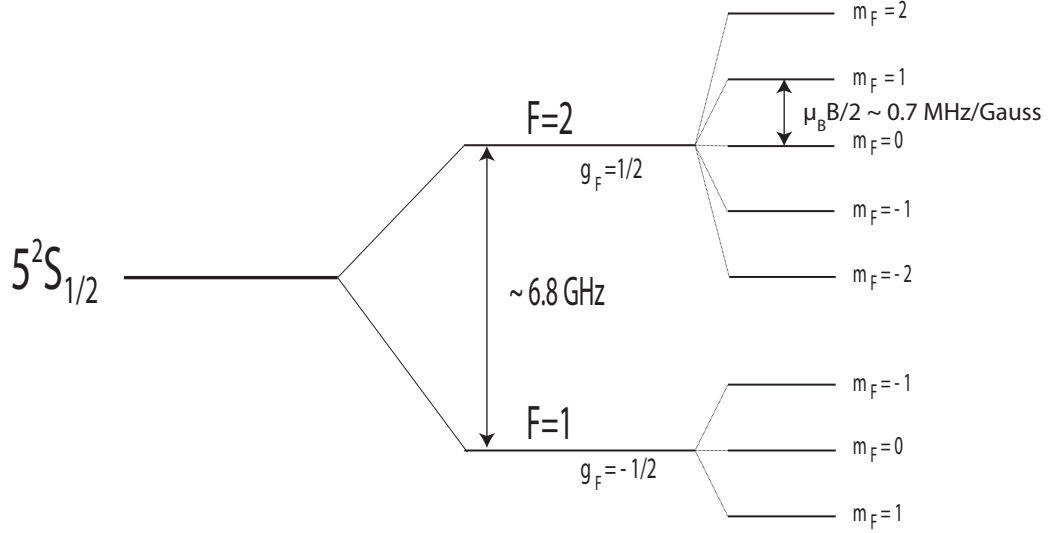
Figure 1.4: Atomic spectroscopy of the ground state of ^{87}Rb in a small bias field.

respectively. In most experiments, and in particular in ours, the BEC is trapped in a magnetic potential. In the bias field at the minimum of the trap, a hyperfine level is split into $2F + 1$ non-degenerate Zeeman states. For weak magnetic fields, in which the Zeeman effect is small and may be treated as a perturbation, the splitting between two Zeeman states characterized by their projection m_F and m'_F can be approximated as

$$\hbar \delta_{Zeeman} = \Delta m_F g_F \mu_B |B| \tag{1.12}$$

where $\Delta m_F = m'_F - m_F$, μ_B is the Bohr magneton and $|B|$ is the magnetic field amplitude. Zeeman states experience differently the magnetic trapping potential. In the case of ^{87}Rb, the $|F = 2, m_F = 2\rangle$, $|F = 2, m_F = 1\rangle$ and $|F = 1, m_F = -1\rangle$ states are trapped and can potentially form the condensate. Any $m_F = 0$ state is un-trapped and insensitive to the magnetic field (under the first order Zeeman effect), whereas the $|F = 2, m_F = -2\rangle$, $|F = 2, m_F = -1\rangle$ and $|F = 1, m_F = 1\rangle$ states are anti-trapped and quickly expelled from the magnetic field region. A state changing process will coherently couple two Zeeman states that can be either inside a given hyperfine state (this is the case of RF and the Raman out-coupling used in our experiment) or from two distinct hyperfine states (which is the case of microwave or sometimes Raman out-coupling).

1.2.3 Radio-Frequency Output Coupling

Mewes *et al.* [18] demonstrated the first pulsed atom laser output coupler based on the application of pulsed radio-frequency (RF) fields, before continuous output coupling was achieved by Bloch *et al.* [60].
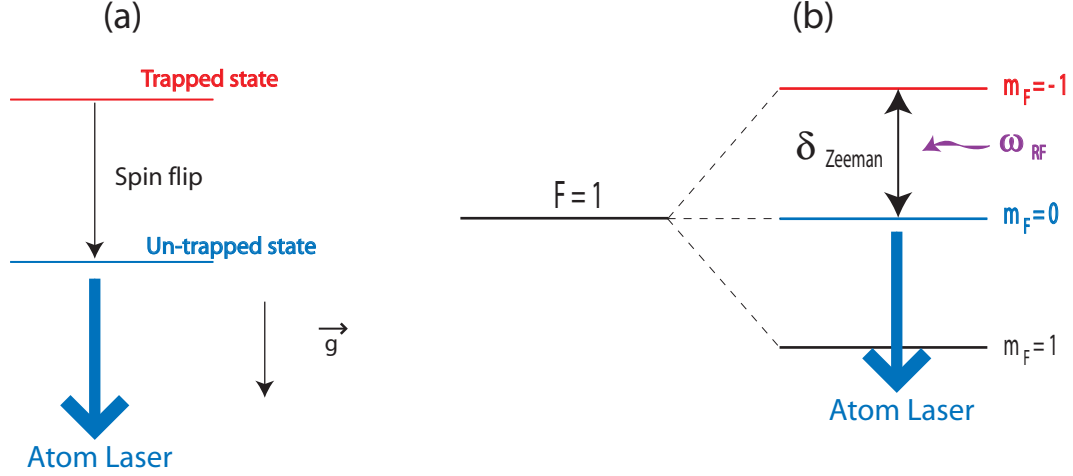
Figure 1.5: The scheme (a) shows the basic principle of RF out-coupling which is applied to the case of the F=1 manifold (b) in our experiment.

Radio-frequency output coupling consists of applying a monochromatic RF magnetic field B of given amplitude B_{RF} and frequency ω_{RF} in order to induce controlled spin flips between adjacent Zeeman states. The aim is to resonantly and coherently transfer the atoms from their initial magnetically trapped state into a state which is insensitive to magnetic fields. Consequently, the atoms are no longer trapped and will be extracted from the BEC due to gravity, as shown in figure 1.5a. Experimentally, a BEC is produced in the $F = 1$ manifold and the magnetically trapped $|F = 1, m_F = -1 >$ atoms are transferred to the $|F = 1, m_F = 0\rangle$ state (in which they no longer interact with the magnetic potential). The process is resonant provided the frequency of the field satisfies $\omega_{RF} \sim \delta_{Zeeman} = \mu_B B/(2\hbar)$ (figure 1.5b). Because the first order Zeeman shift symmetrically splits adjacent Zeeman states, all $2F + 1$ sublevels are coupled, producing a multi-state atom laser beam. For instance in the $F = 2$ manifold, the condensate atoms initially in the $|F = 2, m_F = 2\rangle$ trapped state are transferred, via the $|F = 2, m_F = 1\rangle$ state, into the $m_F = 0$ un-trapped state but can also populate the anti-trapped $|F = 2, m_F = -1, -2\rangle$ states.

Microwave out-coupling is a similar technique with the difference that it couples two Zeeman levels of different hyperfine states, producing a single-state atom laser.

1.2.4 Raman Output Coupling

The outcoupling mechanism used in most of the experiments described in the thesis is also a state changing technique but utilizes an optical Raman transition. It was originally suggested as a mechanism for atom laser outcoupling by Moy *et al.* [61] and first demonstrated experimentally by Hagley *et al.* [19] who produced a quasi-continuous multi-state atomic beam. The scheme (figure 1.6a) is based on the absorption and stimulated emission of photons from two optical laser beams, again transferring the atoms from a magnetically trapped to an un-trapped state. The process is coherent and inherently controllable. However, the main difference with the previously described RF coupling technique is that the atom laser is produced with an initial momentum kick in any chosen direction defined by the incoming directions of the two laser beams. Experimentally, this two photon transition is applied on the $F = 1$ manifold, as shown in figure 1.6b. An atom in the trapped $m_F = -1$ state coherently absorbs a photon from a beam with frequency ω_1 and is stimulated to emit into the other beam with a frequency ω_2 thus changing its internal state to an un-trapped magnetic level ($m_F = 0$).

The process is reversible and un-trapped atoms can be coherently transferred back into the condensate. In order for this scheme to be efficient, one has to create the following conditions :

1. The two laser beam polarizations must be chosen to allow optical transitions between the Zeeman sublevels. In figure 1.6b, one laser beam is thus linearly (π) polarized whereas the other one has a σ^- circular polarization where the polarization is defined in terms of absorption.

2. The frequency difference between the two lasers ($\delta = \omega_2 - \omega_1$) has to be adjusted to satisfy energy and momentum conservation. An atom, initially at rest, gains a momentum kick $\mathbf{p} = \hbar(\mathbf{k}_2 - \mathbf{k}_1)$ following momentum conservation upon absorption and emission of each photon. Here $\mathbf{k}_{1,2}$ are the wavevectors of the lasers of the two laser beams. When the beams make an angle θ and are produced from the same laser source of wavevector k (which is always the case in our experiments), one can write :

$$p = 2\hbar k sin\left(\frac{\theta}{2}\right).$$

(1.13)
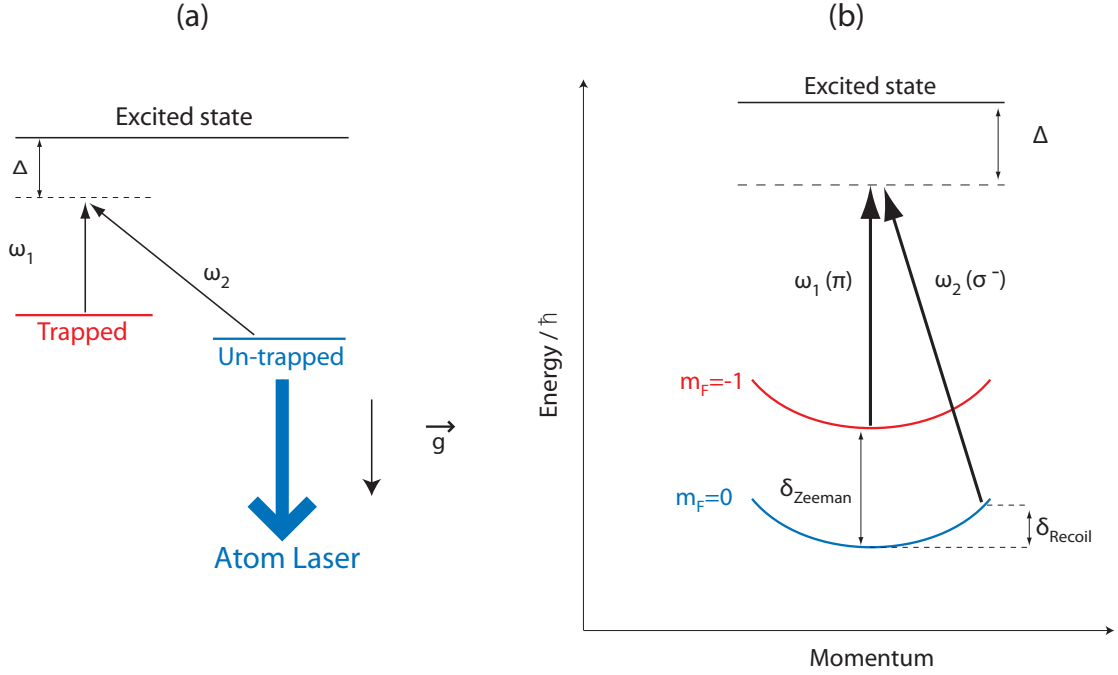
Figure 1.6: Schematic showing the basic principle of Raman out-coupling (a) as well as the restrictions of energy and momentum conservation on a two photon Raman transition in the F=1 manifold of our experiment (b). The parabolas correspond to the kinetic energy of the atoms, equal to $p^2/2m$.

In theory, the laser geometry can range from co- to counter-propagating beams and will determine the magnitude and the direction of the momentum kick received by the atoms. Thus the momentum transfer will be maximum for counter-propagating ($\theta = \pi$) beams. Energy conservation requires that the detuning of the lasers accounts for the total change in energy of the atom and the frequency difference between the two laser beams must consequently correspond to the Zeeman plus kinetic energy difference between the initial and final states of the two-photon process following:

$$\hbar\delta = \hbar\delta_{zeeman} - \hbar\delta_{recoil} \tag{1.14}$$

where

$$\delta_{recoil} = \frac{p^2}{2m\hbar} = \frac{2\hbar k^2 sin^2\left(\frac{\theta}{2}\right)}{m}. \tag{1.15}$$

The recoil frequency depends on the half angle between the two Raman beams. It is zero if the beams co-propagate ($\theta = 0°$) and is maximum if the beams counter-propagate ($\theta = 180°$) with $\delta_{recoil} \sim 2\pi \times 10$ kHz (in the case of Rb atoms and laser beams with $\lambda \sim 780$ nm).

Combining the energy and momentum conservation equations finally results in the resonance condition :

$$\hbar\delta = \Delta m_F g_F \mu_B B - \frac{p^2}{2m} \tag{1.16}$$

which, in the case of the $F = 1$ manifold, can be written as

$$\hbar\delta = \frac{\mu_B B}{2} - \frac{2\hbar^2 k^2 sin^2(\frac{\theta}{2})}{m}. \tag{1.17}$$

3. The transition must be highly detuned by a frequency Δ from the one-photon atomic transition (see figure 1.6a) in order to suppress the population in the upper state and thereby suppress spontaneous emission.

For the case of the 4 photon transition represented in figure 1.7, the outcoupled atoms end up with twice the momentum $p = 4\hbar k sin(\frac{\theta}{2})$. Since $g_F = 1/2$ and $\Delta m_F = -2$ in the $F = 2$ manifold, the resulting resonance condition now satisfies :

$$\hbar\delta = \mu_B B - \frac{4\hbar^2 k^2 sin^2(\frac{\theta}{2})}{m}. \tag{1.18}$$

The two photon resonance condition is no longer satisfied and less coupling is expected to occur to the intermediary $m_F = 1$ state (as shown in figure 1.7), and similarly to the anti-trapped states ($m_F = -1, -2$). However, coupling to these states can still occur depending on the frequency width of the condensate as well as the width of the Raman transition. This point is described in the next section.

In the Raman out-coupling scheme, the directional momentum kick received by the atoms produces a number of effects which are not present in the RF output coupler. First, the output coupler does not require gravity or guiding to operate and hence the atoms can be pushed in any direction. Second, the momentum kick will reduce the interaction time between output coupled atoms and the condensate, leading to a significantly reduced transverse momentum width in the
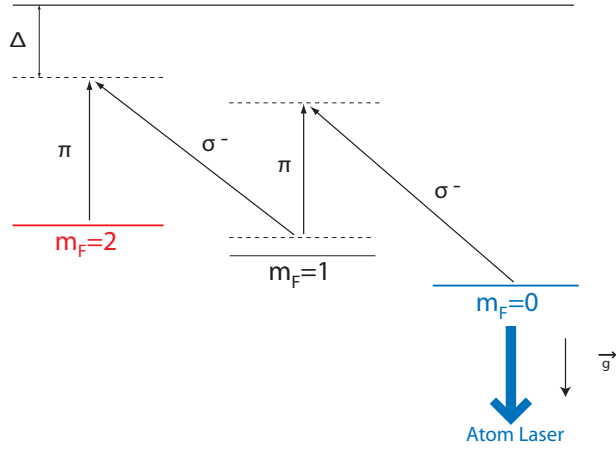
Figure 1.7: The four photon Raman outcoupling scheme in the $F = 2$ manifold

atom laser [19]. This last point will be experimentally studied in more detail in chapter 3.

1.3 RESONANT WIDTH OF THE CONDENSATE

The resonant out-coupling frequencies required in either Raman or RF out-coupling techniques depend on the value of the external magnetic field experienced by the atoms. Since the condensate has a certain size (or width), atoms located at different positions inside the BEC will experience a different magnetic field and, as a consequence, will be out-coupled for different resonance frequencies. This section determines the range of frequencies (or 'resonant width') which allow out-coupling of atoms, taking into account the effect of gravity, inducing a vertical displacement (or 'sag') of the BEC away from the magnetic field minimum.

1.3.1 Gravitational Sag

Any state changing mechanism described above is dependent on the energy spacing of the coupled Zeeman states since it depends on the value of the magnetic field. In particular, the presence of the trapping magnetic field introduces a spatial resonance associated with a given resonance frequency allowing the centre of the resonance to be tuned within and around the condensate. The resonance condition is thus satisfied on the surface of an ellipsoid centered around the minimum of the magnetic field. Without gravity, the resonance condition for a state

changing out-coupling mechanism would be satisfied on an ellipsoid of constant magnetic field B_0. However, gravity introduces an asymmetry which displaces the condensate away from the magnetic field minimum. This displacement (or sag) is found by equating the force of gravity in the downwards direction ($F_g = mg$) with the upwards force (F_{mag}) due to the magnetic field minimum. Here m is the atomic mass and g the acceleration due to gravity. The trapping potential in the direction of gravity is given by $V = m\omega_z^2 z^2/2$ (see section 2.1.8) where ω_z is the radial trapping frequency of the $|F, m_F\rangle$ state given by $\omega_z = \sqrt{\mu_B g_F m_F B_z''/m}$ with B_z'' the second derivative (or curvature) of the magnetic field with respect to the spatial coordinates. Consequently, $F_{mag} = \frac{dV}{dz} = m\omega_z^2 z$. The displacement down from the centre of the magnetic field minimum is finally given by $z_{sag} = g/(\omega_z^2)$. It is important to notice that that radial trapping frequency (and thus the sag) depends on the m_F Zeeman state that is considered. For instance, in the F=2 manifold, the radial frequency of the $|F = 2, m_F = 2\rangle$ state is $\sqrt{2}$ times bigger than the one of the $|F = 2, m_F = 1 >$ state. Consequently, atoms in the $|F = 2, m_F = 1\rangle$ state are displaced from the magnetic field minimum by twice as much as atoms in the $|F = 2, m_F = 2\rangle$ state.

In our experiment (see chapter 2), ^{87}Rb atoms are condensed in the $|F = 1, m_F = -1\rangle$ state and in a trap with typical radial frequency of $\omega_z = 2\pi \times 130$ Hz which corresponds to a sag of $z_{sag} \sim 15\ \mu$m. Out-coupling will consequently occur at the intersection of the displaced condensate with the surface of an ellipsoid as shown in figure 1.8.
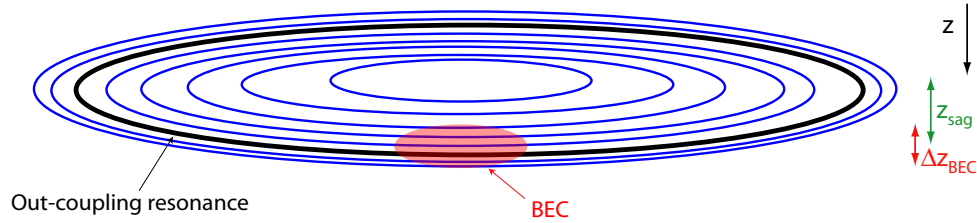
Figure 1.8: The sag of the condensate due to gravity, viewed orthogonal to the weak trapping axis. The red ellipse represents the condensate and the blue contour lines show the magnetic field magnitude, increasing away from the central minimum. An out-coupling frequency resonance is depicted by the thick, black line.

1.3.2 Resonant Frequency Width

In order to estimate the spatial range over which out-coupling should be expected, one has to determine the resonant width of the condensate. Assuming the kinetic energy may be neglected

compared to the interaction energy (Thomas Fermi approximation) [62], the size Δz_{BEC} of the condensate in the vertical direction is given by:

$$\Delta z_{BEC} = 2\sqrt{\frac{2\mu}{m\omega_z^2}} \tag{1.19}$$

where μ is the chemical potential which represents the amount by which the energy of the system would change if an additional particle were introduced. A quantitative value for the chemical potential is determined by considering the constraint on the total number of particles:

$$N = \int n \, d^3x \tag{1.20}$$

where n is the density of particles. Including the effects of interactions and trap confinement gives

$$\mu = \frac{1}{2}(15a\hbar^2\sqrt{m}\bar{\omega}^3 N)^{2/5} \tag{1.21}$$

where $a = 5.77$ nm is the scattering length and $\bar{\omega}$ the mean geometric trapping frequency. In our experiment ($N \sim 5 \times 10^4$ atoms, $\omega_\rho = \omega_x = \omega_z \sim 2\pi \times 130$ Hz, $\omega_y \sim 2\pi \times 13$ Hz) Δz_{BEC} is typically of order of 10 μm.

The frequency width of a condensate is usually given by the chemical potential following $\Delta\omega = \mu/\hbar \sim 2\pi \times 1$ kHz. However, in a magnetic trap, the sag of the BEC into regions of higher magnetic field gradient modifies the resonance. Assuming that the resonance is centered on the condensate, the resonant width of the BEC is found by considering the difference in resonant frequencies between the upper edge of the condensate, located at $z_{up} = g/\omega_z^2 - \Delta z_{BEC}/2$ and the lower edge at $z_{down} = g/\omega_z^2 + \Delta z_{BEC}/2$. As mentioned before, the resonant frequency at any point in the vertical direction can be written as $\omega_{BEC} = \mu_B B/2\hbar$, where B is the magnetic field of expression $B = B_0 + \frac{m\omega_z^2}{2g_F m_F \mu_B}z^2$ in the z-direction. Thus, the resonant width for the $|F = 1, m_F = -1\rangle$ state is given by

$$\Delta\omega_{BEC} = \frac{m\omega_z^2}{2\hbar}(z_{down}^2 - z_{up}^2) = \frac{mg}{\hbar}\Delta z_{BEC} \tag{1.22}$$

which can be re-written as

$$\Delta\omega_{BEC} = \frac{2g}{\hbar\omega_z}\sqrt{2m\mu} \tag{1.23}$$

In our experiment, the range of resonant out-coupling frequencies is $\Delta\omega_{BEC} \sim 2\pi \times 10$ kHz which is much larger than the 'bare' frequency width $\Delta\omega$ of the condensate when no sag is considered.

1.4 RABI-FREQUENCY AND THE DIFFERENT OUT-COUPLING REGIMES

Rabi frequency is an important parameter when producing an atom laser because both the strength and the relative time scales of the out-coupling process can be described in terms of this parameter. The aim of this section is to qualitatively distinguish between two out-coupling regimes (weak or strong) of an atom laser depending on the value of the Rabi frequency.

1.4.1 Output Coupling Strength

The strength of the out-coupling is determined by the Rabi frequency. For RF out-coupling, the Rabi frequency is given by

$$\Omega_{RF} = \frac{g_F \mu_B B_{RF}}{2\hbar} \tag{1.24}$$

where B_{RF} is the amplitude of the applied magnetic field. For a two photon Raman out-coupling, the Rabi frequency can be written as

$$\Omega_{Raman} = \frac{\Omega_1 \Omega_2}{2\Delta} \tag{1.25}$$

where Δ is the detuning to the atomic transition and Ω_1 and Ω_2 are the one photon Rabi frequencies of the coupling introduced by each laser, with $\Omega_1 \alpha \sqrt{I_1}$ and $\Omega_2 \alpha \sqrt{I_2}$ if I_1 and I_2 are the intensities of each laser beam respectively.

1.4.2 Pulsed and Quasi-Continuous Output Coupling

In section 1.3.2 we estimated the spatial range over which out-coupling could be expected by calculating the resonant width of the condensate in the vertical direction:

$$\Delta z_{BEC} = 2\sqrt{\frac{2\mu}{m\omega_z^2}} \tag{1.26}$$

Similarly, one can define the spatial extent of a resonant output coupling pulse following equation 1.23 as:

$$\delta z_{res} = \frac{\hbar}{mg} \delta \omega_{res} \tag{1.27}$$

where $\delta \omega_{res}$ is the frequency width of the out-coupling resonance. For a pulse of length τ_{out}, the frequency width is determined by the larger of the power broadened width given by Ω or the natural width of the pulse $4\pi/\tau_{out}$.

We will define quasi-continuous coupling as the regime where the width of the out-coupling region is significantly narrower than the width of the condensate ($\delta z_{res} < \Delta z_{BEC}$). Conversely, short pulse output coupling is characterized by a large frequency width of the output coupling resonance and occurs over a large region in space ($\delta z_{res} > \Delta z_{BEC}$). This is illustrated in figure 1.9a) and 1.9b) respectively.

1.4.3 Out-coupling regimes

In an out-coupling process, the BEC can be thought of as a discrete state coupled to a continuum of un-trapped states, resulting in a width broadening Γ and a time scale $2\pi/\Gamma$ characterizing the dynamics of the system. In order to characterize the out-coupling regime, one can compare this time scale to the memory time t_m of the continuum [63] which is defined as the characteristic time for an out-coupled atom to loose the initial information of the condensate. In the case where only the gravitational continuum is considered, a classical interpretation of this memory time can be thought of as the time it takes for an atom to leave the region of the condensate, leading to $t_m \sim 2\pi/\Delta\omega_{BEC}$ [64].

If $\Gamma t_m/2\pi \ll 1$ the out-coupled atomic wave has lost the memory of the condensate during the time scale $1/\Gamma$. This regime characterizes a weak out-coupling where it is appropriate to calculate the atomic output rate from the Fermi golden rule as described in [65]. The validity of this regime implies that

$$\Gamma \ll \Delta\omega_{BEC} \tag{1.28}$$

or equivalently

$$\Gamma \ll \frac{m}{\hbar} g\Delta z_{BEC} \tag{1.29}$$

In the first order perturbation theory, the typical broadening Γ can be expressed as [63]:

$$\Gamma \sim \frac{\hbar \Omega^2}{mg\Delta z_{BEC}} \tag{1.30}$$

leading to a similar condition over the Rabi frequency to characterize the weak out-coupling regime:

$$\Omega \ll \frac{m}{\hbar} g \Delta z_{BEC} \tag{1.31}$$

We can point out that, since $\Omega \ll mg\Delta z_{BEC}/\hbar$ in the weak coupling regime, the spatial region where out-coupling takes place ($\delta z_{res} \sim \hbar\Omega/mg$) is very thin compared the the BEC size, as pictured in figure 1.9a).

Conversely, for $\Gamma t_m/2\pi > 1$, the atom laser will be considered in a regime of strong coupling. In this case, only a small fraction of the condensate is coupled to the atom laser beam and the initial wave-function of the condensate is preserved in the process. The coupling rate is such that the output-coupled atoms do not have time to propagate while the coupling is in progress and increasing the out-coupling time will result in Rabi oscillations to be observed in the condensate, as described in [18].
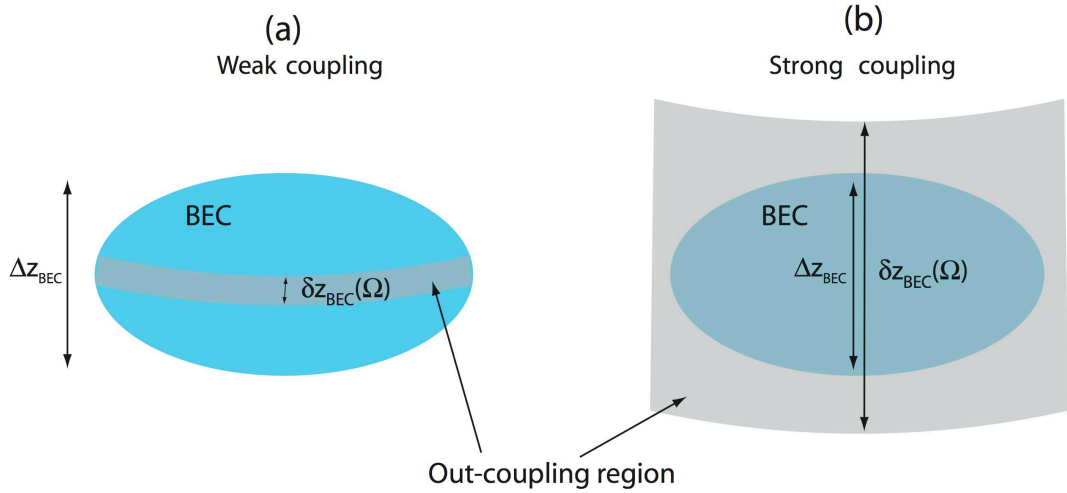
Figure 1.9: Schematics of the model for weak (a) and strong (b) out-coupling regimes.

1.5   CONCLUSION

In this chapter, a general overview on atom lasers in analogy to optical lasers was given. Several techniques to out-couple the atoms from the BEC source were described and the advantages of an optical Raman out-coupling over an RF method were also introduced. Additionally, the resonant width of a condensate, with respect to the gravitational sag, and the different out-coupling regimes of an atom laser were discussed. The ANU part of this thesis mainly focusses on the state-changing Raman method in the weak out-coupling regime in order to create an atom laser. The following chapter presents the experimental layout which we use to produce both the Rb BEC and the optical Raman beams.

CHAPTER 2

RUBIDIUM CONDENSATE AND RAMAN BEAMS

The source of the atom laser is a Bose-Einstein condensate (BEC). The first Rb BEC achieved in our lab was in 2001 [66], before a major improvement of the experiment was undertaken in 2002 [67]. This chapter is split into 2 different sections. The first part describes the third generation of our BEC machine which allows us to repeatedly produce condensates of constant number of atoms in a very stable magnetic trap. The apparatus is based on a double Magneto-Optical Trap (MOT) structure (see figures 2.1 and 2.2) where a 3D MOT is loaded from a 2D MOT using a push beam. The system also involves a physical transport of the atoms in a strongly confining magnetic field from the 3D MOT to a quadrupole-Ioffe configuration (QUIC) magnetic trap where Bose-Einstein condensation occurs. The second part describes and discusses the optical setup used to produce the optical Raman beams.
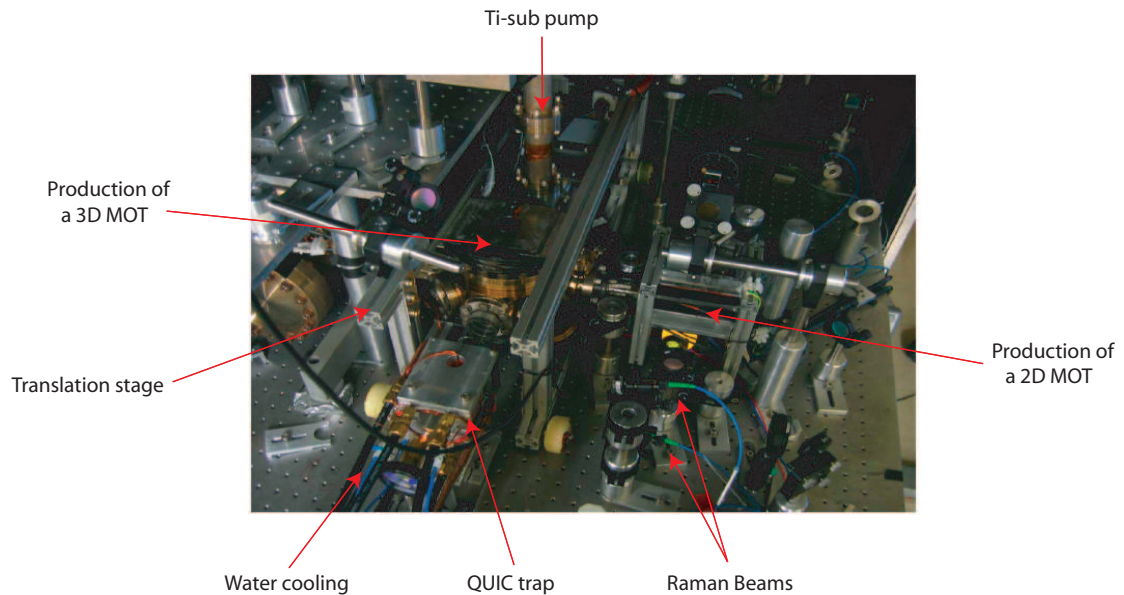
Figure 2.1: Picture of the BEC machine. One can see the location of the 2D and 3D MOT as well as the translation stage used to transport the atoms from the 3D MOT to the QUIC trap. The output of the optical fibers used for the Raman beams can also be seen.
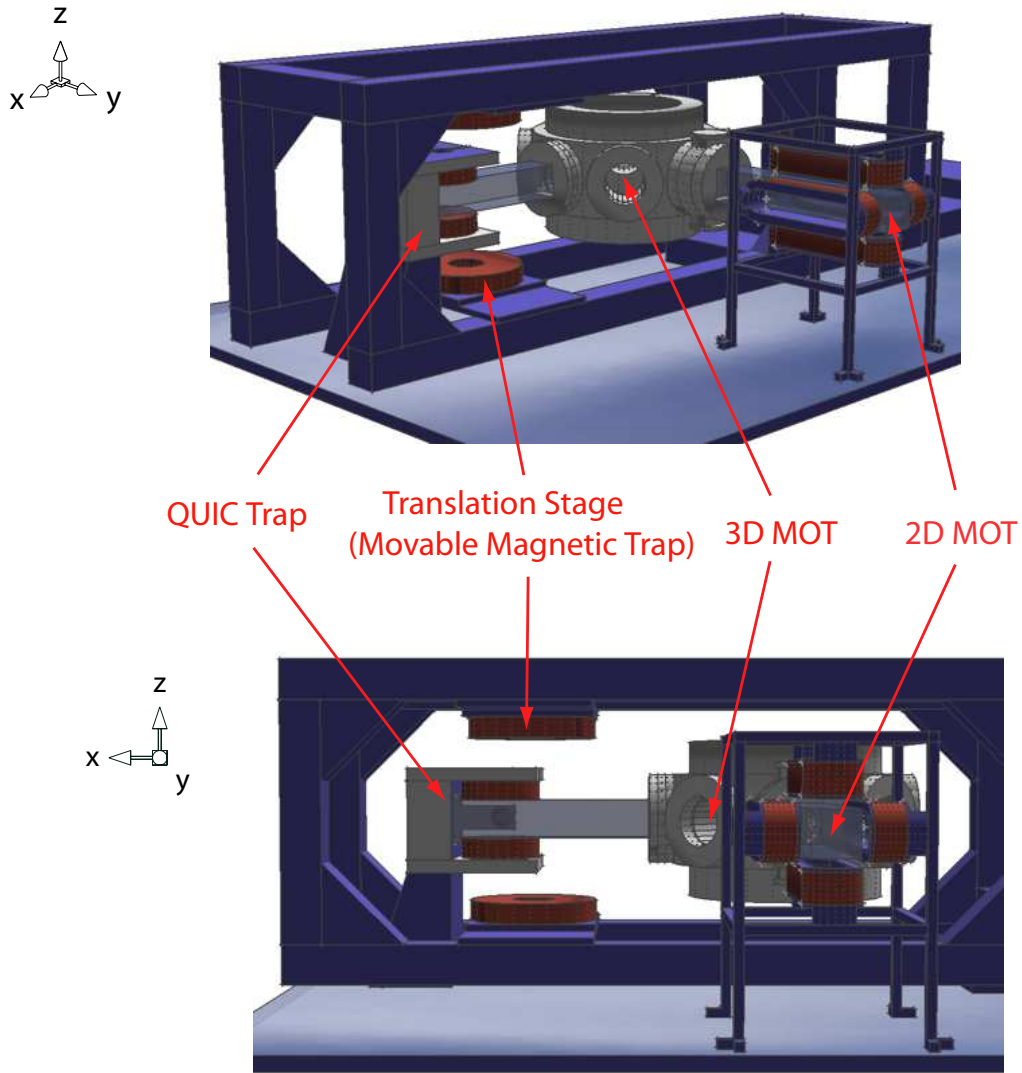
Figure 2.2: Experimental machine used to produce the Bose-Einstein condensate. Optical laser beams are not shown. The 2D MOT cools the atoms from room temperature in both transverse directions. The 3D MOT is loaded in an ultra-high vacuum from the 2D MOT by a near-resonance laser push beam. The 3D MOT coils are mounted on a translation stage. They not only provide confinement for the 3D MOT stage but they are also used to transport the atoms across to the QUIC trap where they are transferred and condensed after evaporative cooling.

2.1 EXPERIMENTAL SETUP TO PRODUCE BEC

In the following sections, the laser and vacuum systems are described yielding an overview of the entire experimental setup. Each step of the experiment is then briefly discussed, starting from the 2D MOT to the production of a BEC in the QUIC trap.

2.1.1 Atomic structure of ^{87}Rb

Alkali atoms (Li[3], Na[2], K[68, 69], Rb[1], Cs[70]) are often used in BEC experiments due to their advantageous atomic properties. ^{87}Rb is the most popular choice. It was the first atomic species condensed and hence expertise was built up rapidly and is now widely available. Additionally, Rb atoms have large elastic cross-sections at low temperatures which allow efficient evaporative cooling. Also, optical transitions from the Rb $5^2S_{1/2}$ ground state are easily accessible using commercially available, relatively cheap lasers.

The atomic spectroscopy of ^{87}Rb is presented in figure 2.3 showing both the $D1$ and $D2$ optical transitions and the relevant optical splitting. In particular, the two hyperfine levels of the atomic ground state are split by ~ 6.8 GHz and can be split further by the Zeeman effect in the presence of a magnetic field. Various optical frequencies are required to cool and manipulate the atoms on the path to BEC. The cooling is performed on the $5^2S_{1/2}, F = 2 \rightarrow 5^2P_{3/2}, F' = 3$ transition. However, approximately one in every thousand atoms will be excited to the $5^2P_{3/2}, F' = 2$ state and one in every two of these atoms will decay to the $5^2S_{1/2}, F = 1$ state, taking the atoms out of resonance with the cooling laser. Consequently, in order to avoid a loss of atoms, a second laser, known as the repump, is used to repopulate the $5^2S_{1/2}, F = 2$ state via the $5^2P_{3/2}, F' = 2$ state. Finally, an optical pumping beam driving the $5^2S_{1/2}, F = 2 \rightarrow 5^2P_{3/2}, F' = 2$ transition is used to polarize the atoms in order to achieve an efficient transfer of the atoms from the 3D MOT into a magnetic trap (see section 2.1.6).

2.1.2 Laser system

The schematics of the laser system, which involves three independent diode lasers to produce the required optical beams, is shown in figure 2.4. Each laser and its function in the setup are independently described in the following points:

1. A Toptica-TA 100 provides a maximum power of 330 mW at 780 nm. A small amount
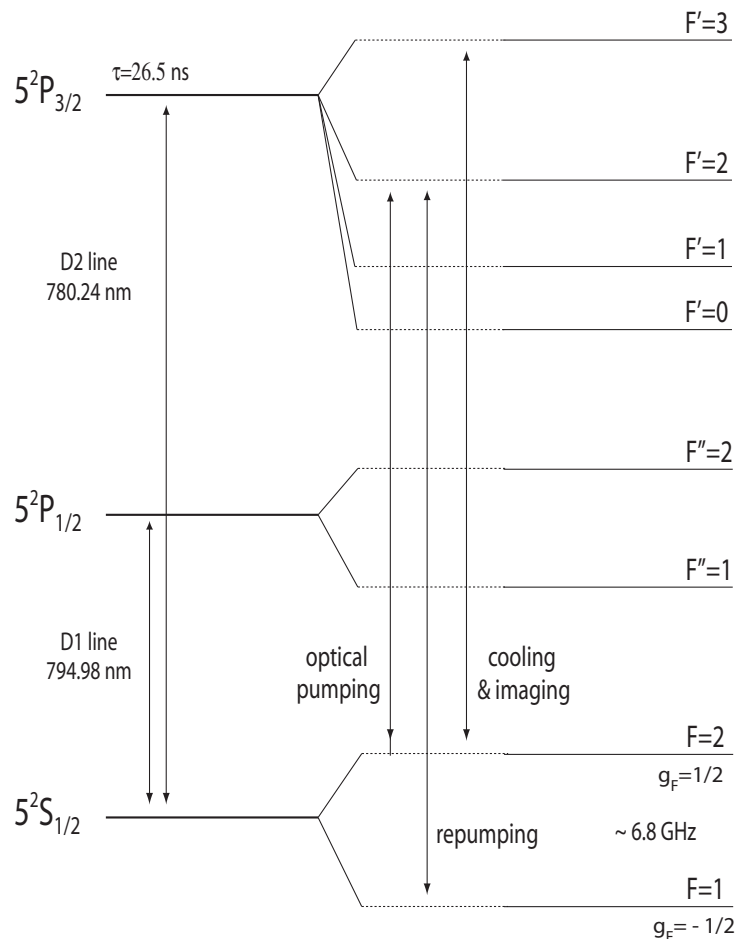
Figure 2.3: Atomic structure of ^{87}Rb. Several hyperfine levels of the $D2$ optical transition are used to cool and image the atoms.

of light (~ 1 mW) is sent to a saturated-absorption locking circuit and the laser is locked to the $F = 2 \rightarrow F' = 1,3$ cross-over [67] which is shown at the top of figure 2.4. Two independent acousto-optic modulators (AOM, 110 ± 20 MHz) are aligned in double-pass configuration in order to up-shift the light frequency on resonance to the $F = 2 \rightarrow F' = 3$ transition. One of the AOMs provides the 3D MOT beams whereas the second AOM creates the imaging light and the push beam. In addition, the 0-order of the second AOM single-passes through a 60 MHz AOM which down-shifts the light on resonance to the $F = 2 \rightarrow F' = 2$ transition for optical pumping. Each laser beam injects independent single-mode polarization-maintaining (SM-PM) fibers which are sent to the BEC table.

Figure 2.4: Laser system. The top pictures show the spectroscopy relevant to the experiment, together with a theoretical plot of the saturated absorption spectrum which is used to lock the light frequency. The bottom diagram represents the optical setup used to produce the beams to cool, pump, image, and push the atoms.

Accounting for the important losses through the AOMs and optical fibers, a total of ~ 100 mW of light is available for the 3D trapping, imaging, optical pumping and push beams. Note that the intensity balance between the imaging and push beams can be adjusted on the BEC table using a controllable liquid-crystal half wave-plate that can shunt the light from one beam to the other.

2. A Toptica-DLX 100 provides a maximum power of 500 mW at 780 nm which is used to produce the 2D MOT beams. A small amount of the light (~ 1 mW) is double-passed through an AOM (110 ± 20 MHz) which down-shifts its frequency. This light is sent to a saturated-absorption locking circuit and locked on the $F = 2 \rightarrow F' = 1, 3$ cross-over. As a result, the frequency of the 2D MOT beam is set close to resonance of the $F = 2 \rightarrow F' = 3$ transition. However, the frequency of the beam cannot be easily tuned without affecting the locking circuit, and the light must be switched on and off using a mechanical shutter. The 2D MOT beam is sent to the BEC machine in free space with a total power of approximately 480 mW onto the atoms.

3. A Toptica-DL 100 provides a maximum power of 90 mW at 780 nm which is used to produce the repump beams for both the 2D and 3D MOT. A small amount of the light is locked to the $F = 1 \rightarrow F' = 2$ transition which is shifted off the natural resonance by ~ 20 MHz using a Zeeman shift on the saturated absorption cell. The repump light is sent to the BEC table using SM-PM optical fibers and is split equally to provide independent repumping beams for the 2D and 3D MOT. In particular, the 2D MOT repump is combined with the push beam whereas the 3D MOT repump is mixed with each of the 3D MOT beams.

2.1.3 Vacuum system

A schematic of the vacuum system is shown in figure 2.5. It consists of two vacuum chambers, a Creation and a Science chamber, which are connected through a differential pumping tube.

The Creation chamber is a quartz cell of $3.6 \times 3.6 \times 20$ cm dimension with a wall thickness of approximately 4 mm. Two 'Alvasource' dispensers (from Alvatec), based on stable intermetallic compounds, contain the ^{87}Rb natural isotope. Each dispenser is 115 mm long with a 4 mm diameter and has a capacity of 50 mg. The Rb metal is initially protected in a sealed stainless

steel housing which makes it chemically stable under ambient air. The sealing can melt under a thermal activation process, which is done during the baking of the vacuum system. Under normal operation, the dispensers are run continuously and a heating current controls the amount of pure ^{87}Rb released in the chamber so that the vapor cell can be filled up close to the saturated vapor pressure of rubidium ($\sim 1 \times 10^{-7}$ Torr at 20°C). The only pumping of the vapor cell is achieved through a differential pumping tube, consisting of a 14 cm long stainless steel cylinder (external diameter 10 mm, internal diameter 7 mm).
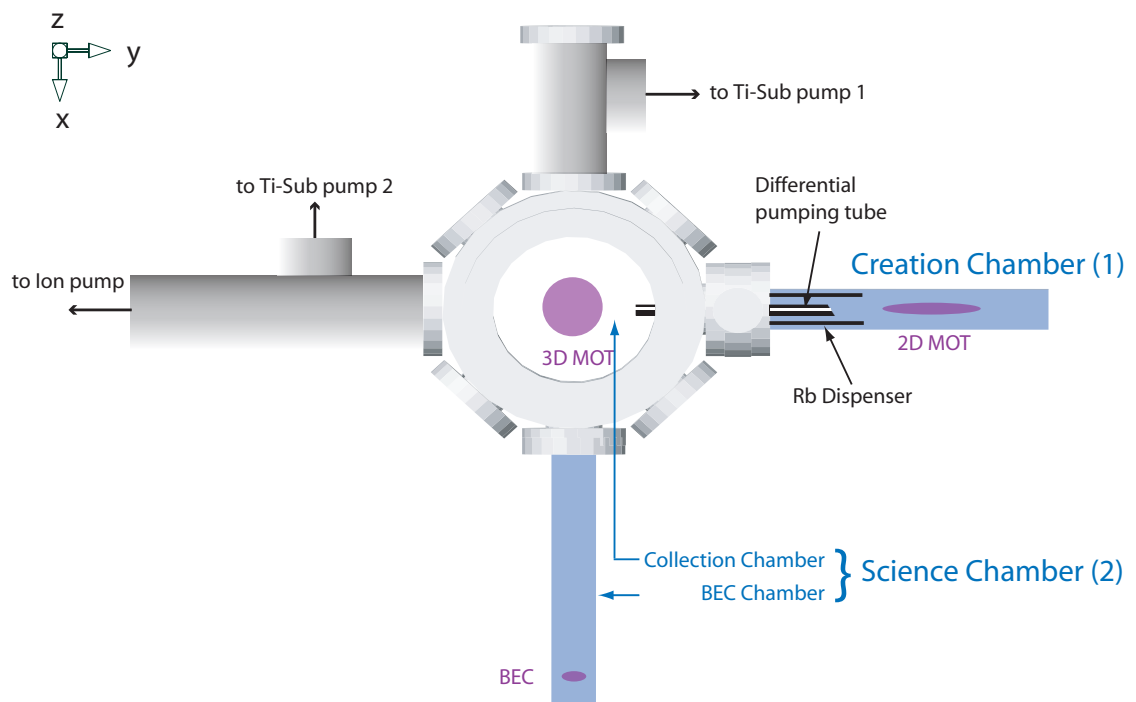
Figure 2.5: Schematic of the vacuum system. The Collection chamber is pumped by a 40 l.s^{-1} ion pump running continuously. Two titanium-sublimation pumps were also used a few times in order to improve the ultra-high vacuum in the BEC Chamber. The Creation chamber is pumped through a differential pumping tube and holds a vapor pressure of Rb atoms which are produced by two dispensers.

The ultra-high vacuum (UHV) Science chamber consists of two parts. The first is the Collection chamber which collects the atoms from the Creation cell and holds a 3D-MOT in the center. The frame of this chamber is a 316 stainless-steel (non-magnetic) standard hexagon. It has eight 3.5 cm diameter windows on the side providing a large optical access whereas two large diameter

windows offer additional optical access in the vertical direction. This chamber is pumped by a $40 \, \mathrm{l.s^{-1}}$ ion pump which is connected by a high conductance metal tube. The pump magnet is located 90 cm away from the chamber, thus avoiding any fringing field to distort the magnetic trapping field in the UHV chamber. The pumping efficiency is also enhanced by two titanium sublimation (Ti-Sub) pumps which were run three times in total to improve the pressure in the UHV chamber. The final pressure in the UHV chamber ($\sim 5 \times 10^{-11}$ Torr) was measured by a pressure gauge as well as from the lifetime of the 3D MOT. The second is the BEC chamber which is a quartz cell of $3.6 \times 3.6 \times 20$ cm dimension and is directly attached to the Collection chamber. A translation stage (see section 2.1.7) transports the atoms from the Collection chamber to the end of the glass cell where the sample is transferred into a magnetic trap and condensed.

2.1.4   2D MOT

In the Creation chamber, the atoms released by the two dispensers are confined and cooled in a 2D MOT. A radial laser-cooling is performed by two orthogonal pairs of retro-reflected beams (2 cm diameter, ~ 500 mW of laser power in total) with opposite polarization σ^+/σ^- (see figure 2.6). Four magnetic coils (see figure 2.2) provide a radial quadrupolar trapping field with the zero of the magnetic field along the axial y-direction. Consequently, a beam of atoms is created along the y-direction. The atoms are transferred to the Collection chamber through the differential pumping tube by a low power push beam ($\sim 200 \, \mu\mathrm{W}$). The tube is attached by stainless steel nuts to the gaskets. It is cut at a $45°$ angle at one end and holds a polished mirror which has a 1 mm hole in its center. Initially, this mirror was planned to retro-reflect a laser beam in order to provide additional laser-cooling along the axial x-direction. However, a single push beam is used in our experiment to transfer the atoms from the Creation to the Collection chamber. Finally, the flux of atoms is optimized by adjusting the heating current applied to the dispensers.

2.1.5   3D MOT

In the Collection chamber, three orthogonal pairs of retro-reflected beams (1.4 cm diameter, ~ 30 mW of laser power in total) with opposite polarization σ^+/σ^- provide a cooling in three directions. Two internally water-cooled quadrupole coils, which were operated by using 60 A currents in opposite directions, provided confinement for the atoms. These quadrupole coils

Figure 2.6: Arrangement of the optical beams onto the atoms. The imaging beam, the push beam, two pairs of 3D MOT beams as well as a pair of 2D MOT beams are represented by the red lines in the *xy*-plane. The red dots on the 2D and 3D MOT clouds represent the additional pair of 2D and 3D MOT beams respectively, along the vertical *z*-direction.

are mounted on a translation stage which can be moved all the way to the end of the BEC cell (see section 2.1.7). The 3D MOT is typically loaded in 10 s with a rate of $\sim 5 \times 10^9$ atoms.s^{-1}, resulting in approximately 5×10^{10} atoms to be trapped in the 3D MOT. Note that the laser beams of both the 2D and 3D MOTs are slightly focussed in order to account for absorption and to keep the intensity constant as the beams go through the atomic clouds. A 10 ms compressed MOT (CMOT) stage is performed by attenuating the repump beam and ramping up the current in the magnetic coils. The MOT lasers are then far-detuned from the $F = 2 \rightarrow F' = 3$ atomic transition by ~ 40 MHz and the magnetic trap is abruptly switched off in ~ 100 μs, followed by 10 ms of Polarization Gradient Cooling (PGC) [71].

2.1.6 Transfer to a magnetic trap

In a magneto-optical trap, atoms are generally distributed approximately equally across all hyperfine states. In contrast, pure magnetic trapping requires the atoms to have $g_F m_F > 0$ [72]. For the two hyperfine states of ^{87}Rb, where $g_{F=2} = 1/2$ and $g_{F=1} = -1/2$, the only magnetically trappable Zeeman sub-states are thus: $|F = 2, m_F = 2\rangle$, $|F = 2, m_F = 1\rangle$ and $|F = 1, m_F = -1\rangle$. Consequently, in order to achieve high transfer efficiencies from a 3D MOT to a magnetic trap, the atoms must initially be spin polarized in one of these states. For that purpose, all laser beams are turned off and an optical pumping cycle, illustrated schematically in figure 2.7, is applied to the atoms. To transfer the atoms to the $|F = 2, m_F = 2\rangle$ state (see figure 2.7a), the repump light is switched on and a σ^+ polarized light drives the $S_{1/2}, F = 2 \rightarrow P_{3/2}, F' = 2$ transition. Once the atoms are pumped into the magnetically trapped $|F = 2, m_F = 2\rangle$ dark state they are no longer interacting with the pumping laser and remain in a dark state. Alternatively, it is possible to transfer the atoms to the $|F = 1, m_F = -1\rangle$ state (see figure 2.7b) using a σ^- polarized light to drive the $S_{1/2}, F = 2 \rightarrow P_{3/2}, F' = 2$ transition and a short repump pulse. This process is less efficient than pumping the $|F = 2, m_F = 2\rangle$ state since the $|F = 1, m_F = -1\rangle$ state is not dark when the repump is on and other Zeeman sub-states can also be populated in this scheme. However, by choosing appropriate timing and laser power for both the optical pumping and repump beams, a transfer of up to 80% of the atoms into the $|F = 1, m_F = -1\rangle$ state was performed experimentally.
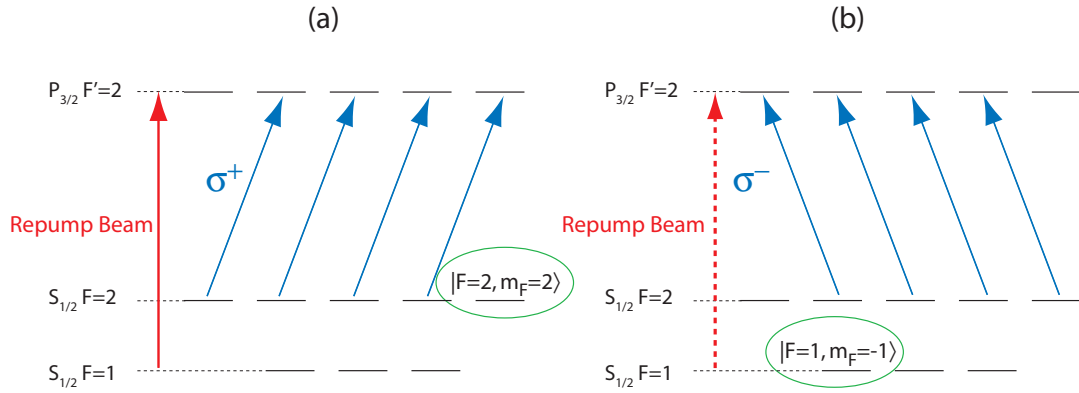

Figure 2.7: Schematics of optical pumping cycles to polarize the atoms in a) the $|F = 2, m_F = 2\rangle$ state or b) the $|F = 1, m_F = -1\rangle$ state using σ^+ or σ^- light respectively. In (b), the dashed line for the repump illustrates that it is a short pulse which is switched off before the end of the optical pumping sequence.

In early experiments carried out in our group, the atoms were transferred to the $|F = 2, m_F = 2\rangle$ dark state as the process is the most efficient and the characteristic trapping frequency is $\sqrt{2}$ larger than that for the other states, leading to higher collision rates which are advantageous for evaporative cooling. However, when working with atom lasers, it is more appropriate for the source of atoms to be in the $|F = 1, m_F = -1\rangle$ state in order to increase the flux and decrease the classical noise in the atom laser beam (see chapter 5).

2.1.7   Transport by a Translation Stage

In order not to make any compromise on the creation of a large MOT and on the efficiency of the magnetic trapping of the condensate, the setup is designed so that the positions of the 3D MOT and the final location of the magnetic QUIC trap do not coincide (see figure 2.2). Consequently, the atoms are transported from the Collection to the BEC chamber using the technique developed at JILA [73]. Following the 3D MOT and optical pumping stages, all optical beams are switched off and the current in the quadrupole coils is ramped up from 0 to 360 A in 10 μs in order to strongly confine the spin-polarized atoms. The coils, which are mounted on a computer controlled 25 cm high precision linear translation stage (PI M-521), subsequently transport the atoms all the way to the BEC cell. Figure 2.8 shows the position of the quadrupole transport coils at different locations, from their initial position around the 3D MOT (1) to their final position where the atoms are transferred to a QUIC trap (3). In order to minimize losses or heating of the atoms, a smooth transport of the magnetic coil is achieved in 7 s. The first second of transport consists of a very smooth acceleration to reach a constant velocity, whereas the last second is a very smooth deceleration to zero velocity. All magnetic coils are water-cooled and have an interlock which switches the power supplies off if any overheating is detected.

2.1.8   QUIC Trap

2.1.8.1   Transfer to the QUIC Trap

Following the transport of the atoms, the imaging beam ($\sim$ 15 mW), which is resonant with the $F = 2$ atoms, is applied for about 50 μs in order to blow away any residual atoms in the $|F = 2, m_F = 2\rangle$ state. The $|F = 1, m_F = -1\rangle$ atoms are subsequently transferred from the magnetic quadrupole trap into a Ioffe-Pritchard type QUIC trap. The QUIC trap consists of three magnetic coils: two quadrupole coils are placed horizontally, above and underneath the glass cell
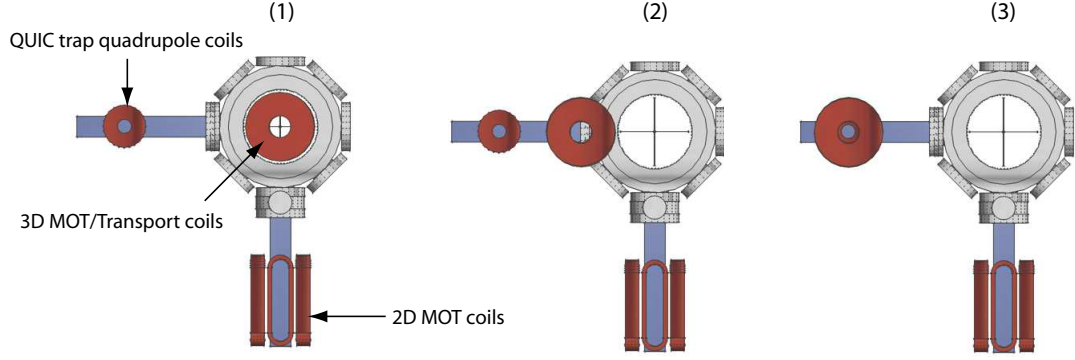
Figure 2.8: Transport of the magnetically trapped atoms by a translation stage. The quadrupole coils, initially above the Collection chamber (1), are moved across the frame (2) to the far end of the BEC chamber (3).

(see figure 2.2), whereas a Ioffe coil is positioned vertically, on the side of the cell. The resulting magnetic field of such a configuration is presented in more detail in section 6.2.8 and can be approximated as:

$$B(x,y,z) = B_0 + \frac{B''}{2}y^2 + \left(\frac{B'^2}{2B_0} - \frac{B''}{4}\right)(x^2 + z^2) \qquad (2.1)$$

where only the second order terms are significant in the three spatial directions and where B_0, B' and B'' are the bias, gradient and curvature of the magnetic field respectively. The trapping frequencies in the axial and radial directions are given by:

$$\omega_y = \sqrt{\frac{g_F m_F \mu_B B''}{m}} \qquad \text{and} \qquad \omega_\rho = \omega_z = \omega_x = \sqrt{\frac{g_F m_F \mu_B}{m}\left(\frac{B'^2}{B_0} - \frac{B''}{2}\right)}. \qquad (2.2)$$

respectively. $g_F = 1/2$ is the Landé factor of the F hyperfine state, m_F is the projection of the total angular momentum, μ_B is the Bohr magneton and m is the mass of the atom. The transfer is achieved in 500 ms by ramping up the current (~ 16 A) in the two quadrupole coils of the QUIC trap and simultaneously ramping down the current in the transport coils. Finally, the current in the Ioffe coil is ramped up in 1 s. Additional cooling of the atoms down to the critical temperature for Bose-Einstein condensation is achieved after an evaporative cooling stage by applying an *RF* field whose frequency is ramped over 25 s from 30 MHz to ~ 1.4 MHz (which corresponds to

a magnetic bias field of $B_0 \sim 2$ G). During evaporation, the number of atoms decreases from 5×10^9 to a final value of $\sim 10^6$ condensed atoms.

2.1.8.2 Optical Imaging

With our current setup it is possible to image the condensate along two axes (*x* and *y*) as shown in figure 2.6. Along the *x*-axis, an imaging beam passes all the way through the vacuum system and images the BEC in the *yz*-plane onto a CCD camera. The camera is a 12 bit Photometrics SenSys with a 786×512 array of $9 \, \mu$m square pixels and a quantum efficiency of 42%. It is mounted on a stabilized x, y, z translation stage to allow precise positioning at the image plane. This imaging beam is used to image the 3D MOT as well as the combined weak and strong axes of the condensate in the plane of the Raman beams (see section 2.2 and chapter 4).

Along the *y*-axis, an imaging beam passes across the QUIC trap through the Ioffe coil and images the BEC in the *xz*-plane on a 16 bit frame transfer camera which has the ability to take very fast sequences of images. This imaging beam is used in chapter 3 to measure the divergence of the atom laser.

2.1.8.3 Trap Frequencies

To measure the trap frequencies, it is possible to study the sloshing mode of the atoms [62, 74]. A cloud of atoms is preliminarily cooled to a temperature of $\sim 1 \, \mu$K by ramping the frequency of the *RF* cut down to ~ 1.6 MHz. The axial and radial oscillations of the cloud are then driven by modulating the current of the trapping potential. The following measurements were performed for a sample of atoms polarized in the $|F = 2, m_F = 2\rangle$ state. The trapping frequencies of a sample spin-polarized in the $|F = 1, m_F = -1\rangle$ state are easily deduced since they are smaller by a factor $\sqrt{2}$.

To measure the radial trapping frequency, an additional coil is placed in the horizontal plane, between the glass and a quadrupole coil, approximately 3 cm away from the atoms. A small alternating current (0.08 A - 200 Hz) is applied for 100 ms so that the center of the trap is moved sinusoidally, causing the atoms to oscillate. The position of the atomic center-of-mass (x_ρ) is measured after a variable delay time which is varied in steps of 200 μs from 0 to 12 ms (see figure 2.9a) and can be fitted to an exponentially damped sinusoidal function following:

$$x_\rho(t) = a + b\exp(-t/\tau)\sin(\omega_\rho t + \varphi)). \tag{2.3}$$

In this equation, b is the amplitude of the oscillation around the offset value a, τ is the damping time and φ a phase factor. The result from the fit yields to a radial trapping frequency of $\omega_\rho = \omega_x = \omega_z = 2\pi \times 204.6$ Hz.

To measure the trapping frequency in the axial direction, a similar approach was first attempted by adding an additional coil along the axis of the Ioffe coil. However, because the divergence of the field from the Ioffe coil is large and because only a small coil could be added close enough to the cell, the position of the trap could not be changed significantly in order for the atoms to oscillate. Alternatively, an extra current (0.3 A) is ramped up directly into the Ioffe coil, displacing the minimum of the trap away from its original position. The current is suddenly turned off, allowing the atoms to freely oscillate in the trap. The same imaging technique is used and an absorption picture taken after a delay time, varying from 0 to 90 ms in steps of 2 ms (see figure 2.9(b)). The same fitting routine yields a measurement of the axial trapping frequency $\omega_y = 2\pi \times 20.4$ Hz.
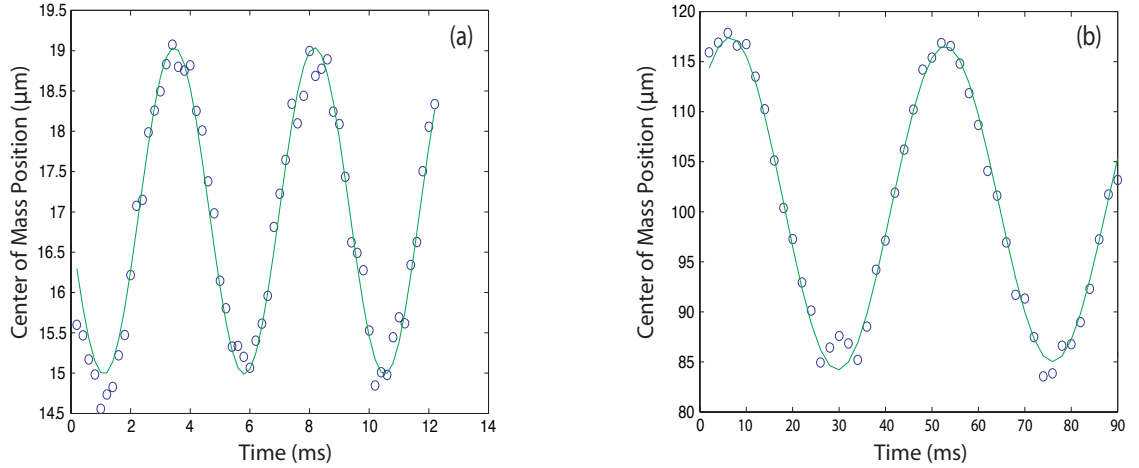

Figure 2.9: Trap oscillations of the cloud center-of-mass. The measurements (circles) are fitted to an exponentially damped sinusoidal function (solid lines). For atoms in the $F = 2, m_F = 2$ state, a radial frequency of $\omega_\rho = 2\pi$ x 204.6 Hz (a) and an axial frequency of $\omega_y = 2\pi \times 20.4$ Hz (b) are measured.

2.2 EXPERIMENTAL SETUP TO PRODUCE RAMAN BEAMS

As previously explained in chapter 1, it is possible to couple atoms out of the Bose-Einstein condensate using a two-photon Raman transition. Under appropriate optical conditions, the atoms can be transferred from their initial magnetically trapped state to a state that does not interact with the magnetic field and consequently falls under gravity. This section presents the optical layout producing optical Raman beams for our experiment. In chapter 3, these beams are used as a state changing out-coupler to create a Raman atom laser with low divergence and improved spatial profile. Alternatively, in chapter 4, each Raman beam is used independently as a beam splitter diffracting up to 60% of an incoming beam of atoms.

2.2.1 Optical setup

The optical setup used to produce the two optical beams for Raman out-coupling is shown in figure 2.10.

A single tunable high power single mode diode laser (DLX110 from Toptica) provides an output beam of about 700 mW in the $TEM_{0,0}$ mode. The light is red-detuned by 300 GHz from the D2 transition of ^{87}Rb in order to suppress any heating due to spontaneous emission. The laser power in the rest of the setup can be turned on or off in less than 200 ns using a fast switching 110 MHz AOM in a double pass configuration. In order to control the switching AOM, a pulse generator (Agilent) produces a pulse of variable width and variable delay time which is sent to the switching AOM amplitude. The light is subsequently split into two independent beams which are double-passed through separate 80 MHz AOMs. Having the AOMs in double-pass configuration allows the frequency of each laser beam to be shifted by a few MHz without deviating the laser beam paths throughout the optics. The AOMs are driven by two phase locked Agilent 80 MHz function generators operated in external amplitude control mode from a single oscillator. By measuring the beat note on a spectrum analyser, the frequency difference between the two beams was inferred to be stable to at least 10 Hz which is the resolution of the spectrum analyser. It is likely that the frequency difference is actually stable to 6 μHz (which is the precision of the function generators) although the use of additional optics will be a limiting factor. As mentioned in the previous chapter, the frequency difference between the AOMs must correspond to the Zeeman plus kinetic energy difference between the initial and final states of the two-photon Raman transition. This value depends on the magnetic field bias as well as on the angle between
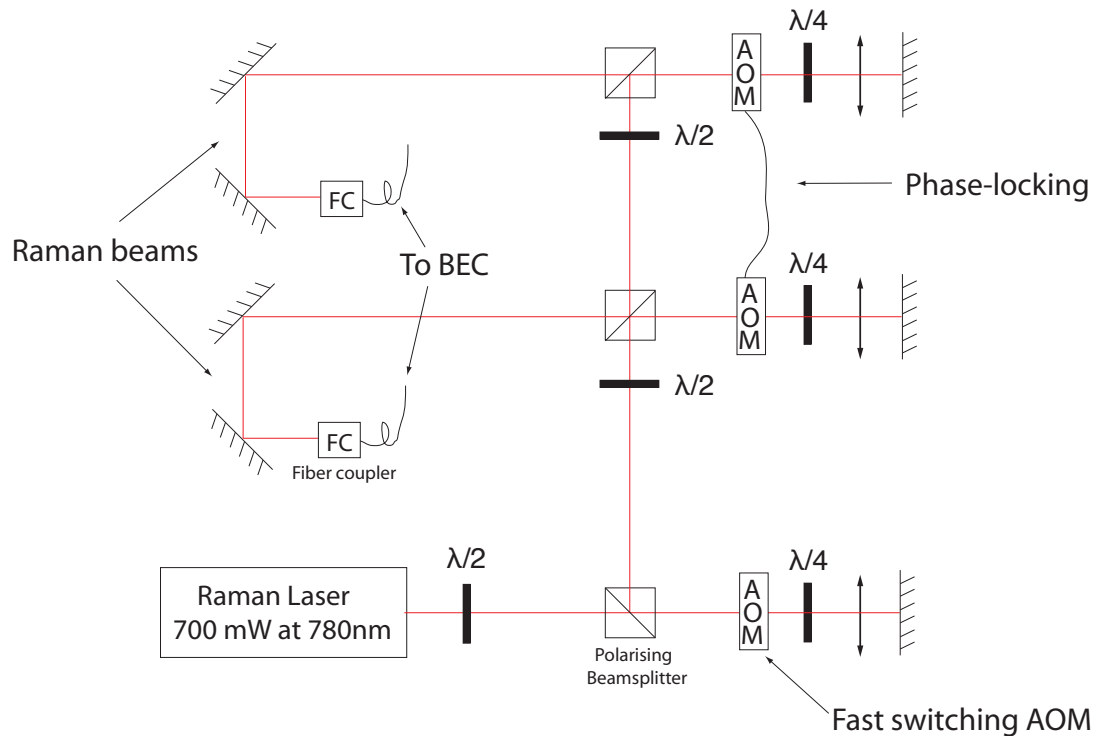
Figure 2.10: Optical setup used to prepare the laser beams for Raman outcoupling. A fast AOM can switch the Raman beams in less than 200 ns with an extinction ratio greater than 60 db. The frequency difference between the two Raman beams is tuned using two distinct AOMs. The light is fiber-coupled and sent to the BEC machine where the polarization of each beam is adjusted (figure 2.11).

the two Raman beams and is typically on the order of 1 MHz in our experiment. However, the frequency difference between the two Agilent function generators is only set to ~ 0.5 MHz in order to allow for the double-pass configuration of the AOMs. Both Raman beams are separately coupled to a SM-PM optical fiber and sent to the BEC table. They pass through independent collimating lenses to provide collimated beams of about 500 μm radius on the atoms. One of the beams also passes through a quarter wave-plate in order to adjust its polarization (see section 2.2.2). Upon reaching the condensate, the maximum intensity in each beam is measured to be approximately ~ 2500 mW/cm^2 and the extinction ratio of the setup is greater than 60 dB. The two optical Raman beams propagate in the vertical plane defined by gravity and the magnetic bias field. They are symmetric with regard to the y-direction with a separation θ between them. Because of spatial restrictions due to the presence of magnetic coils, vacuum system and other

optics, only two configurations with $\theta = 30°$ and $\theta = 140°$ were achieved (see figure 2.11) so that the atoms could be out-coupled with a momentum kick given by $2\hbar k sin(\theta/2)$, equivalent to initial velocities of 0.3 cm.s^{-1} and 1.1 cm.s^{-1} respectively.
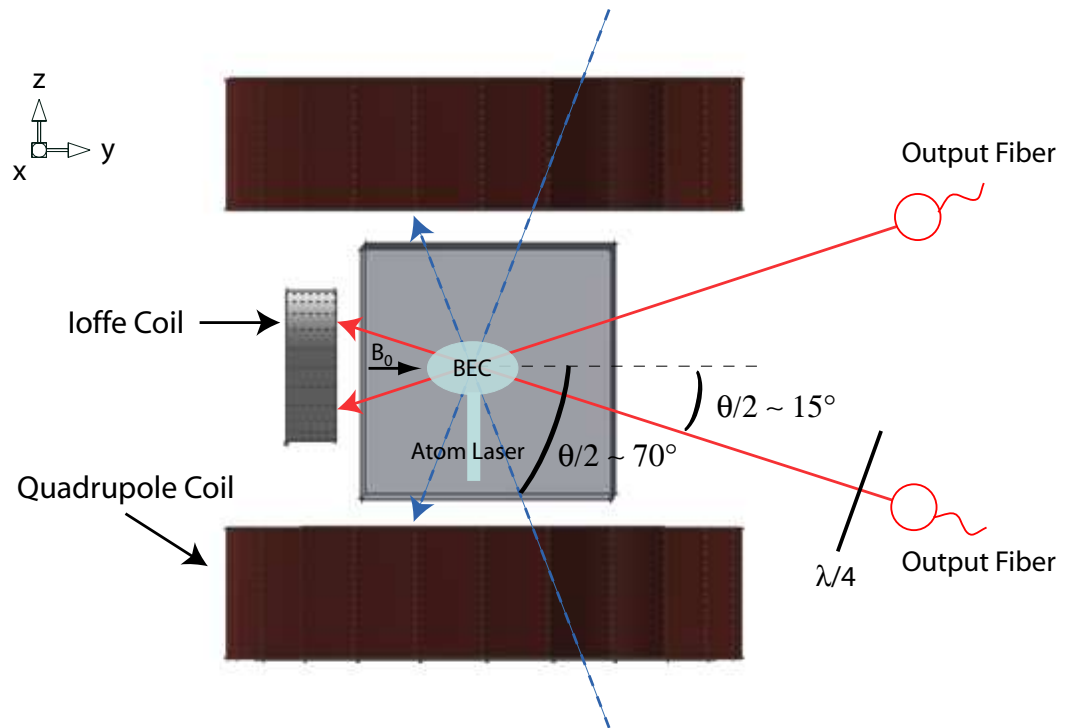
Figure 2.11: Optical layout used to illuminate the BEC with the two Raman beams of appropriate polarization. In our setup two configurations are used with the angle between the beams being set to 30° or 140°.

2.2.2 Adjusting the polarization of each of the beams

In order to drive the Raman transition, optical polarization is critical. Both laser beams are linearly polarized at the output of the optical fiber. However, in order to drive the Raman transition in the $F = 1$ manifold with a downward kick transferred to the atoms, the upward propagating beam must have a circular σ^+ polarization. Consequently, this beam additionally passes through a quarter wave plate which is adjusted to produce the appropriate polarization.

With the Raman beams at an angle to the magnetic field bias (which defines the quantization axis), it is necessary to consider the projection of the polarization upon the axis of the bias field

rather than along the axis of the beam. In our setup, the magnetic field bias is along the axis of the Ioffe coil. For a laser beam of linearly polarized light, propagating at an angle θ to the field axis and with a polarization orthogonal to the plane defined by the bias field axis and gravity, the projected polarization is independent of the angle θ. However, for light linearly polarized in the opposite direction (i.e. in the plane of the page), the amplitude of the linearly polarized light with respect to the field axis is reduced by a factor of $cos(\theta)$. Therefore, circularly polarized light, which is a combination of the two orthogonal linear polarizations, will be projected as an elliptical polarization with an eccentricity of $sin(\theta)$. Thus, in order to approach a circularly polarized light along the field axis, it is necessary to input elliptically polarized light along the beam path. Experimentally, estimating the appropriate eccentricity of an elliptically polarized beam is rather difficult and the quarter wave-plate is simply rotated until the maximum out-coupling efficiency is obtained.

2.3 CONCLUSION

In this chapter, the entire experimental setup used to produce our Bose-Einstein condensates of up to 10^6 Rb atoms is presented. The machine separates the UHV Collection region from the BEC cell, allowing an improved optical access along all primary axes of the BEC. We took advantage of this configuration to implement two high power optical Raman beams in the system. These beams are used in the next chapter to investigate the divergence properties of a Raman atom laser compared to the atom laser extracted with the widely used RF method.

CHAPTER 3

DIVERGENCE OF AN ATOM LASER

Atom laser beams show great promise for studies of fundamental physics and in high precision measurements [75] due to atoms responding far more strongly than light to gravity, rotations and external fields. For all applications based on these properties it is crucial to develop atom lasers with output modes that are simple and as clean as possible in both amplitude and phase in order to allow stable mode-matching to other beams or cavities just as it was crucial for optical lasers. The aim of this chapter is to compare the quality of Raman and RF out-coupled atom laser beams. The quality factor of an atom laser is defined in analogy to optical lasers. The importance of out-coupling the atoms from the center of the BEC is also discussed. Experimental results on the improved divergence of a Raman atom laser are finally presented and discussed with regard to a theoretical model.

3.1 M^2 QUALITY FACTOR

In order to quantitatively measure the atom-laser beam quality, it is tempting to take advantage of the methods that were developed in optics to deal with non-ideal laser beams above the diffraction limit. In analogy to optical lasers, a beam quality factor M^2 was introduced for atom lasers [21] to measure how far an atomic beam deviates from the Heisenberg limit. This M^2 factor is defined as :

$$M^2 = \frac{2}{\hbar} \Delta x_0 \Delta p_{0_x} \tag{3.1}$$

where Δx_0 is the beam width of the atom laser, measured at the waist, and Δp_{0_x} is the transverse momentum spread. Equation 3.1 plays the same role as the Heisenberg dispersion relation : it expresses how much the beam deviates from the diffraction limit. In analogy to a Gaussian optical beam, an ideal atom laser beam will therefore have $M^2 = 1$ along both its principal transverse axes, whereas any other non-ideal atomic beam will have $M^2 > 1$. It has already been shown in a number of experimental and theoretical works [20, 21, 76–78] that the beam quality factor of an atom laser is strongly affected by the interaction of the out-coupled atoms with the BEC from which it is produced. Therefore, as the atoms fall through the condensate, the repulsive interac-

tion they experience acts as a diverging lens to the out-coupled atoms, leading to a divergence in the atom laser beam. Also, because the BEC can be considered as a non-ideal lens, the transverse beam profile will be of poor quality. Such behavior may cause problems in mode matching the atom laser beam to another atom laser, to a cavity or to a waveguide. Alternatively, experiments on atom lasers in waveguides have produced beams with improved spatial profile [22]. However, precision measurements with atom interferometry are likely to require propagation in free space in order to avoid introducing noise from the fluctuations in the waveguide itself [79]. The experimental results presented in the following are obtained in free space using the experimental setup described in the previous chapter.

3.2 OUT-COUPLING FROM THE CENTER OF THE BEC

The quality of a free space radio-frequency atom laser can be greatly improved by setting the out-coupling cut at the lower edge of the condensate, as demonstrated experimentally by Riou *et al.* [21]. Indeed in this case, the out-coupled atoms only experience the mean-field repulsive interaction over a short time, thus reducing the divergence of the atomic beam. However, when creating an atom laser beam, one needs to worry about the flux, fluctuations and lifetime of the beam as essential parameters for any useful application. Consequently, there are many reasons why it is actually much more desirable to produce an atom laser while out-coupling from the center of the condensate:

1. Flux: The output flux of the atom laser beam can be approximated by multiplying the number of atoms in the coupling region of interest by the Rabi frequency [30] following

$$F \sim N_{\delta z_{res}}(N, \Omega)\Omega \tag{3.2}$$

where N is the total number of atoms in the condensate, $N_{\delta z_{res}}(N, \Omega)$ is the number of atoms within the out-coupling region δz_{res} and Ω is the Rabi frequency. It appears from equation 3.2 that increasing the Rabi frequency can potentially improve the flux in the atomic beam. However, the classical noise level of an atom laser is also determined by Ω [28] and is inherent to the state-changing out-coupling process. Thus, the flux is somehow limited by the maximum possible Rabi frequency allowing the atom laser to work in a quiet regime. Consequently, for a given classical noise level, the highest possible output flux will be

obtained when out-coupling the atoms from the region where the density is the greatest, which is the center of the BEC.

2. Operating time: Any quasi-continuous atom laser beam operates on a limited time-scale since the source of atoms is not continuously replenished during the draining process. Moreover, due to the mean field interactions, the BEC progressively shrinks towards its center as the total number of atoms decreases inside the condensate. As a result, out-coupling from the edge of the condensate requires that the resonance frequency is continuously swept to smaller values in order to permanently address the BEC. Alternatively, out-coupling from the center of the cloud allows the longest operating time, draining the whole condensate for a fixed frequency.

3. Sensitivity to fluctuations: Finally, out-coupling from the center also minimizes the sensitivity of the output coupling to external fluctuations since the atomic density is maximum. This can be understood from the density profile showed in figure 3.1b. It is clear that small variations around the central out-coupling frequency will not affect the out-coupling process much if the frequency is set at the center of the BEC (indicated by the arrow). This is no longer the case when out-coupling from the edges, since small variations of the out-coupling frequency can shut-off completely the output of the atomic beam.

As mentioned before, out-coupling from the center of the BEC using an RF out-coupling technique dramatically degrades the transverse profile of the atomic beam [21]. However, a substantial improvement is expected to arise from Raman out-coupling because the momentum kick imparted to the atoms allows them to leave the condensate much more quickly, thus reducing the adverse effects due to the mean-field repulsion from the condensate.

In order to set the output-coupling resonance at the center of the BEC, a spectroscopy of the condensate is performed. The condensed atoms are initially produced in the $|F = 1, m_F = -1\rangle$ state following the experimental procedure described in the previous chapter. A weak RF output-coupling is applied on the BEC for ~ 100 ms and the number of atoms remaining in the condensate is measured after the out-coupling time for different frequencies of the RF field. The resonance frequency addressing the center of the BEC, where the atom density is the greatest, is given by the point of maximum out-coupling rate. The system is observed using standard absorption imaging along the y (weak trapping) direction as shown in figure 3.1a. The imaging beam frequency is tuned to the $F = 2 \rightarrow F' = 3$ transition (see chapter 2) and an initial 200
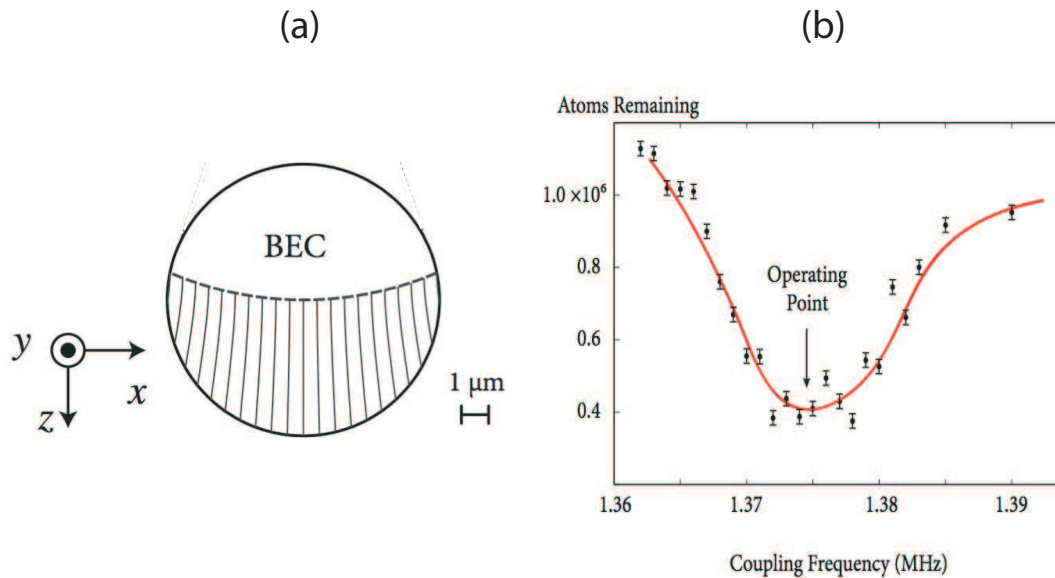
Figure 3.1: (a) Represents a cross-section of the condensate along the two directions of strong confinement. The long axis is along the y direction and the BEC has a cigar shape with an aspect ratio of about 10. The dashed line is the out-coupling cut at the center of the condensate. (b) Shows a typical RF output coupling spectroscopy of the BEC from which the operating point at the center of the condensate (designated by the arrow) is determined. The solid line is only to guide the eye. Error bars are based upon typical standard deviation.

μs pulse of repumping light ($F = 1 \rightarrow F' = 2$) is applied 1 ms prior to imaging in order to transfer the atoms into the $F = 2$ hyperfine state. A typical calibration curve is shown in figure 3.1b where RF output coupling was used. Both RF and Raman output-couplers are operated at the frequency indicated by the arrow which gives the maximum out-coupling rate. The Raman two-photon detuning is smaller than the RF frequency by the kinetic energy of the momentum recoil (see equation 1.17). However, it remains almost the same as the RF resonance frequency since the maximum recoil energy $2\hbar^2 k^2/m$ (obtained when $\theta = 180°$) is on the order of $h \times 16$ kHz $\ll \mu_B B_0/2 \sim h \times (1.3 - 1.4)$ MHz. In order to further check this optimal frequency for both RF and Raman out-coupling, we ensure that a continuous beam can still be produced when the initial condensate is made very small (by lowering the frequency of the evaporation cooling ramp), which only happens when out-coupling from the center of the BEC.

3.3 REDUCING THE DIVERGENCE OF THE ATOM LASER

We compare experimentally the divergence properties of atom laser beams of both RF and Raman out-coupling techniques, always setting the resonance frequency to out-couple from the center of the condensate. The initial BEC contains approximately 5×10^5 atoms in the $|F = 1, m_F = -1 >$ state and is trapped in a magnetic potential of axial and radial frequencies of $\omega_y = 2\pi \times 13$ Hz and $\omega_\rho = 2\pi \times 130$ Hz respectively. The resulting chemical potential is $\mu/\hbar \sim 2\pi \times 3$ kHz. The cloud is cigar-shaped with a size of $\Delta z_{BEC} \sim 13$ μm in the direction of gravity with an aspect ratio of about 10. We produce an atom laser beam by continuously transferring the atoms to the magnetically un-trapped $|F = 1, m_F = 0 >$ state over 10 ms. The results are shown in figure 3.2.

In figure 3.2a, the atoms are transferred to the magnetically un-trapped $|F = 1, m_F = 0 >$ state after a spin flip process induced by RF out-coupling. They fall under gravity with no initial velocity since this coupling implies only a negligible momentum transfer to the atoms. In figure 3.2b-c, the atom laser beams were produced using a Raman two-photon transition where the angle between the Raman beams was changed from $\theta = 30°$ to $\theta = 140°$ respectively. Such configurations correspond to momentum transfer of $0.5\hbar k$ and $1.9\hbar k$ respectively and the out-coupled atoms thus leave the condensate with an initial velocity of $v_i = 0.3$ cm.s^{-1} and $v_i = 1.1$ cm.s^{-1} respectively. Qualitatively, the divergence of the laser beam is clearly reduced and the beam profile improved as the momentum kick is increased. At the bottom of the pictures we show a comparison of experimental and theoretical beam transverse intensity profiles at a distance 500 μm below the BEC (indicated by the horizontal dashed line). The theoretical plots were obtained from the model described in the following section whereas the experimental data simply represent the number of atoms across a horizontal slice of the atomic beam.

From the images, we can extract the rms width of the atom laser as a function of the falling distance, which will be used to calculate the M^2 quality factor of the atom laser. The experimental results are represented by the dots in figure 3.3. Each dot was obtained by measuring the rms width of a transverse intensity profile at a given position along the z-axis. Theoretical predictions are used to fit the experimental data and will be briefly described in the following section. This theoretical work was performed by M. Jeppesen and detailed explanations can be found in his PhD thesis [80]. Therefore, only an overview of the work is given on how we obtained the value of M^2 quality factor of an atom laser.
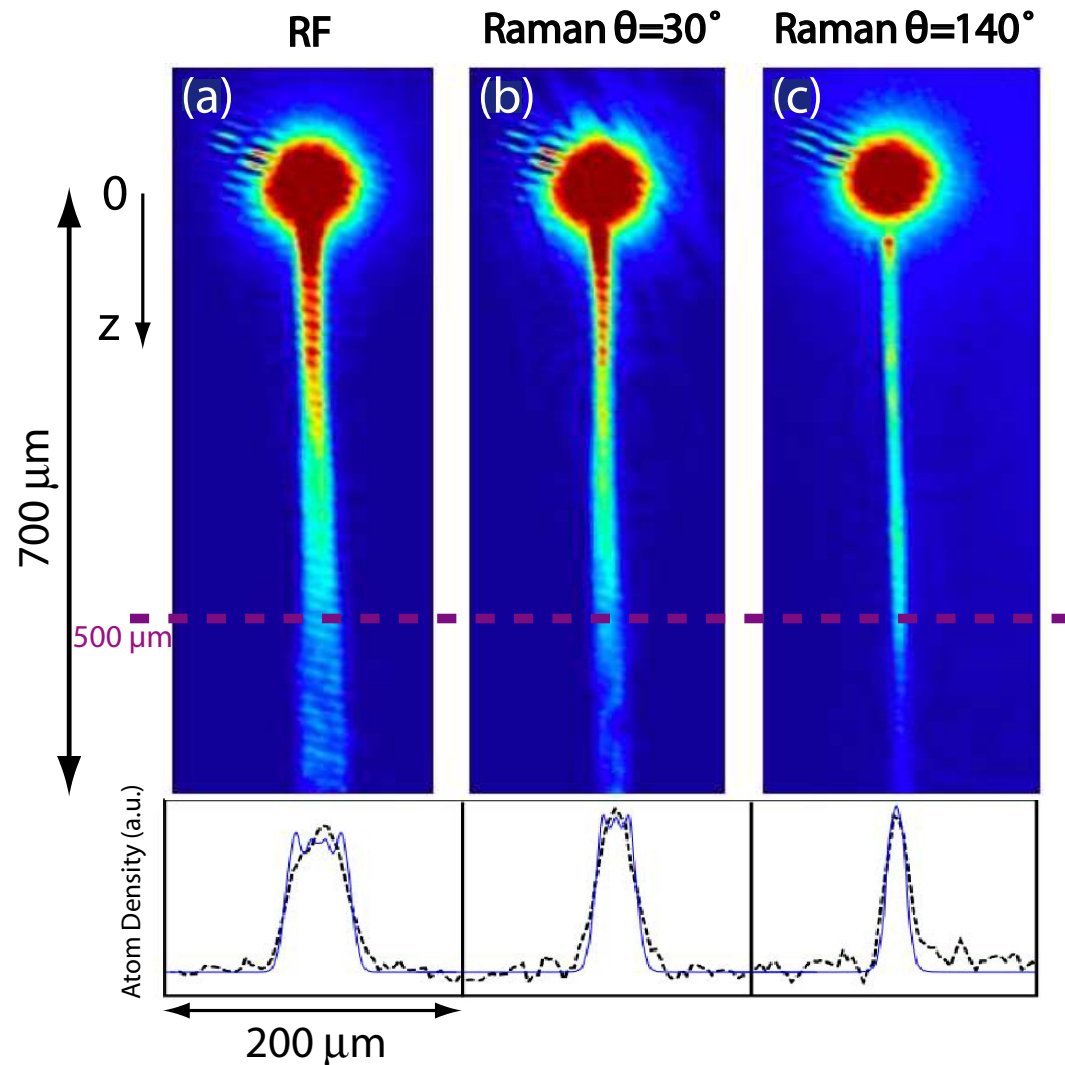
Figure 3.2: The top images show a sequence of atom laser beams produced using RF (a) and Raman (b and c) transitions with the out-coupling cut set at the center of the BEC and imaged after a 3 ms time-of-flight. The angle between the Raman beams was $\theta = 30°$ in (b) and $\theta = 140°$ in (c), corresponding to momentum kicks of 0.5 $\hbar$k (0.3 cm.s^{-1}) and 1.9 $\hbar$k (1.1 cm.s^{-1}) respectively. The out-coupling rate differs between each atom laser and the time-off-flight was set to approximately 3 ms. One can see the improved beam profile of a Raman atom laser. Note that the fringes that can be observed in the condensates are an imaging artifact due to interferences on the CCD cover plate. The bottom plots show a comparison of experimental (dashed) and theoretical (solid) beam profiles at a distance 500 μm below the BEC (indicated by the horizontal dashed line). The heights have been normalized and each theoretical curve has been scaled to match the experimental data.
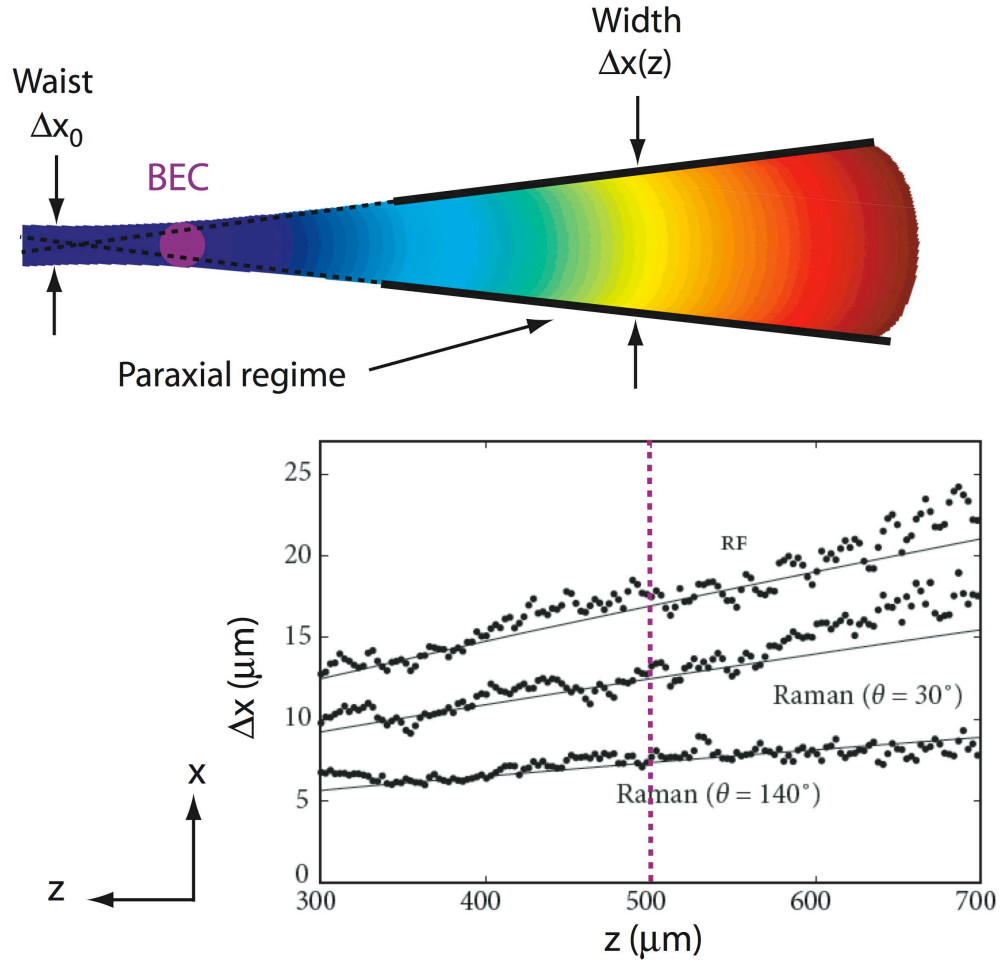
Figure 3.3: The top figure illustrates the paraxial regime in which the atoms propagate at some distance below the BEC. In the bottom graph, the dots represent experimental measurements of the width of the atom laser as a function of the position below the BEC. Solid curves show a comparison to our theoretical predictions. Note that observations at distances less than 300 μm are prevented by the condensate expansion after trap switch-off. At distances greater than 700 μm, the density in the atomic beam gets low and measurements are less accurate. The vertical dashed line represents the position considered in figure 3.2.

3.4 THEORETICAL MODEL OF THE EXPERIMENT

Calculating the quality factor M^2 of the atom laser directly from 3.1 requires measurement of the beam width at the waist (Δx_0) as well as the transverse momentum (or velocity) spread. However, because the BEC acts as a diverging lens on the atom laser, the beam waist is virtual and

located above the BEC. Therefore, it is not possible to solely do an experimental measurement of the beam quality M^2 using equation 3.1. Consequently, a complementary theoretical model is required.

3.4.1 The model

To model the atom laser spatial mode, a three-step method was used following the work of Riou *et al.* [21]. At each step, the atom laser beam propagates in different regions of space and an appropriate description was used as follows :

1. Inside the condensate, we perform a Wentzel-Kramers-Brillouin (WKB) approximation [81–83] by finding the classical trajectories of the atoms inside the condensate, from where they are produced to where they leave the BEC. This is done by integrating the phase along the classical trajectories of the atoms moving in the Thomas-Fermi potential of the condensate (which is an inverted parabola) [77]. In the WKB approximation, the atom laser wavefunction on the edge of the condensate ($\psi(\mathbf{r}_f)$) can be related to the one on the out-coupling surface ($\psi(\mathbf{r}_i)$) by :

$$\psi(\mathbf{r}_f) = \sqrt{\left|\frac{\partial(\mathbf{r}_i)}{\partial(\mathbf{r}_f)}\right|} \; exp\left(i\int_C \mathbf{k}.d\mathbf{r}\right) \; exp(i\mathbf{k}_0.\mathbf{r}_i) \; \psi(\mathbf{r}_i) \tag{3.3}$$

where $\mathbf{r}_f$ and $\mathbf{r}_i$ are the coordinate of the atoms on the edge of the condensate and on the out-coupling surface respectively, with the origin being at the center of the BEC. C is the classical atomic trajectory to go from $\mathbf{r}_i$ to $\mathbf{r}_f$. $\mathbf{k}$ is the atomic wave-vector ($\mathbf{k} = \mathbf{p}/\hbar$) of the condensate atoms along C and $\mathbf{k}_0$ is the initial momentum kick imparted to the atoms. $\left|\frac{\partial(\mathbf{r}_f)}{\partial(\mathbf{r}_i)}\right|$ is the Jacobian determinant and the wavefunction on the out-coupling surface $\psi(\mathbf{r}_i)$ is proportional to the condensate wavefunction $\psi_c(\mathbf{r}_i)$ in the weak coupling limit which is considered in this model. The condensate wave-function is easily calculated in the Thomas-Fermi approximation by solving

$$|\psi_c(\mathbf{x})|^2 = \frac{m}{4\pi\hbar^2 a}\left(\mu - V_{eff}((\mathbf{x}))\right) \tag{3.4}$$

where μ is the chemical potential of the system and V_{eff} includes the gravitational, magnetic, and mean-field terms of the Hamiltonian.

The atom laser wavefunction and its gradient on the edge of the condensate are finally derived [80] as:

$$\psi(\mathbf{r}_f) = \frac{1}{cosh(\omega_\rho t_e)} \, e^{i\phi} \, exp(\frac{imv_iz_i}{\hbar}) \, \sqrt{1 - \frac{|\mathbf{r}_i|^2}{R^2}} \tag{3.5}$$

and

$$\nabla\psi(\mathbf{r}_f) \approx i\frac{m}{\hbar}\mathbf{v}(\mathbf{r}_f)\psi(\mathbf{r}_f) \tag{3.6}$$

In these equations, ω_ρ is the strong trapping frequency, t_e is the escape time for the atoms to reach the edge of the BEC, m is the mass of an atom, v_i is the velocity kick due to the photon recoil (in the case of a Raman out-coupling), and R is the size of the condensate (Thomas-Fermi radius). Finally, ϕ represents the phase determined from the integral of the de Broglie wavelength along the classical trajectory ($\phi = \int_C \mathbf{k}.d\mathbf{r}$).

2. Outside the condensate we propagate the atom laser wavefunction using a Kirchoff-Fresnel diffraction integral over the surface of the condensate and using the Green's function for the gravitational potential. This technique allows to solve homogeneous differential equations of some function in space given values of the function and its gradient on the boundary of space, following:

$$\psi(\mathbf{r}) = \int_S d\mathbf{S}'.[G\nabla'\psi - \psi\nabla'G] \tag{3.7}$$

In this expression, S is the entire region outside the condensate with the boundaries being the edge of the condensate and an imaginary surface at infinity where the atom laser and its derivatives vanish. The values of the function ψ and its gradient $\nabla'\psi$ are obtained from the previous expressions 3.5 and 3.6. $G = G(\mathbf{r},\mathbf{r}')$ is the Green's function for the Hamiltonian in the gravitational potential $V_{grav}(\mathbf{r}) = -mgz$ only [84]. Therefore, the model includes only interactions inside the BEC between condensate atoms and beam atoms. In particular, interactions between atoms within the beam (that have left the condensate) are ignored (they are negligible for the very dilute beam constituting the atom laser). The integral in equation 3.7 is formally a two-dimensional surface integral over the whole condensate.

However, following [21], we can neglect divergence in the weak trapping axis and only consider the dynamics of cross sections in the plane of the two strong trapping axes. In this case, the integral becomes one dimensional.

3. Finally, the third region is where the atom laser has accelerated sufficiently under gravity to have entered the paraxial regime where the M^2 factor can be calculated away from the waist as it becomes a constant of propagation. In this regime, the transverse part ($\psi_\perp(x,z,t)$) of the atom laser wavefunction can be calculated from the equation of propagation. Assuming an envelope varying slowly along z and in the paraxial approximation, the equation of propagation can be expressed as [80]:

$$i\hbar \frac{p(z)}{m} \frac{\partial \psi_\perp}{\partial z} = -\frac{\hbar^2}{2m} \frac{\partial^2 \psi_\perp}{\partial x^2} \tag{3.8}$$

where $p(z) = \sqrt{2m(E - V_{grav}(z))}$ is the classical momentum and E the total energy. The solutions can be expressed in terms of Hermite-Gauss polynomials and the lowest order Gaussian mode is given by

$$\psi_\perp(x,t) = \left(\frac{2}{\pi w_0^2} \right)^{1/4} exp \left(-\frac{x^2(1 + 2i\hbar t/(mw_0))}{w_0^2(1 + 4\hbar^2 t^2/(m^2 w_0^2))} \right) \tag{3.9}$$

From there, the M^2 factor can be calculated equivalently to 3.1 at some height z below the BEC, following :

$$\left(\frac{M^2}{2} \right)^2 = \frac{m^2}{\hbar^2} [\Delta x(z)]^2 [\Delta v_x(z)]^2 - C(z)^2 \tag{3.10}$$

where $\Delta x(z)$ is the beam width and $\Delta v_x(z)$ is the velocity spread of the atom laser wavefunction. $C(z)$ is the curvature-beam width product [?] given by :

$$C(z) = \frac{i}{2} \int_{-\infty}^{\infty} x \left(\psi \frac{\partial \psi^*}{\partial x} - \psi^* \frac{\partial \psi}{\partial x} \right) dx \tag{3.11}$$

The model ignores the effects of the magnetic field on the atom laser. Indeed, the atom laser state $m_F = 0$ is unaffected to first order by the magnetic field and is only weakly anti-trapped due to the second-order Zeeman effect with an effective trapping frequency of $\omega_{2nd} = 2\pi \times 2.6$ Hz.

The transverse position of an atom in such a potential is given by [80]

$$x(t) = x_0.cosh(\omega_{2nd}t) \approx x_0(1 + \omega_{2nd}^2 t^2/2) \qquad (3.12)$$

For a propagation over 1 mm ($\sim$ 14ms), the transverse position will be affected by less than 3%. We also ignored the ac Stark effect of the Raman optical beams because the intensity of the beams does not change significantly over the 1 mm propagation. Finally, the validity of the model was checked against a solution of the full 3D Gross-Pitaevskii (GP) equation including beam-beam interactions. The GP model was transferred to a freely falling frame after the atom laser had reached a steady state, in order to find the atom laser wavefunction at large distances below the condensate. The two models gave good agreement and the results of this comparison can be found in the thesis of M. Jeppesen.

The results of the calculated quality factor M^2 of an atom laser are shown (solid line) in figure 3.4 as a function of the momentum recoil k_0 received by the atom. The following sub-section explains how it is possible to compare these theoretical predictions to the experimental measurements of figure 3.3.

3.4.2   Data analysis

It is not possible to get the M^2 beam quality factor using equation 3.1 since the beam waist is located at a virtual position above the BEC and thus cannot be measured. Equation 3.10 was given as an alternative method to calculate the M^2 factor in the paraxial regime where it remains constant. In practice, it is however difficult to measure the wavefunction phase, and hence, $C(z)$. Consequently, this quantity will always be derived from our calculations. In the paraxial regime, the beam width can be written as

$$[\Delta x(t)]^2 = (\Delta x_0)^2 + (\Delta v_x)^2 (t - t_w)^2 \qquad (3.13)$$

where t_w is the time when the beam is at its waist, and Δx_0 is the beam waist. It is interesting to note that the beam waist is not necessarily the BEC itself. In principle, M^2 may thus be determined simply from measuring the beam width at different heights. However, in our experiment, we can only measure the beam width in the far field, at distances greater than 300 μm below the condensate as shown in figure 3.3. Observations at distances less than 300 μm are prevented by the very fast condensate expansion directly after trap switch-off.
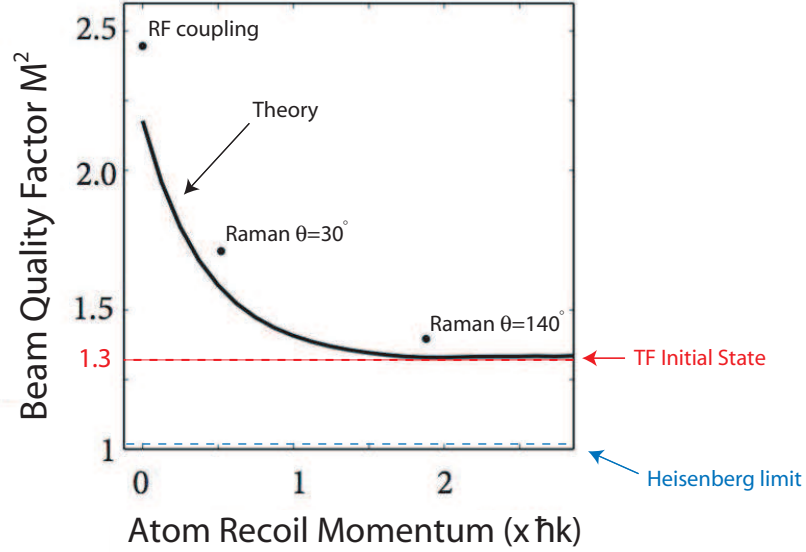
Figure 3.4: Calculated and measured quality factor M^2 of an atom laser. The solid line is the theoretical prediction whereas the three dots are the experimental measurements obtained after RF or Raman out-coupling at 2 different angles. The discrepancy between theory and experiment seems to be due to systematic errors which we attribute to the second order Zeeman effect, ignored in the model. The theoretical line does not converge towards $M^2 = 1$ but rather $M^2 = 1.3$ due to the Thomas-Fermi initial state of the condensate.

Since in the far field the second term of equation 3.13 dominates, only the velocity spread (Δv_x) can be determined experimentally by fitting equation 3.13 to the experimental data of figure 3.3. Therefore, we must calculate Δx_0 and t_w from the model. t_w is obtained by calculating the curvature beam-width product following $t_w = \hbar C(z)/(m\Delta v_x^2)$. Since the waist is virtual and located above the BEC, t_w is negative. Values of M^2 are finally derived from combining the experimental result on Δv_x with the calculated $C(z)$ and Δx to give the three dots in figure 3.4. We find that the beam quality is improved and the beam divergence is reduced as the momentum kick increases. For our parameters, an RF atom laser is produced with $M^2 = 2.4$ whereas we can reach $M^2 = 1.4$ with the maximum two-photon kick of a Raman atom laser ($p = 2\hbar k$). We see that as the kick increases M^2 continues to improve and approaches the Heisenberg limit of $M^2 = 1$. However, it is asymptotic to a limit slightly above 1, which is equal to 1.3 with our parameters. In this limit reached for large kicks, the interaction of the out-coupled atoms with the condensate becomes negligible. Thus, the transverse atom laser wave-function is approximately the free space evolution of the condensate wave-function along the out-coupling surface. It is therefore

limited by the non-ideal (non-Gaussian) condensate wave function itself.

3.5   DEPENDENCE ON TRAPPING FREQUENCIES

In addition, the simulations show that it is possible to reach the limit due to the Thomas-Fermi initial state ($M^2 = 1.3$) even for much tighter trapping potentials, using the maximum two-photon kick. This result is presented in figure 3.5 where we plot the theoretical evolution of the M^2 factor when increasing the radial trapping frequency up to $\omega_\rho = 2\pi \times 300$ Hz. Again, the calculation is performed assuming the out-coupling cut is set at the center of the condensate. As the trap frequency increases, the M^2 factor deteriorates to $M^2 = 14$ in the case of RF output coupling. For the maximum Raman two-photon kick, the increase is limited to only $M^2 = 1.7$. Traps of less than 50 Hz trapping frequencies must be used to maintain the quality factor of an RF output coupler within 5% of the quality factor of a Raman coupler. For any other trapping frequencies, a Raman out-coupler will be a significant improvement on the atom laser divergence.
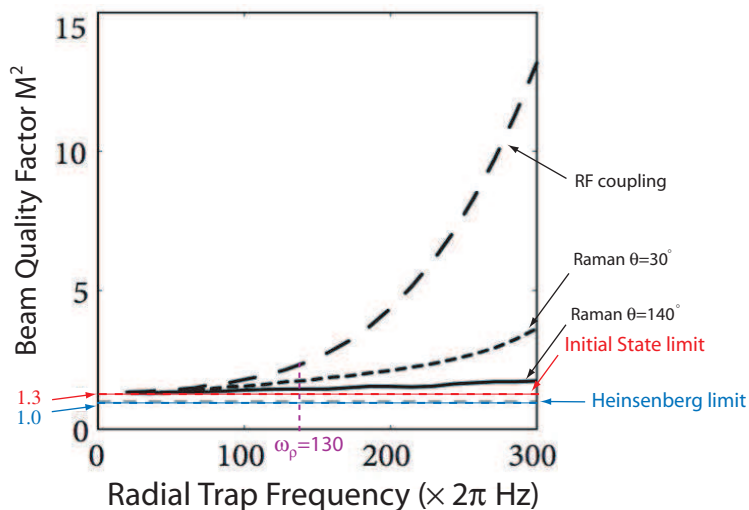
Figure 3.5: Comparison of the calculated beam quality factor M^2 as a function of the trapping frequency for RF and Raman out-coupling. The simulation always assumes out-coupling from the centre of the condensate. Whereas both techniques are comparable for small trapping frequencies, one can see the large improvement of using Raman out-coupling over RF in the case of large trapping frequencies.

3.6 CONCLUSION

In this chapter, experimental results on the divergence properties of a Raman atom laser were presented and compared to an RF technique. Compared to RF, the Raman out-coupling system used in our experiment can improve the beam quality factor M^2 of an atom laser by 50% down to a factor of 1.4 above the Heiseinberg limit (see figure 3.4). For a given initial BEC, such an atom laser has the highest possible flux, longest operating time and lowest sensitivity to any excitation or external fluctuations since it is out-coupled from the center of the condensate. Only in the case of a Raman out-coupler, the limit of interactions can be approached nearly independently of the trapping frequencies (see figure 3.5). It should be possible to approach this limit even for experiments with tightly confining traps of several kilohertz using higher order Raman transitions where the detuning is set so that more than two photons are required to transfer the atoms to an un-trapped state [85]. It should also be possible to reach the ultimate Heisenberg limit by completely removing the atomic interaction which can be done using Feshbach resonances. Finally, one could also prevent populating any anti-trapped state using Raman lasers that are phase locked to the 6.8 GHz hyperfine splitting (see figure 2.3), thus creating a two-state atom laser [78, 86, 87]. Such lasers, combined with the high quality transverse mode of Raman atom lasers could be used in a continuous version of the atomic Mach-Zehnder Bragg interferometer [88] and are very promising in the development of atomic local oscillators [89].

CHAPTER 4

COHERENT ATOM BEAM SPLITTING

The high phase-space density and coherence properties of Bose-Einstein condensates allow for atom-optic experiments that have previously only been performed with optical lasers [75]. Among these, atom-laser interferometers are of particular interest because of their potentially high sensitivity. In order to utilize high quality atom lasers (such as those described in chapter 3) in the same way as one utilizes optical lasers, atom-wave versions of optical elements, such as mirrors or 50/50 beam splitters, are needed. Reflection, beam splitting and diffraction of atoms can actually be thought of as mechanisms that change the momentum of atoms from a given initial value to either a single final value or a superposition of momenta. It is important that the coherence of the atoms is preserved during their manipulation. For that purpose, momentum-transfer between laser light and atoms can assure coherent interactions, provided the frequencies of the optical laser beams are detuned far enough from atomic resonance in order to avoid spontaneous emission which would lead to decoherence. One way to manipulate atoms is based on Bragg diffraction from an optical standing wave [90, 91], which coherently splits matter waves with unidirectional momentum transfer. Bragg diffraction preserves the coherence properties of the condensate while providing efficient, selectable momentum transfer.

In this chapter experimental results are obtained by taking advantage of the Raman beams described in section 2.2 to perform coherent atom beam splitting following a Bragg diffraction process. A brief overview on Bragg diffraction is firstly given. This is followed by a description of the atomic diffraction process observed in our experiment. It is demonstrated to arise from an optical grating created from each of the Raman beams (independently) and from a very small fraction of back-reflected light. The process is shown to be velocity resonant and a diffraction efficiency of approximately 60% is measured, which is sufficient for applications such as atomic beam-splitters.

4.1 OVERVIEW ON BRAGG DIFFRACTION

Diffraction of atoms from an optical grating has led to a wealth of insights into atomic physics, and to practical applications such as coherent beam splitting for precision atom interfer-

ometry [8, 91, 92]. Bragg diffraction of thermal atomic beams has been done mostly under nearly normal incidence to the optical grating [90, 93–95]. In the experiments recalled here, great care had to be taken to meet the Bragg condition by precisely matching the angle of the optical grating to the velocity of the atoms. The process is analogous to the diffraction of electrons by a crystal lattice and the Bragg relation is given by

$$\lambda_L sin(\theta_n) = n\lambda_{dB} \tag{4.1}$$

where λ_{dB} is the de Broglie wavelength of the atoms scattered from a standing light wave of wavelength λ_L and θ_n is the Bragg angle at which n^{th} order scattering occurs.

With the advent of dilute gas BEC [1, 2], a source of cold atoms emerged that is ideal for studying and utilizing atom-light interactions in a highly controllable way. BEC diffraction using short pulses of light at normal incidence was investigated and led to the observation of periodic focusing, collimation and the atomic Talbot effect [96, 97]. It was soon realised that controllable Bragg diffraction could also be generated in a stationary condensate by applying an optical running wave [85], similarly to what had been achieved with thermal clouds. In these experiments, energy and momentum conservation for Bragg diffraction were met by precisely setting the frequency difference between the two incident lasers which is equivalent to satisfying the Bragg condition on the angle of incidence in atomic beam experiments. In this case, the Bragg condition is given by

$$\frac{(np_{recoil})^2}{2m} = n\hbar\delta_n \tag{4.2}$$

where $p_{recoil} = 2\hbar k sin(\theta/2)$ is the recoil momentum from a two-photon process involving Raman beams separated by the angle θ, $k = 2\pi/\lambda$ is the wavevector of the light and δ_n is the frequency difference between the two lasers in order for the nth order Bragg diffraction process to be resonant. Bragg diffraction from two detuned optical beams became a very powerful tool. It has been used as a coherent beam splitter in interferometry [8, 91, 92], as a spectroscopic probe of a BEC [98, 99], as the basis for demonstrating superradiance and matter wave amplification [100–103], as a tool to measure the relative phase between two BECs [104], and as a mechanism for producing [19] and manipulating [105, 106] an atom laser.

4.2   DIFFRACTION FROM A SINGLE LASER BEAM

In section 3, the Raman beams were used as an out-coupler to extract a collimated beam of atoms from the condensate. It appears very appealing to take advantage of these two optical beams to simultaneously manipulate the atoms using Bragg diffraction. Two optical standing waves can potentially be created, from each of the Raman laser beams, provided an additional counter-propagating laser beam is aligned on each Raman beam. However, in our setup arrangement, at small angles between the beams, the Ioffe coil is in the way of the lasers so that any addition of a counter-propagating beam is ruled out. Moreover, the coil is too close to the glass cell to implement a mirror which would retro-reflect the incident beam (see figure 4.1). Similarly, for larger angles, the quadrupole coils are in the way of the beams after they have passed the glass cell nearby.

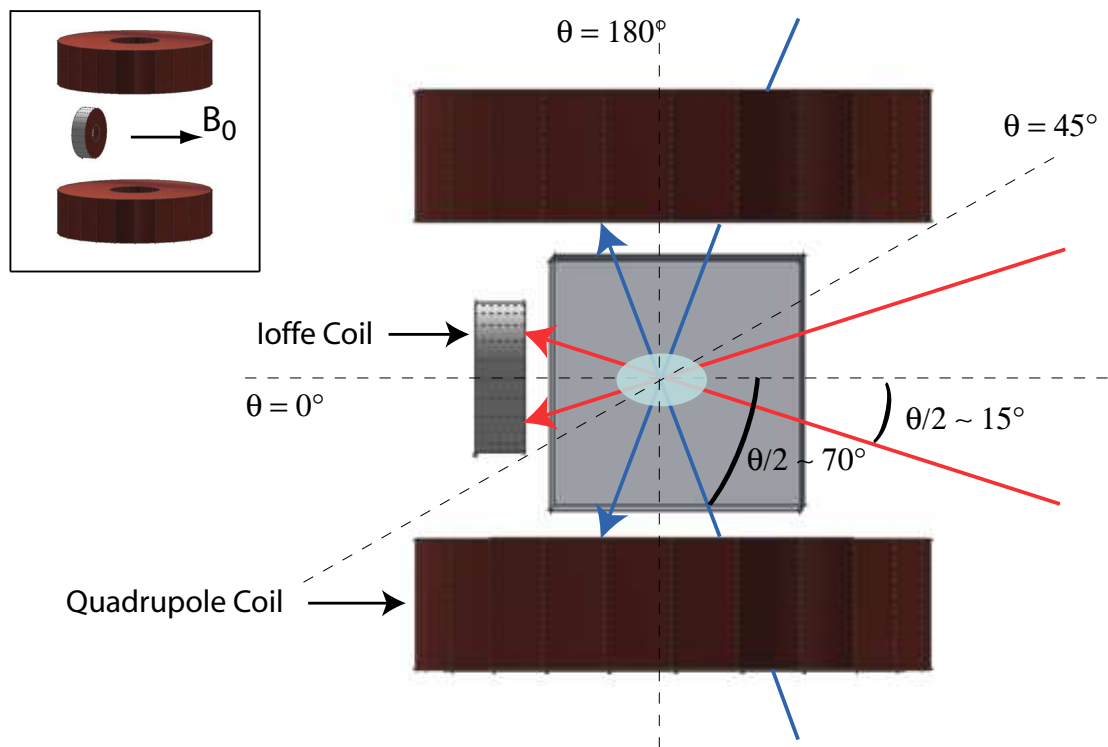Figure 4.1: Experimental setup showing the position of the magnetic coils with respect to the glass cell. Two sets of optical Raman beams hitting the coils after they have passed through the BEC are also represented at small and larger incidence angles $\theta/2$. Note that due to the magnetic field from the Ioffe coil the condensate does not sit at the center of the glass cell but is displaced towards the Ioffe coil.

Only for a small range of angles the beams can pass through the atoms without clipping the apparatus, typically when $\theta \sim 0°$, $\theta \sim 45°$ and $\theta \sim 180°$. For $\theta \sim 0°$ a Raman out-coupling can be achieved simultaneously to a diffraction grating but only with a negligible momentum kick which would increase the divergence of the resulting atomic beams (see chapter 3). If the angle is set to $\theta \sim 180°$ the out-coupling process is inefficient for reasons of polarization: in this case, each optical laser beam is orthogonal to the quantization axis (defined by the direction of the magnetic bias field $\vec{\mathbf{B}}_0$), preventing any circular σ^+ polarization to be experienced by the atoms.

Alternatively, for a large range of angles, it is possible to take advantage of the laser beams hitting the coils in order to create Bragg diffraction gratings. In this case, the optical standing wave is formed by a single Raman beam together with its diffuse back-scattered light from the coils. Diffracted atomic beams from these gratings are shown in the absorption image of figure 4.2a where atoms have been Raman out-coupled for 20 ms and simultaneously split under Bragg diffraction. The splitting, as opposed to the output coupling, is induced by the interaction of the out-coupled atoms with each of the Raman beams separately: the upward propagating laser imparts a momentum into the laser direction resulting in the atom beam on the left of the picture, whereas the downward propagating laser imparts a momentum against the laser direction resulting in the atom beam on the right. It is also possible, from the picture, to distinguish second order atomic beams on the right or on the left of the central atom laser beam. These higher order structures appear for high laser intensities only and were too weak to be used for a quantitative study. For this reason, only the first order atomic splitting will be considered in the following.

Further checks were made to show that the diffraction process is not a consequence of the Raman out-coupling technique but really is due to diffuse light. The initial check was done for a small range of angles where the laser beam passes through the atoms without clipping the apparatus ($\theta \sim 45°$). In this case, no measurable transfer into the momentum side-mode can be observed. However, deliberately placing black cardboard as a diffuse scatterer in the path of the laser, after it has passed through the glass cell, always brings the diffraction back. A final check was performed by decoupling the extraction of atoms and the splitting process. This was done by creating an atom laser pulse by RF out-coupling (instead of the optical Raman method). The RF out-coupled atom laser pulse was then illuminated with only one of the laser beams. After 20 ms of free fall, absorption images revealed two separate momentum components, either on the left of the extracted atoms (figure 4.2b) when the pulsed RF atom laser was exposed to the upward beam only or on the right (figure 4.2c) when only the downward propagating laser illuminated

the extracted atoms. Consequently, a single laser beam can drive a Bragg diffraction process, independently of the Raman out-coupling process.
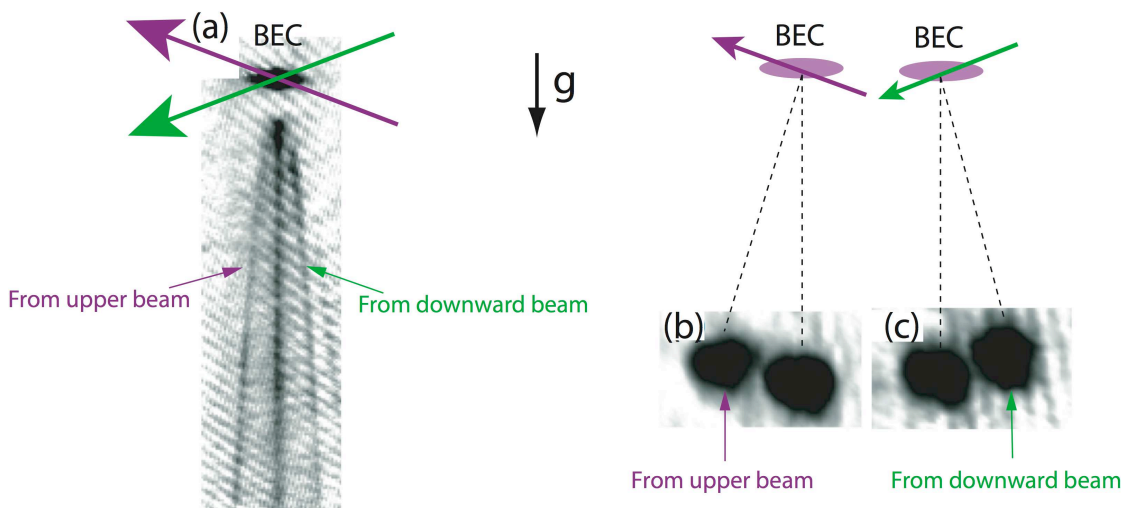
Figure 4.2: (a)Absorption image ($360 \times 1100 \mu m^2$) of a multibeam atom laser after 20 ms of long-pulsed Raman out-coupling with an angle $\theta = 30°$ between the Raman beams (which are symmetric with respect to the horizontal). Each Raman beam contributes to creating an atomic beam diffracted to the left (right) by the upward (downward) laser beams. (b) and (c) are absorption images of a short-pulsed RF atom laser exposed to the upward (b) or downward (c) propagating Raman laser only. The image size is $540 \times 320 \mu m^2$.

4.3 A VELOCITY RESONANT PROCESS

A characteristic of Bragg diffraction is that it is a resonant process which depends on the velocity of the atoms or on the frequency and geometry of the laser beams. In our setup, the frequency of both Raman laser beams is far-detuned from the atomic transition and will be considered fixed in this chapter. Only the angle between the two beams can be adjusted, although it is experimentally difficult to align the Raman beams onto the BEC. Alternatively, this section characterizes the velocity resonance of the process when falling atoms are illuminated by the grating, first theoretically from a simple model, and second experimentally by performing a time-resolved measurement.

4.3.1 Theoretical Model

Diffraction from a standing wave occurs from absorption and emission of a photon, leading to a momentum transfer of $2\hbar\vec{\mathbf{k}}$. Consequently, the first condition fulfilled by the atoms is simply given by

$$\vec{\mathbf{p}}_f = \vec{\mathbf{p}}_i + 2\hbar\vec{\mathbf{k}} \tag{4.3}$$

where $\vec{\mathbf{p}}_i$ and $\vec{\mathbf{p}}_f$ are the momentum of the atoms before and after they are diffracted respectively. The energy of the absorbed and emitted photon is the same and there is no change in the internal state of the diffracted atoms. Consequently, the kinetic energy of the atom remains unchanged during the process leading to

$$\frac{|\vec{\mathbf{p}}_f|^2}{2m} = \frac{|\vec{\mathbf{p}}_i|^2}{2m}. \tag{4.4}$$

Both conditions are simultaneously fulfilled and the Bragg diffraction occurs only when the atoms reach the resonance velocity

$$v_{res} = \frac{\hbar k}{m sin(\theta/2)} \tag{4.5}$$

where m is the atomic mass and $\pi/2 - \theta/2$ is the angle of the single laser beam with the propagation direction ($\vec{\mathbf{u}}$) of the atoms. For a given angle θ, one can distinguish 3 cases depending on the initial velocity of the atoms leaving the condensate (see figure 4.3).

- If the atoms are dropped with no initial velocity (figure 4.3(a)), they will simply accelerate under gravity, and diffraction will be achieved for any value of the angle θ at a time $t = v_{res}/g$ when they are $z = v_{res}^2/2g$ below the condensate.

- If the atoms are launched with an initial velocity v_i smaller than the resonance velocity ($v_i < v_{res}$), the atoms will be diffracted at a position that depends on the direction of their initial velocity (figure 4.3b). This is equivalent to having an upper limit on the angle $\theta/2$, namely $sin(\theta/2) < \hbar k/(mv_i)$.

  For the Raman out-coupler of our experiment where the lasers are symmetric with respect to the horizontal, the initial downward velocity is given by $v_i = 2\hbar k sin(\theta/2)/m$ and the resulting upper limit on θ is $\theta/2 < 45°$. Consequently, in this case, the Bragg diffraction
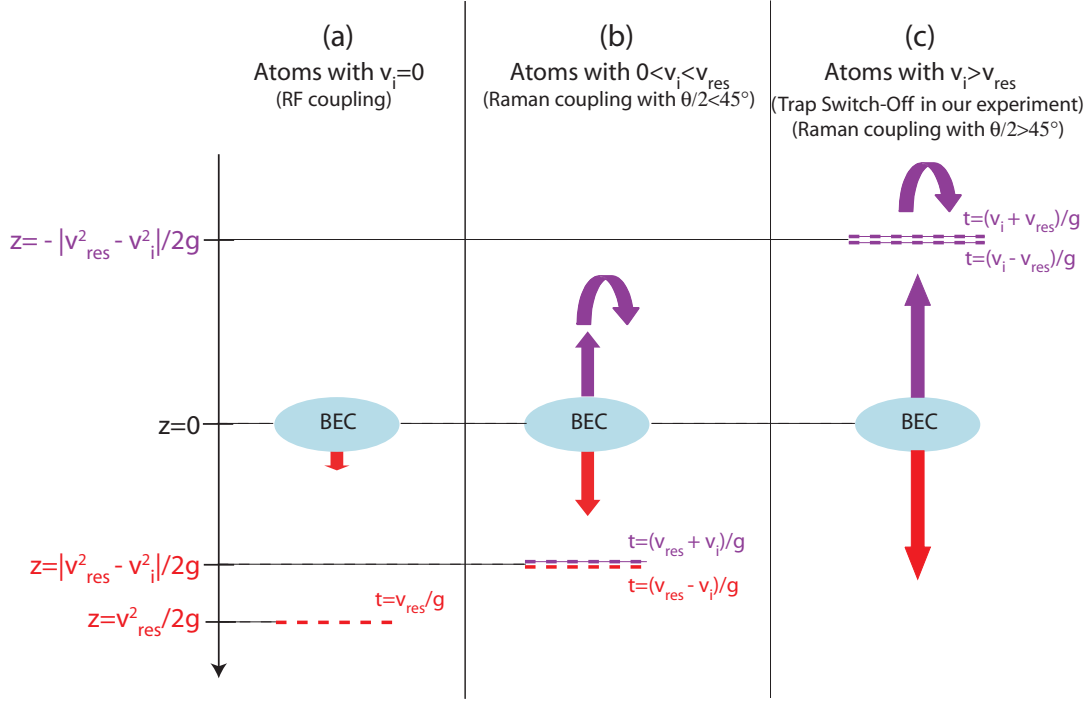
Figure 4.3: Position of the velocity resonance for Bragg diffraction after (a) RF and (b) Raman out-coupling. (c) Illustrates the case of our experimental trap switch-off (see section 4.3.2) where the atoms are initially launched upwards. Note that there are 2 velocity resonances in the latter case, first when the atoms propagate upwards, and then after they have turned back and propagate downwards.

would happen at a time $t = (v_{res} - v_i)/g$ when the atoms are located at $z = (v_{res}^2 - v_i^2)/2g$ below the condensate.

If the atoms are sent upwards with $v_i < v_{res}$ (which is the case in 4.4.1) they will not pass through a resonance velocity during their upwards propagation but only on their way down $t = (v_{res} + v_i)/g$ ms after trap switch-off, at $z = (v_{res}^2 - v_i^2)/2g$ below the condensate.

- If the atoms are launched with an initial velocity larger than the resonance velocity ($v_i > v_{res}$), they will not be diffracted unless they are sent in the upwards direction (figure 4.3c). In the particular case of an upward initial momentum, the atoms can be diffracted twice, first during their deceleration down to a zero-velocity, and second when they are subsequently accelerated downwards under gravity. Both diffraction effects take place at the same position in space ($z = (v_i^2 - v_{res}^2)/2g$ above the condensate) but for different times of $t_1 = (v_i - v_{res})/g$ and $t_2 = (v_i + v_{res})/g$ respectively.

4.3.2 Experimental measurement

The mechanism responsible for the continuous coherent splitting is investigated in order to verify that it is indeed Bragg diffraction. For that purpose, the angle of each Raman beam is set to be $\theta/2 = 70°$ with respect to the horizontal which corresponds to a resonance velocity of $v_{res} \sim 0.6$ cm.s^{-1}. In order to achieve a time resolution sufficient to measure the velocity resonance, short pulses of atoms must be out-coupled. For the best signal-to-noise ratio, the flux of out-coupled atoms was maximized by dropping the entire condensate (atoms in the $|F = 1, m_F = -1 >$ state) after a magnetic trap switch-off. Upon trap switch-off the atoms are launched upwards due to transient magnetic field gradients. In order to determine the launching velocity (v_i), the difference in position between the condensate and a pulse of atoms that have been RF out-coupled in the $m_F = 0$ un-trapped state is measured. The condensate was launched with the initial upward velocity v_i and imaged at a time τ_{im} after trap switch-off. The out-coupled atoms, falling with no initial velocity, were imaged at a similar time τ_{im} after the start of the out-coupling process. The launching velocity can thus be determined by

$$v_i = \frac{z_i - z_0}{\sqrt{2z_0/g}} \qquad (4.6)$$

where z_i and z_0 are the positions of the condensate and the RF out-coupled atoms at the time τ_{im} after trap switch-off or out-coupling pulse respectively. A launching velocity of $v_i \sim 1.0$ cm.s$^{-1} > v_{res}$ is found and the atoms are thus expected to experience two velocity resonances (similarly to figure 4.3c) after $t_1 = 0.4$ ms and $t_2 = 1.6$ ms respectively.

In order to probe the resonances, a short pulse (~ 300 μs) from one of the Raman lasers is applied after a variable delay time and keeping the laser power and pulse duration fixed. The atoms of different momentum components are then allowed to separate in free fall before an absorption image is taken 22 ms after the magnetic trap switch-off. The experimental measurement is shown in figure 4.4. The atoms go through two velocity resonances. The first diffraction occurs when the atoms are traveling upwards, 0.4 ms after the trap switch-off as predicted under Bragg diffraction. The second velocity resonance is when the atoms travel downwards, about 1.6 ms after the trap switch-off. The value of the velocity resonance can be increased by decreasing the angle θ. For $\theta/2 < 35°$ the resonance velocity becomes smaller than the initial upward velocity of the atoms. Consequently, the atoms move upwards too slowly to be diffracted and are only diffracted during their downward trajectory as illustrated in figure 4.3(b).
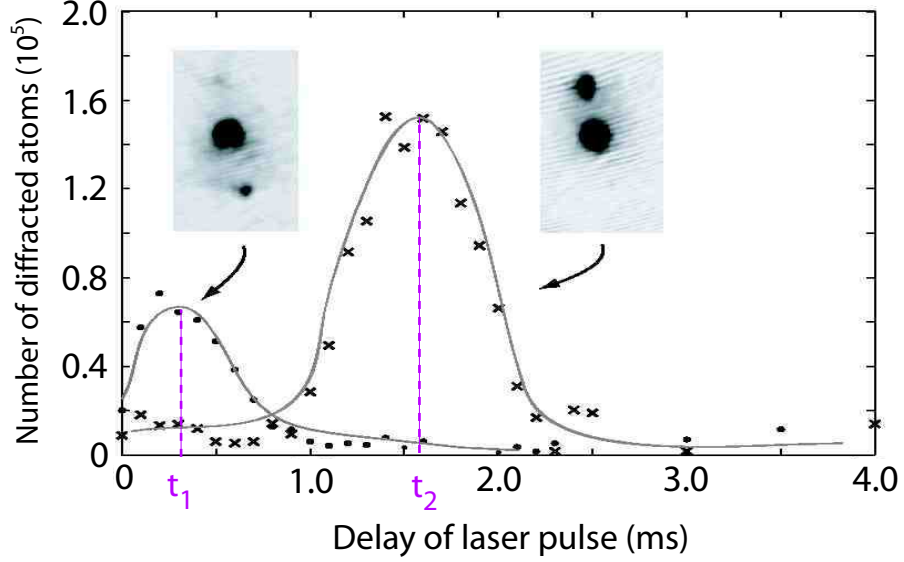
Figure 4.4: Number of diffracted atoms as a function of pulse delay relative to trap switch-off. Upon trap switch-off, the entire BEC was released with an initial velocity in the upward direction due to remnant magnetic fields (see figure 4.3c)). Shown are the two possible velocity resonances for the atoms traveling upwards (circles) and then traveling downwards (crosses). Pulse duration is 300 μs (the delay is given from the start of the pulse) and $\theta/2 = 70°$. The insets show the corresponding images, each 480×890 μm^2. The lines are interpolations to guide the eye.

4.4 BRAGG DIFFRACTION EFFICIENCY

4.4.1 Measurement

In order for Bragg diffraction to be used for interferometric applications, efficiency is a crucial parameter. If a diffraction efficiency of 50% can be reached, the tool can be of potential use as a 50-50 beam splitter. Similarly, a diffraction efficiency close to 100% would make it appropriate as a mirror to reflect the atoms.

Bragg diffraction can be considered as a transfer of atoms from one initial state to another after a two-photon transition inducing a momentum difference $2\hbar\vec{k}$. It is thus driven by the two-photon Rabi frequency $\Omega = \Omega_1\Omega_1'/2\Delta$, where Ω_1 and Ω_1' are the one-photon Rabi frequencies of the Raman laser beam and its retro-diffused light respectively. In our Raman out-coupling experiments (see section 3), where both Raman lasers are applied to the condensate with maximum intensity, a two-photon Rabi frequency of $\Omega = 2\pi \times 40$ kHz is achieved. For the Bragg diffraction process, the back-scattered intensity I_1' is estimated to be between 0.01% and 0.06% of the

incoming intensity I_1. Because the single-photon Rabi frequency scales with the square-root of the light intensity ($\Omega'_1 \alpha \sqrt{I'_1}$), the combination of the incident laser and the diffuse back-scattered light should be able to drive a two-photon Rabi frequency of $\Omega \approx 2\pi \times (0.4 \rightarrow 1.0)$ kHz. In the naive model where the atoms are assumed to Rabi-flop between the two momentum components, the time-dependent population of a Rabi-flopping state is given by $sin^2(\Omega t)$ and a laser pulse on the order of ms could realize the population transfer from one state to the other.
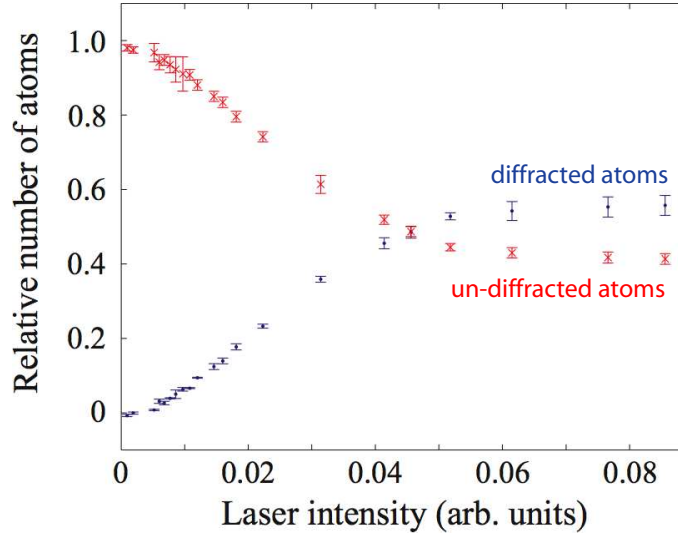
Figure 4.5: Diffraction efficiency as a function of laser intensity for a fixed pulsed duration of 2 ms. The laser beam is at an angle of $\theta/2 = 15°$ to the horizontal. The entire BEC is released after trap switch-off and the laser pulse is applied after 3.4 ms. The relative number of diffracted and un-diffracted atoms is measured after absorption imaging and is represented by the blue dots and red crosses respectively.

In order to study experimentally the diffraction efficiency as a function of laser intensity (proportional to the two-photon Rabi frequency), the delay time and angle of the laser beam are chosen so that the atoms are resonantly diffracted. In order to have a single resonance velocity, an angle of $\theta/2 = 15°$ is chosen, corresponding to a resonance velocity of $v_{res} = 2.3$ cm.s^{-1} > v_i, and the delay time after trap switch-off is consequently chosen to be $t = 3.4$ ms. The pulse duration is set to 2 ms and the intensity of the laser beam is varied from 0 to its maximum value. The results are shown in figure 4.5 where the relative number of both diffracted and un-diffracted atoms is plotted against to the laser intensity. A maximum transfer efficiency of approximately 60% is measured into the momentum side-mode. In particular, one can see that it is possible to

operate the grating as a 50-50 beam splitter by choosing the appropriate laser intensity.

4.4.2 Theoretical Model

The simple model, described in the previous section, of a Rabi-flopping between the two momentum states is useful to determine a rough estimate of the pulse duration needed to drive an efficient Bragg diffraction. However, it does not consider the velocity selectivity of the process. A more accurate description results in a situation equivalent to an avoided crossing between the diffracted and un-diffracted atoms. The diffracted atoms can be considered to be in a distinct state from the un-diffracted atoms because their momentum difference ($2\hbar k \sim 2 \times 10^{-27}$ kg.m.s^{-1}) is significantly greater than the momentum width of the falling atoms ($\Delta p = mg\Delta t \sim 5 \times 10^{-28}$ kg.m.s^{-1} where $\Delta t \sim 0.5$ ms is the width of the diffracted pulse of atoms, obtained from figure 4.4). The un-diffracted and diffracted atom states are coupled by the diffraction grating leading to an avoided crossing in momentum space. As the atoms are in free fall, their momentum varies linearly in time and so does the energy difference between the diffracted and un-diffracted atoms. Consequently, it is possible to apply the Landau-Zener theory to the system which gives a diffraction probability of

$$P = 1 - exp\left(-\frac{\pi\Omega^2}{|\vec{\mathbf{k}}.\vec{\mathbf{g}}|}\right) \tag{4.7}$$

where Ω is the two-photon Rabi frequency and $\vec{\mathbf{g}}$ is the acceleration due to gravity. Hence, for a sufficiently high two-photon Rabi frequency ($\Omega \gg \sqrt{|\vec{\mathbf{k}}.\vec{\mathbf{g}}|/\pi}$), equation 4.7 predicts a perfect transfer of atoms from the un-diffracted state to the diffracted state as shown in figure 4.6. The model does not consider a second diffraction of the diffracted pulse or diffraction into higher orders because they occur at different resonance velocities which are not reached during the 2 ms when an optical grating is present.

The validity of the Landau-Zener model was verified by solving the Gross-Pitaevskii equation for several two-photon Rabi frequencies for the diffracted and un-diffracted atomic state, including the effect of s-wave scattering between the atoms. The data points are superimposed on the Landau-Zener model in figure 4.6. The results from both approaches agree well and reproduce the general shape of the experimental data, in particular the plateau towards high Rabi frequencies. The simulations also confirm our estimate that the very small intensity of the reflected light (resulting in a Rabi frequency of about $2\pi \times 1$kHz) can create a strong Bragg diffraction
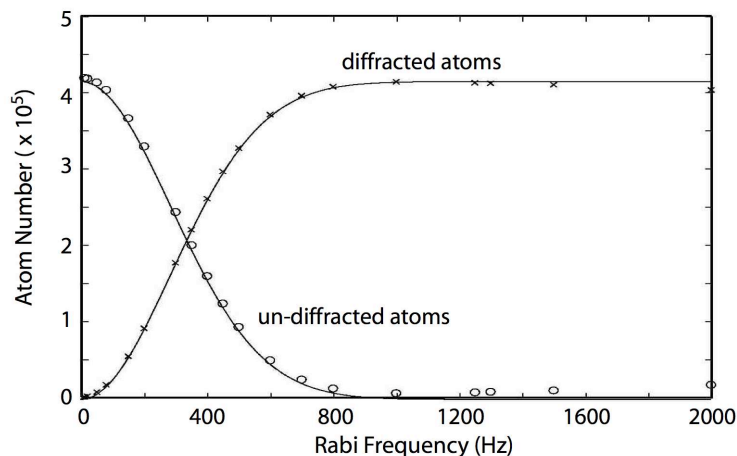
Figure 4.6: Theoretical predictions of the efficiency of the Bragg diffraction process showing the number of diffracted and un-diffracted atoms as a function of the two-photon Rabi frequency. Solid lines are the predicted Landau-Zener transition probabilities whereas the symbols are the results from a Gross-Pitaevskii simulation. The angle between the laser beam and the horizontal is $\theta/2 = 15°$.

grating. However, the model shows some discrepancy in the maximum transfer probability since only approximately 60% of the atoms are diffracted in our measurement. This difference can be attributed to the fact that the diffuse nature of the reflection is not taken into account in the calculations. Moreover, for high Rabi frequencies it can be seen that the transition probability from the GP simulation (discrete points in figure 4.6) departs the Landau-Zener theory (solid lines in figure 4.6) due to power broadening causing the state changing process to begin closer to the BEC where the inter-particle interactions are non-negligible.

4.5 CONCLUSION

It is possible to achieve high efficiency atomic Bragg diffraction from a single laser together with its own diffuse backscattering. The process is suitable for use in an atom interferometer as the ability to vary the scattering probability with the laser intensity allows us to operate our grating either as a 50-50 beam splitter or as a (partially) reflecting mirror. The very large detuning of the laser beam forming the grating ensures negligible spontaneous emission so that coherence is maintained during the Bragg process. The method is an experimentally simple and versatile tool

for atom optics and presents the significant experimental simplification that only a single laser beam is involved. In vacuum systems which do not allow optical access from two sides, it may be the only possibility to implement an atomic beam splitter. The direction of the momentum transfer can also be controlled, together with the resonance velocity and thus the resonance position, by the angle of the incident laser beam. For future atom interferometry applications Raman out-coupled atom laser beams, as presented in the previous section, are well suited since they offer large brightness and an improved beam profile. Our setup has the advantage that it can run the Raman output coupler in a regime where it serves at the same time as two beam splitters, thus significantly simplifying the experimental demands.

CHAPTER 5

RF OUT-COUPLING FROM TWO- AND MULTI-LEVEL SYSTEMS

When creating an atom laser beam, from either RF or Raman output-coupling techniques, it is important to consider the quality of the beam as a critical parameter for any applications. This chapter compares theoretically the atom laser output of several atomic systems out-coupled using an RF technique. The first part of the chapter presents a one-dimensional (1D) numerical model which is used to investigate the spatial structure and temporal dynamics created in a Bose-Einstein Condensate by an RF output-coupling on five-, three- and two-level atom laser systems. The five- and three-state systems correspond to the experimentally relevant Zeeman levels of the $F = 2$ and $F = 1$ ground states of ^{87}Rb (see figure 2.3) and the two-state simulations to the recent experiments of Y. Le Coq *et al.* [20] and A. Öttl *et al.* [78]. The 1D model is validated by comparing the theoretical predictions on the bound state and spatial structure of an atom laser to previous experiments carried out in our lab [29]. Finally, the results of the simulations are described and some of the properties of two- and multi-state systems are compared with respect to experimentally important properties. In particular, the population and spatial dynamics were investigated as well as the peak homogeneous output flux and classical density fluctuations in the atomic beam. The question which is answered here is whether the significant amount of experimental effort required to make a 'true' two-state system has an actual influence on the quality of the atom laser.

5.1 THEORETICAL MODEL

5.1.1 Time-dependent Gross-Pitaevskii Equations (GPE)

The theoretical model presented here is meant to describe the dynamics of RF out-coupling on two- and multi-level systems and is based on solving the GPE of the system.

5.1.1.1 GPE for a condensate

From the development of many-body quantum mechanics [107] the Hamiltonian of a weakly interacting Bose gas confined by an external potential V_{trap} can be written down in terms of creation and annihilation field operators for bosons [62] in second quantisation formalism. In

general, the field operators can be written as a sum of single-particle wavefunctions and their respective annihilation operators as :

$$\Psi(\hat{\mathbf{r}},t) = \sum_{\alpha} \Psi_{\alpha}(\mathbf{r},t)\hat{a}_{\alpha}, \tag{5.1}$$

where the summation is carried out over all single-particle states α, and where $\hat{a}_{\alpha}$ lowers the atom number in mode Ψ_{α} by 1. However, because BEC occurs when the number of particles in a single ground state becomes very large compared to the occupation of other states, the condensate contribution to the field operator can be separated out as follows :

$$\Psi(\hat{\mathbf{r}},t) = \phi(\mathbf{r},t) + \hat{c}(\mathbf{r},t), \tag{5.2}$$

where $\phi(\mathbf{r},t) \equiv \langle \Psi(\hat{\mathbf{r}},t) \rangle$ and $\hat{c}(\mathbf{r},t)$ is the annihilation operator for uncondensed particles which has the property that $\langle \hat{c}(\mathbf{r},t) \rangle = 0$. The function $\phi(\mathbf{r},t)$ is a complex scalar field constituting an order parameter for the condensate. The atoms in a BEC are essentially all in the same quantum mechanical state and can be thought of as forming a macroscopic coherent system. Thus, to describe the condensate mathematically, it is not necessary to keep track of the individual wavefunctions of the atoms forming the condensate. Rather, it is usually sufficient to describe the whole condensate in terms of a single wavefunction defined by the order parameter $\phi(\mathbf{r},t)$ and from which the density of atoms can be calculated as $|\phi(\mathbf{r},t)|^2$.

To a very good approximation, the dynamics of such a BEC can be modeled in terms of the time-dependent GPE for the macroscopic wavefunction of the condensate [108–110] which is commonly written as :

$$i\hbar \frac{\partial \phi(\mathbf{r},t)}{\partial t} = -\frac{\hbar^2 \nabla^2}{2m}\phi(\mathbf{r},t) + V_{trap}(\mathbf{r})\phi(\mathbf{r},t) + U\phi(\mathbf{r},t)|\phi(\mathbf{r},t)|^2 \tag{5.3}$$

In this equation, $U = 4\pi\hbar^2 a/m$ is the interaction potential (also called two-body interaction strength), with m the mass of an atom and a the s-wave scattering length of the atoms forming the condensate. $V_{trap}(\mathbf{r})$ is the external trapping field which is usually of the form :

$$V_{trap}(\mathbf{r}) = V_0 + \frac{m}{2}(\omega_x^2 x^2 + \omega_y^2 y^2 + \omega_z^2 z^2) \tag{5.4}$$

where $\omega_{x,y,z}$ are the characteristic frequencies of the harmonic trap along the corresponding axes and V_0 represents the bottom of the trap.

As it is derived from a nonlinear Schrödinger equation involving a macroscopic wavefunction, this theoretical model takes into account not only the density properties but also the coherence inherent to Bose condensates. The GP equation has also been very successful in describing the macroscopic dynamics of trapped and un-trapped Bose condensates in a variety of experimental situations [62].

5.1.1.2   GPE for a multi-level system

Approximately 10 years ago, Ballagh *et al.* [111] introduced a generalization of the GPE as an effective tool for investigating a system of trapped and un-trapped states coupled via an RF field, within the semi-classical mean-field approximation. Provided a coherent coupling mechanism is used to extract atoms from the condensate, the macroscopic behavior of the output beam constituting the atom laser can also be described by a spatio-temporal evolution equation similar to equation 5.3. In the case of RF coupling all the $2F + 1$ m_F Zeeman states are coupled by the magnetic dipole interaction via the oscillating RF magnetic field $B = B_{RF}cos(\omega_{RF}t)$. The Zeeman states can be either trapped, un-trapped or even anti-trapped and will thus experience different trapping potentials. Consequently, in order to generalize the GPE to multi-level systems, a system of $2F + 1$ generalized Gross-Pitaevskii equations is to be considered, where each component can be written as :

$$i\hbar\frac{\partial \phi_{m_F}(\mathbf{r},t)}{\partial t} = \left(-\frac{\hbar^2\nabla^2}{2m} + V_{m_F}(\mathbf{r}) - \hbar m_F \omega_{RF} + U|\phi(\mathbf{r},t)|^2\right)\phi_{m_F}(\mathbf{r},t)$$
$$+ \hbar\Omega\sum_{m_F'}(c_{m_F'}\delta_{m_F,m_F'+1} + c_{m_F}\delta_{m_F,m_F'-1})\phi_{m_F'}(\mathbf{r},t)$$

$$(5.5)$$

This equation is derived from 5.3 by applying the transformation $\phi(\mathbf{r},t) \rightarrow e^{-im_F\omega_{RF}t}\phi(\mathbf{r},t)$ and a rotating wave approximation. ϕ_{m_F} is the macroscopic wavefunction of a given m_F Zeeman sublevel $m_F \in \{-F,...,F\}$ and $|\phi(\mathbf{r},t)|^2 = \sum_{m_F}|\phi_{m_F}(\mathbf{r},t)|^2$. We assume the interaction potentials between two Zeeman sub-states ($U_{m_F,m_F'}$) are all approximately constant and equal to U. The external potentials V_{m_F} are due to the trapping magnetic field and the gravitational field experienced by each of the m_F Zeeman sub-states. They can be written as

$$V_{m_F} = sgn(g_F)m_F\left(V_0 + \frac{m}{2}(\omega_x^2x^2 + \omega_y^2y^2 + \omega_z^2z^2)\right) - mgz$$

$$(5.6)$$

where $V_0 = \mu_B B_0/2$ is the potential at the bottom of the trap (B_0 is the bias field). Finally, Ω is the RF Rabi frequency ($\hbar\Omega = g_F \mu_B B_{RF}/2$) which describes the spin-flip transitions between the different Zeeman sub-levels. The c_{m_F} coefficients are the matrix elements of the angular operators $F_{\pm}$ [112] and are represented by $c_{m_F} = \sqrt{F(F+1) - m_F(m_F+1)}$ in equation 5.5.

Consequently, for the $F = 2$ manifold:

- ϕ_2 is only coupled to ϕ_1 with $c_1 = 2$.

- ϕ_1 is coupled to both ϕ_2 and ϕ_0 with $c_1 = 2$ and $c_0 = \sqrt{6}$ respectively.

- ϕ_0 is coupled to both ϕ_1 and ϕ_{-1} with $c_0 = \sqrt{6}$ and $c_{-1} = \sqrt{6}$ respectively.

- ϕ_{-1} is coupled to both ϕ_0 and ϕ_{-2} with $c_{-1} = \sqrt{6}$ and $c_{-2} = 2$ respectively.

- ϕ_{-2} is only coupled to ϕ_{-1} with $c_{-2} = 2$.

5.1.1.3 Dimensionality reduction

A number of groups found good agreement between theory and experiment using similar 3D mean-field models of the RF out-coupled atom laser described above [112–114]. However, Ioffe-type traps often used in experiments are usually elongated in the horizontal plane and axial-symmetric in the remaining directions. Moreover, the atomic laser beam extracted from the trapped condensate is always directed downwards in the privileged vertical z-direction of gravity. In order to simplify the numerics, it is therefore possible to transform a true 3D model into a system of lower dimensions (1D along z), still taking into account part of the physics involved in the other two dimensions. This dimensionality reduction can be performed non rigorously by writing an equivalent equation for the system in the dimension(s) of interest [112]. The $F = 2$ (five-state) GP model [28] of an RF atom laser in one dimension (z, the coordinate over which gravity acts) can thus be re-written as:

$$i\dot{\phi}_2(z,t) = (\mathscr{L} + z^2 + Gz - 2\Delta)\phi_2(z,t) + 2\Omega\phi_1(z,t)$$

$$i\dot{\phi}_1(z,t) = (\mathscr{L} + \frac{1}{2}z^2 + Gz - \Delta)\phi_1(z,t) + 2\Omega\phi_2(z,t) + \sqrt{6}\Omega\phi_0(z,t)$$

$$i\dot{\phi}_0(z,t) = (\mathscr{L} + Gz)\phi_0(z,t) + \sqrt{6}\Omega\phi_1(z,t) + \sqrt{6}\Omega\phi_{-1}(z,t) \qquad (5.7)$$

$$i\dot{\phi}_{-1}(z,t) = (\mathscr{L} - \frac{1}{2}z^2 + Gz + \Delta)\phi_{-1}(z,t) + 2\Omega\phi_{-2}(z,t) + \sqrt{6}\Omega\phi_0(z,t)$$

$$i\dot{\phi}_{-2}(z,t) = (\mathscr{L} - z^2 + Gz + 2\Delta)\phi_{-2}(z,t) + 2\Omega\phi_{-1}(z,t),$$

These equations have been made dimensionless for simplicity. They are exactly derived from 5.5 with the following dimensionality reduction:

- Δ and Ω are respectively the detuning of the RF field from the bottom of the trap ($\hbar\Delta = \hbar\omega_{RF} - V_0$), and the Rabi frequency. They are both measured in units of the radial trapping frequency ω_z of the $F = 2, m_F = 1$ state obtained in [29], with $\omega_z = 2\pi \times \frac{260}{\sqrt{2}}$ Hz.

- The time and spatial coordinates are measured in units of ω_z^{-1} and $(\hbar/m\omega_z)^{1/2}$ respectively in order to make the equations dimensionless. We will thus define the dimensionless spatial coordinate in the vertical z direction by $\tilde{z} = z/(\hbar/m\omega_z)^{1/2}$.

- Each of the five Zeeman sub-levels of the $F = 2$ manifold are represented by a GP function ϕ_{m_F} ($m_F = \{-2, ..., 2\}$) measured in units of $(\hbar/m\omega_z)^{-1/4}$.

- G is gravity measured in units of $(m/\hbar\omega_z)(\hbar/m\omega_z)^{1/2}$. With our parameters, the dimensionless gravity is $G = 9.24$.

- Finally, $\mathscr{L} \equiv -\frac{1}{2}\frac{\partial^2}{\partial z^2} + U(\Sigma_{i=-2}^2 |\phi_i|^2)$ where U is the interaction strength coefficient, measured in units of $(\hbar\omega_z)^{-1}(\hbar/m\omega_z)^{-1/2}$. This nonlinear interaction strength is determined similarly to Schneider *et al.* [112] by requiring that the 1D and 3D Thomas-Fermi chemical potentials are equal leading to $U = 6.6 \times 10^{-4}$.

Since the g_F factors for the $F = 2$ and $F = 1$ ground states of ^{87}Rb are the same except for a change of sign (see figure 1.4), the three-state and two-state atom laser systems of equations are simply subsets of the five-state equations presented above. The only difference comes from the modification of the Rabi-frequency coupling 'pre-factors' (c_{m_F}) which are always equal to $\sqrt{2}$:

$$i\dot{\phi}_{-1} = (\mathscr{L} + \frac{1}{2}z^2 + Gz - \Delta)\phi_{-1} + \sqrt{2}\Omega\phi_0$$
$$i\dot{\phi}_0 = (\mathscr{L} + Gz)\phi_0 + \sqrt{2}\Omega\phi_{-1} + \sqrt{2}\Omega\phi_1 \qquad (5.8)$$
$$i\dot{\phi}_1 = (\mathscr{L} - \frac{1}{2}z^2 + Gz + \Delta)\phi_1 + \sqrt{2}\Omega\phi_0$$

and

$$i\dot{\phi}_{-1} = (\mathscr{L} + \frac{1}{2}z^2 + Gz - \Delta)\phi_{-1} + \sqrt{2}\Omega\phi_0$$
$$i\dot{\phi}_0 = (\mathscr{L} + Gz)\phi_0 + \sqrt{2}\Omega\phi_{-1} \qquad (5.9)$$

There are no free parameters in the model and, as mentioned before, all numerics are done in dimensionless units although data will be presented in the International System of Units for a better understanding. The Rabi frequency is varied in the range $\Omega = 0 - 14$, which corresponds to $\Omega = 0 - 16$ kHz. The RF coupling resonance is also set to be at the centre of the trapped BEC by selecting an appropriate value for the detuning Δ. Therefore, the appropriate detuning in a five-state system will be different from the detuning in the three- or two-state systems because of the different sag and trapping frequencies experienced by the $F = 2$ and $F = 1$ hyperfine states. The effective potentials experienced by an atom in the m_F state can be expressed as:

$$V_{m_{Feff}} = g_F m_F z^2 + G z - 2 g_F m_F \Delta \tag{5.10}$$

where z is the distance below the center of the condensate. The appropriate detuning for each F hyperfine state is obtained by imposing that the center of the BEC coincides with the intersection $V_{Feff} = V_{0eff}$, as shown in figure 5.1. For $N = 5 \times 10^4$ atoms, the detunings are found to be $\Delta = 10.7$ and $\Delta = 43$ for the $F = 2$ and $F = 1$ states respectively.
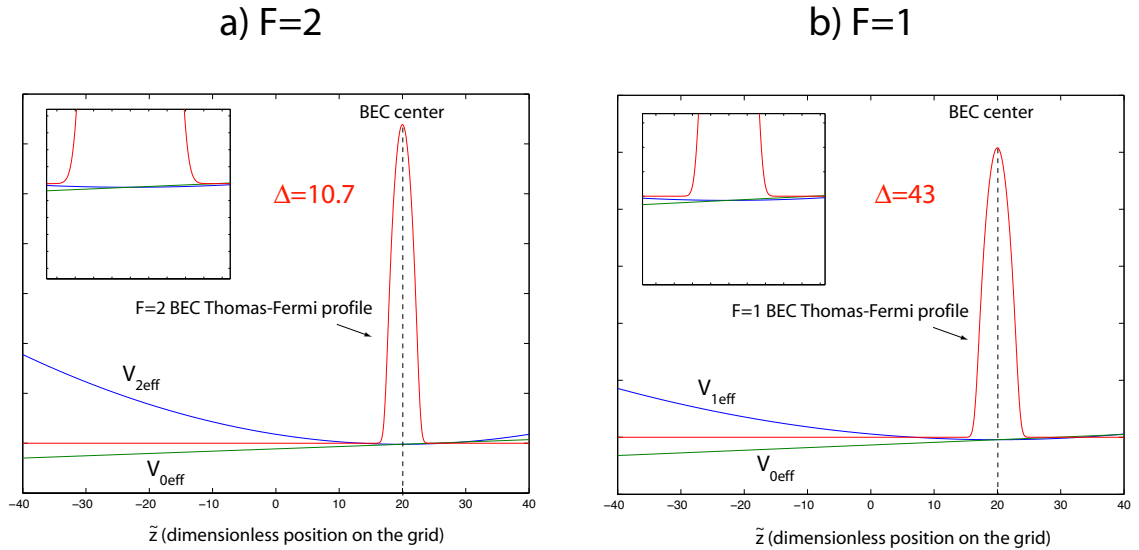

Figure 5.1: Thomas-Fermi profile of the BEC and effective potentials experienced by the atoms for the $F = 2$ state (a) and $F = 1$ state (b) where the detunings have been set to 10.7 and 43 respectively in order for the out-coupling resonance to be at the center of the BEC. $N = 5 \times 10^4$ atoms.

5.1.1.4   Initial conditions

In addition to solving the time-dependent GP equations for the atom laser, the time-independent GP equations are used to provide accurate initial conditions for our simulations. For the five-state system described above, the time-independent GP equation is derived by substituting $\phi_2(\mathbf{r},t) = \varphi(\mathbf{r})e^{i\mu t}$ in Eq.5.7 and can be written as

$$\mu_2 = \left(-\frac{1}{2}\frac{\partial^2}{\partial z^2} + U_2|\phi_2|^2 + z^2 \right)\phi_2. \tag{5.11}$$

The exact ground state numerical solution to this equation (for our trapping parameters and condensate atom number) is found by a relaxation technique [115] and used as the initial condition in Eq.5.7.

Similarly the solution of the time-independent equation :

$$\mu_1 = \left(-\frac{1}{2}\frac{\partial^2}{\partial z^2} + U_1|\phi_{-1}|^2 + \frac{1}{2}z^2 \right)\phi_{-1}. \tag{5.12}$$

is used as the initial condition in the case of two- or three state systems.

5.1.2   Numerical method

5.1.2.1   The grid

Our simulations were performed using the commercially available and widely used Matlab$^{\text{TM}}$ software packaging. Our program uses a Fourier based, symmetric split step algorithm [67]. Investigating the behavior of the out-coupled laser beam faces some numerical difficulties. An initial problem is that numerical descriptions of an atom laser within the mean-field frame work are complicated by the large velocities that atoms reach when falling in gravitational potentials. The resultant small de Broglie wavelengths require very fine temporal and spatial numerical grids in order to control numerical instabilities and accurately follow the dynamics. Additionally, since the atomic beam travels away from the condensate, one needs to increase the numerical grid size. Indeed, if the beam interacts with the boundaries of the grid, the numerical scheme will break down as it requires periodic boundary conditions.

In order to solve these problems and run simulations that reflect experiments on a time scale longer than a few milliseconds, an apodising mechanism must be introduced to absorb the beam. For that purpose, a boundary absorber is included. This is a numerical device that reduces the

field to zero as it approaches the boundary of the spatial grid, without affecting accurate solutions of the system away from the boundary. In our model, apodising boundaries for each state have a simple exponential form and are positioned in order that no spatial aliasing occurs. The strength of the absorber can be varied and also its position. Using this method, our numerical grid can be restricted to a region around the condensate while still being able to observe the behavior of both the BEC and the laser mode. For this work, a 2048 point spatial grid was used from -40 to 40 with the equilibrium position of the condensate at 20 and a temporal resolution of 10^{-4}. However, although apodising boundaries are used in the numerical simulations, one can keep track of the total population in each state by calculating at each time step the 1D flux passing through a point on the numerical grid, provided this point is located below the trapped condensate and above the apodising boundary. Hence, our numerical grid can be thought of as two distinct sections : above and below the detection point. Thus, at any time during the simulation the total number of atoms in a particular Zeeman state can be determined by summing the number of atoms still on the grid above the detector with the number of atoms that have already passed through it. An interesting feature of this method is that it allows us to monitor the normalization of the numerics.

5.1.2.2   Results of the simulations

The raw data obtained from our simulations are the GP functions $\phi_{m_F}(z,t)$ (for a given Rabi-frequency Ω) from which all the results described in the latter part of this chapter are derived:

- The density of atoms in a given Zeeman state on the spatio-temporal grid is simply given by $|\phi_{m_F}(z,t)|^2$.

- In order to calculate the temporal evolution of the number of out-coupled atoms, a position (z_D) is chosen for the detector on the grid. The total number of atoms in a given Zeeman state is the sum of the number of atoms still on the grid above the detector after the out-coupling time t_{out} and the flux of atoms that have passed through the detector during t_{out}:

$$N_{m_F} = \int_{\tilde{z}_D}^{40} |\phi_{m_F}(z,t_{out})|^2 dz + \int_0^{t_{out}} J_{m_F}(z_D,t)dt \qquad (5.13)$$

In this equation, $J_{m_F}(z_D,t)$ is the 1D flux passing through z_D as a function of time, given by

$$J_{m_F}(z_D,t) = -\frac{i}{2} \left(\phi_{m_F}^*(z_D,t)\nabla\phi_{m_F}(z_D,t) - \nabla\phi_{m_F}^*(z_D,t)\phi_{m_F}(z_D,t) \right) \qquad (5.14)$$

5.2 EXPERIMENTAL COMPARISON OF THE MODEL

In order to guide theoretically future atom laser experiments, it is important to validate the 1D mean-field model described in the previous section. Because the five-state system is the most computationally and physically complex of the five-, three-, and two-state atom lasers, it can be used to confirm the accuracy of the model by comparing our numerical simulations of a five-state atom laser with experimental data for the $F = 2, m_F = 2$ system. The experimental system to which our five-state system is compared is described in large detail in previous work from our group [29]. ^{87}Rb condensates of around 5×10^4 atoms are produced in a highly stabilized magnetic trap which enables precise, repeatable and highly calibrated RF output-coupling of the condensate. The radial trapping frequency of the system is $\omega_{z_{(F=2)}} = 2\pi \times 260$ Hz and the axial trapping frequency is $\omega_{y_{(F=2)}} = 2\pi \times 20$ Hz at a bias field of $B_0 = 0.25$ G.

5.2.1 Bound state of an atom laser

A number of theoretical works [116–118] have suggested that, under given out-coupling conditions, a large fraction of the condensate could remain magnetically trapped and would not populate the atom laser beam. This theory of a 'bound state' for the atom laser is based on the existence of coupling between a single trap mode and a continuum of un-trapped states. Furthermore, it has been shown that trapping of all m_F states is a natural consequence of combining RF coupling with a dc magnetic trap [119, 120]. This trapping can be understood by considering the 'dressed-state' basis in which the RF coupling and dc potentials seen by the atoms are diagonalised. In this basis, the dressed eigenstates are linear combinations of the bare Zeeman states, trapped in effective potentials created by the avoided crossings. Assuming a strong coupling regime and a sudden non-adiabatic projection onto the dressed-states, diagonalization yields a prediction of up to 62.5% of the initial condensate atoms remaining trapped for the $F = 2$ atom laser (four of the five dressed-states allow some trapping).

In figure 5.2, a measurement (open circles) of the total atomic population in the $m_F = 2$ and $m_F = 1$ trapped states after $t_f = 100$ ms of output coupling is displayed as the angular Rabi frequency is scanned from weak to strong out-coupling regime. This population is given by $\int_{-40}^{40} (|\phi_2(z,t_f)|^2 + |\phi_1(z,t_f)|^2) dz$. One can see that the condensate is progressively depleted at increasing, but weak, Rabi frequencies until no remaining atoms can be observed in the magnetic trap. As the Rabi frequency is increased further, atoms start to reappear before the atom number
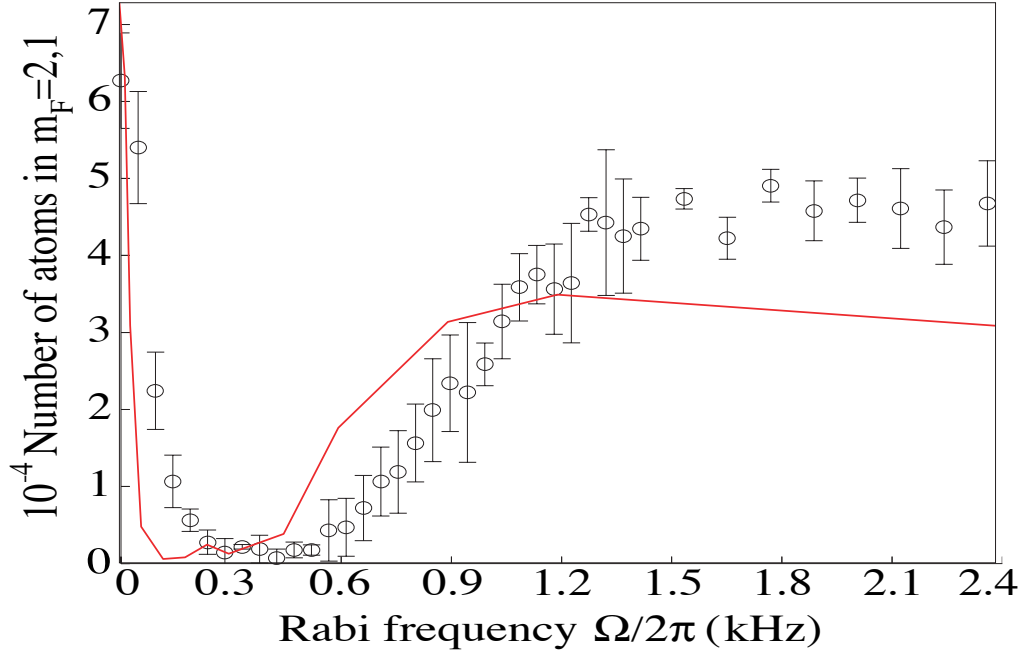
Figure 5.2: Total atomic population remaining in the magnetic trap after 100 ms of output coupling as a function of Rabi frequency for both our numerical model (solid line) and previous experimental measurements performed by our group [29] (open circles).

stabilizes to about 70% of the initial condensate number which is consistent with the previously mentioned theoretical predictions although the discrepancy suggests some degree of adiabatic transfer. Similar behavior can be observed for out-coupling durations as short as 50 ms. For shorter out-coupling times the condensate is not fully depleted before the onset of the bound state. The experimental data were collected in a way that ensured no systematic shifts occurred in the trap bias field. For every ten data points, five runs were made at coarsely separated Rabi frequencies and compared with a reference set which was taken at the beginning of the data collection. 10 ms out-coupling runs were also performed periodically to locate the bottom of the trap as mentioned in the previous chapter. The error bars in the figure were produced from averaging four successive data sets taken after 100 ms of out-coupling.

The prediction from our 1D model (solid line) qualitatively matches well the behavior of the experiment with no adjustable parameters. The predicted number of atoms remaining in the trap lies within the range of the strong coupling estimates but still differs by about 30% from our experimental results. The quantitative discrepancy between theory and experiment is explained

by the use of reduced dimensionality of the simulation. A full 3D model is expected to capture the dynamics of the experiment and improve the quantitative agreement of the numerics with the measurements. However, such simulations were not achieved in this work but will be part of the future research in the group.

5.2.2 Spatial structure of an atom laser

Theory and experiment are also compared in terms of the spatial structure of an atom laser for a short period of continuous output coupling and for different Rabi frequencies, once again with no free parameters. In figure 5.3(a-d) the spatial structure of the atom laser of [29] is displayed by plotting the experimental optical depth (dashed lines) integrated across the atom laser beam profile in the direction perpendicular to gravity. The condensate (about 5×10^4 ^{87}Rb atoms in the $F = 2$ state) was trapped in a highly stable magnetic trap of radial and axial trapping frequencies $\omega_{z(F=2)} = 2\pi \times 260$ Hz and $\omega_{y(F=2)} = 2\pi \times 20$ Hz respectively with a bias field of $B_0 = 0.25$ G. In this experiment, a short burst of 3 ms RF output coupling was applied before the system was left to evolve for a further 4 ms. The magnetic trap was then switched off and 2 ms later the image was acquired using standard absorption imaging.

Superimposed to the experimental data are the theoretical results (solid lines) showing the atomic density ($|\phi_0(z,t_f)|^2$) of the atomic beam ($m_F = 0$ state). The results were obtained for $t_f = 2.6$ ms of output coupling followed by transformation of the numerical data to account for the 6 ms of free fall. The full 3 ms of output coupling could not be simulated while keeping all out-coupled atoms on the numerical grid because of the numerical issues discussed earlier.

Since the total time, including the out-coupling process and the free fall under gravity, is different between theory (8.6 ms) and experiment (9 ms), the corresponding results were plotted on two slightly different horizontal time scales in order to have a better comparison. The top axis of each graph represents the position scale of the theoretical results whereas the bottom scale is displayed for experimental results. The two curves were superimposed by linear adjustment of the horizontal axis. Finally, although the theoretical data is given in arbitrary units, it was vertically scaled in order to satisfy the conservation of the number of atoms.

There is a very good qualitative agreement between the experimental results and our numerical model (with no free parameter), validating the 1D mean-field simulations and allowing us, in the following, to study and compare the qualitative behavior of the different atom laser systems of interest. However, accurate quantitative measurements cannot be derived from the 1D
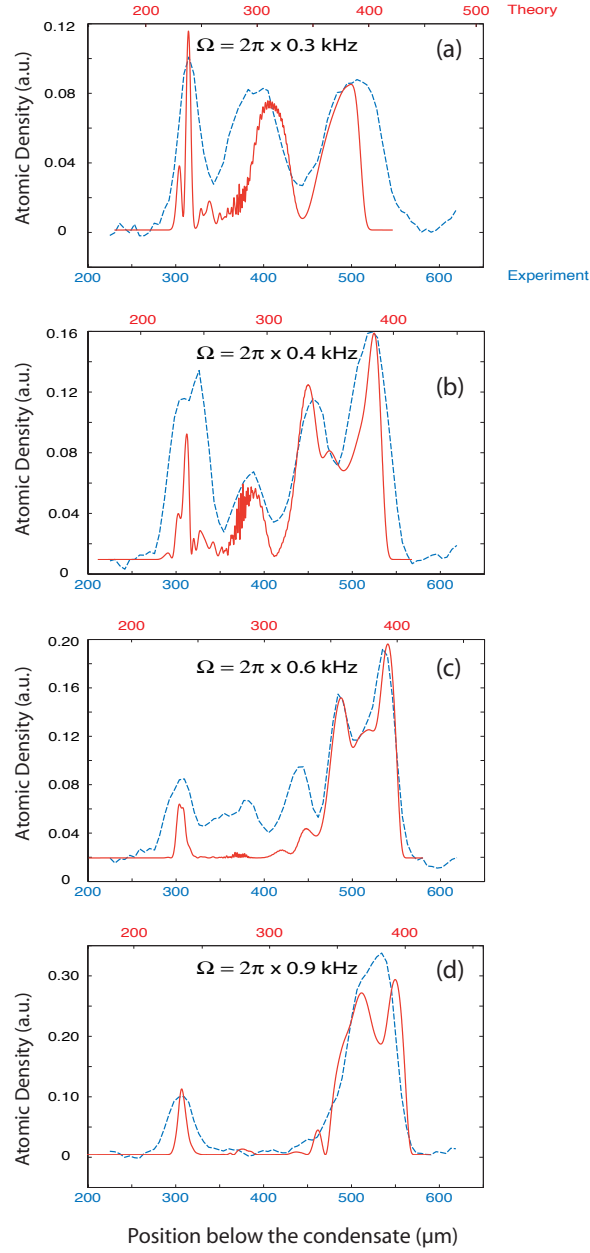
Figure 5.3: Comparison of theoretical (solid lines) and experimental (dashed lines) results showing the spatial structure of an atom laser (atoms in the $m_F = 0$ state) for various Rabi frequencies. The theoretical simulations were performed with 2.6 ms of RF out-coupling followed by a 6 ms free fall. The experimental data were obtained after 3 ms of RF out-coupling and again a free evolution of 6 ms. Important parameters are : $N = 5 \times 10^4$ atoms, $\omega_z = 2\pi \times \frac{260}{\sqrt{2}}$ Hz, $\omega_y = 2\pi \times \frac{20}{\sqrt{2}}$ Hz, $\Delta = 10.7$ and $U = 6.6 \times 10^{-4}$.

model as there is some discrepancy occurring in the width and amplitude of some of the density peaks. The width of the peaks is determined by both the natural broadening due to dispersion in the condensate and broadening due to gravity (which becomes more important as the atoms fall further away). These two effects are taken into account in the GPE used in our simulations. The discrepancy is attributed to the fact that our model is one-dimensional and one would expect the theory to match the experiment better in 3D.

5.3   COMPARISON OF TWO- AND MULTI-STATE SYSTEMS

The sensitivity of precision interferometric devices is ultimately limited by the particle flux. Previous experiments in our group [28, 29] have shown that there are fundamental limits of the flux in atom lasers using state changing out-coupling mechanisms like the RF or Raman techniques. Such limitations are due to the previously described bound state effect as well as a back-coupling effect occurring when atoms that have made a transition to the un-trapped state make a transition back into the trapped state before they have time to leave the condensate. As well as decreasing the flux, this also introduces dynamic fluctuations onto the atom laser beam. In order to characterize these effects, a comparison of the flux and fluctuation properties between the experimentally accessible two-, three-, and five-state systems must be performed.

5.3.1   Flux of the atom laser

In figure 5.4, the two-, three-, and five-state systems are compared with respect to the total number of atoms remaining in the condensate (a) as well as the number of atoms transferred in the atom laser beam (b), as a function of the Rabi frequency after 15 ms of long-pulsed output-coupling.

The evolution of the condensate is described by the total number of trapped atoms remaining after 15 ms of output coupling. It is simply given by the population in the $m_F = -1$ trapped state (N_{-1}) in the case of three- and two-state systems, and by summing the populations of both the $m_F = 2$ and $m_F = 1$ magnetically trapped-states ($N_2 + N_1$) in the case of a five-state system. On the other hand, the atom laser is represented by the number of atoms N_0 transferred in the $m_F = 0$ state, again after 15 ms of out-coupling. In each case, a clear peak in the flux of the laser beam is observed. However, the maximum flux amplitude, as well as the associated out-coupling strength, are different for each system. The two-state system has the highest coupling efficiency
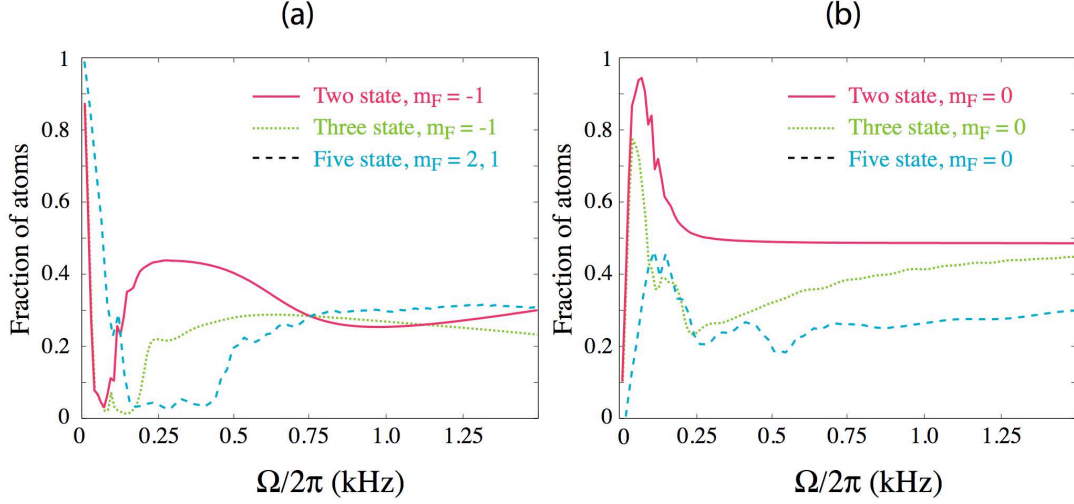
Figure 5.4: Comparison of the normalized number of atoms remaining in the condensate (a) and the number of atoms that have been transferred to the atom laser state (b) for the two-, three, and five-state systems after 15 ms of output coupling. The initial atom number is $N = 5 \times 10^4$ atoms. Parameters are $\omega_z = 2\pi \times \frac{260}{\sqrt{2}} Hz$, $U = 6.6 \times 10^{-4}$, $G = 9.24$, and $\Delta = 10.7$ or $\Delta = 43$ for the five-state or three- and two-state respectively.

with a peak flux of about 95 % of the condensate atoms being transferred into the atomic beam when the out-coupling strength is around $\Omega/2\pi = 80$ Hz. For the three-state system, the peak flux is obtained at $\Omega \sim 40$ Hz where about 80 % of the atoms will populate the atom laser. Less than 50 % of the atoms can ever populate the atom laser beam in the case of the five-state system even when working at the resonant out-coupling strength of $\Omega/2\pi \sim 200$ Hz. For strong out-coupling (high Rabi frequency), all systems exhibit a plateau with less than 100% of the atoms being transferred to the atom laser beam, characteristic of a bound-state of the atom laser. Again the two- and three-state systems have the maximum flux.

It already appears that two- and three-state systems would always provide the best out-coupling flux over a five-state system. However, an atom laser beam not only requires the highest possible flux but also the output beam needs to be homogeneous, meaning having no fluctuations. It is thus important to study comparatively the dynamics of each output beam in terms of population, as well as spatial and density fluctuations, in both cases of weak and strong out-coupling strengths.

5.3.2 Population dynamics

5.3.2.1 Five-state system

Population dynamics in the five-state system for weak and strong coupling are presented in figure 5.5. The RF coupling is turned on at $t = 0$ and maintained for 15 ms.

Figure 5.5: Comparison of the population dynamics in the five-state system for (a) weak and (b) strong coupling. Parameters are $N = 5 \times 10^4$ atoms, $\omega_z = 2\pi \times \frac{260}{\sqrt{2}} Hz$, $U = 6.6 \times 10^{-4}$, $G = 9.24$, and $\Delta = 10.7$.

Figure 5.5a shows the case of weak coupling. Figure 5.4 was used in order to choose an appropriate coupling strength ($\Omega/2\pi$=110 Hz) allowing a high efficiency process in the weak coupling regime. Again, the evolution of the condensate atoms is described by summing the number of trapped atoms in both the $m_F = 2$ and $m_F = 1$ states whereas the anti-trapped atoms include both the $m_F = -2$ and $m_F = -1$ states. One can see the number of atoms in the condensate decaying slowly and monotonically with very small modulations introduced by the out-coupling process itself. Around 50% of the atoms are transferred to the $m_F = 0$ un-trapped state as previously observed from figure 5.4. Such a smooth behavior is clearly indicative of the weak (or intermediate) coupling regime in which most experiments are usually operated. In contrast, the evolution in figure 5.5b, where the coupling is much stronger ($\Omega/2\pi$=1.1 kHz), is entirely different. As soon as the high power RF coupling is switched on, the $m_F = 2$ Zeeman state is projected onto the new dressed state basis as discussed above. After a short ($\sim$ 1 ms) high frequency exchange, a fraction of un-trapped dressed states is ejected [29] and the remnant dressed states are

left to oscillate in the magnetic trap. The condensate is no longer continuously depleted and the formation of the bound state appears. Finally, in both cases, a non-negligible fraction of atoms ($\sim 30\%$) is coupled into one of the anti-trapped states (either $m_F = -1$ or $m_F = -2$) resulting in a loss in the flux of the atom laser ($m_F = 0$) beam.

5.3.2.2 Three- and two-state systems

The behavior of the three- and two-state population dynamics for weak and strong coupling regimes is presented in figures 5.6 and 5.7 respectively.

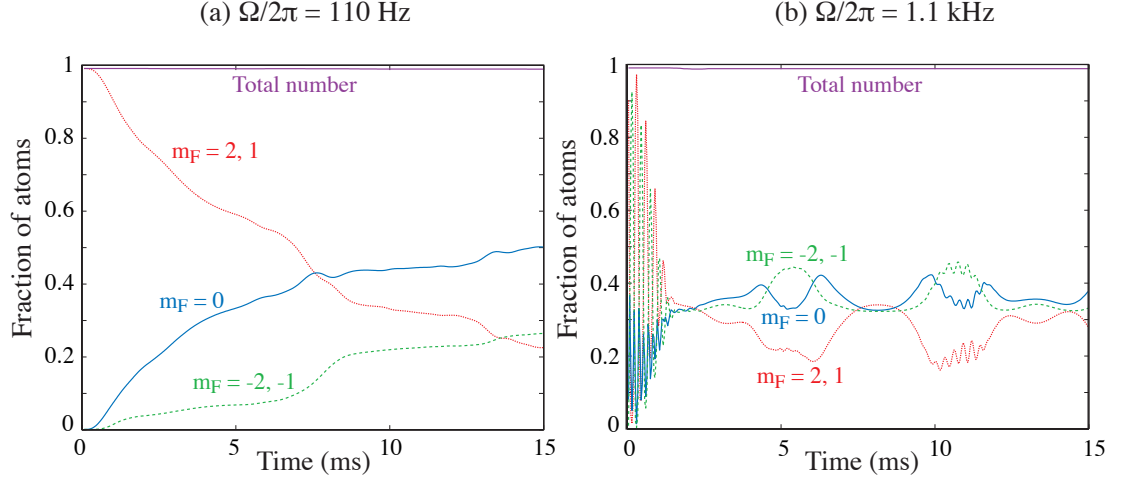(a) $\Omega/2\pi = 60$ Hz   (b) $\Omega/2\pi = 1.1$ kHz

Figure 5.6: Comparison of the population dynamics in the three-state system for (a) weak and (b) strong coupling. Parameters are $N = 5 \times 10^4$ atoms, $\omega_z = 2\pi \times \frac{260}{\sqrt{2}} Hz$, $U = 6.6 \times 10^{-4}$, $G = 9.24$, and $\Delta = 43$.

It is found to be qualitatively similar to the five-state system. For weak coupling strengths (see figures 5.6a and 5.7a) the condensate decays monotonically with a greater fraction of condensed atoms being transferred to the $m_F = 0$ un-trapped state. In the case of the three-state system, a fraction of atoms ($\sim 20\%$) is coupled into the anti-trapped ($m_F = -1$) state, limiting the flux of atoms into the atom laser ($m_F = 0$) beam to about 70%. In the case of a pure two-state system, the atoms can only be either trapped or un-trapped so that any atom out-coupled from the condensate will exclusively populate the atom laser beam. Again figure 5.4 was used in order to choose the coupling strength ($\Omega/2\pi = 60$ Hz) providing the highest efficiency process in the weak coupling regime. In the strong coupling limit ($\Omega/2\pi$=1.1 kHz), the behavior is again similar to the five-
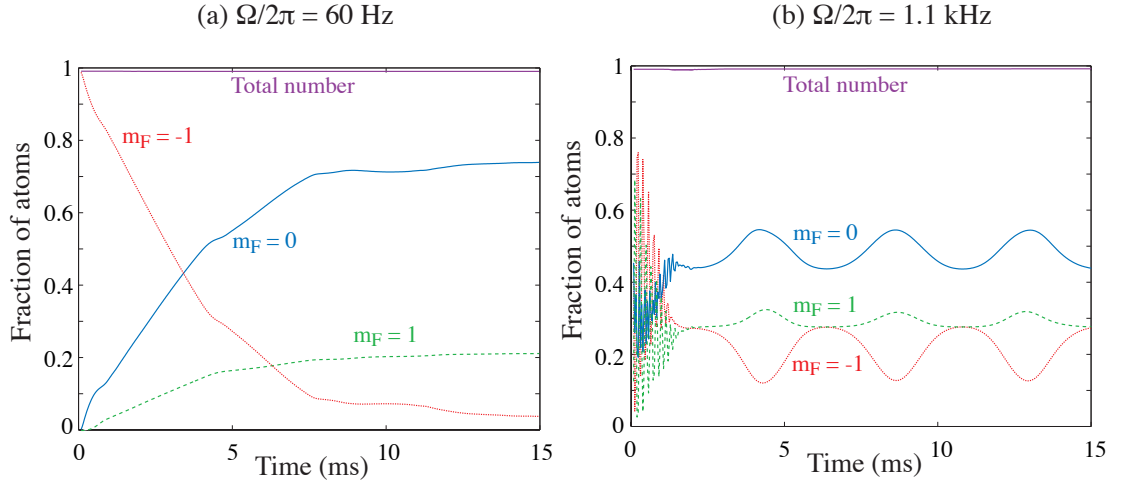
(a) $\Omega/2\pi = 60$ Hz

(b) $\Omega/2\pi = 1.1$ kHz
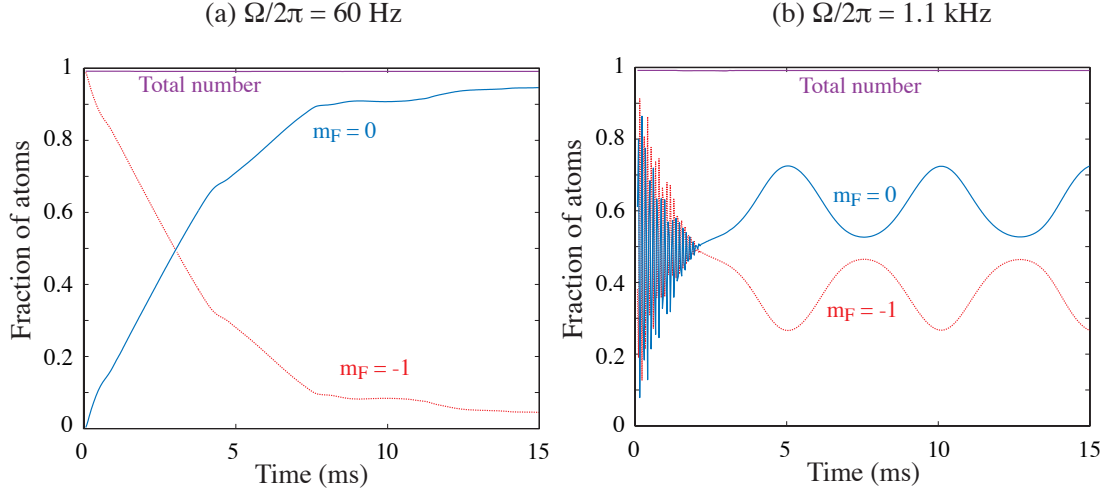
Figure 5.7: Comparison of the population dynamics in the two-state system for (a) weak and (b) strong coupling. Parameters are $N = 5 \times 10^4$ atoms, $\omega_z = 2\pi \times \frac{260}{\sqrt{2}} Hz$, $U = 6.6 \times 10^{-4}$, $G = 9.24$, and $\Delta = 43$.

state system (see figures 5.6b and 5.7b), although the cyclic oscillations of atoms between the different Zeeman states is much cleaner. Again, a percentage of all states remain trapped in the condensate.

In terms of population dynamics, the three systems studied here have extremely similar behaviors, apart from the two- and three-state systems being cleaner in the strong coupling regime. However, the population dynamics only takes into account the total number of trapped or untrapped atoms on the spatial grid and it is thus necessary to consider the details of the spatial dynamics, *i.e.* the density of atoms at any point over the spatial grid.

5.3.3 Spatial dynamics

Although the population dynamics in figure 5.5(a) are smooth, we anticipated that the details of the spatial dynamics would not be. In fact, for the case of a five-state system, atoms trapped in the $m_F = 2$ state must pass through the $m_F = 1$ state to get to the un-trapped $m_F = 0$ state. Since atoms in the $m_F = 1$ state have a different equilibrium position to that of the $m_F = 2$ state (the gravitational sag is different for each state), the $m_F = 1$ atoms start to oscillate in the magnetic trap. The dynamics of such an oscillation is shown in figure 5.8 where an atom laser beam was

created after 15 ms of continuous weak output coupling of Rabi frequency $\Omega/2\pi = 200$ Hz. In each image, the atomic density of different Zeeman states is shown with the complete spatial grid and temporal grid in the vertical and horizontal directions respectively. In figure 5.8a, the sum of the atomic densities in all five Zeeman states is plotted and oscillations in the spatial profile can be observed. After plotting the contribution of each Zeeman state independently (figure 5.8b-d), one can see that this effect on the output mode is due to the important sloshing of the $m_F = 1$ state (figure 5.8c). This phenomenon is independent of the output-coupling strength and is also observed for higher or smaller Rabi frequencies, which indicates that even at low flux a five-state atom laser system will be modulated by this classical noise.
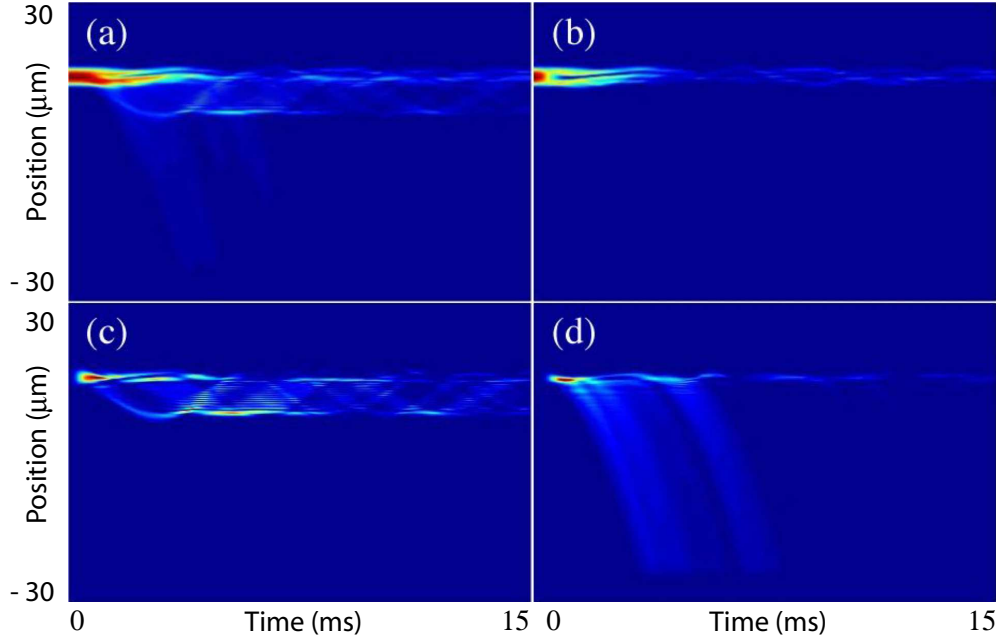
Figure 5.8: Spatial profiles of the five-state system after 15 ms of weak ($\Omega/2\pi = 200$ Hz) output coupling. Each plot shows the atomic density of atoms with the complete spatial grid in the vertical direction and the temporal grid in the horizontal direction. (a) Represents the total density, i.e. the sum of the densities in all five Zeeman states, as a function of time. (b) Is the density of the $m_F = 2$ state, (c) $m_F = 1$ and (d) $m_F = 0$. The color axes are adjusted to give the best contrast for each of the Zeeman states. $N = 5 \times 10^4$ atoms, $\omega_z = 2\pi \times \frac{260}{\sqrt{2}} Hz$, $U = 6.6 \times 10^{-4}$, $G = 9.24$, and $\Delta = 10.7$.

In the case of the three- and two-state systems, where a single Zeeman state is confined in the magnetic trap, the sloshing effect almost disappears in the weak out-coupling regime as shown in figure 5.9.
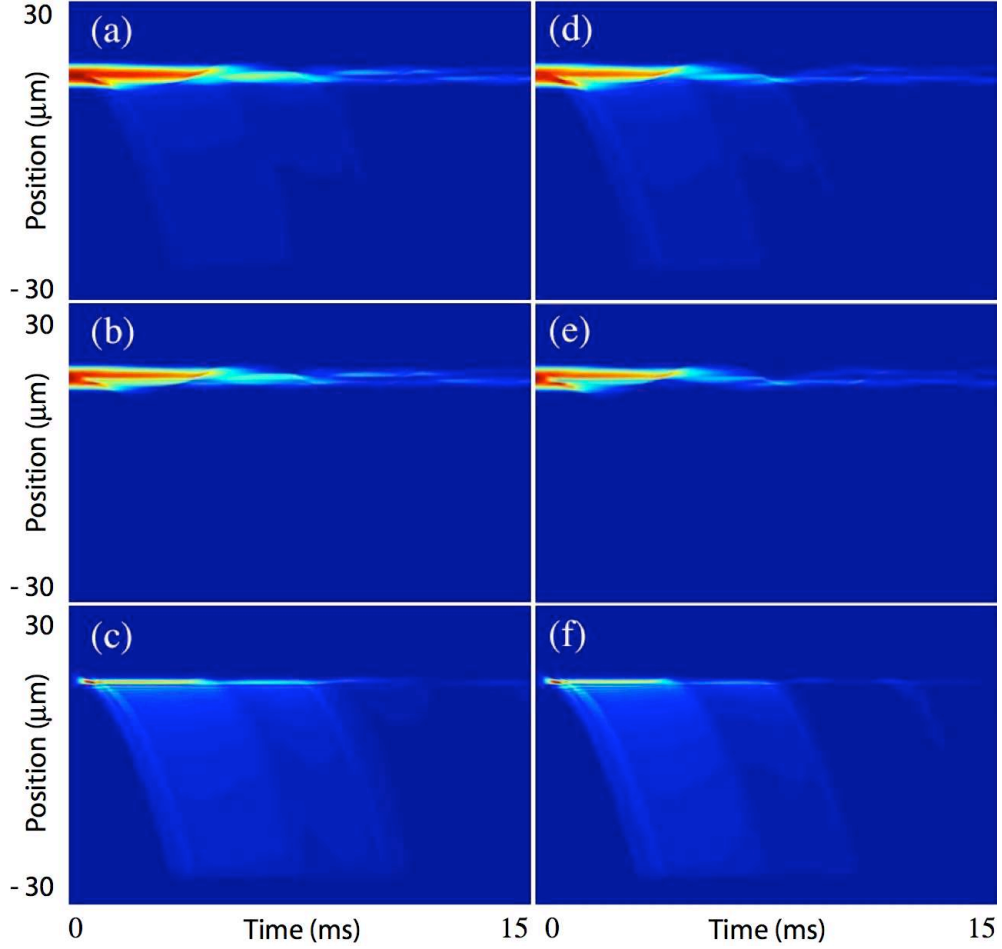
Figure 5.9: Spatial profiles of the three- and two-state systems, after 15 ms of weak ($\Omega/2\pi = 80$ Hz) output coupling. (a-b-c) Represents the three-state system with respect to the total density, the density of the $m_F = -1$ state and the density of the $m_F = 0$ state respectively. (d-e-f) Represents similarly the two-state system with respect to the total density, the density of the $m_F = -1$ state and the density of the $m_F = 0$ state respectively. The color axes are adjusted to give the best contrast for each of the Zeeman states. $N = 5 \times 10^4$ atoms, $\omega_z = 2\pi \times \frac{260}{\sqrt{2}} Hz$, $U = 6.6 \times 10^{-4}$, $G = 9.24$, and $\Delta = 43$.

In the strong coupling limit, the oscillatory population dynamics observed in figures 5.5(b), 5.6(b), and 5.7(b) can be explained by these periodic spatial oscillations. A clear example is shown in figure 5.10 where the population density of the magnetically trapped states ($|\phi_2(z,t)|^2 + |\phi_1(z,t)|^2$) of a five-state system is plotted over the entire spatio-temporal grid and for $\Omega/2\pi$=1.9 kHz. One can see the initial ejection of the un-trapped dressed state early in the simulation (characteristic of a bound state) and then a clean periodic oscillation inside the trap. Two oscillation

periods are clear from this figure and correspond to the $F = 2$ and $F = 1$ radial trapping frequencies. These oscillations have their upper maximum positions at the minimum of the magnetic trapping potential and hence oscillate up only one side of the potential. The spatial dynamics imposed on the atom laser beam by this mechanism of the $m_F = 1$ sloshing in the trap are independent of the back-coupling dynamics investigated previously in our group [28].
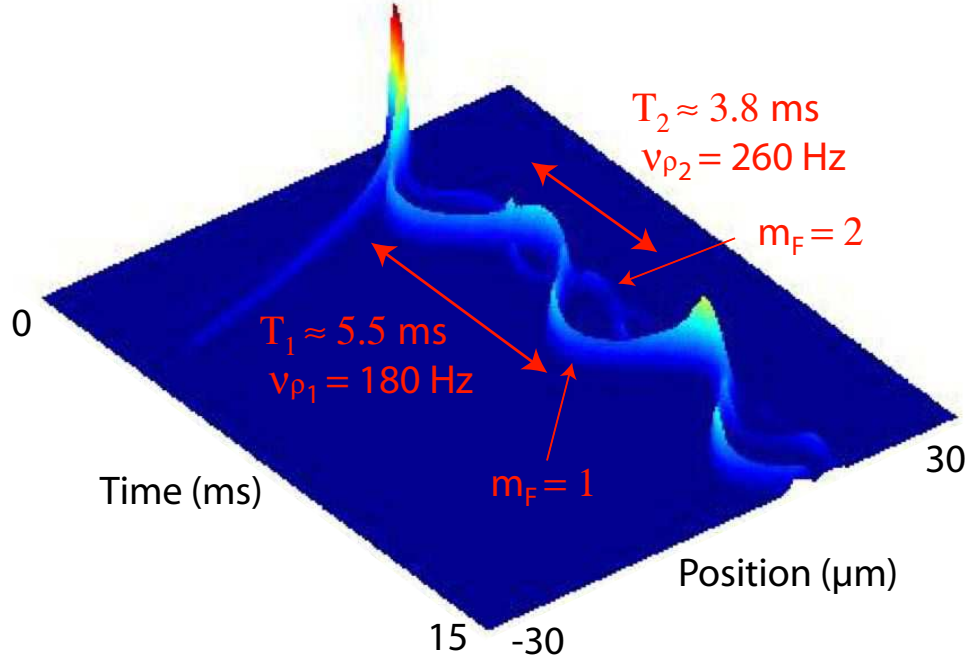
Figure 5.10: Periodic spatial oscillations in the population dynamics of a five-state system for $\Omega/2\pi$=1.9 kHz. One can see the early ejection of the un-trapped dressed states as well as both oscillation periods corresponding to the $F = 2$ and $F = 1$ radial trapping frequencies. Note that the upper edge of the oscillations is at the minimum of the magnetic trap potential. Parameters are $N = 5 \times 10^4$ atoms, $\omega_z = 2\pi \times \frac{260}{\sqrt{2}}Hz$, $U = 6.6 \times 10^{-4}$, $G = 9.24$, and $\Delta = 10.7$.

5.3.4 Density fluctuations

5.3.4.1 Five-state system

The density fluctuations in the output beam ($m_F = 0$ state) at a given point (z_D) in the atomic beam are simply given by $|\phi_0(z_D,t)|^2$. For instance, density fluctuations in the output beam at

a point located 30 μm below the condensate are shown as a function of time in figure 5.11, for different Rabi frequencies. The Rabi frequencies are chosen to be in the very weak coupling regime, where any classical noise due to the back-coupling dynamics is negligible. One can see that the fluctuations in the output beam are increasingly severe as the out-coupling strength is increased, although the atom laser is operated in a weak coupling regime, which shows that classical noise due to the sloshing of the $m_F = 1$ is inherent to the system.
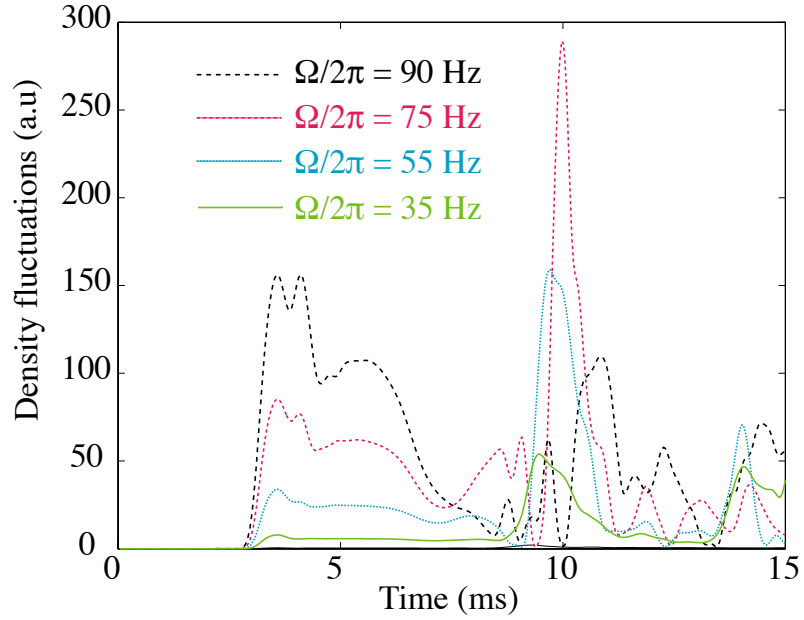
Figure 5.11: Density fluctuations in the $m_F = 0$ state of a five-state system at a single point in the beam as a function of time. The fluctuations due to the sloshing of the $m_F = 1$ are increasingly severe as the coupling strength is increased. Parameters are $N = 5 \times 10^4$ atoms, $\omega_z = 2\pi \times \frac{260}{\sqrt{2}}$ Hz, $U = 6.6 \times 10^{-4}$, $G = 9.24$, and $\Delta = 10.7$.

5.3.4.2   Three- and two-state systems

The three- and two-level systems offer the possibility of a cleaner output than the five-level as there is no intermediate state between the trapped condensate ($m_F = -1$ Zeeman state) and the un-trapped beam ($m_F = 0$). Fluctuations in the output beam will then be solely due to the back coupling and depletion of atoms to the anti-trapped $m_F = 1$ Zeeman state as observed in previous work from the group [29]. However, in the limit that the output-coupling is weak, such effects are expected to be negligible and the system should produce a classically quiet atom laser

beam. It is even more true in the case of a true two-level system where no anti-trapped state is involved. As mentioned in the introduction of this chapter, significant effort is required in order to produce a 'closed' two-state atom laser as the relevant alkali-metal atom manifolds have at least three Zeeman states linked by allowed RF transitions. Since back-coupling fluctuations and the 'bound' state arise even in the two-level system it is prudent to ask whether the two- and three-state atom lasers actually differ much, in particular in the weak coupling regime where they are meant to operate.
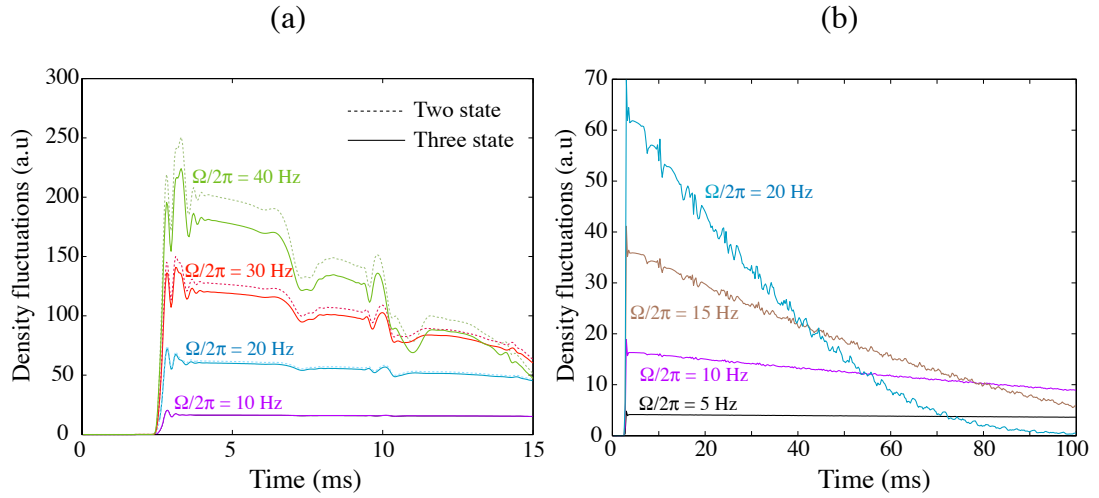
Figure 5.12: (a) Shows a comparison of the time-dependent density of the two- and three-state atom lasers at a point located 30 μm below the condensate, after 15 ms of output coupling and for different Rabi frequencies in the low coupling regime. (b) Is the time-dependent density of the two-state atom laser measured at the same point, at very low intensities, after 100 ms of output coupling. Parameters are $N = 5 \times 10^4$ atoms, $\omega_z = 2\pi \times \frac{260}{\sqrt{2}}$ Hz, $U = 6.6 \times 10^{-4}$, $G = 9.24$, and $\Delta = 43$.

Figure 5.12 shows the comparison in the dynamics of the two- and three-state atom lasers after out-coupling times of $t_f = 15$ and $t_f = 100$ ms respectively. In 5.12a, the time dependent densities of the two- (dashed line) and three-state (continuous line) atom lasers are plotted at a point below the condensate after 15 ms of output coupling and for different Rabi frequencies in the weak coupling regime. It is remarkable that, for the 1D model described here, the two systems are essentially indistinguishable. Even when increasing the strength of the coupling, which results in an increase of the classical noise, the details of the classical fluctuations on the beam are still mirrored in the two systems. However, a small difference in amplitude is observed

between the simulations. This difference is accounted for by the loss of atoms to the anti-trapped Zeeman state in the three-level system. Moreover, in the extremely weak coupling limit, the anti-trapped atoms are expelled from the system on a time scale much faster than the back-coupling time (set by the inverse of the Rabi frequency). Thus, they have little effect on the dynamics of the system. In (b) the density fluctuations are represented as a function of time for the two-state atom laser after 100 ms of very low output coupling. Even in the weak coupling limit taken here, the density fluctuations due to back-coupling are a significant contribution to the noise in the atom laser. For extremely weak out-coupling ($\Omega/2\pi = 5$ Hz), these fluctuations are negligible, but at the expense of a high flux in the atom laser beam. This has major implications for the use of atom lasers in precision measurement systems where high flux and minimal classical noise are essential features required for the atom beam.

5.3.5   Flux and fluctuations trade-off

Comparing figure 5.4 and 5.12(a) reveals that it is actually not possible to operate the atom laser near the peak output-coupling rate because of increasingly severe density fluctuations. For example, the peak in the two-state system is around $\Omega/2\pi = 80$ Hz. However, density fluctuations are already significant for a Rabi-frequency of $\Omega/2\pi = 20$ Hz (see figure 5.12(a)). This means that the peak homogeneous output-coupling rate (meaning the rate for which the atom laser beam remains classically quiet) achievable in an RF atom laser is significantly lower than the maximum output-coupling rate. In this homogeneous regime, there is practically no difference between the three- and two-state atom lasers. The only significant difference of a three-state atom laser over a two-state one is the creation of a small amount of atoms in the anti-trapped state.

5.4   CONCLUSION

In this chapter, a theoretical model was described and used to study the effect of RF out-coupling on two- and multi-level systems. The model was validated by comparing the theoretical results to experimental measurements performed earlier in our goup [29]. Finally, the atom laser output was characterized depending on the out-coupling strength. In particular crucial experimental properties of an atom laser, such as fluctuations, flux and spatial structure were studied. On that matter, the five-state system ($F = 2$) seems clearly inappropriate for any measurement using atom laser beams, due to the intermediate coupling to the $m_F = 1$ sloshing in the trap and

disturbing the out-coupling process.

Consequently, a 'natural' three-state system can generally be preferred for any classical measurement provided it is performed in the weak out-coupling regime. For example, in the recent Ramsey interferometer experiment performed in our group [89], it is not essential to have a two state output coupler. Indeed, if some atoms were coupled into other states, there would only be a slight loss in flux and therefore minor degradation of the signal to noise ratio when measuring fringe visibility.

However, it will be more important to have a pure two state output-coupler in any experiment designed to measure quantum properties (statistics), such as squeezing, of an atom laser beam using quantum state transfer from an optical beam. In such an experiment it would be important to have a high efficiency conversion of photons (in a squeezed optical beam) into atoms in a given internal state (in the squeezed atomic beam). Any atoms that are out-coupled to another state in such an experiment would degrade the squeezing. Similarly, in the Zurich group [27], measurements on the $g^{(2)}$ function were performed using RF out-coupling at 6.8 GHz between the hyperfine levels to ensure a two state system.

HELIUM BEC: EXPERIMENTAL SETUP

This chapter introduces the characteristics of the helium atom followed by a general description of the setup used in our experiment. The method to reach Bose-Einstein Condensation uses a similar route to that of alkali atoms, namely laser cooling and trapping followed by a final step of evaporative cooling. However, due to the specificities of He, significant differences will arise compared to the case of Rb (chapter 2). The experimental setup at ENS has been constructed almost 10 years ago and condensation of metastable helium atoms was achieved in 2001 [121]. In 2006, the scattering length of metastable helium atoms was accurately measured, using a two-photon photo-assocation method [122]. From there, it was decided to largely renew the experimental setup, in order to make it more reliable in view of a new generation of experiments where the BEC will be manipulated optically. It is this new setup that is described in this chapter. In particular, a Channel Electron Multiplier was added in the Science cell where the BEC is produced, providing a non-destructive real-time method to detect ions or electrons resulting from background or inter-atomic collisions. The optical setup was also redesigned and entirely fiber-coupled in order to improve the stability when manipulating and cooling the atoms.

6.1   THE METASTABLE HELIUM ATOM ^{4}He*

6.1.1   The metastable 2^3S_1 triplet state

Like the ^{87}Rb alkali atom studied in the previous chapters, the isotope 4 of helium (^{4}He) is also a bosonic atom. Its internal structure is much simpler than the one of rubidium since it involves only two electrons and a zero nuclear spin leading to the absence of hyperfine structure. As a consequence, ^{4}He is an ideal candidate for theoretical ab initio calculations for atomic or molecular physics. However, it is interesting to note that only a few groups [121, 123–125] have produced a BEC using He atoms in a metastable state, compared to the tens of groups working on BECs of alkali atoms. This results from experimental complications due to the properties of the helium atom which can be explained from the energy level diagram of He, shown in figure 6.1.

Under typical conditions, ^{4}He is in the 1^1S_0 initial ground state with the closest excited state
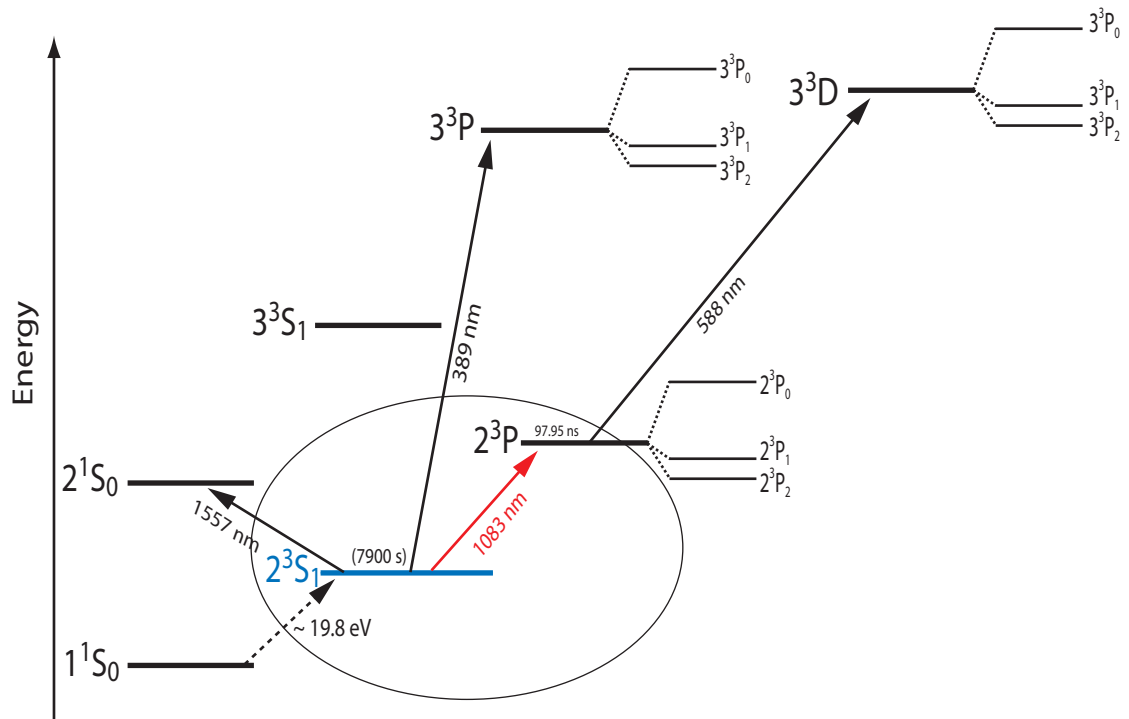
Figure 6.1: Energy levels of ^{4}He. In our experiment, we prepare the atoms in the 2^3S_1 metastable state which is considered as an effective ground state due to its very long lifetime. We use the $2^3S_1 \rightarrow 2^3P_2$ optical transition at 1083 nm to manipulate and cool the atoms.

being the 2^3S_1 triplet state, 19.8 eV (~ 60 nm) above. The $1^1S_0 \rightarrow 2^3S_1$ transition is forbidden optically, and in the far UV regime which is not easily accessible using standard commercial lasers. The 2^3S_1 state is metastable: the electric dipole transition is prohibited and consequently its lifetime is extremely long (~ 7900 s) compared to the typical time scale of laser cooling experiments. Moreover, optical transitions to other triplet states ($2^3S_1 \rightarrow 2^3P$ at 1083 nm and $2^3S_1 \rightarrow 3^3P$ at 389 nm) can easily be driven. These transitions are closed due to the $\Delta S = 0$ selection rule, and any atom excited into these triplet states will preferentially decay back into 2^3S_1. Consequently, one can consider the metastable 2^3S_1 state (He*) as an effective ground state for typical laser cooling experiments, with the $2^3S_1 \rightarrow 2^3P_2$ optical transition at 1083 nm being generally used to manipulate the atoms. The natural linewidth of the 2^3P_2 excited state is $\Gamma = 2\pi \times 1.62$ MHz which corresponds to a lifetime of $\tau = \Gamma^{-1} \sim 98$ ns, and the saturation intensity of the transition is $I_{sat} = 0.16$ mW.cm^{-2}.

The first experimental challenge is thus to create an intense source of He* which is done by applying an electrical discharge to an incoming flux of He gas in the $1^1 S_0$ ground state. The atoms are accelerated during this process and, in contrast to ^{87}Rb, an initial cooling stage using a Zeeman slower is necessary in order to capture the metastable atoms in a MOT.

A specificity of He* is its very high internal energy (~ 19.8 eV). This energy is easily released when a metastable atom collides with a surface (either metallic or dielectric), ejecting an electron which can be detected after electron multiplication by a Channel Electron Multiplier (CEM) or a Microchannel Plate (MCP). Individual atoms can then be monitored with high spatial (a few $10 - 100$ μm) and temporal (a few 10 ns) resolutions. However, the high internal energy of He* raises the problem of inelastic Penning collisions between metastable atoms as described in the next paragraph.

6.1.2 Penning collisions

The metastable nature of He atoms is a major issue for reaching condensation. A pair of He* atoms has sufficient energy to ionize one of the partners giving:

$$\text{He}^* + \text{He}^* \longmapsto \begin{cases} \text{He}^+ + \text{He}(1^1 S_0) + e^- & \text{(a)} \\ \text{He}_2^+ + e^- & \text{(b)} \end{cases} \tag{6.1}$$
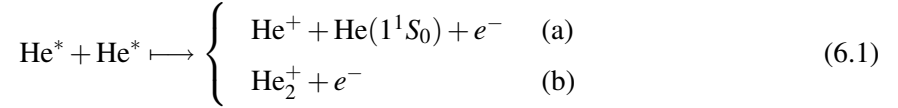
The second reaction (b) is called associative ionization, resulting in an electron and a molecular ion, and is usually less probable than (a) [126]. The first reaction (a) creates an electron, an ion and an atom in the $1^1 S_0$ ground state and is called Penning ionization. The process is extremely efficient, with an ionization loss rate on the order of $\sim 10^{-10}$ cm^3.s^{-1} [127]. However, if both He* atoms are spin polarized ($He^* \uparrow$), the Penning ionization process

$$He^* \uparrow + He^* \uparrow \longmapsto He^+ + He(1^1 S_0) + e^- \tag{6.2}$$
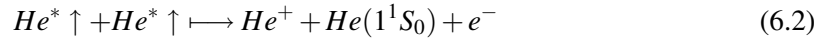
is strongly inhibited due to spin conservation rules, with an ionization rate reduced by 4 orders of magnitude to $\sim 10^{-14}$ cm^3.s^{-1} [128, 129]. Indeed, in equation 6.2, the total spin of the reagents (on the left) is $S = 1 + 1 = 2$ whereas it is either 0 or 1 for the products (spin 1/2 for the ion and the electron and spin 0 for the He atom). The possibility to achieve a He* BEC in a magnetic trap where spins are oriented is a consequence of this inhibition limiting the losses from Penning ionization. Indeed, such a reaction can only happen if the orientation of the atomic spins

is not preserved during the collision. If the total electronic spin was always maintained, the reaction would be completely forbidden. However, the spin can relax due to spin-spin interactions between the two magnetic moments of the atoms.

Two loss mechanisms of He* atoms are induced by spin relaxation and will be described in more details in the next chapter (section 7.3). The first one is a direct consequence of the spin-relaxation process: following the collision, one (or both) of the atoms is no longer in the initial $m_J = +1$ magnetically trapped state (where m_J is the projection of the total angular moment J of the atom) and escapes from the trapping potential. The second mechanism is induced by this spin-relaxation process: during the collision the spin-spin interaction modifies the spin of the atoms which are thus no longer polarized and can interact following the standard Penning ionization process of equation 6.1a. This mechanism dominates in the regimes of very low temperatures (< mK) and small magnetic fields (< 100 G) of usual experiments [128, 129].

6.2 EXPERIMENTAL SETUP

In this section, details on the experimental setup which we use to produce and cool metastable helium atoms are given. First, the description of the vacuum system and of the optical setup provide a general overview of the experiment. This optical setup was entirely reconstructed and largely fiber-coupled. The pumping of the vacuum system was slightly modified with the use of additional turbopumps to replace previously installed ion pumps and diffusion pumps. Each experimental step, from producing metastable atoms to reaching BEC, is then discussed briefly. Additional information on the experimental setup can be found in the thesis of former PhD students of the group [130–132], except for the optical setup arrangement and the use of a channeltron which are both original to this thesis and will be largely described.

6.2.1 Vacuum system

The experimental setup can be thought of as 3 distinct vacuum chambers that can be completely isolated from each other by gate valves with pneumatic actuators, all connected to a safety system in case the vacuum suddenly fails. Each of the 3 chambers have their own individual purpose (see figure 6.2). The Source Chamber produces a collimated beam of metastable helium atoms whereas the Zeeman slower stage reduces the longitudinal velocity of the atoms to typical capture velocities (~ 130 m.s^{-1}) of a MOT [133]. Finally, the Science Chamber traps and
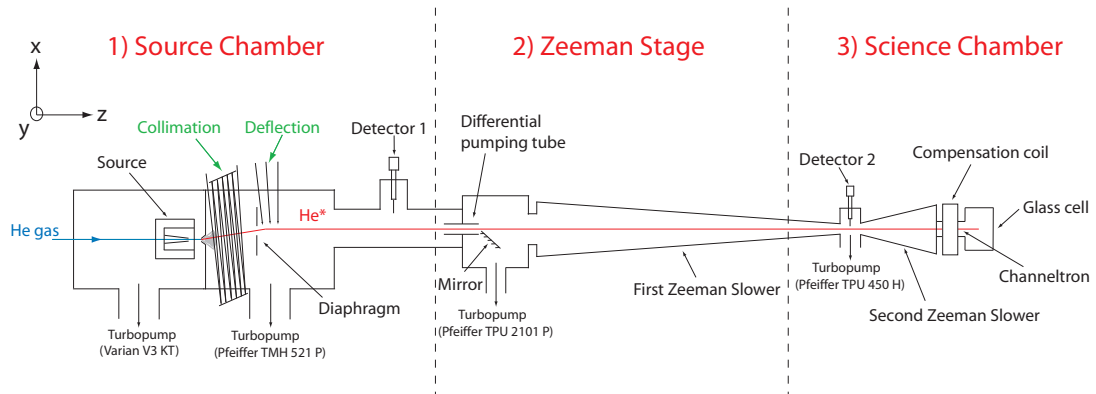
Figure 6.2: Experimental setup. The vacuum system is segmented into 3 parts: 1) the Source Chamber, 2) the Zeeman slower Stage and 3) the Science Chamber. The metastable helium beam is successively collimated, deflected, decelerated and trapped, in the Science Chamber, a 5cm×5cm×4cm quartz cell.

condenses the atoms in the quartz cell.

1. <u>The Source Chamber</u>: It consists of two distinct chambers physically separated by only a small hole (skimmer) which allows the atoms to pass through. The first part is the production chamber where helium atoms are excited in the metastable state via an electrical discharge, whereas the second part is the collimation-deflection chamber, where the metastable beam is collimated and deflected in order to be aligned to the axis of the Zeeman slower, and where atoms in the ground state are filtered out. Since the production of metastable atoms is not an efficient process (see section 6.2.3), a high flux of ground-state He gas is initially needed. It has to be pumped into the vacuum system so that the pressure in the experimental setup does not deteriorate. For that purpose, the production chamber is pumped by a Varian V-3KT turbo pump (Pumping Speed $\sim$ 2000 l/s for He) which maintains a pressure of $\sim 4 \times 10^{-5}$ mbar (when the source operates under optimal conditions), whereas a second turbo pump (Pfeiffer TMH 521 P, Pumping Speed $\sim$ 500 l/s), together with the differential pumping induced by the skimmer, allow for a pressure of $\sim 5 \times 10^{-7}$ mbar in the collimation-deflection chamber.

2. <u>The Zeeman Slower</u>: A cylindrical differential pumping tube ($\oslash = 1$cm, $L = 10$cm) separates the collimation-deflection chamber from the Zeeman Slower area where a pressure of $\sim 10^{-10}$ mbar is maintained using an additional turbo pump (Pfeiffer TPU 2101 P, Pump-

ing Speed ~ 2000 l/s).

3. <u>The Science Chamber</u>: Finally, at the far end of the Zeeman Slower, a quartz cell is adjoined where the atoms are trapped, condensed and studied. A final turbo pump (Pfeiffer TPU 450 H, Pumping Speed ~ 400 l/s), together with a differential pumping stage through a second Zeeman slower (see figure 6.2), allow an ultrahigh vacuum ($\sim 10^{-11}$ mbar) to be achieved in the quartz cell.

6.2.2 Optical Setup

The optical setup presented here has been completely renewed compared to the pre-existing scheme described in previous theses from our group [130–132]. In particular, the paths followed by the different laser beams have been largely fiber-coupled, not only to improve the optical quality of the beams and the general stability, but also to provide fast and accurate alignment at each step of the setup. Additionally, the important losses of power through these optical fibers was balanced by using two high power laser amplifiers, providing a total power of ~ 6 W of light at 1083 nm.

1. <u>Light source</u>: The light source of the entire laser system is shown in figure 6.3. The seed laser is a single mode Diffracted Bragg Reflector (DBR) laser diode emitting at 1083 nm with a maximum output power of ~ 10 mW. The linewidth of the laser diode is reduced from 3 MHz to 300 kHz by an external extended cavity using a semi-reflecting mirror of 80% transmission. The initial elliptical shape of the output light is corrected to a Gaussian profile by passing through two anamorphic prisms and the diode is protected from potential back-reflected light using two 30 dB optical isolators. A fraction ($\sim 300 \mu$W) of the laser power double-passes an AOM up-shifting the frequency by +240 MHz. The light is then frequency-locked on the $2^3S_1 \rightarrow 2^3P_2$ atomic transition by saturated absorption in a low pressure cell of helium where a continuous RF discharge transfers He atoms in the 2^3S_1 metastable state. A photodiode detects the saturated absorption signal and the frequency locking is achieved by active feedback on the current of the laser diode as well as on the position of the output mirror of the cavity which is mounted on a piezo-electric support. The remaining light that doesn't pass through the AOM and is locked -240 MHz away from the $2^3S_1 \rightarrow 2^3P_2$ atomic transition, injects a polarization maintaining (PM) fiber-amplifier from Keopsys (Amplifier 1 INPUT on figure 6.3) providing a collimated output

Figure 6.3: Schematic of the laser diode setup. The beam frequency is locked -240 MHz away from the $2^3S_1 \rightarrow 2^3P_2$ atomic transition by saturated absorption and is used as a seed to be amplified by a 3 W laser-amplifier.

beam of 3W in a TEM_{00} mode (Amplifier 1 OUTPUT in figure 6.4).

2. <u>Main optical setup</u>: The optical arrangement used to create all the optical beams needed in the experiment is shown in figure 6.4. It is mainly fiber-coupled for improved stability, and consequently requires high laser power which is provided by two 3W laser amplifiers (Amplifiers 1 and 2 on figure 6.4).

The laser output of amplifier 1 is split into several optical beams which are used for:

• the collimation and deflection of the atomic source, which is described in 6.2.4.

• the imaging beam, which is used for absorption and fluorescence detection to image the cloud of atoms in the quartz cell. The AOM in double-pass configuration tunes the frequency of the imaging light.
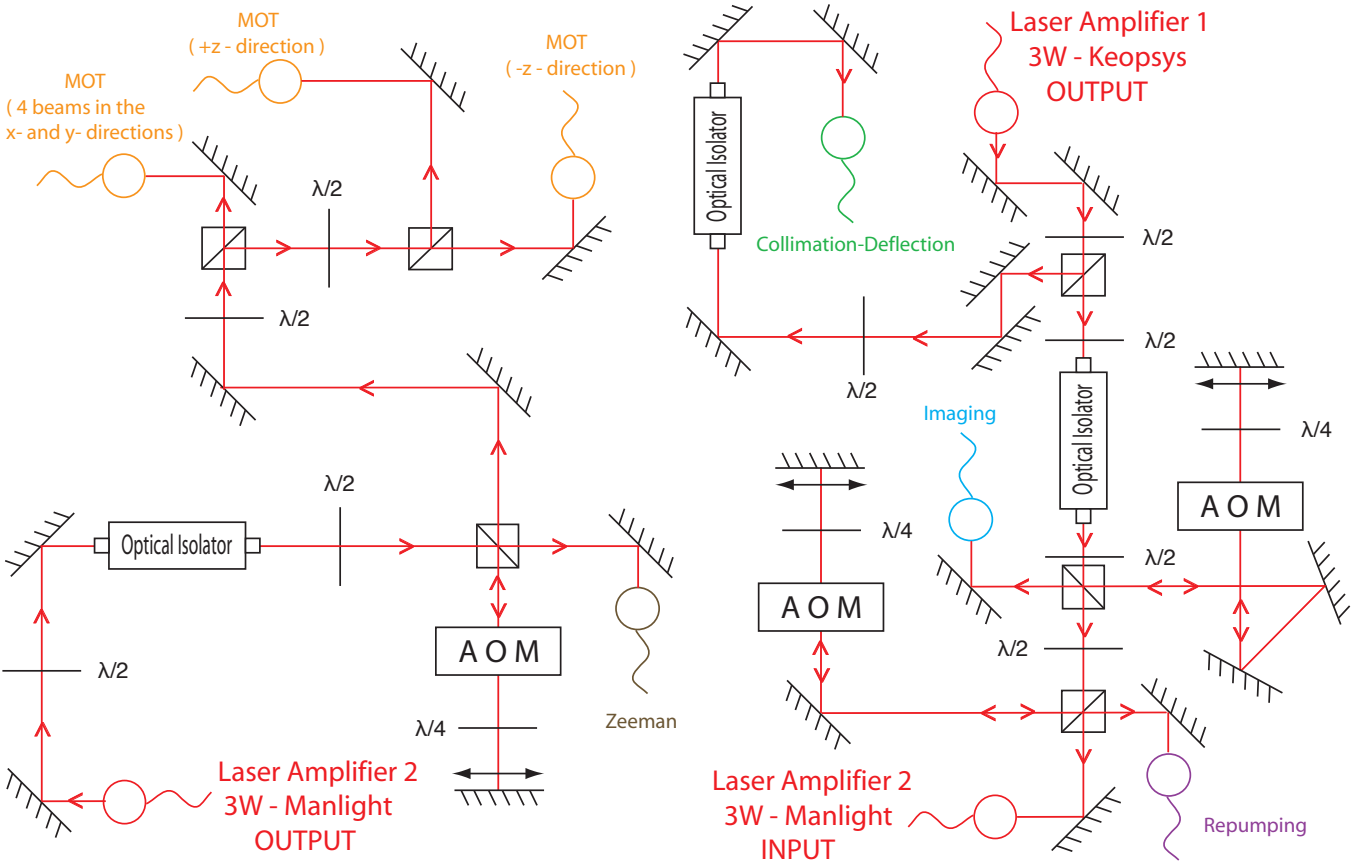
Figure 6.4: Main optical setup used to create all required optical beams. The output of amplifier 1 provides 3 W of light which is used for collimation, deflection, imaging as well as for injecting a second laser amplifier (amplifier 2 input). This second amplifier provides enough power for both the Zeeman and MOT beams.

- the repumping beam which is used to optimize the Zeeman slower stage (see section 6.2.7) and is also double-passed through an AOM to adjust its frequency.

- the input beam of a second 3W (PM) fiber-amplifier (Amplifier 2) from Manlight.

The laser output of amplifier 2 is also split to provide:

- the Zeeman Slower beam which remains at the frequency of the laser diode, shifted -240 MHz away from the atomic transition (see section 6.2.5).

- the two MOT beams in the z-direction as well as a beam which will be used for the 4 MOT beams in the vertical plane orthogonal to the z-axis (see section 6.2.7). The frequency of these beams is shifted close to resonance using an AOM.

6.2.3   The source of atoms

In chapter 2, loading a magneto-optical trap directly from a vapor of ^{87}Rb atoms initially in the ground state is described. However, a somewhat different approach is used to load a MOT of helium and initially requires creating He* metastable atoms. This is performed using an electrical discharge between an anode and a cathode. The discharge source of atoms is shown in figure 6.5 and consists of a cylindrical gas reservoir of boron nitride, a material with high heat conductivity as well as high electrical and chemical resistance. The external part of the boron nitride is pressed into a copper cylinder which is continuously cooled by liquid nitrogen. A copper flange, held by an electrically isolating support of araldite, closes the reservoir on the backside and serves as an inlet for the helium gas as well as a mount for the cathode. The front side of the boron nitride has a 0.4 mm diameter outlet which is directly connected to the anode, an aluminium plate with a similar 0.4 mm hole in its center. An intense, continuous discharge is produced between the two electrodes by applying a 2 kV voltage onto the cathode while the anode is kept at a ground potential. After undergoing electronic collisions, a fraction (between 10^{-4} and 10^{-6}) of the helium atoms (in the initial 1^1S_0 ground state) is excited to upper states before decaying to the long-lived metastable 2^3S_1 state. For efficient production of metastable helium atoms, many parameters are involved such as the He gas purity, pressure and temperature, the current of the discharge, the size of the boron nitride outlet, the cleanliness of both the cathode and the anode, and the respective alignment of the hollowed pieces (boron nitride, anode and skimmer). All these parameters were previously carefully optimized in our group [134] to obtain a good

trade-off between the highest flux from the source and moderate heating from the discharge. Although the source has been taken out and a few pieces have been changed (like the boron nitride piece or the cathode), optimal parameters remain approximately the same as the ones previously determined in [134]. In the experiment, the gas reservoir is filled with helium gas to a pressure of about 4×10^{-5} mbar, and a current of 6 mA is chosen for the discharge. Under optimal conditions, the source ensures a high flux ($\sim 10^{14}$ atoms.s^{-1}.sr^{-1}) of triplet metastable helium atoms which are accelerated and escape from the reservoir in a diverging beam with a mean longitudinal velocity of approximately 1000 m.s^{-1}.

The setup was improved in order for the source to be moved mechanically in all three spatial directions (x, y, z) with very high accuracy. For that purpose, the araldite support is attached to three translation stages and micrometric displacement of each translation stage is provided by rotating flexible cables. The torsion of each cable is controlled independently from outside the chamber and is converted into translation displacements by toothed wheels meshing with endless screws. The output of the source can thus be precisely aligned to the skimmer in order for the atoms to enter the collimation-deflection chamber. A vertically movable Faraday cup (detector 1 in figure 6.2), located 1.2 m away from the skimmer, is used to monitor the intensity of the metastable helium beam and optimize the alignment of the system as well as other important parameters. On the surface of the detector, an atom in the $2^3 S_1$ excited state can release its internal energy and extract an electron. This process is very efficient and the increase in the metastable flux is measured from the resulting current on a picoammeter, connected to the Faraday cup.

6.2.4 Collimation-Deflection

The need for ultra high vacuum in BEC experiments requires that the intense He beam of atoms remaining in the ground state ($1^1 S_0$) is prevented from reaching the quartz cell. Since the metastable beam (created from the discharge) initially merges with the ground-state beam (which did not experience the discharge), it is therefore advantageous to spatially separate them. This is done by taking advantage of the sensitivity of He* atoms to resonant light at 1083 nm in contrast to ground-state He atoms which are insensitive to this wavelength. Consequently, not only is it possible to collimate the initially diverging beam of metastable atoms using radiation pressure forces, but one can also deflect the atoms and modify their trajectory. The general principle is described in figure 6.6. The effusive beam of atoms coming out of the source has a uniform spatial profile which allows for collimation of only the metastable beam to be performed slightly
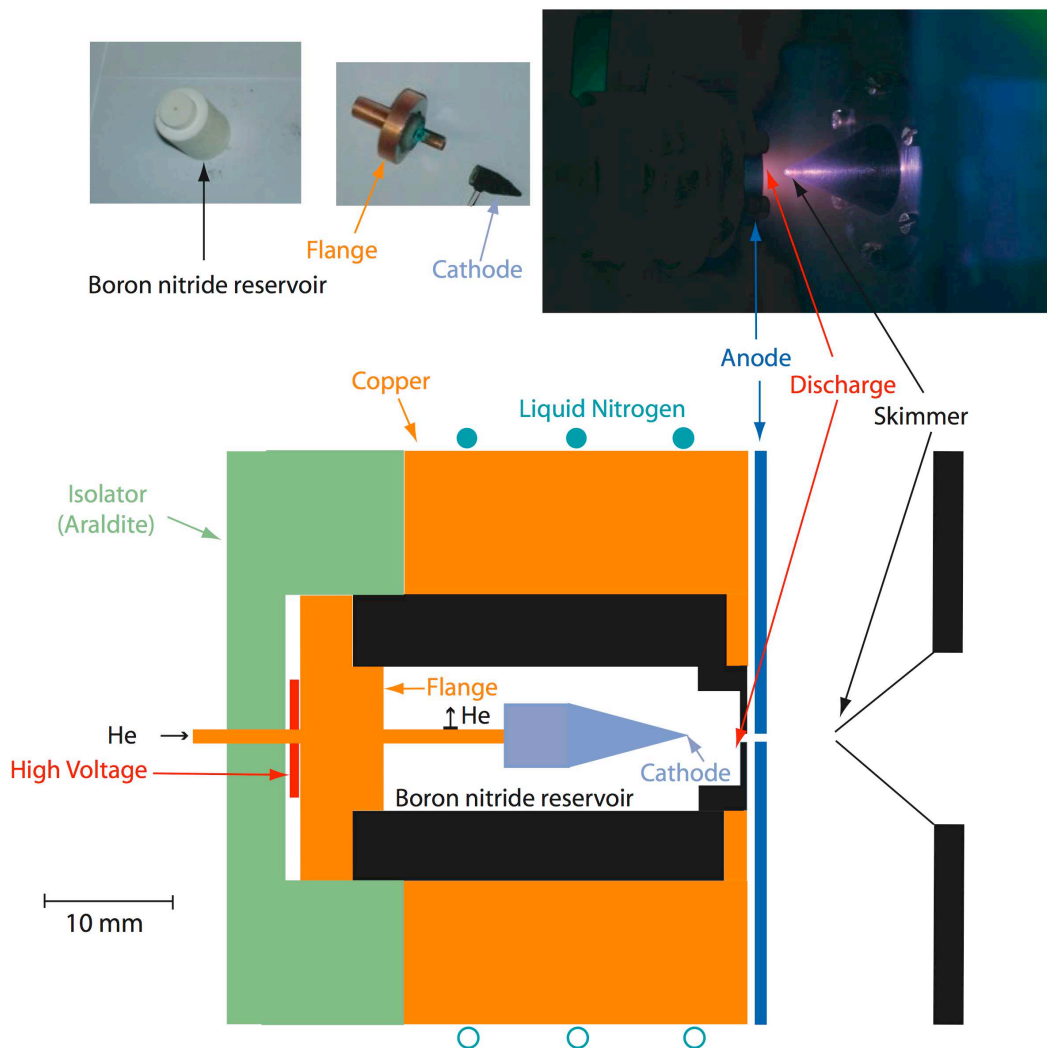
Figure 6.5: Compact discharge source of metastable helium atoms. The top pictures show the boron nitride reservoir, the cathode and its flange, as well as the discharge, just before the skimmer. The bottom drawing represents the discharge source. The boron nitride reservoir as well as the metallic anode are cooled by liquid nitrogen.

off axis. Two apertures (a 5 mm diameter diaphragm and the 1 cm diameter differential pumping tube at the entrance of the Zeeman Slower) selectively block the He atoms whereas the He* beam is carefully deflected to enter the Zeeman Slower.

The collimation-deflection optical layout was largely improved from the previous arrangement. In particular, all the optics are now set on a very stable platform attached on top of the

Source
(Discharge)

Source
(Collimation-Deflection)

To Zeeman Slower

Collimation

Deflection

Metastable Helium

Ground state Helium gas

Differential Pumping Tube

Skimmer

Diaphragm

Figure 6.6: Scheme used for separating the beam of metastable atoms from atoms in the He ground-state. First, the metastable atoms are collimated to reduce the initial divergence. Second, the beam of metastable atoms is deflected to enter the differential pumping tube of the Zeeman Slower whereas atoms in the ground-state are selectively blocked and pumped out of the vacuum system.

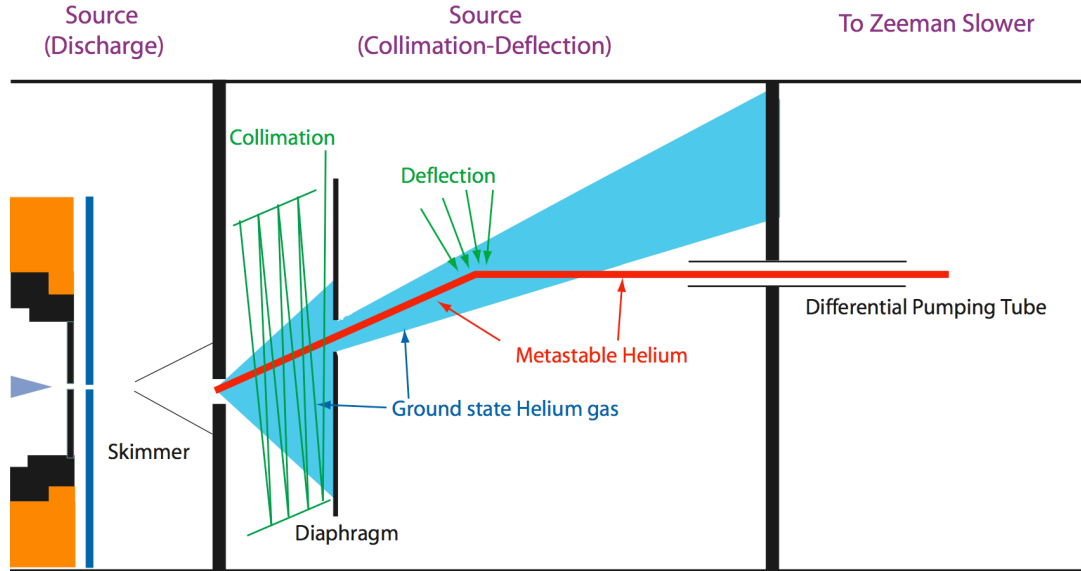Source chamber and the light is transported from the main optical table using a fiber which reduces the propagation in free space and improves the beam profile. A total power of ~ 700 mW is extracted from the output light of amplifier 1, which is sent to the collimation-deflection stage via a PM single-mode (SM) optical fiber. The resulting beam (~ 350 mW) double-passes an AOM in order to shift its frequency by $+240$ MHz, back to resonance with the atomic transition. The remaining power (~ 270 mW) is subsequently split in three beams; for vertical collimation, horizontal collimation and deflection (see figure 6.7).

In order to collimate the atomic beam for each transverse direction, we use a "zig-zag" configuration where the resonant laser beam ($P \sim 50$mW and $\oslash = 1$ cm) is multi-reflected between two mirrors (3×15 cm) and crosses the atoms about 10 times. The collimation process is done slightly off axis ($1°$ upwards with respect to the horizontal), as shown in figure 6.6.

To deflect the collimated beam, a cylindrical telescope is used to produce an elongated (2×8 cm) laser beam ($P \sim 100$ mW) that is slightly converging in order to account for the change in

Doppler effect during the deflection process. The deflection angle is given by $\theta \sim L/R \sim 1°$ where $R = 5$ m is the curvature of the beam and $L = 8$ cm its longitudinal dimension. The direction of the propagating beam of metastable helium atoms is consequently brought back to the horizontal in order for the atoms to pass through the entire Zeeman setup and reach the quartz cell. A second Faraday cup (detector 2 in figure 6.2), located 2.4 m away from the differential pumping tube entrance, is used to optimize the flux of the collimated-deflected beam.
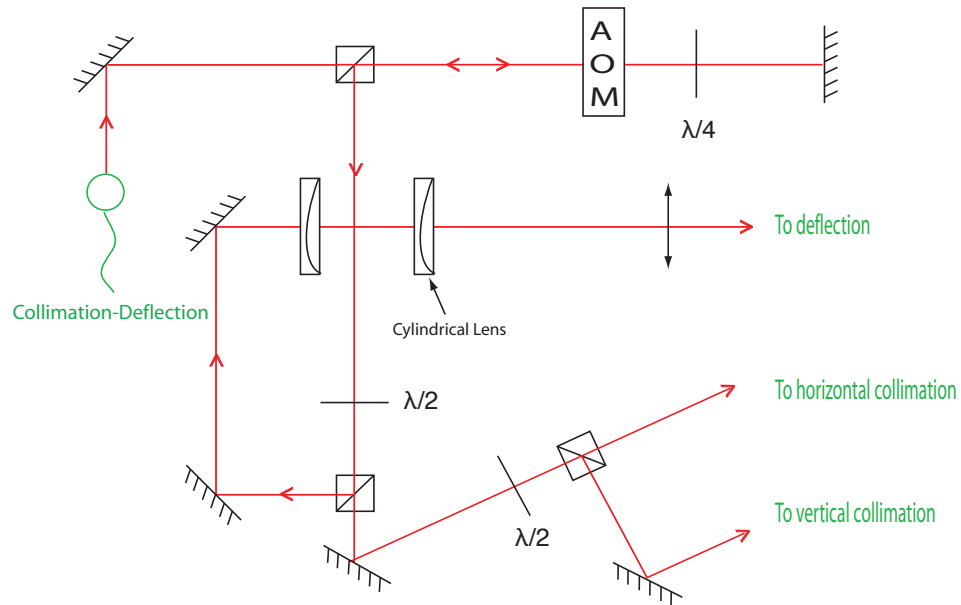
Figure 6.7: Schematic of the optical setup used to create the laser beams for collimation and deflection. These beams are on resonance with the $2^3S_1 \rightarrow 2^3P_2$ atomic transition.

6.2.5 The Zeeman Slower

As mentioned in section 6.2.3, the beam of He* atoms created by the discharge escapes the reservoir with a typical longitudinal velocity of approximately 1000 m.s^{-1}, which is much higher than standard capture velocities in a MOT (~ 100 m.s^{-1}). Consequently, the metastable helium beam is preliminarily decelerated by a Zeeman slowing technique [135]. For that purpose, a laser beam enters the quartz cell before propagating in the two Zeeman slowers, anti-parallel to the atomic beam. To create this Zeeman beam, ~ 300 mW from the output power of amplifier 2 is used to inject a PM-SM optical fiber (see figure 6.4). The fiber output beam is expanded to a

diameter of approximately 2 cm before entering the cell. The light polarization is made circular σ^+ in order to induce optical transitions between the two Zeeman sub-levels $2^3S_1, m_J = +1 \rightarrow 2^3P_2, m_J = +2$ when the resonance condition

$$\omega_a(z) = \omega_L - \mathbf{k}_L \cdot \mathbf{v}(z) \tag{6.3}$$

is satisfied, with $\mathbf{v}(z)$ the velocity vector of an atom, $\mathbf{k}_L$ and ω_L the wave-vector and frequency of the laser beam and $\omega_a(z)$ the resonance frequency of the $2^3S_1, m_J = +1 \rightarrow 2^3P_2, m_J = +2$ transition. During the slowing process, the velocity of the atom is progressively reduced, varying the Doppler shift and thus changing the resonance condition. It is however possible to compensate the changes in the Doppler effect by the energy shift due to an external magnetic field $B(z)$. In such a field, the resonance frequency $\omega_a(z)$ is shifted from the atomic transition frequency ω_0 giving:

$$\omega_a(z) = \omega_0 + (g_P m_{J_P} - g_S m_{J_S}) \frac{\mu_B B(z)}{\hbar} \tag{6.4}$$

where $g_P = 3/2$ and $g_S = 2$ are the Landé factors of the 2^3P_2 excited state and of the 2^3S_1 metastable state respectively and $m_{J_P} = +2$ and $m_{J_S} = +1$ the respective magnetic moments of these two states.

Consequently, the resonance condition to be maintained along a Zeeman slower can be expressed as:

$$\delta_{ZS} + k_L v(z) = \frac{\mu_B B(z)}{\hbar} \tag{6.5}$$

where $\delta_{ZS} = \omega_L - \omega_0$ is the laser detuning from the atomic transition. In our experiment, the laser detuning is fixed to $\delta_{ZS} = -2\pi \times 240$ MHz and the initial Doppler shift for atoms entering the Zeeman slower at $v_i \sim 1000$ m.s^{-1} is compensated by a magnetic field $B_i = 540$ G. Assuming a constant deceleration a along both Zeeman slowers, the velocity of the atoms can be written as $v(z) = \sqrt{v_i^2 - 2a(z - z_i)}$ and a non-homogeneous magnetic field configuration is designed for the process to be resonant with this condition all along the path as shown in figure 6.8.

In the experiment, the first Zeeman slower is a cylindrical tube ($\oslash = 2.2$ cm, $L \sim 2$ m) on top of which are wound 20 independent layers of copper wire ($\oslash = 2$ mm) powered by a 3 A current to create the parabolic magnetic field from 540 to 0 G. The atomic velocity is approximately reduced to $v \sim 300$ m.s^{-1} before entering the second Zeeman slower tube ($\oslash = 40$ mm, $L = 15$
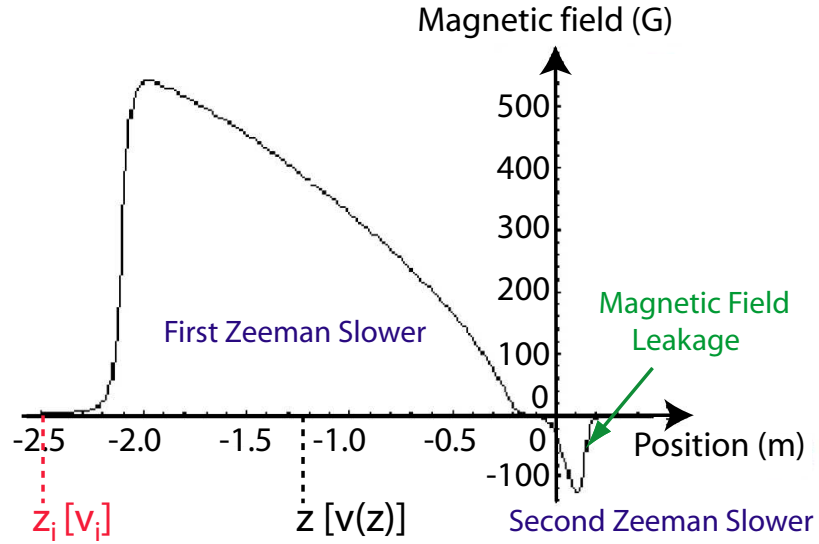
Figure 6.8: Magnetic field configuration in both Zeeman slowers, calculated from the Biot-Savart law [130].

cm) on which 10 layers of copper wire are wound and operated by 4 A of current in a direction opposite to that of the first Zeeman slower, creating the appropriate ($B = 0 \rightarrow -140$ G) field to slow the atoms down to a final velocity of ~ 40 m.s^{-1}. Finally, a compensation coil ($\oslash = 12$ cm, 70 turns, 3 A) minimizes the magnetic field leakage (see figure 6.8) from the second Zeeman slower into the cell region. Control and optimization of the successive decelerations was performed using the channeltron located in the quartz cell (see following section).

There are three reasons why we use a double-Zeeman configuration with a magnetic field between 540 and -140 G rather than a single Zeeman slower starting at $B_i \sim 700$ G. The first one is practical and consists of limiting the heating in the coils so that standard water cooling techniques are still efficient. The second reason relates to the physics of the He atom. It can be shown that in a magnetic field of 600 G, the transitions $2^3S_1, m_J = +1 \rightarrow 2^3P_2, m_J = +2$ and $2^3S_1, m_J = +1 \rightarrow 2^3P_1, m_J = 0$ are degenerate. Although a σ^+ laser polarization should only allow transitions to the $2^3P_2, m_J = +2$ Zeeman sub-state, the laser polarization is never perfect and possible transitions to the $2^3P_1, m_J = 0$ state can complicate the physics of the slowing process and result in losses in the total number of atoms that can be trapped in the quartz cell. FInally, using a non-zero field at the end of the second Zeeman slower also allows the Zeeman beam to be far-detuned from the atomic transition and to limit its effect on the atoms trapped in

the 3D MOT. Consequently, the use of a second Zeeman slower allows us to work with an initial magnetic field which is lower than 600 G while keeping an appropriate magnetic gradient along the path.

6.2.6 Channel Electron Multiplier (Channeltron)

At the end of the Zeeman slower, just before the quartz cell, a channeltron is placed (see figure 6.9a). Channel Electron Multipliers (CEMs or channeltron) are detectors with a high surface resistance responding to charged particles (typically ions or electrons). When a potential (~ 3 kV in our experiment) is applied between the input and the output end of the CEM, the resistive surface forms a continuous 'dynode' which has the property of emitting secondary electrons when primary particles impinge upon it. This process is called secondary electron emission and allows the channeltron to detect a single particle that has entered the input aperture. Indeed, any incoming particle will generate secondary electrons that are accelerated down the channel by a positive bias. Upon striking the interior surface of the channel walls, these electrons generate further electrons. The resulting avalanche process produces an easily detectable output pulse containing up to 10^8 electrons for each incident particle with a duration (Full Width Half-Maximum) of approximately 8 ns and a dark count rate of less than 0.02 cps. Consequently, individual pulses produced from the avalanche process can be monitored on an oscilloscope or a photon counter.

A cut view of a typical CEM as used in our experiment is shown in figure 6.9b. The supporting body of the channeltron is made of ceramic material and the black channel is a lead glass with a secondary electron emitting surface. The electron avalanche generated by a primary particle follows the channel to the positively charged end and is collected by an anode providing the output signal. The curvature of the channel is necessary to prevent ion feedback due to the high electron density at the end of the channel. In a straight channel, ions would acquire too much kinetic energy and generate additional secondary electrons leading to an unstable operation of the channeltron.

The channeltron can be used as a very efficient detection method in our experiment where He ions are easily produced due to Penning or background collisions. First, it is possible to measure the velocity of the atoms entering the glass cell, taking advantage of the ions produced when a metastable He atom collides with the walls of the glass cell. Typical experimental signals are shown in figure 6.10 where a pulse of metastable atoms was sent through the Zeeman slower stage. Such a pulse of atoms was produced from the discharge by modulating the RF power
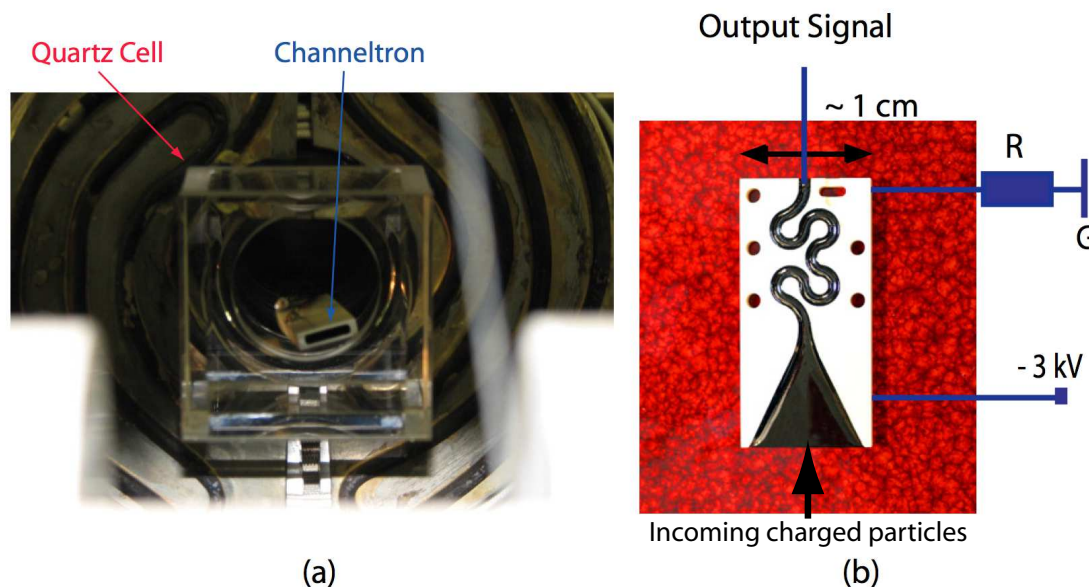
Figure 6.9: a) Picture of the channeltron, located just before the quartz cell where the atoms are trapped. b) Cut view of the channeltron, showing the external ceramic structure and the lead glass channel where the electron avalanche occurs.

of the collimation-deflection AOM. The output signal of the channeltron was monitored on an oscilloscope and recorded in both cases: when the first Zeeman slower stage is turned on (solid black curve) or off (solid red curve). The velocity of the atoms can be deduced from each of these signals by considering a constant deceleration in the Zeeman slower. It is thus possible to control and optimize the successive decelerations induced by both Zeeman slowers (a similar curve is obtained when the second Zeeman slower is also switched on). Additionally, in the case of an atomic cloud which would be confined in either a magnetic or optical trap, it is possible to detect individual ions emitted from Penning collisions processes. This detection method is planned to be used for the two experiments described in chapters 7 and 8.

6.2.7   The MOT

- Laser Beam Geometry: Our scheme aims to trap the spin-polarized helium gas ($He^* \uparrow$) at the center of a quartz cell of dimension 5cm×5cm×4cm (see figure 6.11). The MOT beams are 3 pairs of counter-propagating laser beams of opposite (σ^+/σ^-) polarization

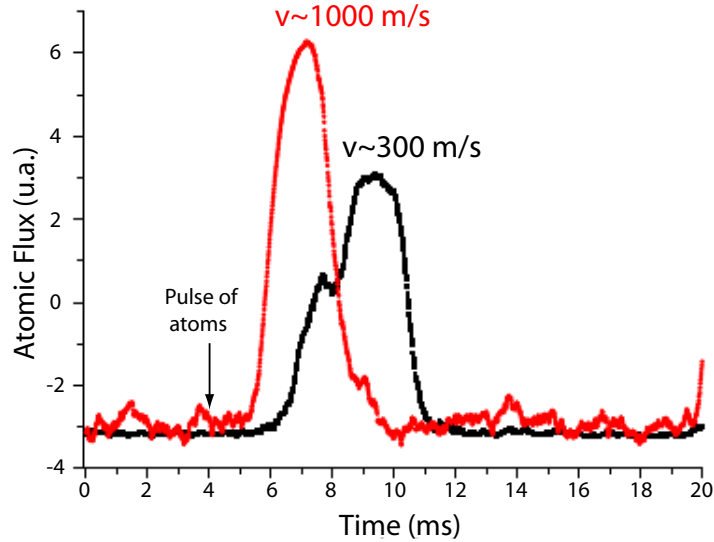Figure 6.10: Effect of the first Zeeman slower on the atoms, measured using the channeltron. In red is the atomic signal without Zeeman slowing whereas the black curve corresponds to an atomic jet which has experienced longitudinal cooling. The shoulder of the black curve represents a fraction of atoms which do not experience the slowing effect and cannot be trapped in the MOT.

and crossing at the center of the cell. Four of these beams are in a plane orthogonal to the z-axis of the experiment whereas the two additional MOT beams along the z-direction are almost superimposed with the Zeeman slowing beam and the atomic beam. A σ^+ MOT beam enters the Zeeman chamber by a side viewport at the entrance of the first Zeeman slower and is directed towards the $+z$-direction by a mirror at 45° as shown in figure 6.2. It propagates all the way through both Zeeman slowers before reaching the glass cell. The σ^- MOT beam propagates in the $-z$-direction after it has been combined with the Zeeman beam on a polarizing beam-splitter.

The MOT beams are produced from the output of amplifier 2 (see figure 6.4) which is initially shifted -240 MHz away from the atomic resonance. A fraction of the output power is used to produce the Zeeman beam (see section 6.2.5) whereas the remaining light creates the MOT beams after double-passing an AOM in order to shift the laser frequency closer to resonance ($\delta_{MOT} \sim -40$ MHz). The light is subsequently split into three beams which inject independent PM single-mode optical fibers. Two of these fibers are redirected to each end of the Zeeman slower system to produce the two MOT beams along the $+z/-$
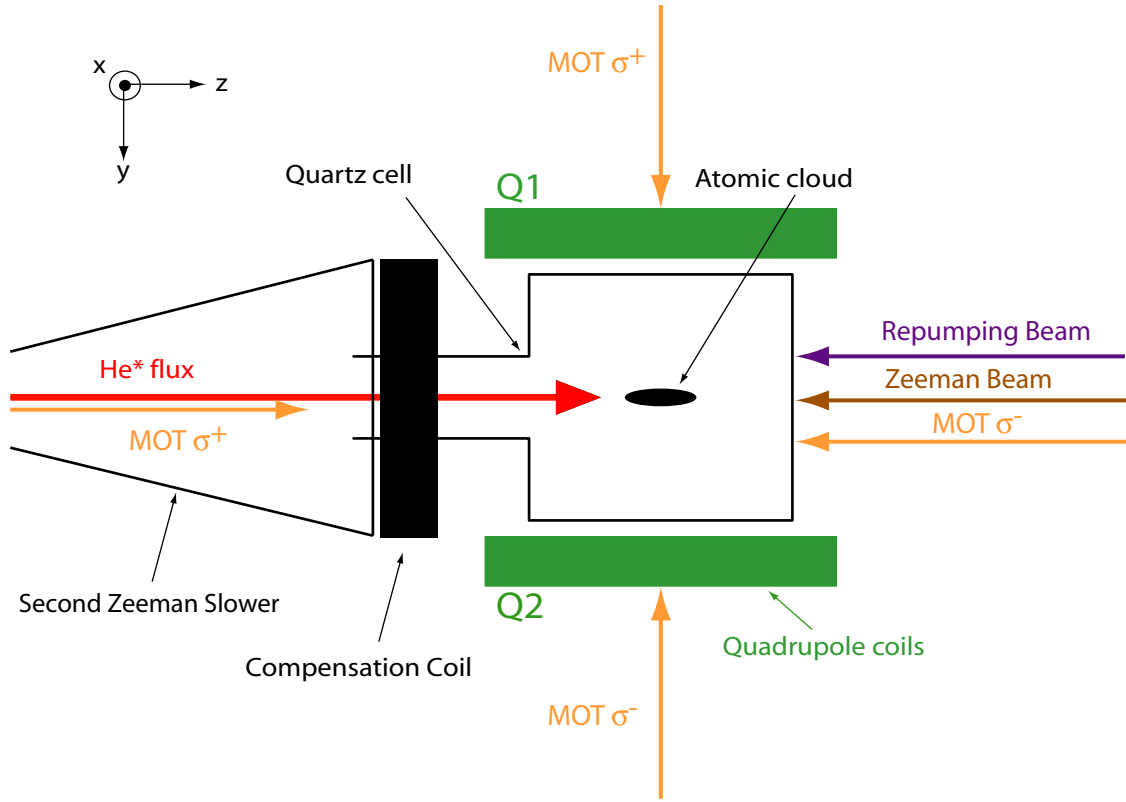
Figure 6.11: Schematics of the MOT. The 6 optical MOT beams (only 4 are visible in the plane of the figure) intersect at the center of the quartz cell. The Zeeman and repumping beams are also shown. The quadrupolar magnetic field is created by the two coils Q_1 and Q_2.

z-axis respectively. The last fiber is redirected towards the glass cell where an additional optical setup (see figure 6.12) produces four MOT beams in a vertical plane, orthogonal to the z axis. All MOT beams are expanded ($\oslash = 2$ cm) in order to capture a large number of atoms and their polarization is adjusted to be σ^+ or σ^- using quarter wave-plates.

In this geometry, both the σ^+ and σ^- beams along the z-axis can affect the slowing process as explained in [136]. On one hand, the σ^+ MOT beam parallel to the atomic beam (see figure 6.12), can introduce transitions to the $2^3P_2, m_J = +2$ state and thus accelerate the atoms when they reach the velocity $v \sim 100$ m.s^{-1} (which occurs before the end of the second Zeeman slower). Consequently, the intensity of the Zeeman slowing beam must be adjusted in order to be higher than the intensity of the σ^+ MOT beam. On the other hand, the σ^- MOT beam can induce transitions to the $2^3P_2, m_J = 0$ sub-level, which depolarizes
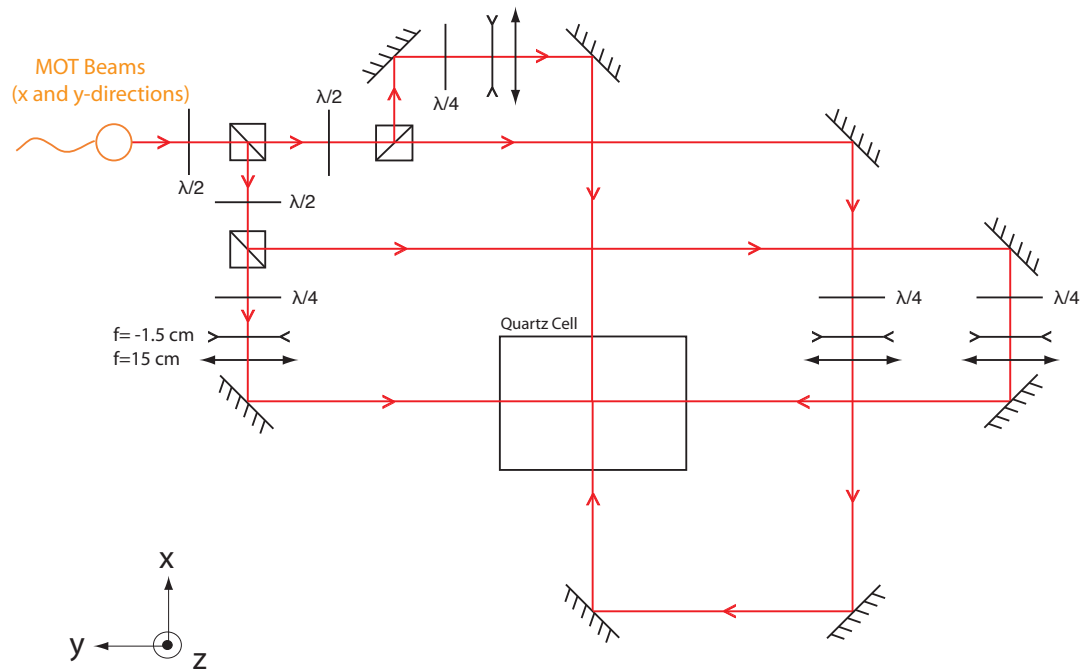
Figure 6.12: Schematic of the MOT beams in the vertical xy-plane. The third pair of beams along the z-direction is not represented. The power balance can be adjusted using half wave-plates and polarizing beam-splitters. Each MOT beam is expanded 10 times in a telescope.

the atoms if they subsequently decay to the $2^3S_1, m_J = 0$ or $2^3S_1, m_J = -1$ sub-levels. The process is resonant when $v \sim 200$ m.s^{-1} which, again, occurs before the end of the second Zeeman slower. Re-pumping light thus needs to be used in order to optimize the slowing process [136]. Finally, the MOT beams must be far-detuned (~ -40 MHz) from the atomic resonance in order to reduce the process of light induced Penning collisions [133, 137] which would result in losses of atoms.

- MOT Coils: The magneto-optical trap utilizes magnetic confinement simultaneously to the optical configuration described above. The magnetic field is created by using two magnetic coils (Q1 and Q2 in figure 6.11) with currents flowing in opposite directions. The two cylindrical coils are separated by 5.2 cm along the y-axis and create a quadrupolar field with a magnetic gradient of 40 G/cm along the symmetry axis for a given current of 5 A.

6.2.8 Magnetic trap and evaporative cooling

Further cooling is achieved by evaporation after transfer of the atoms in a non-dissipative magneto-static trap producing a Ioffe-Pritchard type magnetic field [138] similar to the one described in chapter 2. The QUIC configuration creating such a field is shown in figure 6.13 and involves 5 coils: Q1 and Q2 produce a quadrupolar field whereas B3 allows for a non-zero B_0 magnetic field at the center of the trap (called the 'bias field') and two additional coils H1 and H2, in a Helmoltz configuration, are used to adjust the bias field B_0.
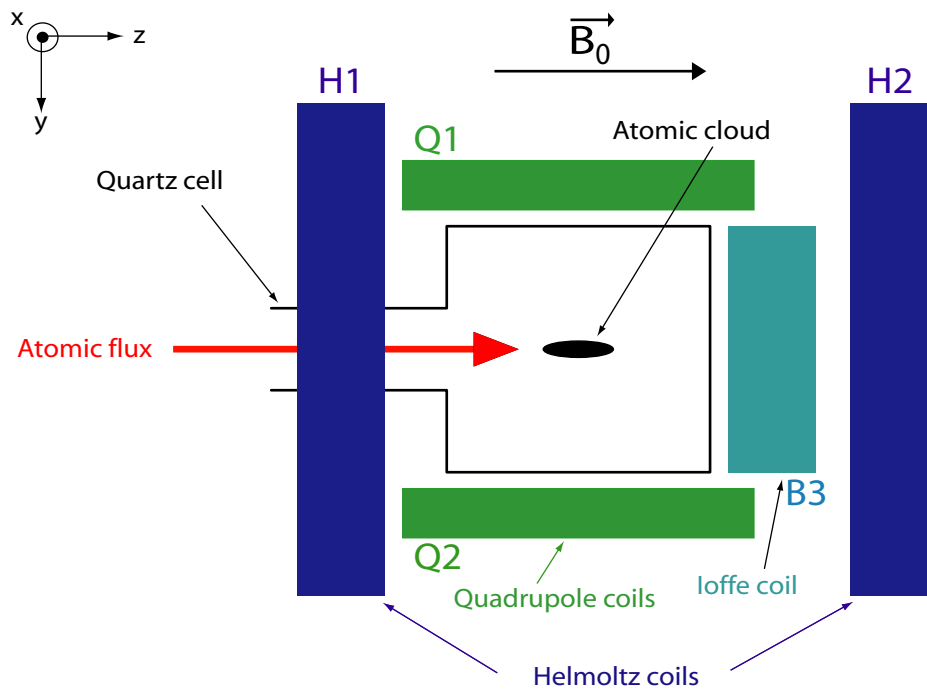
Figure 6.13: Schematics of the magnetic trap, where Q_1, Q_2 and B_3 form the Ioffe-Pritchard trap whereas H_1 and H_2 are the Helmoltz coils that can compensate the bias field B_0.

Atoms with a magnetic moment anti-parallel to the magnetic field (spin $m_J = +1$) are trapped in the region of minimal potential whereas atoms with $m_J = 0$ and $m_J = -1$ spin states are respectively un-trapped and expelled from the center of the trap. In the vicinity of the minimum B_0 of the magnetic field produced by these 5 coils, the magnetic field is inhomogenous and can be written to second order as [139]:

$$\vec{B}(x,y,z) = \begin{pmatrix} 0 \\ 0 \\ B_0 \end{pmatrix} + B' \begin{pmatrix} -x \\ y \\ 0 \end{pmatrix} + \frac{B''}{2} \begin{pmatrix} -xz \\ -yz \\ z^2 - \frac{1}{2}(x^2+y^2) \end{pmatrix} + O(3)\,, \tag{6.6}$$

where only the second order terms are significant in the three spatial directions. B_0, B' and B'' are the bias, gradient and curvature of the magnetic field respectively and the field modulus can be written as:

$$B(x,y,z) = \sqrt{\left(B_0 + \frac{B''}{2}\left(z^2 - \frac{1}{2}(x^2+y^2)\right)\right)^2 + B'^2(x^2+y^2)} + O(4).$$

When $B''z^2 \ll B_0$ and $B'x$, $B'y \ll B_0$ are satisfied, the previous expression can be approximated by a harmonic anisotropic field following:

$$B(x,y,z) = B_0 + \frac{B''}{2}z^2 + \left(\frac{B'^2}{2B_0} - \frac{B''}{4}\right)(x^2+y^2)\,.$$

If the size of the cloud is small enough compared to the spatial variations of the B field (B_0/B' and $\sqrt{B_0/B''}$), the magnetic field is harmonic close to the center of the trap, and the modulus of the trapping potential $W(\vec{r}) = -\vec{\mu} \cdot \vec{B}(\vec{r})$ becomes:

$$W(x,y,z) = g_J m_J \mu_B B_0 + \frac{1}{2}m\omega_z^2 z^2 + \frac{1}{2}m\omega_\rho^2(x^2+y^2)\,, \tag{6.7}$$

with the trapping angular frequencies defined as

$$\omega_z = \sqrt{\frac{g_J m_J \mu_B B''}{m}} \qquad \text{and} \qquad \omega_\rho = \sqrt{\frac{g_J m_J \mu_B}{m}\left(\frac{B'^2}{B_0} - \frac{B''}{2}\right)}\,. \tag{6.8}$$

In these expressions, $\mu = -g_J m_J \mu_B$ is the modulus of the magnetic moment of the atom with $g_J = 2$ the Landé factor in the $2^3 S_1$ state, m_J the projection of the total angular momentum of the atom and μ_B the Bohr magneton. m is the mass of the atom. This trapping potential has a cylindrical shape characterized by the two trapping frequencies ω_z and ω_ρ along the longitudinal and radial directions respectively.

When the temperature of the cloud gets too high ($k_B T \gg \mu B_0$) the previous approximation is not valid and although the trap stays harmonic in the z direction it is linear along x and y. However, in our experiment the temperature of the cloud is $\sim 10\,\mu\text{K}$, way below the limit $k_B T \simeq$

μB_0 of 400 μK. The trapping frequencies are $\omega_\rho \sim 2\pi \times 800Hz$ and $\omega_z \sim 2\pi \times 90Hz$ with a bias field of $B_0 = 3$ G and a trap depth in the order of 10 mK. Since $\omega_\rho > \omega_z$ the confinement is less important along the z axis and the cloud is elongated in this direction (see figure 6.13). Once the cloud is transferred from the magneto-optical trap into the magnetic trap, a final evaporative cooling stage is performed [140]. Trapped atoms (spin $m_J = +1$) of kinetic energy greater than $k_B T$ are transferred by an RF transition into the $m_J = 0$ and $m_J = -1$ states and thus removed from the trap. The average kinetic energy per atom is reduced and elastic collisions allow the cloud to rethermalize quickly. By ramping down the frequency of the RF field in about 10 s, we can condense the sample to typical temperatures of a few μK.

6.3 CONCLUSION

This is the exact setup which will be used to obtain a He* BEC. It was largely modified from the previous arrangement. In particular, the optical layout was entirely renewed and improved in terms of optical power and stability by using a combination of optical fibers and high power laser amplifiers. The vacuum system and the source of atoms were also optimized and a new detection method was added with the implementation of a channeltron. At the time of writing some progress has been made towards obtaining a He* BEC back and a MOT was reproduced recently. Once the BEC is obtained, an optical dipole trap will be implemented into the system. This is described in the following chapter.

CHAPTER 7

OPTICAL TRAPPING OF ^{4}HE ATOMS

The need for dense samples of cold atoms for applications such as high precision interferometry and spectroscopy, or studies of cold atomic collisions, has motivated the development of controllable trapping of neutral atoms. As presented in previous sections (see chapters 2 and 6), only atoms with $g_F m_F > 0$ (low-seeking states) can be confined in a magnetic trap. Other substates are either un-trapped or anti-trapped and, as a consequence, expelled from the magnetic region under gravitational and/or magnetic interactions. However, in some experiments, it could be of great interest to also trap these other sub-states in a conservative potential. On that matter, an optical trap is capable of confining neutral atoms regardless of their internal state, making it possible to explore properties of states (or mixtures of states) which cannot be controlled in a magnetic trap. In this case, the magnetic field is no longer a constraint of the experiment but rather an experimental parameter than can be freely varied without modifying the trapping conditions, which is another advantage. In this chapter, the general principle and properties of an optical trap are firstly presented and discussed (a complete review can be found in [141]). This is followed by a description of the laser configuration, based on a red-detuned dipole trap, which is currently being characterized in the lab and will soon be implemented on the setup described in chapter 6. Several experiments with He* are planned using an optical dipole trap, in particular a measurement of characteristic rate constants of inelastic decay processes in a gas of spin-polarized metastable helium (^{4}He* ↑), taking advantage of the freedom to change the external magnetic field. A brief synopsis on theoretical results predicted by Shlyapnikov *et al.* [128, 129] is thus finally summarized, together with an experimental sequence which will be used in order to achieve these measurements.

7.1 OPTICAL DIPOLE POTENTIALS

Neutral atoms interact with a light field in both dissipative and conservative ways. The dissipative component of the interaction arises from the absorption of photons followed by subsequent spontaneous emission. The resulting dissipative force on the atoms is caused by the momentum transfer of the absorbed and spontaneously emitted photons. When the light is close to resonance

with the optical transition of interest, the resulting force is intense and can be used for laser cooling and magneto-optical trapping as discussed in previous chapters. In contrast, the conservative component of the atom-light interaction arises from the interaction of the light field with the light induced dipole moment of the atom. This interaction causes a shift in the potential energy, also called the ac-Stark shift. For large detunings of the light-frequency away from the atomic resonance, effects of spontaneous emission can be neglected and the energy shift can be used to create a conservative trapping potential for neutral atoms [142, 143].

The following sections provide two simple models to understand the conservative optical dipole trapping of neutral atoms. In a first step, the relevant parameters of a dipole trap (the dipole potential and the photon scattering rate) can be derived from a simple, classical oscillator model. Alternatively, a dressed state picture, yielding similar results, can take into account the multi-level structure of the atom.

7.1.1 Oscillator Model

The origin of the dipolar potential can be thought of in a number of ways. A classical model is described here, where the atom is considered as a harmonic oscillator driven by a light field [141]. This simple model is useful to understand the basic physics of dipole trapping.

7.1.1.1 Interaction with a light field

When an atom is placed in a laser light field, the electric field $\mathbf{E}$ induces an atomic dipole moment $\mathbf{d}$ that oscillates at the driving frequency ω_L of the field. In the usual complex notation one can write $\mathbf{E}(\mathbf{r},t) = \hat{\mathbf{u}}\, E(\mathbf{r}) exp(-i\omega_L t) + c.c.$ and $\mathbf{d}(\mathbf{r},t) = \hat{\mathbf{u}}\, d(\mathbf{r}) exp(-i\omega_L t) + c.c.$ where $\hat{\mathbf{u}}$ is the unit polarization vector of the electric field. The amplitude d of the dipole moment and the amplitude E of the light field are related via

$$d(\mathbf{r},t) = \alpha(\omega_L)E(\mathbf{r},t) \tag{7.1}$$

where $\alpha(\omega_L)$ is the complex polarizability of the atom. The resulting dipolar potential of the induced dipole moment $\mathbf{d}$ in the driving field $\mathbf{E}$ is determined by time averaging of $\mathbf{d}.\mathbf{E}$ over the rapid oscillating terms, yielding:

$$U_{dip}(\mathbf{r}) = -\frac{1}{2}\langle \mathbf{d}.\mathbf{E} \rangle = -\frac{1}{2\varepsilon_0 c}\Re(\alpha)I(\mathbf{r}). \tag{7.2}$$

In this equation, the factor $\frac{1}{2}$ reflects the fact that the dipole moment is induced (not permanent) and the laser field intensity is defined by $I = 2\varepsilon_0 c|E|^2$ with ε_0 the vacuum permittivity. The potential energy of the atom is thus proportional to the laser intensity as well as the real part of the polarizability ($\mathfrak{R}(\alpha)$).

Alternatively, the power absorbed by the oscillator results from the imaginary part of the polarizability ($\mathfrak{I}(\alpha)$) giving

$$P_{abs}(\mathbf{r}) = \langle \dot{\mathbf{d}}.\mathbf{E} \rangle = \frac{\omega_L}{\varepsilon_0 c} \mathfrak{I}(\alpha)I(\mathbf{r}). \tag{7.3}$$

Considering the light field as a stream of individual photons of energy $\hbar\omega_L$, the absorption process can be thought of as absorption-spontaneous emission cycles with a scattering rate defined by

$$\Gamma_{sc}(\mathbf{r}) = \frac{P_{abs}(\mathbf{r})}{\hbar\omega_L} = \frac{1}{\hbar\varepsilon_0 c}\mathfrak{I}(\alpha)I(\mathbf{r}). \tag{7.4}$$

7.1.1.2 Atomic Polarizability

The expressions obtained above are very general since they are valid for any polarizable neutral particle in an oscillating light field. They depend only on the position-dependent intensity $I(\mathbf{r})$, characterizing the light field, and on the polarizability $\alpha(\omega_L)$, characterizing the atom. $I(\mathbf{r})$ is fully determined by the laser configuration (e.g. a focussed Gaussian laser beam in section 7.2.1). Classically, one can calculate $\alpha(\omega_L)$ using Lorentz's model of a classical oscillator, where an electron is considered elastically bound to the core of an atom and where the dipole radiation of the accelerating electron can be thought of as a damping term (γ). The resulting expression can be written as [141]:

$$\alpha(\omega_L) = 6\pi\varepsilon_0 c^3 \frac{\gamma/\omega_0^2}{\omega_0^2 - \omega_L^2 - i(\omega_L^3/\omega_0^2)\gamma}. \tag{7.5}$$

In this equation, ω_0 is the resonance frequency of the oscillator model and γ is the on-resonance classical damping rate due to the radiative energy loss which can be expressed [144] as

$$\gamma = \frac{e^2\omega_0^2}{6\pi\varepsilon_0 m_e c^3} \tag{7.6}$$

where m_e is the electron mass and e is the elementary charge. For many atoms with a strong dipole-allowed transition, this classical formula usually provides a good approximation to the

spontaneous decay rate (or natural linewidth Γ) of the excited state and $\gamma \sim \Gamma$.

An alternative, and more appropriate method to calculate the atomic polarizability is to use a semi-classical approach where the atom is treated as a two-level quantum system interacting with a classical field. In this model, one can introduce the saturation parameter s defined as

$$s = \frac{\Omega^2/2}{(\omega_L - \omega_0)^2 + \Gamma^2/4} \tag{7.7}$$

where Γ is the natural linewidth of the transition and $\Omega = d.E/\hbar$ is the Rabi frequency. If the detuning $(\omega_L - \omega_0)$ is large enough, saturation effects can be neglected ($s \ll 1$) and the calculation yields the same result as equation 7.5. However, in general, the damping rate γ can no longer be calculated using formula 7.6 but is rather determined by the dipole matrix element between the ground $|g\rangle$ and excited states $|e\rangle$ of the two-level atom, corresponding to the spontaneous decay rate of the excited level, following

$$\Gamma = \frac{\omega_0^3}{3\pi\varepsilon_0\hbar c^3} |\langle e|\hat{\mu}|g\rangle|^2 \tag{7.8}$$

where $\hat{\mu} = -e\hat{\mathbf{r}}$ represents the electric dipole operator.

7.1.1.3 Dipole Potential and Scattering Rate

In the case of large detunings and negligible saturation, the dipole potential and the scattering rate can finally be determined from equations 7.2 and 7.5 yielding

$$U_{dip}(\mathbf{r}) = -\frac{3\pi c^2}{2\omega_0^3} \left(\frac{\Gamma}{\omega_0 - \omega_L} + \frac{\Gamma}{\omega_0 + \omega_L} \right) I(\mathbf{r}) \tag{7.9}$$

$$\Gamma_{sc}(\mathbf{r}) = \frac{3\pi c^2}{2\hbar\omega_0^3} \left(\frac{\omega_L}{\omega_0} \right)^3 \left(\frac{\Gamma}{\omega_0 - \omega_L} + \frac{\Gamma}{\omega_0 + \omega_L} \right)^2 I(\mathbf{r}). \tag{7.10}$$

In most experiments, the detuning of the laser frequency from the atomic resonance ($\Delta = \omega_L - \omega_0$) is such that $|\Delta| \ll \omega_0$. Consequently, one can set $\omega_L/\omega_0 \approx 1$ and the term in $1/(\omega_L + \omega_0)$ can be neglected in the rotating-wave approximation. In this case, the general expressions for the dipole potential and the scattering rate simplify to

$$U_{dip}(\mathbf{r}) \approx \frac{3\pi c^2}{2\omega_0^3} \left(\frac{\Gamma}{\Delta} \right) I(\mathbf{r}) = \frac{\hbar\Gamma^2}{8\Delta} \frac{I(\mathbf{r})}{I_{sat}} \tag{7.11}$$

$$\Gamma_{sc}(\mathbf{r}) \approx \frac{3\pi c^2}{2\hbar\omega_0^3}\left(\frac{\Gamma}{\Delta}\right)^2 I(\mathbf{r}) = \frac{\Gamma^3}{8\Delta^2}\frac{I(\mathbf{r})}{I_{sat}} \tag{7.12}$$

where it can be convenient to introduce the saturation intensity $I_{sat} = \hbar\Gamma\omega_0^3/12\pi c^2$.

The basic physics of dipole trapping in far-detuned fields can be largely understood on the basis of these two equations:

- The dipole potential scales as $I(\mathbf{r})/\Delta$ whereas the scattering rate scales as $I(\mathbf{r})/\Delta^2$. Therefore, optical traps generally use large detunings and high laser intensities in order to minimize inelastic scattering processes and still create a conservative potential of reasonable trap depth. Experimentally, the proper detuning depends on the available laser power as well as the maximum scattering rate which can be tolerated.

- The sign of the detuning determines the sign of the optical dipole potential :

  - Blue-detuned trap: Above resonance ($\omega_L > \omega_0 \Leftrightarrow \Delta > 0$), the sign of the optical dipole potential is positive and the dipole interaction repels the atoms out of the field so that the potential minima correspond to the minima of the intensity. Experimentally it is not simple to surround a spatial region with repulsive laser light and the development of appropriate methods to produce the required repulsive trapping configurations (e. g. light sheets [145], hollow laser beams [146], evanescent waves [147]) has played a major role. This trap will not be described any further in the thesis as it will not be used in our setup.

  - Red-detuned trap: Alternatively, below resonance ($\omega_L < \omega_0 \Leftrightarrow \Delta < 0$), the sign is negative and the interaction attracts atoms into the light field so that potential minima are at positions of maximum intensity. Consequently, a single focused laser beam already constitutes a dipole trap confining the atoms in the waist region where the intensity is maximum. Details on the red-detuned laser configuration and of the resulting trapping potential which we plan to use in our experiment are given in section 7.2.

7.1.2 Dressed State Picture

An alternative description of the oscillator model is given by the dressed state picture [148] where a quantized light field (of n photons) interacts with an atom initially in the ground state

$|g\rangle$. This description is interesting because it can take into account the multi-level structure of the atom.

7.1.2.1 Two-Level Atom

In order to present the dressed-state picture, one can first consider a two-level atom initially in the ground state (with a zero internal energy), so that the unperturbed energy of the system is given by $\varepsilon_g = n\hbar\omega_L$. When the atom absorbs a photon from the light field, this energy becomes $\varepsilon_e = \hbar\omega_0 + (n-1)\hbar\omega_L = n\hbar\omega_L - \hbar\Delta$ with $\Delta = \omega_L - \omega_0$. The atom-light interaction couples the atom and the field and can be described by the Hamiltonian $H_{int} = -\hat{\mu}\mathbf{E}$ with $\hat{\mu} = -e\hat{\mathbf{r}}$ representing the electric dipole operator. The effect of the interaction can be determined with second order perturbation theory and is characterized by an energy shift of the ith state following

$$\Delta E_i = \sum_{j\neq i} \frac{|\langle j|H_{int}|i\rangle|^2}{\varepsilon_i - \varepsilon_j} \tag{7.13}$$

where ε_i and ε_j are the unperturbed energies of the ith and j^{th} states respectively. In the case of a two-level atom, the energy shift is thus simplified to

$$\Delta E_{g/e} = \pm \frac{|\langle g|\mu|e\rangle|^2}{\hbar\Delta}|E|^2 = \pm \frac{3\pi c^2}{2\omega_0^3}\left(\frac{\Gamma}{\Delta}\right)I(r) \tag{7.14}$$

where the plus and minus signs represent the case of the ground and the excited state respectively and where we have used the relation $I = 2\varepsilon_0 c|E|^2$ and equation 7.8 to substitute the dipole matrix element. This perturbative result shows that the optically induced shift (also known as the light shift or ac Stark shift) of the ground state exactly corresponds to the dipole potential of the two-level atom in the rotating wave approximation (equation 7.11). For large detunings, where the atom is almost always in the ground state, the effective dipole potential is consequently given by

$$U_{dip} = \Delta E_g = \frac{3\pi c^2}{2\omega_0^3}\left(\frac{\Gamma}{\Delta}\right)I(r) \tag{7.15}$$

which is the same expression as 7.11, obtained from the oscillator model.

7.1.2.2 Multi-Level Atom

The classical oscillator model, or the two-level model described above, does not take into account the complexity of the real multi-level internal structure of the atom. In fact, from equation

7.13, one can see that for a given ground state $|g_i\rangle$, transitions to all excited states $|e_j\rangle$ should be taken into account when calculating the ac Stark shift, with dipole matrix elements given by

$$\mu_{ij} = \langle e_i|\mu|g_j\rangle = c_{ij}||\mu||. \tag{7.16}$$

In this expression, $||\mu||$ is the reduced matrix element and the c_{ij} coefficients take into account the coupling strength between specific sub-levels i and j. These coefficients depend on the laser polarization as well as on the electronic and nuclear angular momenta involved. The resulting dipole potential is thus given by

$$U_{dip}^{(i)}(r) = \frac{3\pi c^2 \Gamma}{2\omega_0^3} I(r) \cdot \sum_j \frac{c_{ij}^2}{\Delta_{ij}} \tag{7.17}$$

where Δ_{ij} is the detuning to the specific transition.

In the case of alkali atoms such as Rb, the coupling to the nuclear spin produces a hyperfine structure and the multi-level structure of the atom must be taken into account [141]. However, one of the advantages of the metastable helium atom is the absence of hyperfine structure and the atomic transition $2S \rightarrow 2P$ is thus very simple (see figure 6.1). Moreover, since the laser detuning ($|\Delta| \sim 10^{14}$ Hz in our experiment, see 7.2.1) is very large compared to the typical frequency scale of the fine structure energy levels ($\sim 10^9$ Hz), the latter is not resolved. Therefore the He* atom can be considered as a pure two-level atom coupled via a unique transition, yielding equation 7.15 as exact.

7.2   RED-DETUNED DIPOLE TRAP FOR HE*

The dipole potential 7.11 and scattering rate 7.12 depend not only on the properties of the atom (via the atomic transition ω_0 and the lifetime of the excited state Γ) but also on the configuration of the optical field (via the intensity $I(\mathbf{r})$ and the detuning Δ). This section illustrates the case of optical trapping of He* atoms. The optical field confining the atoms can be created by focussed Gaussian laser beams in both single- and crossed-beam configurations. This point is first discussed, followed by a description of the experimental layout used to create these optical beams.

7.2.1 Single Gaussian Beam

When the light field is tuned below the atomic frequency (red-detuned), the dipole force points towards increasing intensity, creating an attractive potential where the atoms can be trapped. Therefore, the focus of a laser beam constitutes a dipole trap as first proposed by Ashkin [149]. In particular, a confinement in three dimensions can be realized with a tightly focussed laser beam. The intensity profile of a Gaussian beam is given by

$$I(r,x) = \frac{2P}{\pi w^2(x)} e^{-2r^2/w^2(x)} \tag{7.18}$$

where r is the radial dimension and $w(x) = w_0 \sqrt{1 + (x/z_R)^2}$ is the $1/e^2$ radius of the beam along the direction of propagation (x-axis) of the laser beam, with w_0 the waist of the beam (see figure 7.1). The Rayleigh length

$$z_R = \frac{\pi w_0^2}{\lambda} \tag{7.19}$$

is a measure of the axial extension of the focal region and P is the total laser power. The peak intensity is given by $I_0 = 2P/\pi w_0^2$ at the center of the optical beam.
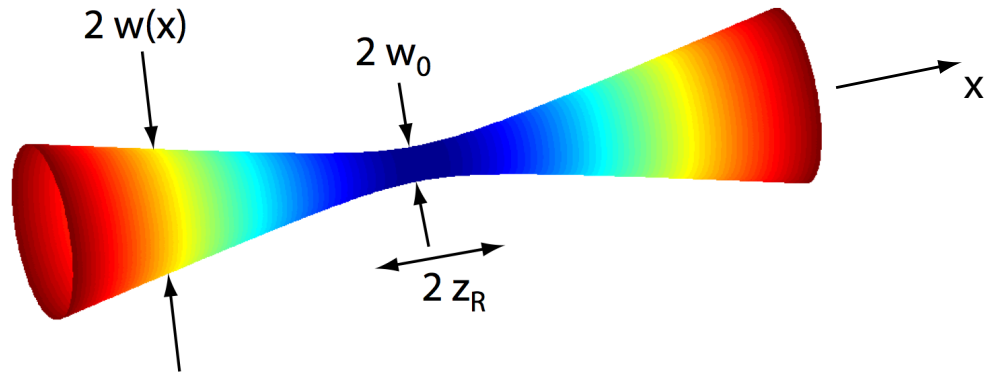

Figure 7.1: Laser beam profile of a single Gaussian beam of waist w_0 and Rayleigh length z_R.

In our experimental setup (section 7.2.3.1), a Gaussian beam will be created with the following parameters:

- $\lambda_L = 1560$ nm.

- $P = 5$ W.

- $w_0 = 100 \ \mu$m.

Following equation 7.11, a single Gaussian beam will form a cylindrically symmetric optical dipole trap given by

$$U_{dip}^{1D}(r,x) = \frac{3\pi c^2}{2\omega_0^3} \cdot \frac{\Gamma}{\Delta} \cdot \frac{2P}{\pi w^2(x)} . e^{-2r^2/w^2(x)} \tag{7.20}$$

which is represented in figure 7.2. In the center of the trap ($r = x = 0$), the potential depth U_0 is given by

$$U_0 = \frac{3\pi c^2}{2\omega_0^3} \cdot \frac{\Gamma}{|\Delta|} \cdot \frac{2P}{\pi w_0^2} . \tag{7.21}$$

so that

$$U_0 \sim 36 \ \mu K \tag{7.22}$$

using our laser parameters. Typically, the thermal energy of condensed He atoms ($E_{cond} \sim 1 \ \mu$K) and the overall heating due to an absorption-emission cycle ($T_{rec} = 2E_{rec} \sim 4 \ \mu$K) are much smaller than the trap depth ($E_{cond} \ll U_0$ and $2E_{rec} \ll U_0$). Consequently, the optical trap is strongly confining and atoms predominantly reside near the center of the trap. The trapping potential can thus be considered harmonic when $x \ll z_R$ and $r \ll w_0$ and approximated by

$$U_{dip}^{1D}(r,x) \approx -U_0 \left[1 - 2 \left(\frac{r}{w_0} \right)^2 - \left(\frac{x}{z_R} \right)^2 \right] . \tag{7.23}$$

The radial and axial trapping frequencies of the potential are obtained from 7.23 and are given by

$$\omega_r = \sqrt{\frac{4U_0}{mw_0^2}} \quad and \quad \omega_x = \sqrt{\frac{2U_0}{mz_R^2}} \tag{7.24}$$

respectively. Both frequencies increase with a tighter waist. However, in most experiments, $w_0 \ll z_R$ (since $\lambda_L \ll w_0$) so that the radial confinement is much greater than the axial trapping, and the cloud is elongated along the axial direction. With our experimental parameters,
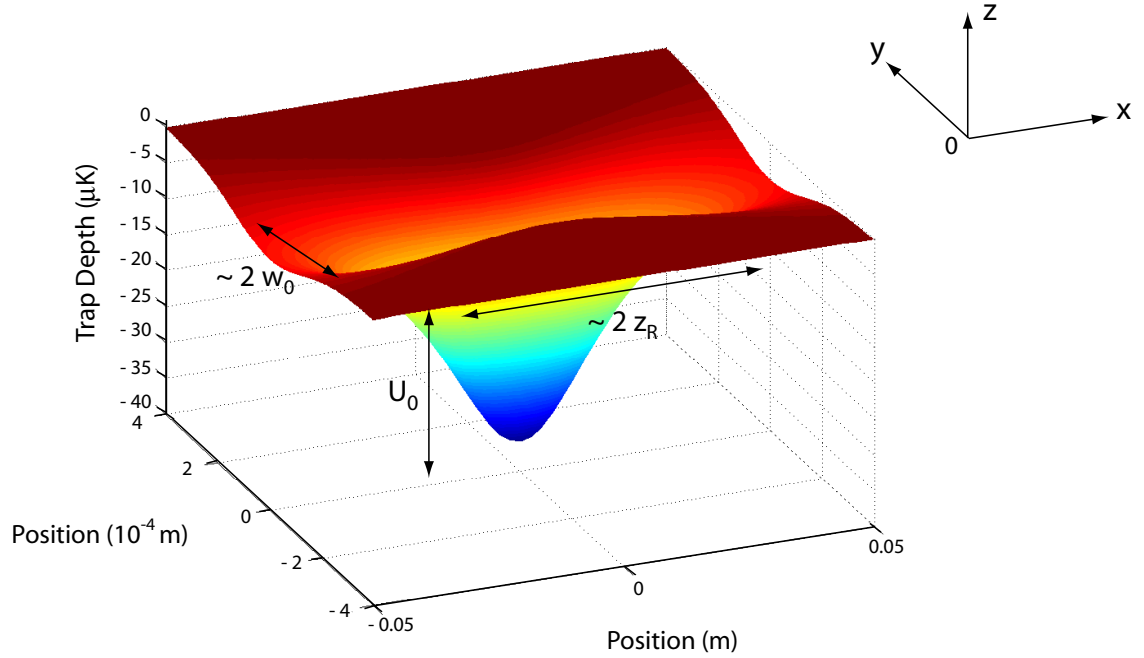
Figure 7.2: Dipolar potential experienced by the atoms in the case of a single dipole trap. The trap depth is characterized by U_0 whereas characteristic lengths are given by w_0 and z_R along the transverse y-direction and the x-direction of propagation respectively.

$$\omega_r = 2\pi \times 865 \; Hz \quad and \quad \omega_x = 2\pi \times 3 \; Hz \tag{7.25}$$

and the dipole trap is strongly anisotropic and elongated along the axial direction with an aspect ratio of $\omega_r/\omega_x = \sqrt{2}z_R/w_0 \sim 300$.

Finally, the maximum scattering rate occurs at the center of the trap and is given by

$$\Gamma_{sc}(0) = \frac{3\pi c^2}{2\hbar\omega_0^3} \cdot \left(\frac{\Gamma}{|\Delta|}\right)^2 \cdot \frac{2P}{\pi w_0^2} \tag{7.26}$$

which gives, with our parameters:

$$\Gamma_{sc}(0) = 2\pi \times 0.09 \; Hz. \tag{7.27}$$

The scattering rate is maximum at the center of the trap where a spontaneous photon is emitted every 10 seconds by a He atom in the 2^3P_2 state. This is much larger than any characteristic

time-scale of the experiment and scattering effects can thus be neglected. Γ_{sc} is a very important parameter, especially in the case of metastable helium atoms since spontaneous emission can leave the atom in any spin state which would lead to Penning ionization and limit the lifetime of the cloud. For instance, a cloud of un-polarized ultracold He* atoms, confined in such an optical trap with an atomic density of $n \sim 10^{13}$ atoms.cm^{-3}, would have a lifetime limited to $(n\alpha_{in})^{-1} \sim 1$ ms $\ll 2$ s, where $\alpha_{in} = 10^{-10}$cm^3.s^{-1} is the Penning collision rate of un-polarized atoms [127].

7.2.2 Crossed Dipole Trap

In order to create a quasi-isotropic trap it is possible to intersect the foci of two orthogonal Gaussian beams (see figure 7.3) of identical waist and orthogonal polarization [141].
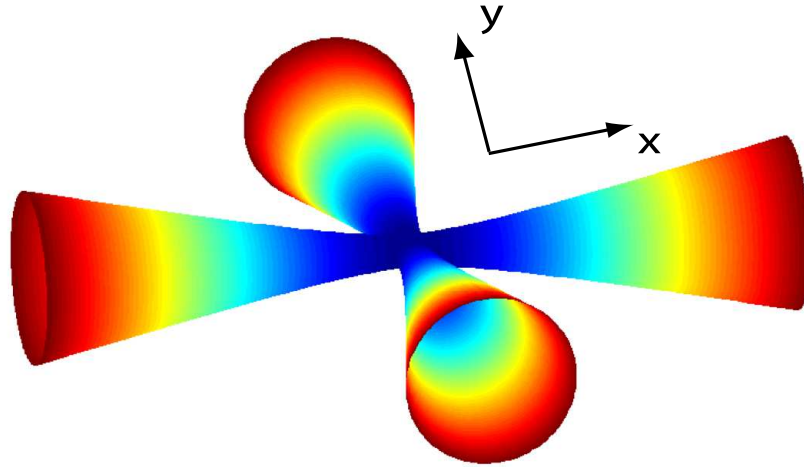

Figure 7.3: Laser beam profile of two crossed Gaussian beams intersecting at their foci.

The resulting dipolar potential is shown in figure 7.4. From 7.23, the dipolar potentials created from the beams propagating along Ox and Oy are respectively given by

$$U_1(x,y,z) \approx -U_0 \left[1 - 2\left(\frac{y^2 + z^2}{w_0^2}\right) - \left(\frac{x}{z_R}\right)^2 \right] \tag{7.28}$$

and

$$U_2(x,y,z) \approx -U_0 \left[1 - 2\left(\frac{x^2 + z^2}{w_0^2} \right) - \left(\frac{y}{z_R} \right)^2 \right] \tag{7.29}$$

where we assume the same power for the two laser beams. Since the two polarizations are considered orthogonal, the dipolar potential in the center ($\vec{r} = \vec{0}$) is simply the sum of U_1 and U_2 which can be written (for $w_0 \ll z_R$) as:

$$U_{dip}^{2D}(x,y,z) \approx -2U_0 \left[1 - \left(\frac{x^2 + y^2 + 2z^2}{w_0^2} \right) \right] \tag{7.30}$$
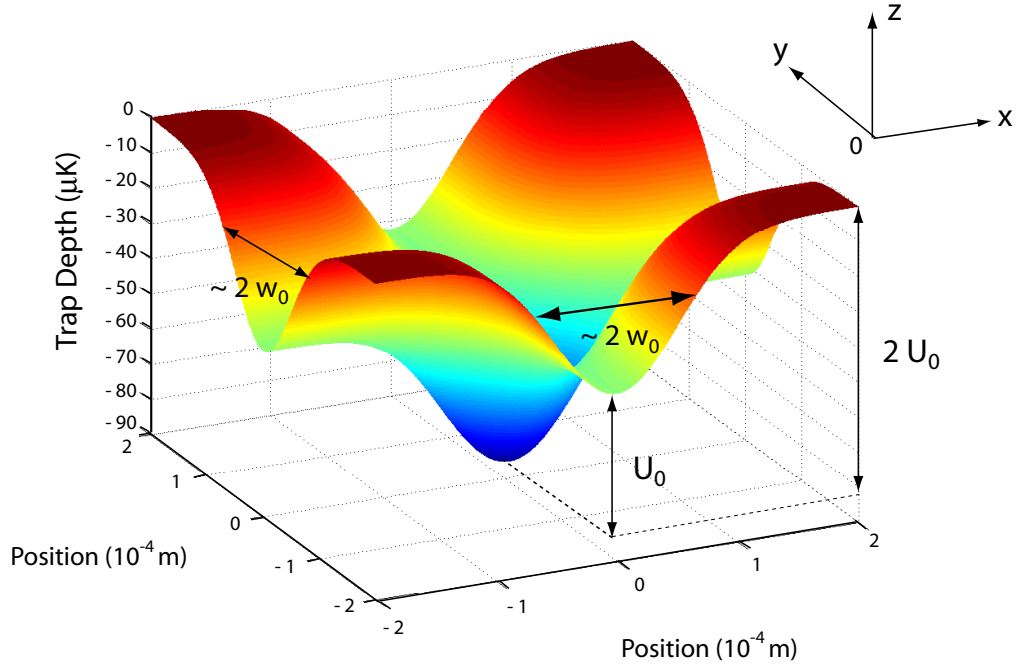
Figure 7.4: Quasi-isotropic dipolar potential experienced by the atoms in a crossed-beam configuration. The effective trap depth is only U_0 because atoms with a higher energy can leave the trapping region along one of the arms (*x*- or *y*-directions) of the laser beams.

The trap depth and scattering rate of such a trap are doubled in comparison with a single beam. However, the effective depth is only U_0 and not $2U_0$ because atoms with a higher energy than U_0 can leave the region of the intersection along one of the arms of the trap (see figure 7.4). Finally, although the radial trapping frequency is unchanged ($\omega_r = \omega_x = \omega_y = \sqrt{4U_0/m\omega_0^2}$), the axial frequency is strongly increased to $\omega_z = \sqrt{2}\omega_r$ and the trap is quasi-isotropic.

7.2.3 Experimental Layout

7.2.3.1 Light Source

A brief schematic of the experimental layout for the laser system is shown in figure 7.5. The system is designed to produce three high power optical beams with the flexibility to create single or crossed dipole traps, and ultimately a 3D confinement which will be discussed in chapter 8. The setup is currently being constructed and characterized in our lab.

Figure 7.5: Schematic of the experimental layout of the laser system used to produce 1-, 2- or 3-D lattice traps. The laser source is split into three outputs. Each laser amplifier provides a total power of 10 W at 1560 nm.
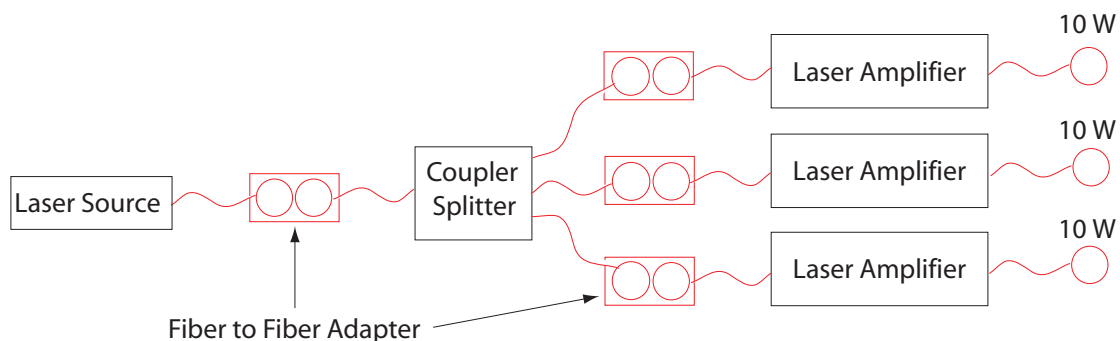
The laser source is an Erbium Micro Fiber Module from NP Photonics. The laser uses a cooled single-mode diode laser, pumping an erbium-doped micro fiber, to provide up to 60 mW of linearly-polarized light at 1560 nm. The wavelength can be tuned 20 GHz around the central frequency by changing the temperature of two internal gratings. The output fiber is coupled to a polarization maintaining single-mode broadband coupler from an Australian company (AFW) which equally splits the power into three outputs. Each of the output fibers injects an Erbium-doped laser amplifier from Keopsys providing 10 W of output power in a collimated Gaussian beam of $w \sim 0.7$ mm waist (see section 7.2.3.2). A single amplifier output can be used for applications where a single dipole trap is required. Alternatively, one or two additional amplifiers will be used when working on a crossed dipole trap or 3D optical lattices respectively (see chapter 8). The laser amplifier output single-passes through an acousto-optic modulator (see section 7.2.3.3) which is used as a fast switch for the light and can also tune the light frequency. The first diffracted order passes through a telescope (see figure 7.6) in order to be expanded to a diameter of ~ 4 mm. Finally, the beam is focussed by a long focal length converging lens, down to a waist

of $w_0 = 100\ \mu$m onto the BEC. Note that the laser power of 5 W considered for the calculations of the previous section accounts for optical losses, mainly when passing through the AOM.
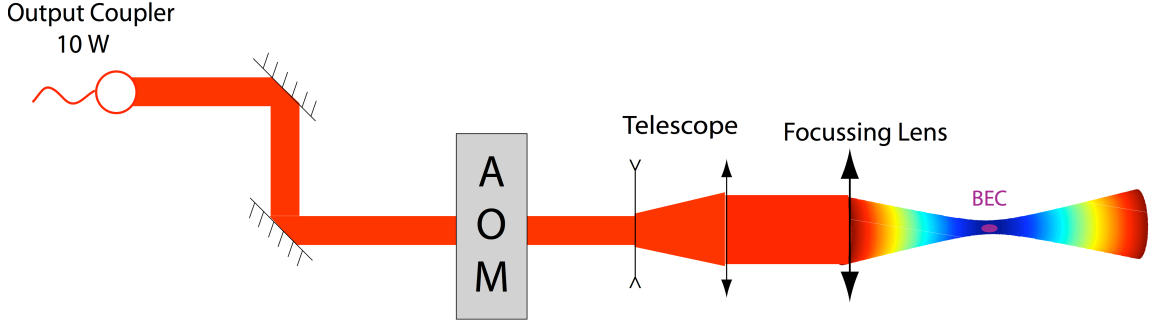
Figure 7.6: Creation of a focussed Gaussian beam. The output beam of the laser amplifier passes through an AOM which can switch the light on and off and change its central frequency. Finally, the beam is expanded before being focussed onto the BEC down to a waist of $\sim 100\ \mu$m.

7.2.3.2   Output Beam Waist

The output beam from the amplifier can be considered perfectly collimated over short distances (~ 1 m) and it is possible to measure the beam waist experimentally. To do so, a razor blade is placed in a vertical plane at some distance from the fiber output coupler. The total power received on a detector behind the razor blade is measured when varying the position (d) of the blade along a transverse axis, from complete extinction to total transmission (dots in figure 7.7). In the vertical plane, the laser intensity of a Gaussian beam can be written as

$$I(x,y) = \frac{2P}{\pi w^2} exp\left(-2\frac{x^2+y^2}{w^2}\right) \tag{7.31}$$

where P is the total power of the beam and w its waist. Consequently, the power $P(d)$ transmitted after the razor blade is given by

$$P(d) = \int_{-\infty}^{d} dx \int_{-\infty}^{+\infty} dy\ I(x,y) = \frac{P}{\sqrt{\pi}} \int_{-\infty}^{d\sqrt{2}/w} dx\ e^{-x^2}. \tag{7.32}$$

This expression can be adjusted to the experimental measurements (solid line in figure 7.7). A beam waist of $w = 0.72 \pm 0.02$ mm is determined from the fit and is in good agreement with the value specified by Keopsys ($w = 0.75$ mm).
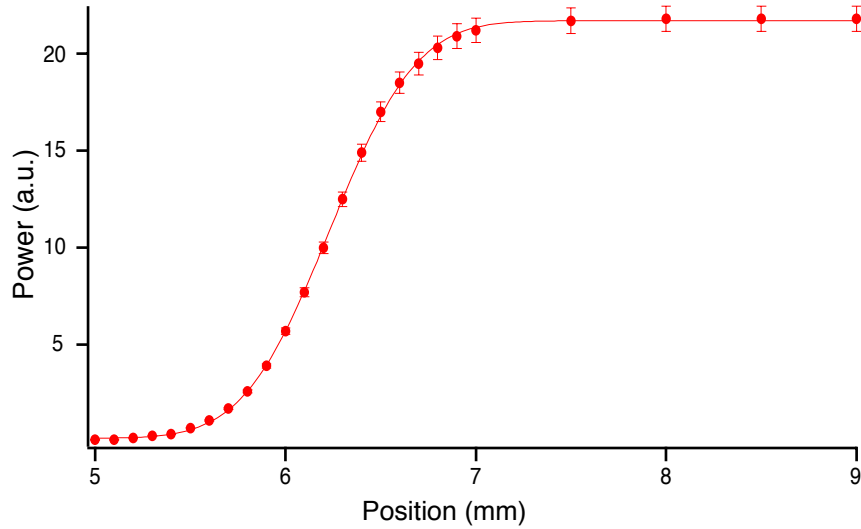
Figure 7.7: Measured laser power (dots) as a function of the position of the razor blade. 10% error bars are considered to account for experimental uncertainties. The solid line is a fit to an Error function. A beam waist of $w = 0.72 \pm 0.02$ mm is determined from the fit.

7.2.3.3 AOM efficiency

The light single-passes through an AOM (AA Opto-Electronic, MTS-1550) which allows for a fast switching on and off (~ 1 μs) and a given frequency shift. Distinct AOMs are used in the setup for each of the three high power output beams independently. Indeed, in the case where optical trapping is performed in two- or three-dimensions (crossed dipole trap or 3D lattice respectively), it is important for each pair of beams to have slightly different frequencies in order to avoid any crossed interference between the beams. Consequently, each AOM drives a different central frequency of 40 MHz, 80 MHz and 110 MHz respectively. The acousto-optic modulators are made of a TeO_2 material and have an active aperture of 3×3 mm^2 which is specified for a laser beam diameter of $1 - 2.5$ mm. The TeO_2 material can withstand a maximum power intensity of up to 5 W.mm^{-2} and a maximum RF power of 2.2 W with no obvious heating. In order to measure the first order diffraction efficiency, the power diffracted in the first order is measured and compared to the total power sent onto the AOM. Results are shown in figure 7.8 where the input power was varied from a minimum (~ 600 mW) to a maximum (~ 10 W) value by slowly increasing the pump current of the laser amplifier. The first order efficiency is measured to be $\sim 70\%$ regardless of the input power, which is significantly less than the performance specified

by AA ($\sim 85\%$) but remains sufficient.
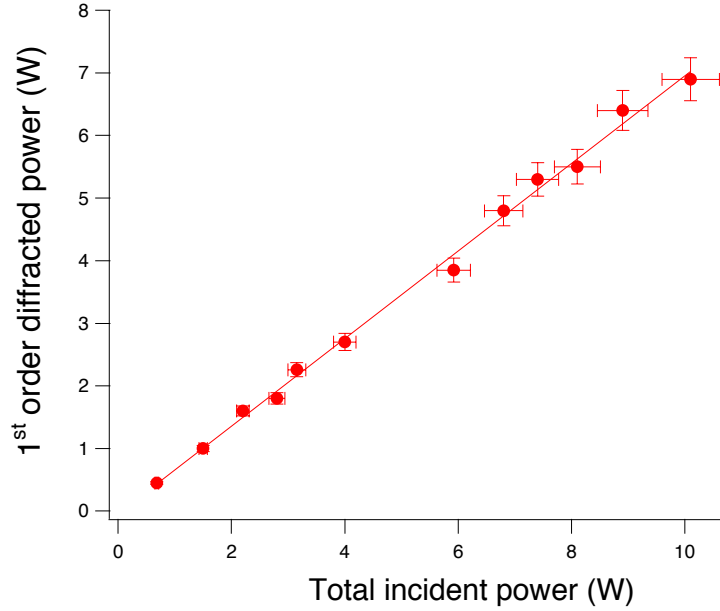
Figure 7.8: First order efficiency of the acousto-optic modulators. The input power is increased from minimum to maximum value and compared to the output power diffracted in the first order. 10% error bars are considered to account for experimental uncertainties.

7.2.3.4 Lens focussing

When a collimated Gaussian beam of waist w and wavelength λ is focussed by a lens of focal length f, its waist w_0 can be approximated by:

$$w_0 = \frac{f\lambda}{\pi w}. \tag{7.33}$$

In our setup, taking into account space limitations due to nearby optics and magnetic coils, we estimate that the focussing lens can be positioned at a distance of approximately 40 cm from the center of the cell. Consequently, it would be possible to focus a Gaussian beam to a waist of $w_0 \sim 100\,\mu$m by choosing a converging lens with $f = 400$ mm, provided the beam is previously expanded to a diameter of ~ 4 mm. The Rayleigh length $z_R = \pi w_0^2/\lambda \sim 20$ mm is very large compared to the size of the condensate so therefore the intensity can be considered constant

across the sample.

7.2.3.5   Loading an optical dipole trap

There are several ways of loading a dipole trap from a pre-cooled MOT. If the maximum attainable optical trap depth is deeper than the temperatures routinely achieved with polarization gradient molasses [71], then a direct loading of the optical trap can be achieved [150]. This is done by leaving the dipole beams switched on at full power while loading atoms into the MOT. After a fixed loading time, the MOT beams and magnetic fields are turned off, leaving the atoms confined solely by the dipole trapping potential. An additional evaporation stage can then be performed to condense the sample. This is achieved by slowly lowering the depth of the dipolar potential [151, 152]. Alternatively, if the maximum attainable optical trap depth is low, the temperature of the atoms has to be further decreased, using evaporative cooling in a magnetic trap, before they can be efficiently transferred into an optical trap. Stamper-Kurn *et al.* [153] transferred Bose-Einstein Condensates of sodium atoms into an optical trap by holding them in a magnetic trap while adiabatically ramping up the laser power and then suddenly switching off the magnetic trap.

In our experiment typical temperatures obtained after Polarization Gradient Cooling ($\sim 200\,\mu$K, [131]) are higher than the dipole trap depth ($U_0 \sim 30\,\mu$K). Consequently, we will consider a preliminary transfer of the atoms into a magnetic trap followed by an evaporative cooling stage in order to lower the temperature of the sample. The transfer into the optical dipole trap will be achieved similarly to [153] by adiabatically ramping up the laser power before switching off the magnetic trap.

This is the exact setup that will be implemented in our experiment. Aside from the experimental challenge of trapping metastable atoms in an optical dipole trap in any chosen Zeeman sub-state, it will be used to measure inelastic collision rates in a BEC of spin-polarized helium atoms as a function of the magnetic field following the theoretical predictions of Shlyapnikov *et al.* [128, 129]. This study is described in the next section.

7.3 INELASTIC COLLISION RATES IN A GAS OF SPIN-POLARIZED METASTABLE HELIUM ATOMS

In this section, theoretical predictions by Shlyapnikov *et al.* [128, 129] are briefly recalled, formulated in an explicit way and finally discussed in relation to future experiments planned in our group. In particular, we focus on the calculations of inelastic collision rates in an ultra-cold gas of spin-polarized metastable helium atoms as a function of an external magnetic field. Trapping helium atoms in an optical dipole trap will allow us to perform such a measurement since the magnetic field is no longer a constraint of the trapping but rather a free parameter that can be varied, independent of the atomic confinement.

7.3.1 Spin-dipole Hamiltonian

The theoretical analysis [128] of the decay kinetics of spin-polarized metastable helium atoms ($^4\text{He}^* \uparrow$) at ultra-low temperatures shows that the two-body ionization process

$$
\text{He}^* \uparrow + \text{He}^* \uparrow \longmapsto
\begin{cases}
\text{He}^+ + \text{He}(1^1S_0) + e^- \\
\text{He}_2^+ + e^-
\end{cases}
. \tag{7.34}
$$
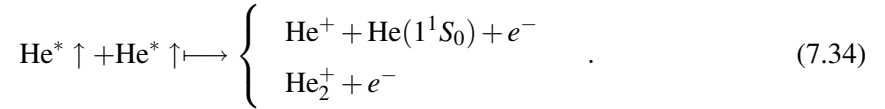
is induced by spin relaxation due to the spin-dipole interaction and is four orders of magnitude slower than Penning collisions in the un-polarized gas. For a collision between two interacting $^4\text{He}^*$ atoms (noted 1 and 2) the hamiltonian of the spin-dipole interaction can be written ([154], appendix B_{XI}) as

$$
\hat{H}_{sd} = -\frac{\mu_0}{4\pi} \frac{(g_S \mu_B)^2}{r^5} \left[3(\mathbf{S}_1 \cdot \mathbf{r})(\mathbf{S}_2 \cdot \mathbf{r}) - (\mathbf{S}_1 \cdot \mathbf{S}_2) r^2 \right] \tag{7.35}
$$

where $g_S = 2$ is the Landé factor for the 2^3S_1 state, $\mathbf{S}_1$ and $\mathbf{S}_2$ are the spin operators of the two colliding atoms, and $\mathbf{r}$ their internuclear position vector. The initial state i which is considered here consists of two metastable atoms with spins aligned and is thus characterized by

$$
|S_i = 2, M_{S_i} = 2\rangle \tag{7.36}
$$

One can show [129, 155] that in a scattering process where the spin-dipole interaction is considered, the following states:

$$|S = 2, M_S = 1\rangle \tag{7.37}$$

$$|S = 2, M_S = 0\rangle \tag{7.38}$$

$$|S = 0, M_S = 0\rangle \tag{7.39}$$

are coupled to the initial state.

7.3.2 Spin relaxation

In the presence of spin-dipole coupling, the final states $|S_f, M_{S_f}\rangle$ are coupled to the initial state $|S_i = 2, M_{S_i} = 2\rangle$ and the scattered wave of atoms for each spin state 7.37 can be written as

$$\Psi_{S_f, M_{S_f}}(r) = \int \mathscr{G}_{S_f, M_{S_f}}(r, r') H_{S_f, M_{S_f}} \Psi_{2,2}^{(0)}(r') dr'. \tag{7.40}$$

Here, $\Psi_{2,2}^{(0)}(r')$ is the wave-function of the relative motion of atoms in the initial state i with energy $E_i = \hbar^2 k_i^2 / 2\mu$. k_i is the wave-vector of the collision and μ is the reduced mass of the system. $H_{S_f, M_{S_f}}$ is the transition matrix element over the spin variables for the spin-dipole operator 7.35. $\mathscr{G}_{S_f, M_{S_f}}(r, r')$ is the Green function of the Schrödinger equation for the relative motion in the final-state potential $U_S(R)$ with energy $E_f = E_i + E_{M_{S_f}}$ where

$$E_{M_{S_f}}(B) = g_s \mu_B B (2 - M_{S_f}) \tag{7.41}$$

is the change of the Zeeman energy in the transition. The spin relaxation rates are thus determined from the radial flux of particles in the scattered wave $\Psi_{S_f, M_{S_f}}(R)$, which is given by

$$J_{S_f, M_{S_f}} = -i \frac{\hbar}{2\mu} \left(\Psi_{S_f, M_{S_f}}^* \frac{d\Psi_{S_f, M_{S_f}}}{dR} - \Psi_{S_f, M_{S_f}} \frac{d\Psi_{S_f, M_{S_f}}^*}{dR} \right). \tag{7.42}$$

7.3.3 Spin relaxation towards $S_f = 2$

In the case of transitions where $S_f = S_i = 2$, the final state of the scattering process remains in the $S = 2$ electronic state from which the ordinary Penning ionization is impossible. Moreover, one can show [129, 155] that the angular dependance of the spin-dipole operator 7.35 implies the selection rules $\ell' = \ell \pm 2$, $\ell' = \ell$ if $\ell \neq 0$, and $|M_{\ell'} - M_\ell| \leq 2$. In the case of ultra-cold atoms,

the initial wave-function of the relative motion of atoms $\Psi_{2,2}$ may be represented by the *s*-wave contribution ($\ell_i = 0$) and the angular momentum of the scattered wave will satisfy $\ell_f = 2$ in accordance with the above selection rule. Consequently, the relative motion of the final state is described by the interaction potential $U_{S_f=2}(R)$ [156, 157] with $\ell = 2$, which is characterized by a radius of interaction of $R_e \sim 70 a_0$ as illustrated in figure 7.9.

Figure 7.9: Interaction potentials of the initial $|S_i = 2, M_{S_i} = 2\rangle$ state (black curve) and a final $|S_f = 2, M_{S_f} = 0, 1\rangle$ state (red curve). The two triplet potentials are coupled by the spin-dipole hamiltonian and separated by the Zeeman energy $E_{M_{S_f}} = g_s \mu_B B (2 - M_{S_f})$. E_i is the initial energy of two colliding spin-polarized metastable helium atoms and the distance R_e is the characteristic radius of interaction.

Since the probability of Penning ionization in the $S_f = 2$ state is negligibly small, the spin-relaxation rate in each relaxation channel ($M_{S_f} = 0$ or 1) is related to the radial flux of particles in the scattered wave $\Psi_{2,M_{S_f}}$ at $R \to \infty$ following

$$\alpha_{2,M_{S_f}}^{rel} = \int J_{2,M_{S_f}}(\mathbf{R}, \mathbf{k}_i) R^2 |_{R \to \infty} \frac{d\Omega_i d\Omega_R}{4\pi} \tag{7.43}$$

where $d\Omega_i$ and $d\Omega_R$ are the elements of the solid angle associated with the vectors $\mathbf{k}_i$ and $\mathbf{R}$ and

where the notation $|_{R \to \infty}$ considers the problem at infinity. The spin-relaxation rates $\alpha_{2,1}^{rel}$ and $\alpha_{2,0}^{rel}$ can be obtained from this calculation using the method described in [128, 129].

7.3.4   Spin relaxation towards $S_f = 0$

In the case of transitions where $S_f = 0$, not only can the final-state spin-relax as described for $S_f = 2$, but an auto-ionization process can also happen via the ordinary Penning mechanism since the atoms are no longer spin-polarized. For ultra-cold atoms the initial wave-function of the relative motion of atoms $\Psi_{2,2}$ may be represented by the s-wave contribution ($\ell_i = 0$) and the angular momentum of the scattered wave will satisfy $\ell_f = 2$ in accordance with the selection rule presented in the above subsection. Consequently, the relative motion of the final state is described by the interaction potential $U_{S_f=0}(R)$ [158] with $\ell = 2$. However, according to [158] the Penning ionization occurs with a probability close to unity at inter-particle distances $R \lesssim 7a_0$. Consequently, in the model of Shlyapnikov *et al.* a perfectly absorbing boundary is placed at a distance $R_0 \sim 7a_0$ and the potential is considered purely elastic at larger distances R as illustrated in figure 7.10. Two distinct regimes can thus occur:

- At distances larger than R_0 ($R > R_0$) a spin-relaxation process similar to the case of $S_f = 2$ occurs and the spin-relaxation rate is simply related to the radial flux of particles in the scattered wave $\Psi_{0,0}$ at $R \to \infty$ following:

$$\alpha_{0,0}^{rel} = \int J_{0,0}(\mathbf{R}, \mathbf{k}_i) R^2 |_{R \to \infty} \frac{d\Omega_i d\Omega_R}{4\pi}. \tag{7.44}$$

- However, when $R \to R_0$, the collision involves 'relaxation-induced' ionization because this state will auto-ionize through the ordinary Penning mechanism. The rate of relaxation-induced ionization is then related to the radial flux of atoms $J_{0,0}$ where the scattered wave $\Psi_{0,0}(R \to R_0)$ is obtained using absorbing boundary at $R = R_0$:

$$\alpha_{0,0}^{ri} = \int J_{0,0}(\mathbf{R}, \mathbf{k}_i) R^2 |_{R \to R_0} \frac{d\Omega_i d\Omega_R}{4\pi}. \tag{7.45}$$
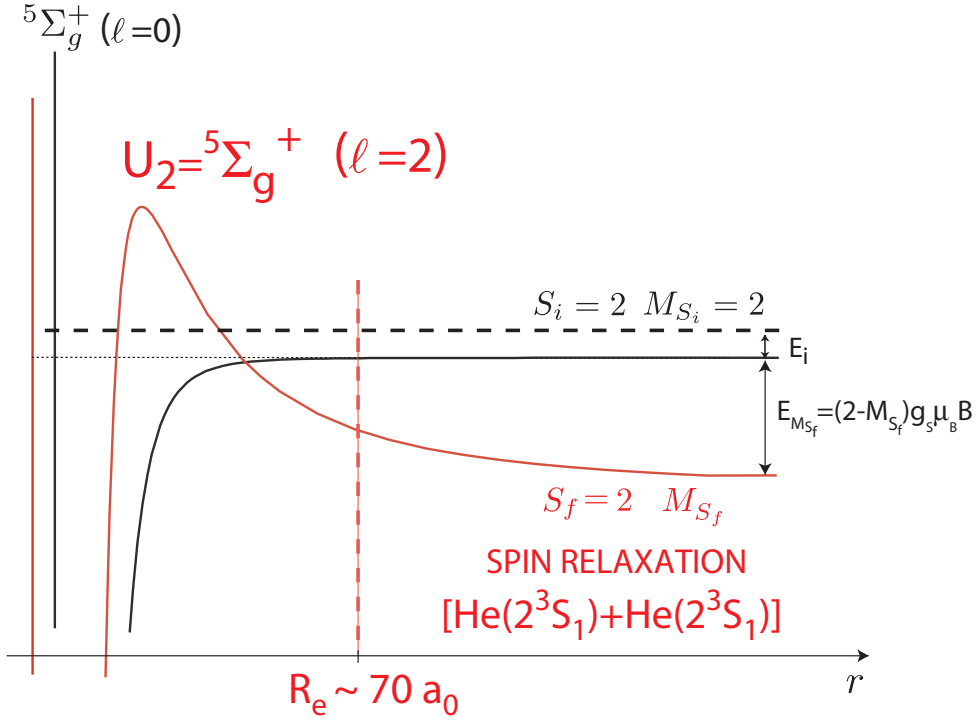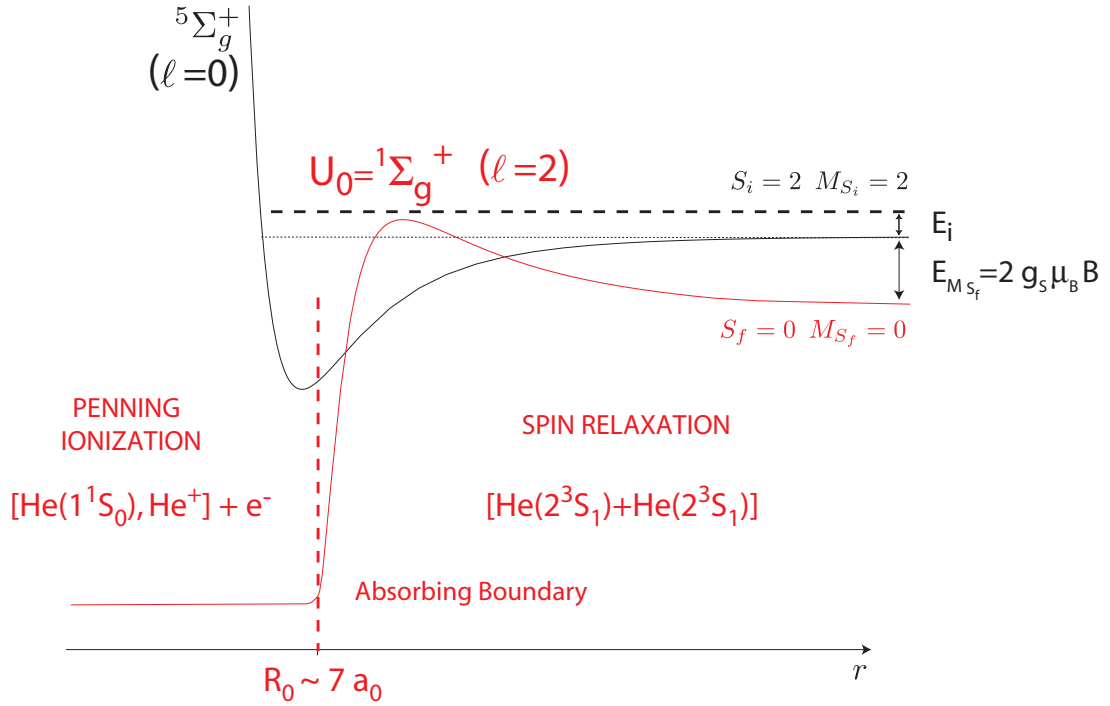
Figure 7.10: Interaction potentials of the initial $|S_i = 2, M_{S_i} = 2\rangle$ state (black curve) and a final $|S_f = 0, M_{S_f} = 0\rangle$ state (red curve). The two triplet and singlet potentials are coupled by the spin-dipole hamiltonian and separated by the Zeeman energy $E_{M_{S_f}} = 2g_s\mu_B B$. E_i is the initial energy of two colliding spin-polarized metastable helium atoms and the distance R_0 is the approximate position of the absorbing boundary at which Penning ionization occurs with a probability close to unity.

7.3.5 Inelastic collision rates and magnetic field dependence

The total spin-relaxation rate can be deduced by summing each of the independent spin-relaxation rates defined as:

$$\alpha^{rel} = \alpha_{2,1}^{rel} + \alpha_{2,0}^{rel} + \alpha_{0,0}^{rel} \tag{7.46}$$

whereas the relaxation-induced collision rate is simply given by:

$$\alpha^{ri} = \alpha_{0,0}^{ri}. \tag{7.47}$$

Finally, the total rate of inelastic processes in $^4\text{He}^* \uparrow$ entails:

$$\alpha^{in} = \alpha^{ri} + \alpha^{rel}. \tag{7.48}$$

Both the spin-relaxation and relaxation induced ionization rates depend on the magnetic field B via the expression of the propagator $\mathscr{G}_{S_f,M_{S_f}}(r,r')$ of the Schrödinger equation for the relative motion in the final-state potential with energy $E_f(B)$. The results obtained in [128] are shown in figure 7.11 where both the relaxation-induced ionization rate (α^{ri}) and the spin-relaxation rate (α^{rel}) are represented as a function of the magnetic field.
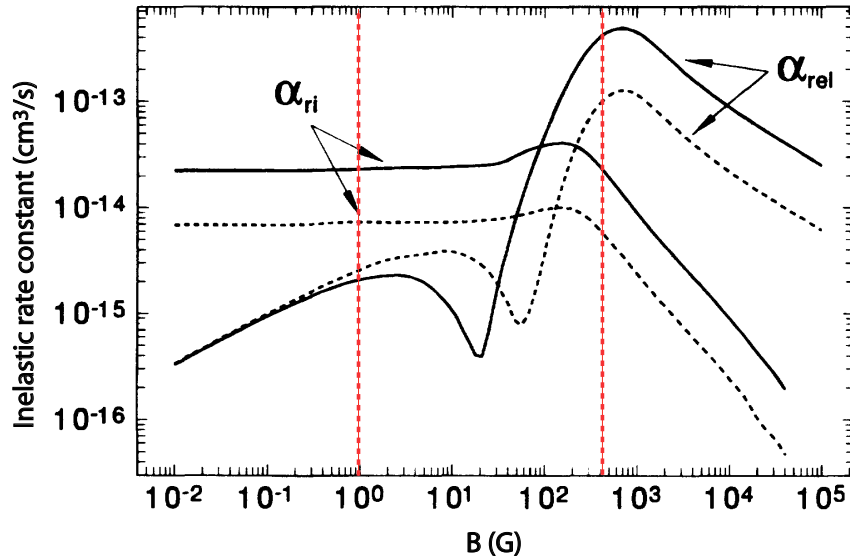
Figure 7.11: Theoretical results obtained in [128]. The rate constants at $T = 0$ K for spin relaxation (α^{rel}) and relaxation-induced Penning ionization (α^{ri}) are given as a function of the external magnetic field. Solid curves correspond to the final potential $U_2(R)$ calculated in [156] and dashed curves to the same potential multiplied by 1.01. The vertical dashed lines represent the range of magnetic field values which we plan to sweep experimentally.

Under typical experimental conditions ($B \lesssim 100$ G) the leading mechanism of the process 7.34 is the relaxation-induced ionization which auto-ionizes through the ordinary Penning mechanism. In low magnetic fields ($B \lesssim 100$ G) relaxation-induced ionization is field independent with a rate constant of $\alpha^{ri} \sim 10^{-14}$ cm^3.s^{-1} Conversely, the relaxation rate constant α^{rel} increases with increasing magnetic fields B, with only a dip for $B \sim 10$ G. In higher fields, α^{ri} decreases and relaxation-induced ionization becomes slower than the process of spin-relaxation

described by α^{rel}. The relaxation rate also decreases with increasing B but remains larger than the low-field value of the rate constant of relaxation-induced ionization. The results highly depend on the expressions of both interaction potentials U_2 and U_0. In figure 7.11, calculations (solid lines) were performed using the U_2 potential derived from [156] and the U_0 potential of [158]. However, one can see (dashed lines) that a small change in one of the potentials leads to substantial differences in the amplitude of both rate constants.

7.3.6   Future experiment

Assuming an ultracold atomic sample of spin-polarized metastable helium atoms is trapped in an optical dipole trap of effective depth $U_0 \sim 30\ \mu$K, it would be possible to perform a measurement of the relaxation rates presented above as a function of an external magnetic field. In order to distinguish between the two loss mechanisms, we will use the channeltron located in the quartz cell as an additional detection method, in combination with the usual absorption imaging technique. In figure 7.11, the area between the two vertical dashed lines represents the range of magnetic field values which we intend to sweep experimentally using the Helmholtz coils of the present experimental setup (section 6.2.8). The lowest value ($B \sim 1$ G) assures a spin-polarized sample of He* atoms. The highest value ($B \sim 300$ G) corresponds to the maximum bias field which can be produced in the current setup. The relaxation-induced ionization rate (α^{ri}) is simply a result of Penning collisions. Consequently, the ions (or electrons) resulting from the ionization process can be monitored in real-time using the channeltron.

Alternatively, the total rate of inelastic process (α^{in}) can also be obtained experimentally, by measuring the total atom losses via an optical absorption imaging technique. During a spin-dipole transition, the change of Zeeman energy is given by $E_{M_{S_f}} = 2\mu_B B(2 - M_{S_f})$, which is minimum when $M_{S_f} = 1$ with $E_1/B \sim 130\ \mu$K.G^{-1}. Consequently, even for magnetic fields on the order of a few Gauss, the final states of the spin-dipole interaction will acquire sufficient kinetic energy to escape from the optical trap. Finally, the spin-relaxation rate will be deduced from $\alpha^{rel} = \alpha^{in} - \alpha^{ri}$.

7.4   CONCLUSION

In this chapter, the general principle and properties of an optical dipole trap are discussed and applied to the case of our experimental laser configuration. There are a few advantages of optical

trapping over magnetic confinement. First, neutral atoms can be confined regardless of their internal state. Second, the external magnetic field is no longer a trapping constraint but a free parameter which can be freely varied. Various experiments can be considered, taking advantage of the possibility to detect individual metastable helium atoms in real-time by monitoring the products (ions or electrons) of Penning ionization processes. In particular, the inelastic collision rates predicted by Shlyapnikov *et al.* are presented here and will be verified experimentally. Alternatively, it would be possible to perform photo-association measurements in a dipole trap or to drive magnetic or optical Feshbach resonances between the different Zeeman sub-states which can all be confined in the optical potential.

CHAPTER 8

NOVEL ATOM TRAP FOR HE ATOMS IN OPTICAL LATTICES

The first part of this chapter presents a general overview on 1-, 2- and 3-dimensional optical lattices, which can confine atoms in wavelength-size regions by means of dipolar forces described in the previous chapter. Such a structure is analogous in many ways to electrons in crystal lattices and is well described by the Bose-Hubbard model. By changing the depth of the optical lattice a phenomenon such as a Superfluid-Mott insulator quantum phase transition is predicted. This was experimentally achieved for the first time by Greiner *et al.* [41] using alkali Rb atoms. We plan to reproduce a similar experiment using metastable helium atoms, taking advantage of Penning ionization to perform a real-time detection and study the kinetics of the transition.

Experiments with Bose-Einstein condensates using a three-dimensional (3D) optical lattice requires improved optical access to the BEC. In addition to the 3 optical axes occupied by the MOT beams, laser light must also be precisely focused onto the condensate from three orthogonal directions in order to create a three-dimensional periodic trapping potential. Most experiments working with alkali atoms can provide an improved optical access by transporting the atoms from the initial MOT stage to the final magnetic trap where condensation occurs and which is physically separated in space. By contrast, in the case of metastable helium atoms, such a transport would result in large atom losses since the sample is much more fragile due to Penning ionization and the strong collisional ionization rate. Consequently, the formation of both the MOT and the BEC must occur at the same location. However, the current apparatus presented in chapter 6 does not provide adequate optical access for all beams. In the second part of this chapter, the design of a new type of magnetic trap is described, to allow for atomic Bose-Einstein condensation to be compatible with in-situ loading of the condensed gas into a 3D optical lattice. For that purpose, the coil geometry is designed to simultaneously maximize in-situ the optical access for the six laser beams of the MOT and independently for the additional six beams of the optical lattice. Technical details on the arrangement of the magnetic coils are given, as well as a description of the electric circuitry.

8.1 PERIODIC LATTICE POTENTIALS

8.1.1 Overview

In 1968, V.S. Letokhov [159] suggested the possibility to create optical lattices by interfering optical laser beams. By means of the dipole force presented in the previous chapter, atoms can be confined in the wavelength-size regions of the resulting interference patterns. The simplest possible lattice is one-dimensional. It is obtained by retro-reflecting a Gaussian laser beam (figure 8.1a) which produces an optical standing-wave potential (figure 8.1b) given by:

$$U_{latt}^{1D}(x,y,z) = -U_{latt} \cdot cos^2(k_L x) \cdot e^{\frac{-2(y^2+z^2)}{w_0^2}} \tag{8.1}$$

with the standing wave of wave-vector $\mathbf{k_L}$ orientated along the x-axis.
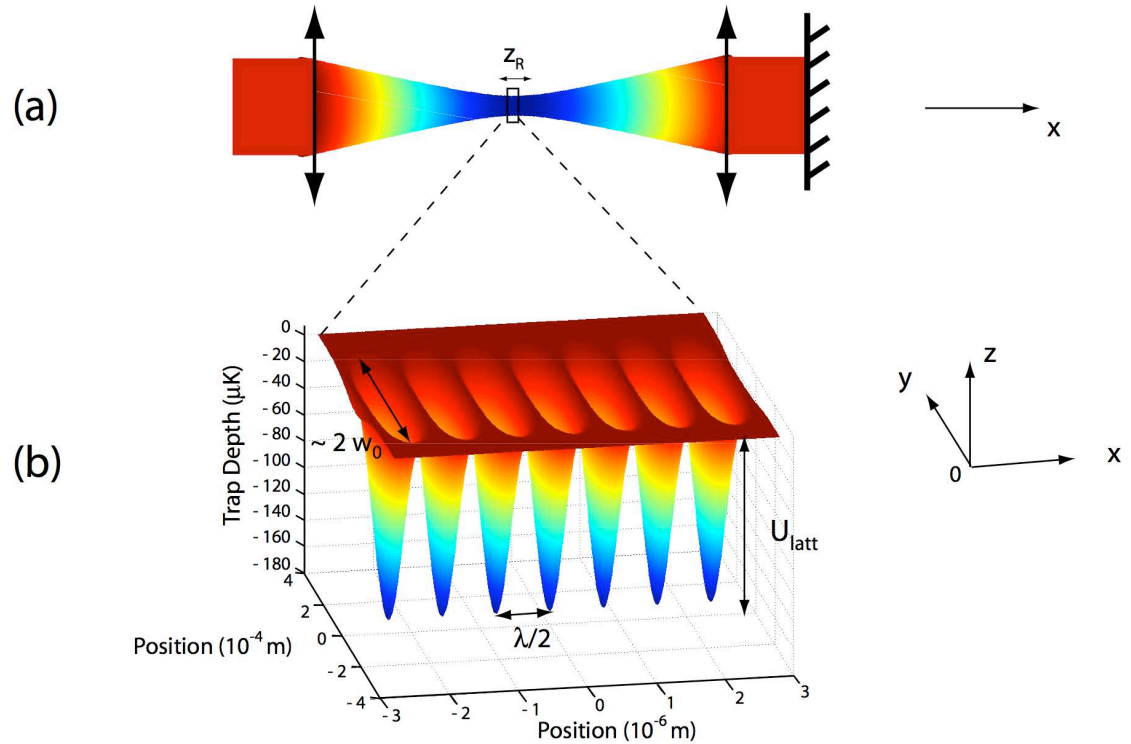

Figure 8.1: (a) Retro-reflected Gaussian laser beam propagating along the x-direction. (b) One-dimensional standing-wave laser field created in the Rayleigh range of the retro-reflected Gaussian laser beam of (a).

Due to constructive interference, the potential depth U_{latt} is four times as large as the corresponding trap depth U_0 for a single focused beam without retro-reflection (see section 7.2.1). Radial confinement is obtained, similarly to the case of a single focused beam, with $\omega_r = \sqrt{4U_{latt}/mw_0^2} \sim 2\pi \times 1.5$ kHz. However, the axial trapping potential is spatially modulated with a period of $\lambda/2$ and atoms are strongly confined in the anti-nodes of the standing wave. The tight confinement along the axial direction leads to very large oscillation frequencies $\omega_x = k_L\sqrt{2U_{latt}/m} \sim 2\pi \times 500$ kHz, resulting in a regular one-dimensional lattice of pancake-like atomic ensembles.

Periodic potentials in higher dimensions can be easily created by superimposing standing waves from different directions. A 2D lattice (see figure 8.2c) can be formed by superimposing the foci of two retro-reflected Gaussian beams orthogonal to each other (see figure 8.2a). If the polarizations of the two standing waves are chosen to be linear and perfectly orthogonal to each other, and if the laser frequencies are different for both standing waves, the resulting potential at the center of the trap has the form

$$U_{latt}^{2D}(x,y,z) = -U_{latt}\left(cos^2(k_Lx) + cos^2(k_Ly)\right) \tag{8.2}$$

forming an array of tightly confining potential tubes. Similarly, a third standing wave, orthogonal to the other two, can be added (figure 8.2b) to create a 3D arrangement of cubic geometry where the resulting optical potential depth is proportional to the sum of the intensities of the three standing-waves [41] following:

$$U_{latt}^{3D}(x,y,z) = -U_{latt}\left(cos^2(k_Lx) + cos^2(k_Ly) + cos^2(k_Lz)\right). \tag{8.3}$$

The first 1D optical lattice was accomplished in 1987 with an atomic beam traversing an intense standing wave [160]. Since then, the study of atoms confined in wavelength-size potential wells has become an important topic in optical control of atomic motion because it opens configurations previously accessible only in condensed matter physics. For that purpose, a 3D lattice configuration forms an intriguing physical system which is closely related to systems of electrons in crystal lattices. However, in contrast to usual condensed matter objects, the flexibility of such an optical lattice is remarkable and a large number of real-time parameters can be controlled:

- The potential depth (U_{latt}) between adjacent sites can be varied by changing the intensity of the light field.

- To some extent, the lattice spacing can be varied by modifying the geometrical configuration of the laser beams creating the lattice.

- Defects and modulations can also be added via the laser frequency.

- It is possible to define 3-, 2-, or 1-dimensional structures by choice of beam geometry.

- Finally, external fields (either magnetic or optical) can be independently added to the trapping lattice in order to drive Feshbach resonances [161, 162] and modify the interaction strength between the particles.
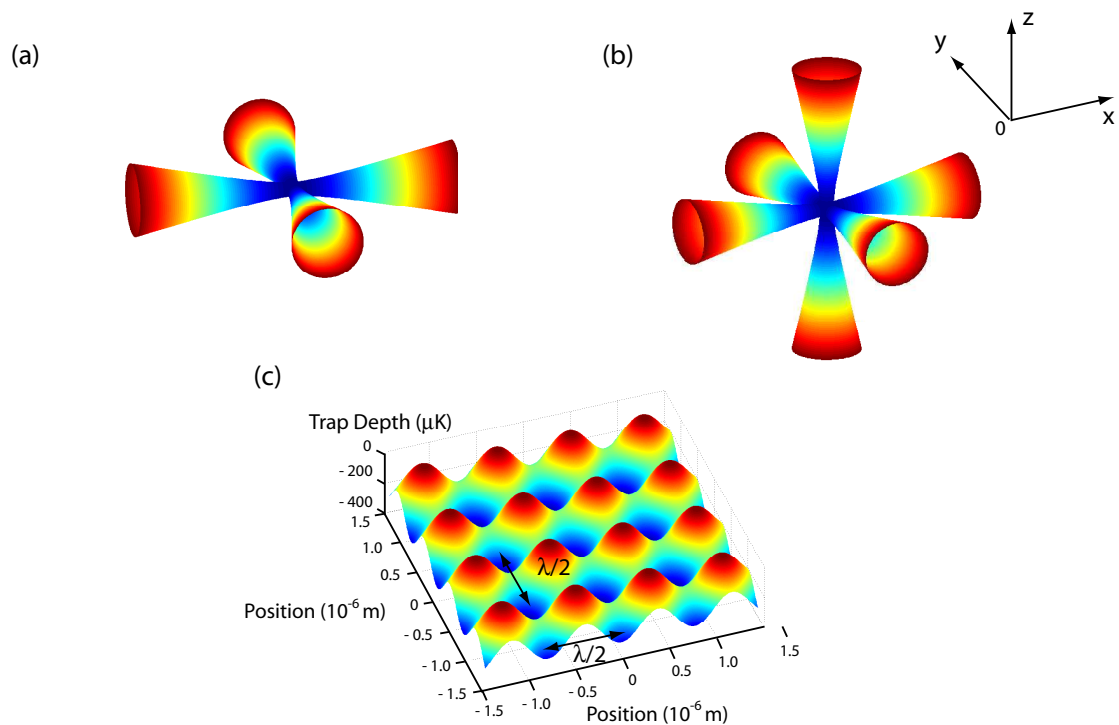
Figure 8.2: a) Shows two orthogonal pairs of retro-reflected Gaussian beams which create the 2 dimensional standing wave represented in c). b) Shows a third orthogonal pair of retro-reflected laser beams. In this case, the resulting 3D confinement has a cubic geometry and is analogous to electrons in a crystal lattice.

Such artificial solids are very appealing to explore a large variety of physical phenomena. The physics of BEC in optical lattices provide a rich playground for both theqory and experiments [35,

36] and has opened new avenues to explore in solid state physics, e.g. studies of fermion-boson mixtures [39, 40], production of cold molecules [163], vortices in lattices [164] and quantum computation [165]. A real breakthrough occurred in 2002 when Greiner *et al.* first reported evidence of the Superfluid-Mott insulator quantum phase transition with a Rb BEC in an optical lattice [41, 42], as explained in the next section.

8.1.2 Quantum Phase Transition from a Superfluid to a Mott Insulator

8.1.2.1 Bose-Hubbard Model

Theoretically, the behavior of bosonic atoms with repulsive interactions confined in a lattice potential is approximately described by a Bose-Hubbard model [166, 167], which is largely used in solid state physics. The Hamiltonian of the system of interacting bosons in an external trapping potential is given by

$$
\begin{aligned}
\hat{H} = \int d^3x\, \hat{\Psi}^\dagger(\mathbf{x}) \left(-\frac{\hbar^2}{2m}\nabla^2 + U_{latt}(\mathbf{x}) + V_{ext}(\mathbf{x}) \right) \hat{\Psi}(\mathbf{x}) \\
+ \frac{1}{2} \cdot \frac{4\pi a \hbar^2}{m} \int d^3x\, \hat{\Psi}^\dagger(\mathbf{x})\hat{\Psi}^\dagger(\mathbf{x})\hat{\Psi}(\mathbf{x})\hat{\Psi}(\mathbf{x})
\end{aligned}
\tag{8.4}
$$

where $\hat{\Psi}(\mathbf{x})$ is the bosonic field operator, $U_{latt}(\mathbf{x})$ is the periodic lattice potential and $V_{ext}(\mathbf{x})$ is an additional external trapping potential. a and m are respectively the scattering length and the mass of an atom. For a periodic potential and local atom-atom interactions [168], it is favorable to work in the Wannier basis where the field operator can be expanded as

$$
\hat{\Psi}(\mathbf{x}) = \sum_i \hat{a}_i w(\mathbf{x} - \mathbf{x_i})
\tag{8.5}
$$

where $\hat{a}_i$ denotes the annihilation operator of a particle in the mode of the Wannier function $w(\mathbf{x} - \mathbf{x_i})$, localized to the ith lattice site. Using this expansion and considering a possible tunneling between adjoining lattice sites, the Bose-Hubbard Hamiltonian 8.4 becomes

$$
\hat{H} = -J \sum_{\langle i,j \rangle} \hat{a}_i^\dagger \hat{a}_j + \sum_i \varepsilon_i \hat{n}_i + \frac{1}{2} U \hat{n}_i(\hat{n}_i - 1)
\tag{8.6}
$$

where the operators $\hat{n}_i = \hat{a}_i^\dagger \hat{a}_i$ count the number of bosonic atoms at the lattice site i and the

annihilation and creation operators $\hat{a}_i$ and $\hat{a}_i^\dagger$ obey the canonical commutation relations $[\hat{a}_i, \hat{a}_j^\dagger] = \delta_{ij}$. The Hamiltonian consists of three terms:

1. The first term is the hopping term and describes the tunneling of bosons with the summation being carried out over neighboring potential wells. The strength of the coupling is characterized by the tunnel matrix element J between adjacent sites i, j :

$$J = \int d^3x \, w^*(\mathbf{x} - \mathbf{x}_i) \left(-\frac{\hbar^2}{2m}\nabla^2 + V_{latt}(\mathbf{x}) + V_{ext}(\mathbf{x}) \right) w(\mathbf{x} - \mathbf{x}_j). \tag{8.7}$$

2. The second term describes an external confinement which gives rise to an energy offset $\varepsilon_i = V_{ext}(\mathbf{x_i})$ on lattice site i. For a homogenous system, $\varepsilon_i = 0$.

3. The last term describes the interaction of n atoms on the same lattice site i, each atom interacting with $n - 1$ other atoms. U quantifies the repulsion between two atoms on a single lattice site and is given by

$$U = \frac{4\pi a \hbar^2}{m} \int |w(\mathbf{x})|^4 d^3x. \tag{8.8}$$

Due to the short range of the interactions compared to the lattice site spacing, the interaction energy is well described by this term, which characterizes a purely on-site interaction. This interaction term tends to localize atoms to lattice sites, thus acting contrary to the hopping term J.

When the depth U_{latt} of the optical lattice is increased, the tunneling barrier between adjoining lattice sites is raised, and the tunneling matrix element $J \propto (U_{latt}/E_{rec})^{3/4} exp(-2\sqrt{U_{latt}/E_{rec}})$ [167] strongly decreases (E_{rec} is the photon recoil energy). In contrast, the on-site interaction term $U \propto (U_{latt}/E_{rec})^{3/4}$ is slightly increased in a deeper lattice due to a tighter confinement of the wave-function in the lattice site. Therefore, the ratio U/J can be continuously adjusted over a wide range simply by changing the depth of the lattice potential.

8.1.2.2   Superfluid-Mott Insulator quantum phase transition

The two counteracting terms (U and J) drive distinct ground states in the Bose-Hubbard Hamiltonian (equation 8.6), depending on their relative interaction strengths [168]:

1. If the tunneling-coupling is much larger than the on-site interaction ($U/J \ll 1$), the first term in the Bose-Hubbard Hamiltonian, i.e. the tunneling process, is dominant. In the ground state, each atom is then delocalized over the entire lattice and the system can be described by a macroscopic wave-function [168]. Therefore, a constant macroscopic phase is well defined across the lattice and the system is called a 'superfluid' (SF). In this case, the number of atoms per lattice site is uncertain and, in a given measurement, a random atom number would be found in each potential well.

2. In contrast, if on-site interactions between atoms are dominant over tunneling ($U/J \gg 1$), the energy of the system is minimized when each atom is localized to a lattice site. In this case, the number of atoms per site is exactly determined whereas the phase coherence vanishes since a matter-wave description of the system is no longer valid. The system is in a 'Mott-insulator' (MI) state.

A striking experimental demonstration showed the occurrence of a clear phase transition between the SF phase and a MI phase when the potential depth was increased above the critical value where $U \sim J$ [41, 42]. The phenomenon was monitored by recording absorption images after releasing the atoms from a 3D lattice. In the SF regime, where all atoms are delocalized over the entire lattice with equal relative phases between different lattice sites, a high-contrast three-dimensional interference pattern was obtained, as expected for a periodic array of phase coherent matter-wave sources. In contrast, as the lattice potential depth was increased above a critical value, an incoherent background of atoms started to grow until no interference pattern was visible, characterizing a loss in phase coherence. However, the phase coherence could be restored very rapidly when the optical potential was lowered again to a value where the ground state of the system is completely SF. The revival of coherence characterizes a transition via a MI state.

8.1.3 New insight with metastable helium atoms

In the case of Rb atoms, the density distribution of the atoms in the MI state is organized in a shell structure where lattice sites located at the center of the lattice contain the highest number of atoms [169]. However, in the case of metastable helium atoms, Penning ionization will tend to empty sites containing more than one atom and a completely different organization of the MI state may be observed. For instance, if the constraint on the polarizing magnetic field is released,

He* atoms in the same lattice site will favorably undergo the Penning ionization process. The resulting repartition over the lattice would thus consist in a 'flat' MI state with either 1 or 0 atoms per site depending on the initial number of atoms in each lattice site. It is interesting to estimate the characteristic time scales involved when two atoms are located in the same lattice site. For an atomic sample of density n and collision rate α, typical decay times of the collision process are obtained as $\tau \sim (n\alpha)^{-1}$. In the case where a sample of ultra-cold atoms ($T \sim 1 \, \mu$K) is confined in the 3D lattice of typical trapping frequencies $\omega \sim 2\pi \times 500$ kHz, one can notice that $\hbar\omega/k_BT \gg 1$ and the atoms remain in the vibrational ground state of the trap. In this regime the atomic density in the trap is simply given by $n \sim 2(m\omega/\hbar)^{3/2}$. Consequently, in the case where the atoms are spin-polarized, the characteristic time for Penning ionization ($\alpha^{ri} \sim 10^{-14}$ cm^3.s^{-1}) results in $\tau_{pol} \sim 8$ ms. Alternatively, if the constraint on the polarizing magnetic field is released, the Penning ionization rate becomes $\alpha^{ri} \sim 10^{-10}$ cm^3.s^{-1} and a 'flat' MI state is reached extremely fast with $\tau_{unpol} \sim 0.8 \, \mu$s.

The true nature of the SF-MI phase transition observed in [41] still remains to be more deeply investigated and it is a real challenge to understand how the initial quantum coherence of the condensate vanishes when one gets deep into the Mott phase. For that reason, it would be important to study the dynamics of the SF-MI transition which has already been theoretically investigated [170]. In the particular case of helium, Penning collisions produce helium ions (He$^+$ or He^{2+}) and an electron (e^-), providing a sensitive method to detect the atomic collisions using a channel electron multiplier (channeltron). This represents a substantial advantage compared with alkali atoms, commonly detected by destructive optical observation methods (absorption or fluorescence). Consequently, in the 'flat' MI state described above, Penning ionization resulting from a tunneling process between two populated adjacent lattice sites can be monitored in real-time using the channeltron in the quartz cell, making it possible to study the dynamics of the quantum transition. The tunneling rate can be changed by varying the characteristic depth of the lattice site. For instance, the appearance of the MI phase is expected to reduce the tunneling between adjacent lattice sites and the Penning ionization rate measured by the channeltron should consequently decrease as the lattice depth increases. Typical time scale of the tunneling process can be estimated by $\tau_{tun} \sim (J/h)^{-1}$. This time is strongly dependent on the lattice depth U_{latt} [167]. For instance, $U_{latt} \sim 10E_{rec}$ leads to $\tau_{tun} \sim 5$ ms, whereas for $U_{latt} \sim 20E_{rec}$ $\tau_{tun} \sim 100$ ms.

8.2 NOVEL ATOM TRAP

In this section a new magnetic trap, allowing for loading of a He condensate in-situ into a 3D optical lattice, is presented. It has been designed and partly built during the time of this PhD and is planned to be implemented in the near future. This original magnetic trap fulfills important experimental challenges, providing an improved optical access with adequate confinement properties.

8.2.1 Experimental challenge

The preparation of a BEC in an optical lattice shares all essential features with usual BEC experiments, with the transfer into the optical lattice as an additional step. It has already been achieved by several groups.

A first method was demonstrated by Burger *et al.* [171] where an atomic sample was cooled close to condensation in a magnetic trap, before imposing the optical lattice and continuing evaporative cooling in the lattice until condensation occurred. Another method used was to first produce the condensate and then load it adiabatically into the lattice [41]. In these first two experiments, numerous technical difficulties arose from both the complexity of the geometry and the large number of laser beams required to prepare and probe the ultra-cold atomic sample. The common starting point (the MOT) requires three orthogonal pairs of counter-propagating laser beams at a frequency slightly detuned ($\sim 10^{-4}$ nm) to the red of the atomic frequency and of opposite polarization σ^+/σ^- (see sections 6.2.7 and 2.1.5). Creating a 3D optical lattice requires an additional set of three orthogonal pairs of counter-propagating laser beams, with very different characteristics compared to the MOT beams: the light must be very far-detuned (~ 100 nm) from the atomic resonance in order to minimize the atom losses through light scattering, and each laser beam is usually set to have a linear polarization π [41]. As a consequence, superimposing the paths of the MOT and the lattice beams poses multiple problems, as for example the arrangement of waveplates (to generate the individual polarization required for each beam), the availability of large range anti-reflective coatings (to optimize transmission at each wavelength) or the difference in the focal lengths of lenses when using two very different wavelengths. These problems can be partly overcome by aligning each pair of co-propagating MOT and lattice beams with a small angle between them, or alternatively by using dichroic mirrors which can combine beams of very different wavelengths. However, such configurations can degrade the polarization

purity of the transmitted light through the nearby optics. Also, in usual experimental setups, magnetic coils compete for physical space with the nearby optics thus limiting the use of any additional component. Finally, although all optical BECs have been successively demonstrated, they require significant laser power and yield comparatively low atom numbers [37, 38].

A different approach to solving the problem of multiple optical beam paths is to physically separate in space the positions of the MOT and magnetic trap confining the BEC, similar to the experimental setup described in chapter 2. In this case, a cold sample is first produced in a region A and then transported towards another region B (usually referred to as the 'Science chamber'), with condensation occurring either in region A or B. The required controlled displacement of the atoms can be achieved by optical, magnetic or mechanical means, such as:

- The focal point of an optical dipole trap, where a sample of atoms is confined, can be shifted by physically displacing the focussing optics [172].

- Arrangements of magnetic field coils can be supplied with modulated currents, resulting in a moving magnetic field minimum [173, 174].

- Magnetic field coils can also be mounted on sledges that are physically displaced [73].

When using a science chamber the positions of the MOT and the BEC are completely separated. Consequently, no MOT beam is involved in the BEC region, which offers superior optical access for implementing optical lattices. However, spatial displacement of atoms adds to the complexity of the setup and occurs at the expense of atom number because of potential atom losses during transport. In the case of alkali atoms, these losses can be minimized by careful optimization of the translation process. In contrast, a BEC of metastable helium atoms appears much more fragile due to Penning ionization and the strong collisional ionization rate. Transport of a sample would thus result in large atom losses, even if the spin polarization could be well maintained all along the path. In the following sections, the novel magnetic trap designed in our group is described. It is compatible with both producing a He BEC and efficiently loading it in-situ into a 3D optical lattice. The arrangement avoids any transport or any co-propagating optical laser beams. The beam and coil geometry are presented, together with details about the electric circuitry and the water-cooling circuit used for the magnetic field coils.

8.2.2   Optical lattice requirements

The He* condensate is intended to be loaded into a 3D lattice, with the goal of studying the superfluid-Mott insulator quantum phase transition. For confinement in an optical lattice, one usually considers that a trap depth of $U_{latt} \sim 10$ E$_r$ is required for efficient trapping, whereas a depth of $U_{latt} \sim 20$ E$_r$ is enough for reaching the Mott-insulator transition [41]. The laser power will be provided by the three high power (10 W) laser-amplifiers described in the previous chapter, resulting in about 5 W per laser beam after passing through all optical components (mirrors, waveplate, AOM). Creating a 3D lattice using gaussian beams with a waist of about 100 μm provides a trap depth of approximately ~ 200 E$_{rec} \gg 20$ E$_{rec}$. The scattering rate ($\Gamma_{scatt} \sim 7$ s^{-1}) is negligible compared to typical experimental time-scales to reach the quantum phase transition. However, implementing the additional set of 6 laser beams to create the lattice is not feasible in our current setup due to the lack of physical space for extra optical components. The new setup presented in the following section has been designed to overcome this problem.

8.2.3   Coil and beam geometry

As mentioned in the previous section, using the concept of a 'science chamber', where the atoms are transported after an initial MOT stage, is not appealing for helium since atom losses are not easily controllable. Moreover, due to the large wavelength difference (~ 500 nm) between the MOT and the lattice beams, it is very difficult to use the same optical components for the different sets of beams. The special design developed in the following avoids these two difficulties. A unique set of coils produces the magnetic field gradients needed for the MOT and the magnetic trap, while the mechanical arrangement leaves optical access to separately inject the beams required for the MOT and the lattice.

Our setup (see figure 8.3) is based on the so-called cloverleaf trap geometry [175] which was modified in order to offer additional corridors for laser beams to pass through. The cloverleaf trap is a variation of the Ioffe-Pritchard trap, with 12 magnetic coils placed exclusively in two vertical planes, creating a similar field but with an improved optical access to the trapped atoms. Two axial coils (the 'pinch coils') are arranged in a Helmholtz configuration, producing a magnetic field which provides axial confinement, with zero gradient near the center of the trap. Each 'pinch coil' is surrounded by four 'cloverleaf' coils, in the form of planar cloverleaves, providing radial confinement. These coils are in a anti-Helmholtz configuration and produce a quadrupolar

waveguide field along the symmetry Y axis. Finally, two larger axial coils ('the compensation coils') are added, creating a quasi-uniform field at the center of the trap, to counter the bias field without making a large compromise on the confining properties induced by the other coils. The 12 coils of the cloverleaf trap allow independent control over the three important parameters of the trapping field: axial bias field, axial curvature, and radial gradient.

The geometric distribution of our trap was designed in a commercial computer aided design software. The arrangements of coils and beams are represented in figures 8.3, 8.4, and 8.5, and are further described in the following three points respectively:

1. A full overview of the three-dimensional geometry of the setup is given in figure 8.3. The coordinate system is defined by choosing the YZ-plane as the horizontal plane, with Z being along the Zeeman slower, in the direction of the incoming beam of atoms. On the figure, some coils are sliced open in order to expose their wiring and a view on the glass cell. The XZ-plane is a plane of symmetry for the coil arrangement and the two sides are mechanically connected by 4 structural support rods. The geometry carefully avoids closing any conducting loop in any plane and the rods are also made of non-conducting material (in our case a 30% glass fiber re-enforced polyamide-nylon). The XZ-plane is intrinsically free as in the standard cloverleaf-type design, with the exception of 4 small angular regions that are blocked by the 4 rods. The mechanical arrangement allows for 2 distinct sets of beams for the MOT (M) and the lattice (L). Indeed, the coils are shaped and positioned to leave enough free space for laser beams to pass along several axes:

   - Along the X-direction is the L_3 lattice beam.
   - Along the Y-direction is the M_1 MOT beam.
   - Along the Z-direction is the counter-propagating Zeeman beam.
   - At $\pm 45°$ with respect to these axes are the M_2/M_3 MOT beams, the L_1/L_2 lattice beams and two free additional axes (for observation during lattice alignment or other laser manipulation).

2. The detail of the coils winding is shown in figure 8.4 where the pinch coils, the compensation coils and the cloverleaf coils are presented. Each square represents the external profile of the wires. The coils are made of copper bars with a square cross section of 6×6 mm^2
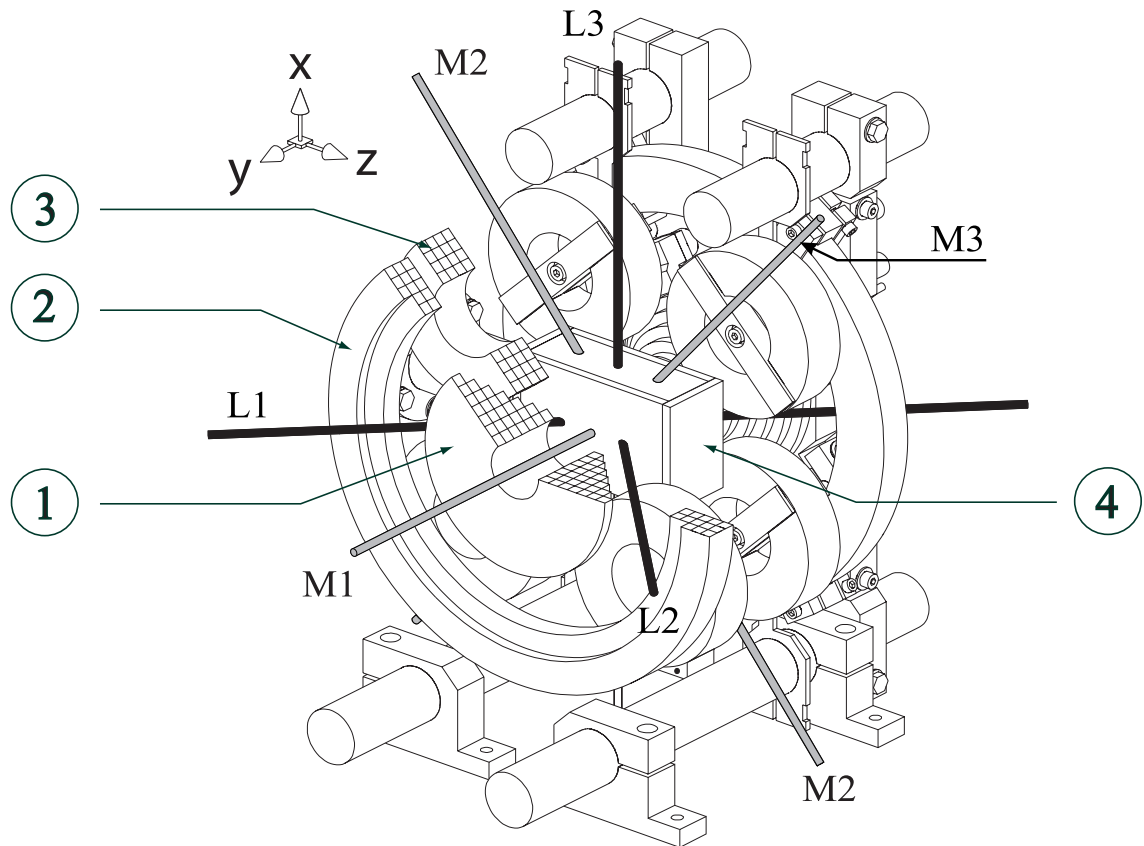
Figure 8.3: Three-dimensional view of the coil and beam geometry. Some mechanical components in the positive Y-direction are sliced open in order to expose the coil wiring. Coils no.1 are the 'pinch coils', coils no.2 are the 'compensation coils' and coils no.3 are the 'cloverleaf coils', spaced by 54 mm in the Y direction. Object no.4 is the $40 \times 40 \times 60$ mm UHV-glass cell. M grey bars represent the MOT beams, L black bars represent the lattice beams.

dimension and a 4 mm-diameter central bore that allows cooling water to flow through (see section 8.2.5.2). The exact number of turns for each coil is reflected in the drawings (e.g. 16 turns for the cloverleaf coils wound in 4 layers of 4 turns each). The pinch coils have a conical shape with a tunnel at their center in order to leave an optical path for the laser beams along the Y-axis. In figure 8.4b the UHV glass cell, of dimensions $40 \times 40 \times 60$ mm, is connected to a DN40CF-flange (Object No. 5) by a metal-glass joint.

3. Finally, all coils on each side of the magnetic trap are supported by a platform with the
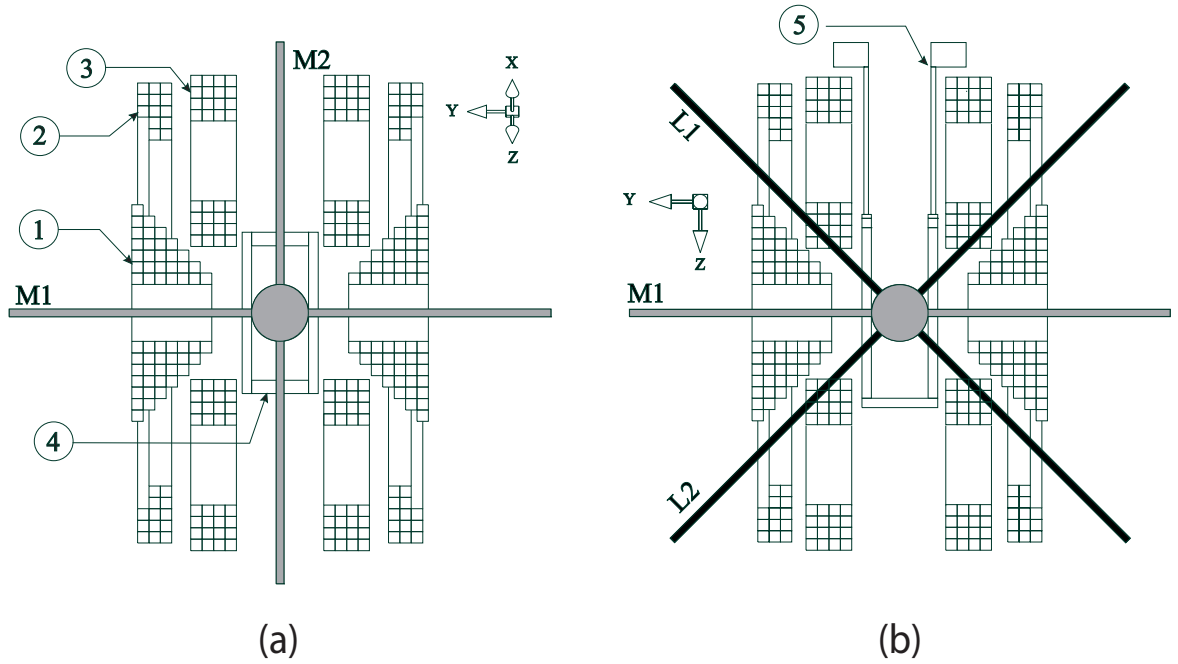
Figure 8.4: Winding configuration of the pinch coils (No. 1), compensation coils (No. 2) and cloverleaf coils (No. 3). a) is a view of a cross section in a plane resulting from a rotation of the YZ-plane by 45°around the Y-axis (see figure 8.3). The grey circle (a sphere of 30 mm diameter) is the largest volume that can be occupied by an atomic cloud trapped in the MOT inside the glass cell (No. 4). b) is a similar view of a cross section in the YZ-plane where No.5 is the DN40CF-flange, connected to the UHV-glass cell by a metal-glass joint.

shape of the letter 'H', as shown in figure 8.5. Each platform holds the axes of the 4 cloverleaf coils and 4 support clamps for each of the pinch and compensation coils. In the figure, M_2, M_3 and L_3 are in the XZ-plane whereas L_1 and L_2 makes a 45°angle to it.

8.2.4 Trap simulations

The new magnetic trap presented here should provide trapping parameters on the order of the ones obtained in our previous setup [132], that is:

- magnetic field bias $B_0 \sim 3$ G.

- axial curvature coefficient $B'' \sim 120$ G.cm^{-2}.

- radial gradient coefficient $B' \sim 170$ G.cm^{-1}
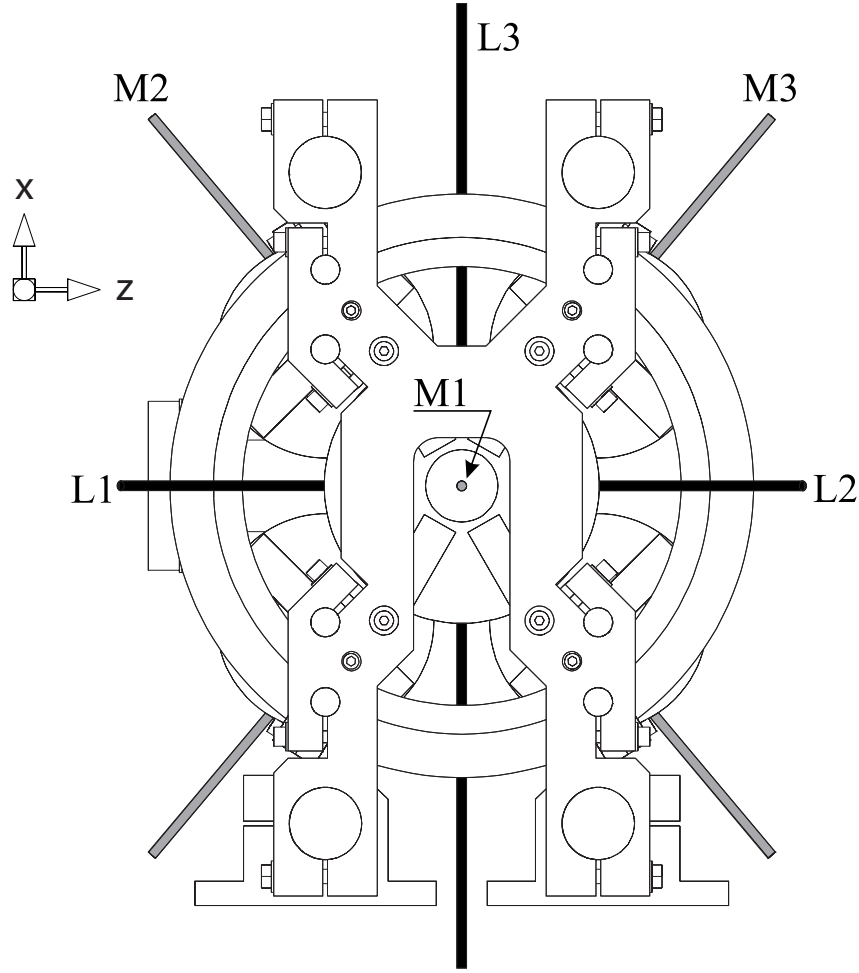
Figure 8.5: View of the mechanical support structure from the positive Y-direction. The 4 support rods are spaced by 270 mm in the X-direction, and 113 mm in the Z-direction.

- axial trapping frequency of $\omega_y = \sqrt{2\mu_B B''/m} \sim 2\pi \times 90$ Hz.

- radial trapping frequency of $\omega_\rho = \sqrt{2\mu_B/m \cdot (B'^2/B_0 - B''/2)} \sim 2\pi \times 800$ Hz.

To achieve high magnetic field gradients, high currents flowing through the coils must be used. In the cloverleaf configuration presented above, opening gaps between the coils to gain optical access significantly reduce the efficiency of the magnetic trapping. This defect has to be compensated by increasing further the current in the coils in order to obtain sufficient confinement. A bias field of $B_0 \sim 3$ G is always required in the case of He in order to maintain spin polarization and avoid Penning collisions. However, the aspect ratio ($\omega_\rho/\omega_y = 9$ in the previous setup) should

rather be smaller in order to have better overlap with the quasi-isotropic shape of a crossed dipole trap or a 3D optical lattice. This can be done by lowering the radial gradient B' without changing too much the axial curvature B''.

The magnetic field configuration is simulated using a commercially available 'Mathematica' interface. In order to minimize the programming and computing times, individual turns of coil (represented in figure 8.4) are re-arranged (in the simulation) into 50 turns (25 on each side) of larger dimension, as shown in figure 8.6. Additionally, each of the resulting 50 turns is approximated and modeled as a set of 64 short linear segments. The total magnetic field is calculated by applying the Biot-Savart law to each of the 3200 (50×64) segments and summing all the resulting fields created in the quartz cell. The calculation is performed for a current of $I = 400$ A which is approximately the maximum current provided by two power supplies (see section 8.2.5.1). The resulting field is finally fitted, in the center of the trap, to a Ioffe-Pritchard type trapping field similar to the one described in section 6.2.8:

$$B(x,y,z) = \sqrt{\left(B_0 + \frac{B''}{2}\left(y^2 - \frac{1}{2}(x^2 + z^2)\right)\right)^2 + B'^2(x^2 + z^2)},$$ (8.9)

All trapping parameters can be deduced from this fit:

- the magnetic field bias is obtained at the center of the trap ($x = y = z$), with $B_0 = 2.9$ G.

- the axial curvature coefficient is obtained by setting $\rho^2 = x^2 + z^2 = 0$. Fitting along the y direction gives $B'' = 86$ G.cm^{-2}.

- the radial gradient coefficient is then deduced for $y = 0$, using the previous value of B''. The fit gives $B' = 103$ G.cm^{-1}.

- axial and radial frequencies of the harmonic potential in the center of the trap are finally obtained with $\omega_y = 2\pi \times 80$ Hz and $\omega_\rho = 2\pi \times 500$ Hz respectively, resulting in an aspect ratio of $\omega_\rho / \omega_y = 6$.

8.2.5 Electric circuitry

8.2.5.1 Wiring circuit

The electrical circuitry used to drive the magnetic coils is represented in figure 8.7. The coils are fed in series, and the path followed by the current is controlled via several insulated gate
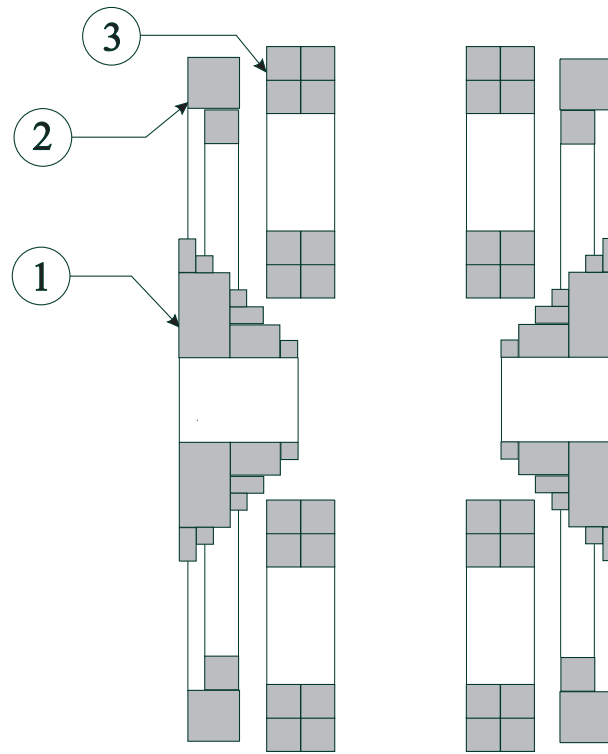
Figure 8.6: Arrangement of individual turns of coils into larger structures (grey rectangles) for improved computation time. Each structure is approximated and modeled as a set of 64 short linear segments.

bipolar transistors (IGBT), which can support high currents of up to 600 A, provided they are water-cooled. The general schematics of the wiring circuit involves two high current power supplies (Agilent 6690A, 15 V, 440 A) that can be programmed independently. They are represented by HCS-A and HCS-B in the schematics. The four IGBT components (Dynex-DIM600BSS12) control the route followed by the current through the different magnetic coils of the setup and the circuit can run following two distinct configurations. The MOT configuration (8.7a) is used to create the quadrupolar field required for the magneto-optical trap stage. In this case, the IGBT components 2 and 3 control the current distribution and HCS-A is set to half the current of HCS-B so that the same current runs in opposite directions through the two pinch coils. A typical current of 40 A will provide a field gradient of 15 G/cm at the center of the trap. After the MOT phase is completed, the circuit can be reconfigured (8.7b) by changing the control voltages of

the IGBTs so that the IGBT components 1 and 4 take control of the distribution. Both power supplies are set to identical values and the current runs in the same direction through all the coils to produce the magnetic trap. A minor amount of current (on the order of 3%) is also diverted from the compensation coils by a bypass circuit in order to controllably adjust the trap bottom offset B_0. For that purpose, the compensation coils are positioned to overcompensate the field at the center of the trap so that draining current from them brings the bias field back to a positive value.
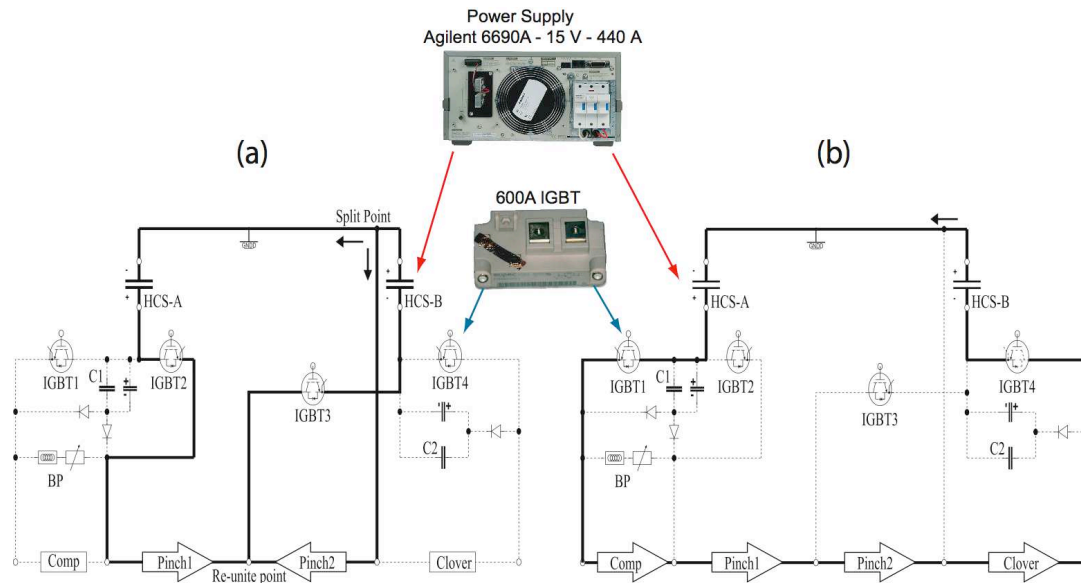
Figure 8.7: Schematics of the coil wiring circuit. HCS-A and HCS-B are two high current power supplies that can be programmed independently. The thick lines indicate the path followed by the current in either the MOT configuration a) or the magnetic trap configuration b). The current route is controlled by adjusting the control voltage of four IGBTs. Capacitors C1 and C2 can absorb the magnetic field energy thus reducing the voltage spikes during the switching off. The bypass circuit BP allows for a controllable drain of current from the compensation coils in order to adjust the level of the bias field B_0.

For applications such as studying the momentum distribution of the atomic cloud in free fall, a fast switch-off of the trap ($\sim 100\ \mu$s) is needed, shorter than the oscillation periods of the trap. However, when switch-off occurs, the emitter-collector junction of the IGBTs is blocked and the large energy stored in the magnetic coils can be driven back into the circuit as a spike of current. As a result, very large induced voltages can appear, which would cause irreversible damage to the IGBTs if exceeding the maximum specified collector-emitter voltage of 1200 V. In order to

divert the spurious pulse from the IGBTs, two alternative paths are added on each side of the circuit, involving two pre-charged capacitors C1 and C2 (see figure 8.7). When the voltage in the circuit rises above the initial voltage of the pre-charged capacitors (typically 15 V), any induced current will be diverted towards the capacitors, thus avoiding going back into the IGBTs. The pre-charging stage of the two capacitors is necessary in order to prevent the current from flowing in these alternative paths during normal operation. C1 and C2 are chosen to be large electrolyte capacitors of 1000 μF which can absorb the entire energy at switch-off. Finally, each capacitor is slowly depleted in the parallel connected power-supply during the MOT loading phase.

8.2.5.2 Water cooling

A critical point when high currents are running through the circuit is the temperature control of the magnetic coils. The electrical Joule energy ΔE_e created when a current I runs through a coil of resistance R during a time Δt is simply given by $\Delta E_e = RI^2 \Delta t$. The resistance of a copper tube can be written as $R = \rho_{Cu} \frac{L}{S}$, where ρ_{Cu} is the electrical resistivity of copper. L is the typical length of a coil and $S = a^2 - \pi r^2$ is the area of the metallic section, with a the external dimension of the copper bar and r the radius of the internal tube where the water flows. Assuming the electrical energy is entirely and efficiently transferred to the water, the rise in temperature ΔT (between the water entering and leaving the tube) is given by

$$\Delta T = \frac{RI^2}{\rho Q C_{Vm}} \tag{8.10}$$

where ρ and C_{Vm} are the density and mass-specific heat capacity of water respectively, and Q is the volumetric flow rate through the tubes. It is important to note that although the current runs in series through all the copper tubes, the water flows in parallel in each coil. Consequently, the typical length that needs to be considered in this cooling estimation is not the total length of the copper wound on the experiment but only the typical length of a coil.

Typical values are:

- $I = 400$ A.

- $L = 5$ m.

- $a = 6$ mm.

- $r = 2$ mm.

- $\rho_{Cu} = 17 \times 10^{-9}$ Ω.m.

- $\rho = 10^3$ kg.m^{-3}.

- $C_{Vm} = 4.2 \times 10^3$ J.m^{-3}.K^{-1}.

In order to estimate the value of the volumetric flow rate Q, one has to characterize the regime in which the water flows through the coils. In the case where velocity fluctuations (e. g. due to external heating) are taken into account, the Reynolds number can be written as [176]

$$Re^* = \sqrt{\frac{2\Delta P r^3}{\rho v^2 L}}.$$ (8.11)

which gives a rough estimate of whether the regime is laminar ($Re^* \ll 1$) or turbulent ($Re^* \gg 1$). Here, ΔP is the pressure gradient maintained between the two ends of the tube, and $v = 10^{-6}$ m^2.s^{-1} is the kinematic velocity of water. It is possible to work in a closed-circuit configuration using a commercial chiller (pressurized water pump) providing a pressure gradient of $\Delta P \sim 6$ bars in the circuit. The Reynolds number is estimated to be $Re^* \sim 1500 \gg 1$, characterizing a turbulent regime where the volumetric flow rate can be calculated as [176]

$$Q = \frac{\pi D^2}{4} \sqrt{\frac{\Delta P D}{4\rho L}} \left(2.5 \ln \sqrt{\frac{\Delta P D^3}{4\rho v^2 L}} - 0.5 \right).$$ (8.12)

Using experimental parameters gives $Q \sim 10^{-4}$ m^3.s^{-1} corresponding to a rise in temperature of $\Delta T \sim 1$ K which is a negligible heating for usual cooling processes.

8.3 CONCLUSION

The device presented in this chapter can be used for producing the MOT, a magnetic trap and ultimately an optical lattice loaded with the atomic sample without overlaying any pair of co-propagating laser beams or physically transporting the sample at any time. All the mechanics of the system have already been built and assembled. At the time of this writing, the coils are being ordered. Such a trap could be compatible for the case of alkali atoms such as ^{87}Rb although a current as high as 1000 A would be required in order to create a harmonic trap with standard trapping frequencies ($\omega_{axial} \sim 2\pi \times 20$ Hz and $\omega_{radial} \sim 2\pi \times 300$ Hz) and a bias field $B_0 \sim 1$ G.

CONCLUSION-OUTLOOK

This thesis presented the work performed jointly between the Department of Quantum Science in Canberra, Australia, and the Laboratoire Kastler-Brossel at ENS in Paris, France. It aimed at providing advanced ultracold atom sources for precision measurement and for investigations in fundamental physics.

The first part of the thesis described several experimental and theoretical results obtained for the atom laser. The introductory chapter gave a general overview on atom lasers in analogy to optical lasers and several techniques to out-couple the atoms from the Bose-Einstein Condensate (BEC) source were discussed. Our BEC apparatus allowed us to repeatedly produce condensates of approximately 10^6 ^{87}Rb atoms in a stable magnetic trap. The machine is based on a double-MOT structure and separates the UHV collection region from the BEC cell, resulting in an improved optical access along all primary axes of the BEC. Two optical Raman beams were implemented in the setup in order to out-couple atoms from the initial condensate.

For applications based on atom interferometry, it is crucial to develop atom lasers with output modes that are simple and as clean as possible. These properties are characterized by the M^2 quality factor of the atomic beam, defined in analogy to optical lasers. Experimental results on the divergence properties of the Raman atom laser were presented with respect to this quality factor and compared to an RF output coupling technique. The main advantage of the optical Raman coupling lies in the initial momentum transfer imparted to the atoms. The atoms do not necessarily require gravity to leave the condensate and can be pushed in a chosen initial direction. Additionally, the time to escape the condensate is strongly reduced, which decreases the effect of interactions from the BEC experienced by the atom laser. This leads to a significantly improved transverse profile in the atom laser beam. In our experiment, we reached a quality factor of $M^2 = 1.4$ for a Raman atom laser compared to $M^2 = 2.2$ when using an RF transition. All the results were obtained by out-coupling the atoms from the center of the condensate where the density is greatest, thus providing the highest possible flux, longest operating time and lowest sensitivity to fluctuations.

We also took advantage of the Raman beams to perform coherent atom beam splitting of an atom laser. The manipulation of the atoms followed a resonant Bragg diffraction process where the very large detuning of the laser beams forming the grating ensured negligible spontaneous emission, so that coherence was maintained during the process. We demonstrated that the diffrac-

tion grating was produced from each of the Raman beams independently and from a very small fraction of back-reflected light from the coils. We characterized the velocity resonance condition driving the Bragg diffraction and we showed that the process was efficient, with up to 60% of the atoms being diffracted, making it suitable for use in an atom interferometer. Our method is an experimentally simple and versatile tool for atom optics. An important advantage of our setup is that the Raman output coupler can run simultaneously in a regime where it serves also as two beam splitters, thus significantly simplifying the experimental demands.

The last result of the first part of the thesis presented a theoretical model which we used to study the effect of RF out-coupling on two- and multi-level systems. The model was validated by comparing the theoretical results to previous experimental measurements performed in our group. Finally, the atom laser output was characterized depending on the out-coupling strength. In particular, important experimental requirements of an atom laser, such as flux, fluctuations and spatial structure were studied. We showed that a five-state system ($F = 2$ hyperfine state) is inappropriate for any measurement using atom laser beams due to intermediate coupling to a Zeeman sub-level oscillating in the trap and disturbing the extraction process. We concluded that the 'natural' three-state system ($F = 1$ manifold) should be preferred for any classical measurement since such a system has similar characteristics to a 'pure' two-state system and is experimentally much simpler to achieve.

The atom laser work will continue to be actively pursued in the next years at the Australian National University and in other laboratories around the world. The ANU group has recently demonstrated a Ramsey fringe interferometer using an atom laser as the source [89]. Such an interferometer provides a local oscillator that could be used to detect and exploit a quadrature squeezed atom laser beam. The ANU group has also recently achieved a ^{85}Rb BEC. ^{85}Rb has an accessible Feshbach resonance that can be used to tune the atom-atom interactions. An atom laser derived from this condensate will be combined with high bandwidth single atom cavity detection (currently in production at ANU) and the local oscillator. This will form the source and detection scheme necessary for a sub-shot noise limited atom interferometer. A future goal is to develop high momentum transfer splitting of atom laser beams to enhance the signal to noise in many interferometric measurements. These future directions and experiments are only possible if the classical properties of the atom laser have been characterised and optimised. This was one of the major goals that was achieved through the work presented in the first part of this thesis and was an essential step along the path to precision measurement at sensitivities exceeding the shot

noise limit with atom laser sources.

The second part of the thesis was orientated towards optical trapping of metastable helium atoms. The initial chapter described the experimental setup, focussing on several improvements which we achieved recently. Apart from making the optical setup more reliable and stable, a Channel Electron Multiplier was added, providing a non-destructive real-time method to detect ions or electrons resulting from Penning collisions involving metastable atoms.

Optical trapping of He* atoms is the next experimental step which we are aiming for in our group. For that purpose, the general principle and properties of an optical trap as well as a description of the laser layout which we are currently implementing were presented. It is based on a red-detuned crossed dipole trap and is meant to be initially used to measure characteristic rate constants of inelastic decay processes in our gas of spin-polarized metastable helium.

Finally, our perspective of trapping a BEC of metastable helium atoms in a 3D optical lattice was described. Amongst many possible experiments, we focussed on briefly presenting the Superfluid-Mott insulator transition which was previously observed with alkali Rb atoms and which we intend to reproduce for He taking advantage of Penning ionization to perform a real-time detection and study the kinetics of the transition. The design of a new and original type of magnetic trap was also presented. It allows for Bose-Einstein condensation to be compatible with in-situ loading of the condensed gas into a 3D optical lattice. For that purpose, the coil geometry was conceived to simultaneously maximize the optical access for six laser beams of the MOT and independently for the six beams of the optical lattice.

The work done in the second part of this thesis was the necessary step of preparation which will now allow our team at ENS to undertake a new generation of experiments with condensed metastable helium gas in either an optical dipole trap or an optical lattice. For instance, photo-association measurements in a dipole trap can be performed. Alternatively, magnetic or optical Feshbach resonances can be driven to control the interactions between the different Zeeman sub-states confined in the optical potential. The flexibility of optical lattices could allow us to investigate various intriguing aspects of 1D or 2D quantum gases. For example, it is envisaged to study quantum transitions in the 2 dimensional regime and the modification of Penning ionization due to the transverse confinement. It would also be interesting to enter the regime of a Tonks-Girardeau gas in the Mott-insulator state, taking advantage of the very deep potential which can be achieved with our experimental setup.

BIBLIOGRAPHY

[1] M. H. Anderson, J. R. Ensher, M. R. Matthews, C. E. Wieman, and E. A. Cornell. Observation of Bose - Einstein condensation in a dilute atomic vapor. *Science*, 269(5221):198–201, 1995. Available from: http://www.sciencemag.org/cgi/content/abstract/269/5221/198.

[2] K. B. Davis, M. O. Mewes, M. R. Andrews, N. J. van Druten, D. S. Durfee, D. M. Kurn, and W. Ketterle. Bose-Einstein condensation in a gas of sodium atoms. *Phys. Rev. Lett.*, 75(22):3969–3973, Nov 1995. Available from: http://link.aps.org/abstract/PRL/v75/p3969.

[3] C. C. Bradley, C. A. Sackett, J. J. Tollett, and R. G. Hulet. Evidence of Bose-Einstein condensation in an atomic gas with attractive interactions. *Phys. Rev. Lett.*, 75(9):1687–1690, Aug 1995. Available from: http://link.aps.org/abstract/PRL/v75/p1687.

[4] T. H. MAIMAN. Stimulated optical radiation in ruby. *Nature*, 187(4736):493–494, 1960. Available from: http://dx.doi.org/10.1038/187493a0.

[5] Clauser J. F. *Physica B*, 151(262), 1988.

[6] F. Riehle, Th. Kisters, A. Witte, J. Helmcke, and Ch. J. Bordé. Optical Ramsey spectroscopy in a rotating frame: Sagnac effect in a matter-wave interferometer. *Phys. Rev. Lett.*, 67(2):177–180, Jul 1991. Available from: http://link.aps.org/doi/10.1103/PhysRevLett.67.177.

[7] M. Kasevich and S. Chu. Measurement of the gravitational acceleration of an atom with a light-pulse atom interferometer. *Applied Physics B: Lasers and Optics*, 54(5):321–332, 1992. Available from: http://dx.doi.org/10.1007/BF00325375.

[8] J. B. Fixler, G. T. Foster, J. M. McGuirk, and M. A. Kasevich. Atom interferometer measurement of the Newtonian constant of gravity. *Science*, 315(5808):74–77, 2007. Available from: http://www.sciencemag.org/cgi/content/abstract/315/5808/74.

[9] G. Lamporesi, A. Bertoldi, L. Cacciapuoti, M. Prevedelli, and G. M. Tino. Determination of the Newtonian gravitational constant using atom interferometry. *Physical Review Letters*, 100(5):050801, 2008. Available from: http://link.aps.org/abstract/PRL/v100/e050801.

[10] S. Gupta, K. Dieckmann, Z. Hadzibabic, and D. E. Pritchard. Contrast interferometry using Bose-Einstein condensates to measure h/m and α. *Phys. Rev. Lett.*, 89(14):140401, Sep 2002. Available from: http://link.aps.org/doi/10.1103/PhysRevLett.89.140401.

[11] Malo Cadoret, Estefania de Mirandes, Pierre Clade, Saida Guellati-Khelifa, Catherine Schwob, Francois Nez, Lucile Julien, and Francois Biraben. Combination of Bloch oscillations with a Ramsey-Bordé interferometer: new determination of the fine structure constant. *Physical Review Letters*, 101(23):230801, 2008. Available from: http://link.aps.org/abstract/PRL/v101/e230801.

[12] Landragin A. and F. Pereira Dos Santos. Accelerometer using atomic waves for space applications. *arXiv:0808.3837*, 2008.

[13] T. Müller, M. Gilowski, M. Zaiser, T. Wendrich, W. Ertmer, and E. Rasel. A compact dual atom interferometer gyroscope based on laser-cooled rubidium. *arXiv:0806.0956*, 2008.

[14] Jonathan P. Dowling. Correlated input-port, matter-wave interferometer: quantum-noise limits to the atom-laser gyroscope. *Phys. Rev. A*, 57(6):4736–4746, Jun 1998. Available from: http://link.aps.org/doi/10.1103/PhysRevA.57.4736.

[15] T. Muller, T. Wendrich, M. Gilowski, C. Jentsch, E. M. Rasel, and W. Ertmer. Versatile compact atomic source for high-resolution dual atom interferometry. *Physical Review A (Atomic, Molecular, and Optical Physics)*, 76(6):063611, 2007. Available from: http://link.aps.org/abstract/PRA/v76/e063611.

[16] T. L. Gustavson, P. Bouyer, and M. A. Kasevich. Precision rotation measurements with an atom interferometer gyroscope. *Phys. Rev. Lett.*, 78(11):2046–2049, Mar 1997. Available from: http://link.aps.org/doi/10.1103/PhysRevLett.78.2046.

[17] Mattias T. Johnsson and Simon A. Haine. Generating quadrature squeezing in an atom

laser through self-interaction. *Physical Review Letters*, 99(1):010401, 2007. Available from: http://link.aps.org/abstract/PRL/v99/e010401.

[18] M.-O. Mewes, M. R. Andrews, D. M. Kurn, D. S. Durfee, C. G. Townsend, and W. Ketterle. Output coupler for Bose-Einstein condensed atoms. *Phys. Rev. Lett.*, 78(4):582–585, Jan 1997.

[19] E. W. Hagley, L. Deng, M. Kozuma, J. Wen, K. Helmerson, S. L. Rolston, and W. D. Phillips. A well-collimated quasi-continuous atom laser. *Science*, 283(5408):1706–1709, 1999. Available from: http://www.sciencemag.org/cgi/content/abstract/283/5408/1706.

[20] Y. Le Coq, J. H. Thywissen, S. A. Rangwala, F. Gerbier, S. Richard, G. Delannoy, P. Bouyer, and A. Aspect. Atom laser divergence. *Phys. Rev. Lett.*, 87(17):170403, Oct 2001. Available from: http://link.aps.org/abstract/PRL/v87/e170403.

[21] J.-F. Riou, W. Guerin, Y. Le Coq, M. Fauquembergue, V. Josse, P. Bouyer, and A. Aspect. Beam quality of a nonideal atom laser. *Physical Review Letters*, 96(7):070404, 2006. Available from: http://link.aps.org/abstract/PRL/v96/e070404.

[22] W. Guerin, J.-F. Riou, J. P. Gaebler, V. Josse, P. Bouyer, and A. Aspect. Guided quasi-continuous atom laser. *Physical Review Letters*, 97(20):200402, 2006. Available from: http://link.aps.org/abstract/PRL/v97/e200402.

[23] M. Köhl, T. W. Hänsch, and T. Esslinger. Line width of an atom laser. *Applied Physics B: Lasers and Optics*, 76(2):109–112, 2003. Available from: http://dx.doi.org/10.1007/s00340-003-1111-0.

[24] Ferdinand Brennecke, Stephan Ritter, Tobias Donner, and Tilman Esslinger. Cavity optomechanics with a Bose-Einstein condensate. *Science*, 322(5899):235–238, 2008. Available from: http://www.sciencemag.org/cgi/content/abstract/322/5899/235.

[25] F. Brennecke, T. Donner, S. Ritter, T. Bourdel, M. Kohl, and T. Esslinger. Cavity QED with a Bose-Einstein condensate. *Nature*, 450(7167):268, 2007. Available from: http://dx.doi.org/10.1038/nature06120.

[26] T. Bourdel, T. Donner, S. Ritter, A. Ottl, M. Kohl, and T. Esslinger. Cavity QED detection of interfering matter waves. *Physical Review A (Atomic, Molecular, and Optical Physics)*, 73(4):043602, 2006. Available from: http://link.aps.org/abstract/PRA/v73/e043602.

[27] Anton Ottl, Stephan Ritter, Michael Kohl, and Tilman Esslinger. Correlations and counting statistics of an atom laser. *Physical Review Letters*, 95(9):090404, 2005. Available from: http://link.aps.org/abstract/PRL/v95/e090404.

[28] N. P. Robins, C. M. Savage, J. J. Hope, J. E. Lye, C. S. Fletcher, S. A. Haine, and J. D. Close. Fluctuations and flux: the limits of multistate atom lasers. *Physical Review A (Atomic, Molecular, and Optical Physics)*, 69(5):051602, 2004. Available from: http://link.aps.org/abstract/PRA/v69/e051602.

[29] N. P. Robins, A. K. Morrison, J. J. Hope, and J. D. Close. Limits to the flux of a continuous atom laser. *Physical Review A (Atomic, Molecular, and Optical Physics)*, 72(3):031606, 2005. Available from: http://link.aps.org/abstract/PRA/v72/e031606.

[30] N. P. Robins, C. Figl, S. A. Haine, A. K. Morrison, M. Jeppesen, J. J. Hope, and J. D. Close. Achieving peak brightness in an atom laser. *Physical Review Letters*, 96(14):140403, 2006. Available from: http://link.aps.org/abstract/PRL/v96/e140403.

[31] N. P. Robins, C. Figl, M. Jeppesen, G. R. Dennis, and J. D. Close. A pumped atom laser. *Nature Physics*, 4:731–736, September 2008. Available from: http://www.nature.com/nphys/journal/vv4/nn9/pdf/nphys1027.pdf.

[32] A. Couvert, M. Jeppesen, T. Kawalec, G. Reinaudi, R. Mathevet, and D. Guery-Odelin. A quasi-monomode guided atom laser from an all-optical Bose-Einstein condensate. *EPL (Europhysics Letters)*, 83(5):50001 (6pp), 2008. Available from: http://stacks.iop.org/0295-5075/83/50001.

[33] T. Lahaye, Z. Wang, G. Reinaudi, S. P. Rath, J. Dalibard, and D. Guéry-Odelin. Evaporative cooling of a guided rubidium atomic beam. *Phys. Rev. A*, 72(3):033411, Sep 2005.

[34] T. Lahaye, G. Reinaudi, Z. Wang, A. Couvert, and D. Guery-Odelin. Transport of atom packets in a train of Ioffe-Pritchard traps. *Physical Review A (Atomic, Molecular, and*

Optical Physics), 74(3):033622, 2006. Available from: http://link.aps.org/abstract/PRA/v74/e033622.

[35] O. Morsch, J. H. Müller, M. Cristiani, D. Ciampini, and E. Arimondo. Bloch oscillations and mean-field effects of Bose-Einstein condensates in 1D optical lattices. *Phys. Rev. Lett.*, 87(14):140402, Sep 2001. Available from: http://link.aps.org/doi/10.1103/PhysRevLett.87.140402.

[36] D. Jaksch, C. Bruder, J. I. Cirac, C. W. Gardiner, and P. Zoller. Cold bosonic atoms in optical lattices. *Phys. Rev. Lett.*, 81(15):3108–3111, Oct 1998. Available from: http://link.aps.org/doi/10.1103/PhysRevLett.81.3108.

[37] M. D. Barrett, J. A. Sauer, and M. S. Chapman. All-optical formation of an atomic Bose-Einstein condensate. *Phys. Rev. Lett.*, 87(1):010404, Jun 2001. Available from: http://link.aps.org/doi/10.1103/PhysRevLett.87.010404.

[38] Toshiya Kinoshita, Trevor Wenger, and David S. Weiss. All-optical Bose-Einstein condensation using a compressible crossed dipole trap. *Phys. Rev. A*, 71(1):011602, Jan 2005. Available from: http://link.aps.org/doi/10.1103/PhysRevA.71.011602.

[39] M. Lewenstein, L. Santos, M. A. Baranov, and H. Fehrmann. Atomic Bose-Fermi mixtures in an optical lattice. *Phys. Rev. Lett.*, 92(5):050401, Feb 2004. Available from: http://link.aps.org/doi/10.1103/PhysRevLett.92.050401.

[40] Robert Roth and Keith Burnett. Quantum phases of atomic boson-fermion mixtures in optical lattices. *Phys. Rev. A*, 69(2):021601, Feb 2004. Available from: http://link.aps.org/doi/10.1103/PhysRevA.69.021601.

[41] Markus Greiner, Olaf Mandel, Tilman Esslinger, Theodor W. Hansch, and Immanuel Bloch. Quantum phase transition from a Superfluid to a Mott insulator in a gas of ultracold atoms. *Nature*, 415(6867):39–44, 2002. Available from: http://dx.doi.org/10.1038/415039a.

[42] Markus Greiner, Olaf Mandel, Theodor W. Hansch, and Immanuel Bloch. Collapse and revival of the matter wave field of a Bose-Einstein condensate. *Nature*, 419(6902):51–54, 2002. Available from: http://dx.doi.org/10.1038/nature00968.

[43] Thilo Stöferle, Henning Moritz, Christian Schori, Michael Köhl, and Tilman Esslinger. Transition from a strongly interacting 1D Superfluid to a Mott Insulator. *Phys. Rev. Lett.*, 92(13):130403, Mar 2004. Available from: http://link.aps.org/doi/10.1103/PhysRevLett.92.130403.

[44] Henning Moritz, Thilo Stöferle, Michael Köhl, and Tilman Esslinger. Exciting collective oscillations in a trapped 1D Gas. *Phys. Rev. Lett.*, 91(25):250402, Dec 2003. Available from: http://link.aps.org/doi/10.1103/PhysRevLett.91.250402.

[45] C. D. Fertig, K. M. O'Hara, J. H. Huckans, S. L. Rolston, W. D. Phillips, and J. V. Porto. Strongly inhibited transport of a degenerate 1D Bose gas in a lattice. *Phys. Rev. Lett.*, 94(12):120403, Apr 2005. Available from: http://link.aps.org/doi/10.1103/PhysRevLett.94.120403.

[46] Belen Paredes, Artur Widera, Valentin Murg, Olaf Mandel, Simon Folling, Ignacio Cirac, Gora V. Shlyapnikov, Theodor W. Hansch, and Immanuel Bloch. Tonks-Girardeau gas of ultracold atoms in an optical lattice. *Nature*, 429(6989):277–281, 2004. Available from: http://dx.doi.org/10.1038/nature02530.

[47] C. Davisson and L. H. Germer. The scattering of electrons by a single crystal of nickel. *Nature*, 119:558–560, April 1927. Available from: http://www.nature.com/nature/journal/v119/n2998/pdf/119558a0.pdf.

[48] A. Einstein. *Sitz. Ber. Preuss. Akad. Wiss. (Berlin)*, 1925:3, 1925.

[49] S. N. Bose. Plancks gesetz und lichtquantenhypothese. *Z. Phys.*, 26(1):178–181, 1924. Available from: http://dx.doi.org/10.1007/BF01327326.

[50] F. W. Sears and G. L. Salinger. *Thermodynamics, Kinetic Theory, and Statistical Thermodynamics*. Addison-Wesley, 1986.

[51] B. Saleh and M. Teich. *Fundamentals of Photonics*. John Wiley and Sons, 1991.

[52] H. M. Wiseman. Defining the (atom) laser. *Phys. Rev. A*, 56(3):2068–2084, Sep 1997.

[53] W. Guerin, J.-F. Riou, J. P. Gaebler, V. Josse, P. Bouyer, and A. Aspect. Guided quasi-continuous atom laser. *Physical Review Letters*, 97(20):200402, 2006. Available from: http://link.aps.org/abstract/PRL/v97/e200402.

[54] Roy J. Glauber. The quantum theory of optical coherence. *Phys. Rev.*, 130(6):2529–2539, Jun 1963.

[55] Michael Köhl, Theodor W. Hänsch, and Tilman Esslinger. Measuring the temporal coherence of an atom laser beam. *Phys. Rev. Lett.*, 87(16):160404, Oct 2001.

[56] I. Bloch, T. W. Hansch, and T. Esslinger. Measurement of the spatial coherence of a trapped Bose gas at the phase transition. *Nature*, 403(6766):166–170, 2000. Available from: http://dx.doi.org/10.1038/35003132.

[57] M. R. Andrews, C. G. Townsend, H.-J. Miesner, D. S. Durfee, D. M. Kurn, and W. Ketterle. Observation of interference between two Bose condensates. *Science*, 275(5300):637–641, 1997. Available from: http://www.sciencemag.org/cgi/content/abstract/275/5300/637.

[58] B. P. Anderson and M. A. Kasevich. Macroscopic quantum interference from atomic tunnel arrays. *Science*, 282(5394):1686–1689, 1998. Available from: http://www.sciencemag.org/cgi/content/abstract/282/5394/1686.

[59] Giovanni Cennini, Gunnar Ritt, Carsten Geckeler, and Martin Weitz. All-optical realization of an atom laser. *Phys. Rev. Lett.*, 91(24):240408, Dec 2003.

[60] Immanuel Bloch, Theodor W. Hänsch, and Tilman Esslinger. Atom laser with a cw output coupler. *Phys. Rev. Lett.*, 82(15):3008–3011, Apr 1999.

[61] G. M. Moy, J. J. Hope, and C. M. Savage. Atom laser based on Raman transitions. *Phys. Rev. A*, 55(5):3631–3638, May 1997. Available from: http://link.aps.org/abstract/PRA/v55/p3631.

[62] Franco Dalfovo, Stefano Giorgini, Lev P. Pitaevskii, and Sandro Stringari. Theory of Bose-Einstein condensation in trapped gases. *Rev. Mod. Phys.*, 71(3):463–512, Apr 1999. Available from: http://link.aps.org/abstract/RMP/v71/p463.

[63] J. F. Riou. *Etude des propriétés de propagation d'un laser à atomes*. PhD thesis, Laboratoire Charles Fabry de l'Institut d'Optique (LCFIO), Universite Paris-Sud XI, 2006. Available from: http://tel.archives-ouvertes.fr/tel-00138450/fr/.

[64] M. W. Jack, M. Naraschewski, M. J. Collett, and D. F. Walls. Markov approximation for the atomic output coupler. *Phys. Rev. A*, 59(4):2962–2973, Apr 1999. Available from: http://link.aps.org/doi/10.1103/PhysRevA.59.2962.

[65] F. Gerbier, P. Bouyer, and A. Aspect. Quasicontinuous atom laser in the presence of gravity. *Phys. Rev. Lett.*, 86(21):4729–4732, May 2001. Available from: http://link.aps.org/doi/10.1103/PhysRevLett.86.4729.

[66] J. E. Lye. *Dynamic non-destructive detection of Bose-Einstein condensates and atom lasers*. PhD thesis, Australian National University of Canberra, 2003.

[67] N. P. Robins. *Bose-Einstein condensation and the atom laser*. PhD thesis, Australian National University of Canberra, 2004.

[68] B. DeMarco and D. S. Jin. Onset of Fermi degeneracy in a trapped atomic gas. *Science*, 285(5434):1703–1706, 1999. Available from: http://www.sciencemag.org/cgi/content/abstract/285/5434/1703.

[69] G. Modugno, G. Ferrari, G. Roati, R. J. Brecha, A. Simoni, and M. Inguscio. Bose-Einstein condensation of potassium atoms by sympathetic cooling. *Science*, 294(5545):1320–1322, 2001. Available from: http://www.sciencemag.org/cgi/content/abstract/294/5545/1320.

[70] Tino Weber, Jens Herbig, Michael Mark, Hanns-Christoph Nagerl, and Rudolf Grimm. Bose-Einstein condensation of cesium. *Science*, 299(5604):232–235, 2003. Available from: http://www.sciencemag.org/cgi/content/abstract/299/5604/232.

[71] J. Dalibard and C. Cohen-Tannoudji. Laser cooling below the Doppler limit by polarization gradients: simple theoretical models. *J. Opt. Soc. Am. B*, 6(11):2023–2045, 1989. Available from: http://josab.osa.org/abstract.cfm?URI=josab-6-11-2023.

[72] C. J. Pethick and H. Smith. *Bose-Einstein condensation in dilute gases*. Cambridge University Press, 2002.

[73] H. J. Lewandowski, D. M. Harber, D. L. Whitaker, and E. A. Cornell. Simplified system for creating a Bose-Einstein condensate. *Journal of Low Temperature Physics*, 132(5):309–367, 2003. Available from: http://dx.doi.org/10.1023/A:1024800600621.

[74] Walter Kohn. Cyclotron resonance and de Haas-van Alphen oscillations of an interacting electron gas. *Phys. Rev.*, 123(4):1242–1244, Aug 1961. Available from: http://link.aps.org/doi/10.1103/PhysRev.123.1242.

[75] Mark A. Kasevich. Coherence with atoms. *Science*, 298(5597):1363–1368, 2002. Available from: http://www.sciencemag.org/cgi/content/abstract/298/5597/1363.

[76] M. Kohl, Th. Busch, K. Molmer, T. W. Hansch, and T. Esslinger. Observing the profile of an atom laser beam. *Physical Review A (Atomic, Molecular, and Optical Physics)*, 72(6):063618, 2005. Available from: http://link.aps.org/abstract/PRA/v72/e063618.

[77] Th. Busch, M. Köhl, T. Esslinger, and K. Mølmer. Transverse mode of an atom laser. *Phys. Rev. A*, 65(4):043615, Apr 2002.

[78] Anton Ottl, Stephan Ritter, Michael Kohl, and Tilman Esslinger. Hybrid apparatus for Bose-Einstein condensation and cavity quantum electrodynamics: single atom detection in quantum degenerate gases. *Review of Scientific Instruments*, 77(6):063118, 2006. Available from: http://link.aip.org/link/?RSI/77/063118/1.

[79] Y. Le Coq, J. A. Retter, S. Richard, A. Aspect, and P. Bouyer. Coherent matter wave inertial sensors for precision measurements in space. *Applied Physics B: Lasers and Optics*, 84(4):627–632, 2006. Available from: http://dx.doi.org/10.1007/s00340-006-2363-2.

[80] M. Jeppesen. *to be published*. PhD thesis, Australian National University of Canberra, 2008.

[81] Gregor Wentzel. Eine verallgemeinerung der quantenbedingungen für die zwecke der wellenmechanik. *Zeitschrift für Physik A Hadrons and Nuclei*, 38(6):518–529, 1926. Available from: http://dx.doi.org/10.1007/BF01397171.

[82] H. A. Kramers. Wellenmechanik und halbzahlige quantisierung. *Zeitschrift für Physik A Hadrons and Nuclei*, 39(10):828–840, 1926. Available from: http://dx.doi.org/10.1007/BF01451751.

[83] L. Brillouin. La mécanique ondulatoire de Schrödinger: une méthode de résolution par approximations successives. *Comptes Rendus de l'Académie des Sciences*, 183:24, 1926.

[84] C. J. Borde. *C. R. Acad. Sci. Hebd Seances Acad. Sci. D*, 4:509, 2001.

[85] M. Kozuma, L. Deng, E. W. Hagley, J. Wen, R. Lutwak, K. Helmerson, S. L. Rolston, and W. D. Phillips. Coherent splitting of Bose-Einstein condensed atoms with optically induced Bragg diffraction. *Phys. Rev. Lett.*, 82(5):871–875, Feb 1999. Available from: http://link.aps.org/doi/10.1103/PhysRevLett.82.871.

[86] J. Dugue, N. P. Robins, C. Figl, M. Jeppesen, P. Summers, M. T. Johnsson, J. J. Hope, and J. D. Close. Investigation and comparison of multistate and two-state atom laser-output couplers. *Physical Review A (Atomic, Molecular, and Optical Physics)*, 75(5):053602, 2007. Available from: http://link.aps.org/abstract/PRA/v75/e053602.

[87] J. E. Debs, D. Döring, N. P. Robins, C. Figl, P. A. Altin, and J. D. Close. *arXiv:0812.2295v3*. Available from: http://arxiv.org/abs/0812.2295.

[88] Yoshio Torii, Yoichi Suzuki, Mikio Kozuma, Toshiaki Sugiura, Takahiro Kuga, Lu Deng, and E. W. Hagley. Mach-Zehnder Bragg interferometer for a Bose-Einstein condensate. *Phys. Rev. A*, 61(4):041602, Feb 2000. Available from: http://link.aps.org/doi/10.1103/PhysRevA.61.041602.

[89] D. Döring, J. E. Debs, N. P. Robins, C. Figl, P. A. Altin, and J. D. Close. A free-space Ramsey interferometer with Bose-condensed atoms. *arXiv:0812.2310v1*. Available from: http://arxiv.org/abs/0812.2310.

[90] Peter J. Martin, Bruce G. Oldaker, Andrew H. Miklich, and David E. Pritchard. Bragg scattering of atoms from a standing light wave. *Phys. Rev. Lett.*, 60(6):515–518, Feb 1988. Available from: http://link.aps.org/abstract/PRL/v60/p515.

[91] David M. Giltner, Roger W. McGowan, and Siu Au Lee. Atom interferometer based on Bragg scattering from standing light waves. *Phys. Rev. Lett.*, 75(14):2638–2641, Oct

1995. Available from: http://link.aps.org/doi/10.1103/PhysRevLett.75.2638.

[92] O. Garcia, B. Deissler, K. J. Hughes, J. M. Reeves, and C. A. Sackett. Bose-Einstein condensate interferometer with macroscopic arm separation. *Physical Review A (Atomic, Molecular, and Optical Physics)*, 74(3):031601, 2006. Available from: http://link.aps.org/abstract/PRA/v74/e031601.

[93] Markus K. Oberthaler, Roland Abfalterer, Stefan Bernet, Jörg Schmiedmayer, and Anton Zeilinger. Atom waves in crystals of light. *Phys. Rev. Lett.*, 77(25):4980–4983, Dec 1996. Available from: http://link.aps.org/doi/10.1103/PhysRevLett.77.4980.

[94] Stefan Bernet, Markus Oberthaler, Roland Abfalterer, Jörg Schmiedmayer, and Anton Zeilinger. Modulation of atomic de Broglie waves using Bragg diffraction. *Quantum and Semiclassical Optics: Journal of the European Optical Society Part B*, 8(3):497–509, 1996. Available from: http://stacks.iop.org/1355-5111/8/497.

[95] David M. Giltner, Roger W. McGowan, and Siu Au Lee. Theoretical and experimental study of the Bragg scattering of atoms from a standing light wave. *Phys. Rev. A*, 52(5):3966–3972, Nov 1995. Available from: http://link.aps.org/abstract/PRA/v52/p3966.

[96] Yu. B. Ovchinnikov, J. H. Müller, M. R. Doery, E. J. D. Vredenbregt, K. Helmerson, S. L. Rolston, and W. D. Phillips. Diffraction of a released Bose-Einstein condensate by a pulsed standing light wave. *Phys. Rev. Lett.*, 83(2):284–287, Jul 1999. Available from: http://link.aps.org/doi/10.1103/PhysRevLett.83.284.

[97] L. Deng, E. W. Hagley, J. Denschlag, J. E. Simsarian, Mark Edwards, Charles W. Clark, K. Helmerson, S. L. Rolston, and W. D. Phillips. Temporal, matter-wave-dispersion Talbot effect. *Phys. Rev. Lett.*, 83(26):5407–5411, Dec 1999. Available from: http://link.aps.org/doi/10.1103/PhysRevLett.83.5407.

[98] J. Stenger, S. Inouye, A. P. Chikkatur, D. M. Stamper-Kurn, D. E. Pritchard, and W. Ketterle. Bragg spectroscopy of a Bose-Einstein condensate. *Phys. Rev. Lett.*,

82(23):4569–4573, Jun 1999. Available from: http://link.aps.org/doi/10.1103/PhysRevLett.82.4569.

[99] S. Richard, F. Gerbier, J. H. Thywissen, M. Hugbart, P. Bouyer, and A. Aspect. Momentum spectroscopy of 1D phase fluctuations in Bose-Einstein condensates. *Phys. Rev. Lett.*, 91(1):010405, Jul 2003. Available from: http://link.aps.org/doi/10.1103/PhysRevLett.91.010405.

[100] Mikio Kozuma, Yoichi Suzuki, Yoshio Torii, Toshiaki Sugiura, Takahiro Kuga, E. W. Hagley, and L. Deng. Phase-coherent amplification of matter waves. *Science*, 286(5448):2309–2312, 1999. Available from: http://www.sciencemag.org/cgi/content/abstract/286/5448/2309.

[101] S. Inouye, T. Pfau, S. Gupta, A. P. Chikkatur, A. Gorlitz, D. E. Pritchard, and W. Ketterle. Phase-coherent amplification of atomic matter waves. *Nature*, 402(6762):641–644, 1999. Available from: http://dx.doi.org/10.1038/45194.

[102] Dominik Schneble, Yoshio Torii, Micah Boyd, Erik W. Streed, David E. Pritchard, and Wolfgang Ketterle. The onset of matter-wave amplification in a superradiant Bose-Einstein condensate. *Science*, 300(5618):475–478, 2003. Available from: http://www.sciencemag.org/cgi/content/abstract/300/5618/475.

[103] Dominik Schneble, Gretchen K. Campbell, Erik W. Streed, Micah Boyd, David E. Pritchard, and Wolfgang Ketterle. Raman amplification of matter waves. *Phys. Rev. A*, 69(4):041601, Apr 2004. Available from: http://link.aps.org/doi/10.1103/PhysRevA.69.041601.

[104] Y. Shin, G.-B. Jo, M. Saba, T. A. Pasquini, W. Ketterle, and D. E. Pritchard. Optical weak link between two spatially separated Bose-Einstein condensates. *Physical Review Letters*, 95(17):170402, 2005. Available from: http://link.aps.org/abstract/PRL/v95/e170402.

[105] Immanuel Bloch, Michael Köhl, Markus Greiner, Theodor W. Hänsch, and Tilman Esslinger. Optics with an atom laser beam. *Phys. Rev. Lett.*, 87(3):030401, Jul 2001. Available from: http://link.aps.org/doi/10.1103/PhysRevLett.87.030401.

[106] Ying Wu and Xiaoxue Yang. Bragg diffraction of an atom laser by an optical standing wave. *J. Opt. Soc. Am. B*, 23(5):913–917, 2006. Available from: http://josab.osa.org/abstract.cfm?URI=josab-23-5-913.

[107] J. J Sakurai. *Advanced quantum mechanics*. Addison-Wesley, 1967.

[108] E. P. Gross. *Nuovo Cimento*, 20(454), 1961.

[109] E. P. Gross. *J. Math. Phys.*, 4(195), 1963.

[110] L. P. Pitaevskii. *Zh. Eksp. Teor. Fiz.*, 40(646), 1961.

[111] R. J. Ballagh, K. Burnett, and T. F. Scott. Theory of an output coupler for Bose-Einstein condensed atoms. *Phys. Rev. Lett.*, 78(9):1607–1611, Mar 1997. Available from: http://link.aps.org/abstract/PRL/v78/p1607.

[112] J. Schneider and A. Schenzle. Output from an atom laser: theory vs. experiment. *Applied Physics B: Lasers and Optics*, 69(5):353–356, 1999. Available from: http://dx.doi.org/10.1007/s003400050819.

[113] H. Steck, M. Naraschewski, and H. Wallis. Output of a pulsed atom laser. *Phys. Rev. Lett.*, 80(1):1–5, Jan 1998. Available from: http://link.aps.org/abstract/PRL/v80/p1.

[114] Weiping Zhang and D. F. Walls. Gravitational and collective effects in an output coupler for a Bose-Einstein condensate in an atomic trap. *Phys. Rev. A*, 57(2):1248–1252, Feb 1998. Available from: http://link.aps.org/abstract/PRA/v57/p1248.

[115] W. Press, S. Teukolsky, W. Vetterling, and B. Flannery. *Numerical recipes in C*. Cambridge University Press, 1992.

[116] John Jeffers, Peter Horak, Stephen M. Barnett, and Paul M. Radmore. Bound mode of an atom laser. *Phys. Rev. A*, 62(4):043602, Sep 2000. Available from: http://link.aps.org/abstract/PRA/v62/e043602.

[117] J. J. Hope, G. M. Moy, M. J. Collett, and C. M. Savage. Steady-state quantum statistics of a non-Markovian atom laser. *Phys. Rev. A*, 61(2):023603, Jan 2000. Available from: http://link.aps.org/abstract/PRA/v61/e023603.

[118] G. M. Moy, J. J. Hope, and C. M. Savage. Born and Markov approximations for atom lasers. *Phys. Rev. A*, 59(1):667–675, Jan 1999. Available from: http://link.aps.org/abstract/PRA/v59/p667.

[119] O. Zobay and B. M. Garraway. Atom trapping and two-dimensional Bose-Einstein condensates in field-induced adiabatic potentials. *Physical Review A (Atomic, Molecular, and Optical Physics)*, 69(2):023605, 2004. Available from: http://link.aps.org/abstract/PRA/v69/e023605.

[120] Y. Colombe, E. Knyazchyan, O. Morizot, B. Mercier, V. Lorent, and H. Perrin. Ultracold atoms confined in rf-induced two-dimensional trapping potentials. *EPL (Europhysics Letters)*, 67(4):593–599, 2004. Available from: http://stacks.iop.org/0295-5075/67/593.

[121] F. Pereira Dos Santos, J. Léonard, Junmin Wang, C. J. Barrelet, F. Perales, E. Rasel, C. S. Unnikrishnan, M. Leduc, and C. Cohen-Tannoudji. Bose-Einstein condensation of metastable helium. *Phys. Rev. Lett.*, 86(16):3459–3462, Apr 2001. Available from: http://link.aps.org/doi/10.1103/PhysRevLett.86.3459.

[122] S. Moal, M. Portier, J. Kim, J. Dugue, U. D. Rapol, M. Leduc, and C. Cohen-Tannoudji. Accurate determination of the scattering length of metastable helium atoms using dark resonances between atoms and exotic molecules. *Physical Review Letters*, 96(2):023203, 2006. Available from: http://link.aps.org/abstract/PRL/v96/e023203.

[123] A. Robert, O. Sirjean, A. Browaeys, J. Poupard, S. Nowak, D. Boiron, C. I. Westbrook, and A. Aspect. A Bose-Einstein condensate of metastable atoms. *Science*, 292(5516):461–464, 2001. Available from: http://www.sciencemag.org/cgi/content/abstract/292/5516/461.

[124] A. S. Tychkov, T. Jeltes, J. M. McNamara, P. J. J. Tol, N. Herschbach, W. Hogervorst, and W. Vassen. Metastable helium Bose-Einstein condensate with a large number of atoms. *Physical Review A (Atomic, Molecular, and Optical Physics)*, 73(3):031603, 2006. Available from: http://link.aps.org/abstract/PRA/v73/e031603.

[125] R. G. Dall and A. G. Truscott. Bose-Einstein condensation of metastable helium in a bi-planar quadrupole Ioffe configuration trap. *Optics Communications*, 270:255–261, feb

2007. Available from: http://dx.doi.org/10.1016/j.optcom.2006.09.031.

[126] H. C. Mastwijk, J. W. Thomsen, P. van der Straten, and A. Niehaus. Optical collisions of cold, metastable helium atoms. *Phys. Rev. Lett.*, 80(25):5516–5519, Jun 1998. Available from: http://link.aps.org/doi/10.1103/PhysRevLett.80.5516.

[127] Paul S. Julienne and Frederick H. Mies. Collisions of ultracold trapped atoms. *J. Opt. Soc. Am. B*, 6(11):2257–2269, 1989. Available from: http://josab.osa.org/abstract.cfm?URI=josab-6-11-2257.

[128] G. V. Shlyapnikov, J. T. M. Walraven, U. M. Rahmanov, and M. W. Reynolds. Decay kinetics and Bose condensation in a gas of spin-polarized triplet helium. *Phys. Rev. Lett.*, 73(24):3247–3250, Dec 1994. Available from: http://link.aps.org/doi/10.1103/PhysRevLett.73.3247.

[129] P. O. Fedichev, M. W. Reynolds, U. M. Rahmanov, and G. V. Shlyapnikov. Inelastic decay processes in a gas of spin-polarized triplet helium. *Phys. Rev. A*, 53(3):1447–1453, Mar 1996. Available from: http://link.aps.org/doi/10.1103/PhysRevA.53.1447.

[130] J. Pereira Dos Santos, F. *Condensation de Bose-Einstein de l'hélium métastable*. PhD thesis, Université Pierre et Marie Curie, 2002. Available from: http://tel.archives-ouvertes.fr/tel-00002267.

[131] J. Léonard. *Photo-association de l'hélium métastable au voisinage de la condensation de Bose-Einstein et formation de dimères géants*. PhD thesis, Université Pierre et Marie Curie, 2003. Available from: http://tel.archives-ouvertes.fr/tel-00004295.

[132] S. Moal. *Photo-association à 2 photons de l'hélium métastable ultrafroid*. PhD thesis, Université Pierre et Marie Curie, 2006.

[133] A. Browaeys. *Piégeage magnétique d'un gaz d'helium metastable : vers la condensation de Bose-Einstein*. PhD thesis, Universite Paris Sud - Paris XI, 2000. Available from: http://tel.archives-ouvertes.fr/docs/00/04/48/26/PDF/tel-00001291.pdf.

[134] F. Pereira Dos Santos, F. Perales, J. Léonard, A. Sinatra, J. Wang, F.S. Pavone, E. Rasel, C.S. Unnikrishnan, and M. Leduc. Efficient magneto-optical trapping of a metastable helium gas. *The European Physical Journal Applied Physics*, 14(1):69–76, apr 2001. Available from: http://dx.doi.org/doi/10.1051/epjap:2001140.

[135] William D. Phillips and Harold Metcalf. Laser deceleration of an atomic beam. *Phys. Rev. Lett.*, 48(9):596–599, Mar 1982. Available from: http://link.aps.org/doi/10.1103/PhysRevLett.48.596.

[136] F. Pereira Dos Santos, F. Perales, J. Léonard, A. Sinatra, J. Wang, F.S. Pavone, E. Rasel, C.S. Unnikrishnan, and M. Leduc. Efficient magneto-optical trapping of a metastable helium gas. *The European Physical Journal Applied Physics*, 14(1):69–76, apr 2001. Available from: http://dx.doi.org/10.1051/epjap:2001140.

[137] F. Pereira Dos Santos, F. Perales, J. Léonard, A. Sinatra, Junmin Wang, F. Saverio Pavone, E. Rasel, C.S. Unnikrishnan, and M. Leduc. Penning collisions of laser-cooled metastable helium atoms. *The European Physical Journal D*, 14(1):15–22, 2001. Available from: http://dx.doi.org/10.1007/s100530170228.

[138] Tilman Esslinger, Immanuel Bloch, and Theodor W. Hänsch. Bose-Einstein condensation in a quadrupole-Ioffe-configuration trap. *Phys. Rev. A*, 58(4):R2664–R2667, Oct 1998. Available from: http://link.aps.org/doi/10.1103/PhysRevA.58.R2664.

[139] Dan. M. Stamper-Kurn. *Peeking and poking at a new quantum fluid: studies of gaseous Bose-Einstein condensates in magnetic and optical traps*. PhD thesis, Massachusetts Institute of Technology, 2000.

[140] Harald F. Hess. Evaporative cooling of magnetically trapped and compressed spin-polarized hydrogen. *Phys. Rev. B*, 34(5):3476–3479, Sep 1986. Available from: http://link.aps.org/doi/10.1103/PhysRevB.34.3476.

[141] R. Grimm, M. Weidemüller, and Y. B. Ovchinnikov. *Advances in atomic, molecular and optical physics*. Academic Press, 2000.

[142] Steven Chu, J. E. Bjorkholm, A. Ashkin, and A. Cable. Experimental observation of

optically trapped atoms. *Phys. Rev. Lett.*, 57(3):314–317, Jul 1986. Available from: http://link.aps.org/doi/10.1103/PhysRevLett.57.314.

[143] J. E. Bjorkholm, R. R. Freeman, A. Ashkin, and D. B. Pearson. Observation of focusing of neutral atoms by the dipole forces of resonance-radiation pressure. *Phys. Rev. Lett.*, 41(20):1361–1364, Nov 1978. Available from: http://link.aps.org/doi/10.1103/PhysRevLett.41.1361.

[144] A. Aspect, G. Grynberg, and C. Fabre. *Introduction aux lasers et à l'optique quantique*. Ellipses, 1997.

[145] Nir Davidson, Heun Jin Lee, Charles S. Adams, Mark Kasevich, and Steven Chu. Long atomic coherence times in an optical dipole trap. *Phys. Rev. Lett.*, 74(8):1311–1314, Feb 1995. Available from: http://link.aps.org/doi/10.1103/PhysRevLett.74.1311.

[146] Roee Ozeri, Lev Khaykovich, and Nir Davidson. Long spin relaxation times in a single-beam blue-detuned optical trap. *Phys. Rev. A*, 59(3):R1750–R1753, Mar 1999. Available from: http://link.aps.org/doi/10.1103/PhysRevA.59.R1750.

[147] J. Dowling and J. Gea-Banacloche. *Evanescent light-wave atom mirrors, resonators, waveguides, and traps*. Academic Press, 1996. Available from: http://www.phys.lsu.edu/~jdowling/publications/Dowling96.pdf.

[148] Claude N. Cohen-Tannoudji. Nobel lecture: Manipulating atoms with photons. *Rev. Mod. Phys.*, 70(3):707–719, Jul 1998. Available from: http://link.aps.org/doi/10.1103/RevModPhys.70.707.

[149] A. Ashkin. Trapping of atoms by resonance radiation pressure. *Phys. Rev. Lett.*, 40(12):729–732, Mar 1978. Available from: http://link.aps.org/doi/10.1103/PhysRevLett.40.729.

[150] Charles S. Adams, Heun Jin Lee, Nir Davidson, Mark Kasevich, and Steven Chu. Evaporative cooling in a crossed dipole trap. *Phys. Rev. Lett.*, 74(18):3577–3580, May 1995. Available from: http://link.aps.org/doi/10.1103/PhysRevLett.74.3577.

[151] S. Jochim, M. Bartenstein, A. Altmeyer, G. Hendl, S. Riedl, C. Chin, J. Hecker Denschlag, and R. Grimm. Bose-Einstein condensation of molecules. *Science*, 302(5653):2101–2103, 2003. Available from: http://www.sciencemag.org/cgi/content/abstract/302/5653/2101.

[152] J Fuchs, G J Duffy, G Veeravalli, P Dyke, M Bartenstein, C J Vale, P Hannaford, and W J Rowlands. Molecular Bose-Einstein condensation in a versatile low power crossed dipole trap. *Journal of Physics B: Atomic, Molecular and Optical Physics*, 40(20):4109–4118, 2007. Available from: http://stacks.iop.org/0953-4075/40/4109.

[153] D. M. Stamper-Kurn, M. R. Andrews, A. P. Chikkatur, S. Inouye, H.-J. Miesner, J. Stenger, and W. Ketterle. Optical confinement of a Bose-Einstein condensate. *Phys. Rev. Lett.*, 80(10):2027–2030, Mar 1998. Available from: http://link.aps.org/doi/10.1103/PhysRevLett.80.2027.

[154] C. Cohen-Tannoudji, B. Diu, and F. Laloë. *Mécanique Quantique*. Hermann, 1973.

[155] M. Portier. *Molécules exotiques d'Hélium*. PhD thesis, Université Pierre et Marie Curie (Paris VI), 2007.

[156] J. Stärck and W. Meyer. Long-range interaction potential of the 3[sigma]g+ state of he2. *Chemical Physics Letters*, 225(1-3):229–232, 1994. Available from: http://www.sciencedirect.com/science/article/B6TFN-44WCW8J-75/2/043679120e0c27207a076bf270d97339.

[157] Michal Przybytek and Bogumil Jeziorski. Bounds for the scattering length of spin-polarized helium from high-accuracy electronic structure calculations. *The Journal of Chemical Physics*, 123(13):134315, 2005. Available from: http://link.aip.org/link/?JCP/123/134315/1.

[158] M. W. Müller, A. Merz, M. W. Ruf, H. Hotop, W. Meyer, and M. Movre. Experimental and theoretical studies of the Bi-excited collision systems He*(23S)+He*(23S, 21S) at thermal and subthermal kinetic energies. *Zeitschrift für Physik D Atoms, Molecules and Clusters*, 21(2):89–112, 1991. Available from: http://dx.doi.org/10.1007/BF01425589.

[159] V. S. Letokhov. Narrowing of the Doppler width in a standing light wave. *JETP. Lett.*, 7:272, 1968. Available from: http://www.jetpletters.ac.ru/ps/1685/article_25663.pdf.

[160] C. Salomon, J. Dalibard, A. Aspect, H. Metcalf, and C. Cohen-Tannoudji. Channeling atoms in a laser standing wave. *Phys. Rev. Lett.*, 59(15):1659–1662, Oct 1987. Available from: http://link.aps.org/doi/10.1103/PhysRevLett.59.1659.

[161] Ph. Courteille, R. S. Freeland, D. J. Heinzen, F. A. van Abeelen, and B. J. Verhaar. Observation of a Feshbach resonance in cold atom scattering. *Phys. Rev. Lett.*, 81(1):69–72, Jul 1998. Available from: http://link.aps.org/doi/10.1103/PhysRevLett.81.69.

[162] M. Theis, G. Thalhammer, K. Winkler, M. Hellwig, G. Ruff, R. Grimm, and J. Hecker Denschlag. Tuning the scattering length with an optically induced Feshbach resonance. *Phys. Rev. Lett.*, 93(12):123001, Sep 2004. Available from: http://link.aps.org/doi/10.1103/PhysRevLett.93.123001.

[163] Tim Rom, Thorsten Best, Olaf Mandel, Artur Widera, Markus Greiner, Theodor W. Hänsch, and Immanuel Bloch. State selective production of molecules in optical lattices. *Phys. Rev. Lett.*, 93(7):073002, Aug 2004. Available from: http://link.aps.org/doi/10.1103/PhysRevLett.93.073002.

[164] K. W. Madison, F. Chevy, W. Wohlleben, and J. Dalibard. Vortex formation in a stirred Bose-Einstein condensate. *Phys. Rev. Lett.*, 84(5):806–809, Jan 2000. Available from: http://link.aps.org/doi/10.1103/PhysRevLett.84.806.

[165] Immanuel Bloch, Markus Greiner, Olaf Mandel, and Theodor W. Hänsch. Coherent cold collisions with neutral atoms in optical lattices. *Philosophical Transactions of the Royal Society A: Mathematical, Physical and Engineering Sciences*, 361(1808):1409–1416, 2003. Available from: http://dx.doi.org/10.1098/rsta.2003.1210.

[166] Matthew P. A. Fisher, Peter B. Weichman, G. Grinstein, and Daniel S. Fisher. Boson localization and the superfluid-insulator transition. *Phys. Rev. B*, 40(1):546–570, Jul 1989. Available from: http://link.aps.org/doi/10.1103/PhysRevB.40.546.

[167] Wilhelm Zwerger. Mott-Hubbard transition of cold atoms in optical lattices. *Journal of Optics B: Quantum and Semiclassical Optics*, 5(2):S9–S16, 2003. Available from: http://stacks.iop.org/1464-4266/5/S9.

[168] Markus Greiner. *Ultracold quantum gases in three-dimensional optical lattice potentials*. PhD thesis, Ludwig-Maxilians-Universität München, 2003.

[169] Simon Folling, Artur Widera, Torben Muller, Fabrice Gerbier, and Immanuel Bloch. Formation of spatial shell structure in the Superfluid to Mott insulator transition. *Physical Review Letters*, 97(6):060403, 2006. Available from: http://link.aps.org/abstract/PRL/v97/e060403.

[170] Corinna Kollath, Andreas M. Lauchli, and Ehud Altman. Quench dynamics and nonequilibrium phase diagram of the Bose-Hubbard model. *Physical Review Letters*, 98(18):180601, 2007. Available from: http://link.aps.org/abstract/PRL/v98/e180601.

[171] S. Burger, F. S. Cataliotti, C. Fort, P. Maddaloni, F. Minardi, and M. Inguscio. Quasi-2D Bose-Einstein condensation in an optical lattice. *EPL (Europhysics Letters)*, 57(1):1–6, 2002. Available from: http://stacks.iop.org/0295-5075/57/1.

[172] T. L. Gustavson, A. P. Chikkatur, A. E. Leanhardt, A. Görlitz, S. Gupta, D. E. Pritchard, and W. Ketterle. Transport of Bose-Einstein condensates with optical tweezers. *Phys. Rev. Lett.*, 88(2):020401, Dec 2001. Available from: http://link.aps.org/doi/10.1103/PhysRevLett.88.020401.

[173] Markus Greiner, Immanuel Bloch, Theodor W. Hänsch, and Tilman Esslinger. Magnetic transport of trapped cold atoms over a large distance. *Phys. Rev. A*, 63(3):031401, Feb 2001. Available from: http://link.aps.org/doi/10.1103/PhysRevA.63.031401.

[174] W. Hänsel, J. Reichel, P. Hommelhoff, and T. W. Hänsch. Magnetic conveyor belt for transporting and merging trapped atom clouds. *Phys. Rev. Lett.*, 86(4):608–611, Jan 2001. Available from: http://link.aps.org/doi/10.1103/PhysRevLett.86.608.

[175] M.-O. Mewes, M. R. Andrews, N. J. van Druten, D. M. Kurn, D. S. Durfee, and W. Ketterle. Bose-Einstein condensation in a tightly confining dc magnetic trap. *Phys. Rev. Lett.*, 77(3):416–419, Jul 1996. Available from: http://link.aps.org/doi/10.1103/PhysRevLett.77.416.

[176] E. Guyon, J. P. Hulin, and L. Petit. *Hydrodynamique Physique*. Savoirs Actuels (EDP Science/CNRS Editions), 2001.

Titre de la thèse : Sources Ultrafroides Avancées pour l'Interféromètrie et la Physique Atomique.

Résumé : Dans ce mémoire nous présentons des sources ultra-froides utilisant des condensats de Bose-Einstein pour des applications en interféromètrie et physique atomique.

Nous produisons un laser à atomes de ^{87}Rb par couplage optique Raman. Initialement piégés magnétiquement, les atomes sont transférés dans un état insensible aux champs magnétiques et tombent sous l'effet de la gravité. Nous montrons qu'à l'inverse d'une méthode d'extraction Radio-Fréquence l'impulsion transférée aux atomes permet de réduire la divergence et d'améliorer le profil spatial du faisceau atomique. Nous prouvons que chacun des deux faisceaux Raman peut être utilisé indépendamment pour diffracter le laser à atomes de manière efficace et cohérente en utilisant une fraction de lumière rétro-diffusée. La dynamique des lasers à atomes extraits par couplage RF est également étudiée théoriquement.

Nous détaillons ensuite les améliorations apportées au dispositif expérimental permettant de condenser des atomes d'hélium métastable (^{4}He*). Nous décrivons l'ensemble du nouveau système laser destiné au piégeage et au ralentissement des atomes, ainsi qu'à leur transfert dans un piège dipolaire ou un réseau optique. L'ajout d'un multiplicateur d'électrons fournit une méthode de détection non-destructive en temps réel fondée sur les collisions Penning. Enfin, nous présentons un nouveau piège magnétique à grande accessibilité optique, conçu et construit pour produire un condensat d'atomes ^{4}He* et le transférer, in-situ, dans un réseau optique à 3 dimensions.

Mots Clés : Atomes ultra-froids, condensat de Bose-Einstein, lasers à atomes, couplage Raman, hélium métastable, piège optique dipolaire, réseau optique.

Title of the thesis : Advanced Ultracold Sources for Atomic Physics and Atom Interferometry.

Abstract : In this thesis we present ultracold sources using Bose-Einstein Condensates for atom interferometry and atomic physics applications.

We produce a ^{87}Rb atom laser using an optical Raman out-coupling technique. The atoms are transferred from their initial magnetically trapped state to a state which is insensitive to magnetic fields and subsequently fall under gravity. We show that, in contrast to a standard Radio-Frequency (RF) out-coupling method, the initial momentum imparted to the atoms reduces the divergence and improves the spatial profile of the beam. Alternatively, we demonstrate that each of the two Raman beams can be used independently to provide efficient and coherent splitting of the atom laser using a fraction of back-reflected light. We also investigate theoretically the dynamics of RF out-coupled atom laser systems.

Then we present details of significant improvements on the experimental setup used to condense metastable helium atoms (^{4}He*). We present the layout of a new laser system operated for trapping and cooling the atoms, as well as the optical configuration to transfer them into a dipole trap or an optical lattice. A channel electron multiplier is added to provide a non-destructive real-time detection method based on Penning collisions. Finally, we describe the design of a new magnetic trap with improved optical access, which we conceived and constructed to allow for ^{4}He* Bose-Einstein condensation to be compatible with in-situ loading of the condensed gas into a 3 dimensional lattice.

Key words : Ultra-cold atoms, Bose-Einstein Condensate, atom lasers, Raman out-coupling, metastable helium, optical dipole trap, optical lattice.